



**GEOFORSCHUNGSZENTRUM POTSDAM**  
STIFTUNG DES ÖFFENTLICHEN RECHTS

---

# Scientific Technical Report

ISSN 1610-0956

Deformation, erosion and natural resources  
in continental collision zones

Insight from scaled sandbox simulations

---

Dissertation  
zur Erlangung des akademischen Doktorgrades  
doctor rerum naturalium (Dr. rer. nat.)  
im Fachbereich Geowissenschaften  
der Freien Universität Berlin  
vorgelegt von

Silvan Hoth

Potsdam, August 2005

Tag der Disputation: 09. November 2005

**Gutachter**

Prof. Dr. Onno Oncken (1. Gutachter)  
Freie Universität Berlin, GeoForschungsZentrum Potsdam

Prof. Dr. Manfred Strecker (2. Gutachter)  
Universität Potsdam

Sie begriffen, daß die Vernunft nur das einsieht, was sie selbst nach ihrem Entwurfe hervorbringt, daß sie mit Principien ihrer Urtheile nach beständigen Gesetzen vorgehen und die Natur nöthigen müsse auf ihre Fragen zu antworten, nicht aber sich von ihr allein gleichsam am Leitbände gängeln lassen müsse; denn sonst hängen zufällige, nach keinem vorher entworfenen Plane gemachte Beobachtungen gar nicht mit einem nothwendigen Gesetz zusammen, welches doch die Vernunft sucht und Bedarf...

*Immanuel Kant, Zweite Vorrede zur Kritik der reinen Vernunft, Königsberg, 1787*



# Contents

<b>Summary</b>	<b>iii</b>
<b>Zusammenfassung</b>	<b>v</b>
<b>1 Introduction</b>	<b>1</b>
<b>2 Orogen-scale erosion</b>	<b>5</b>
<b>3 Continental collision zones</b>	<b>13</b>
3.1 Kinematic concepts of bivergent orogens . . . . .	13
3.2 Kinematic models of fold and thrust belts . . . . .	13
3.3 The Critical Coulomb Wedge concept . . . . .	17
3.4 The minimum work concept of mountain building . . . . .	23
<b>4 Experimental method</b>	<b>25</b>
4.1 Physical properties of analogue materials . . . . .	26
4.2 Experimental setup . . . . .	29
4.3 Data acquisition and processing with Particle Image Velocimetry . . . . .	34
4.4 Data mining and its limitations . . . . .	36
<b>5 Kinematic boundary conditions and their influence on bivergent wedge evolution</b>	<b>41</b>
5.1 Reference experiment . . . . .	41
5.2 Experiments with other kinematic boundary conditions . . . . .	50
5.3 Discussion . . . . .	65
5.3.1 Four-staged evolutionary model for bivergent sand-wedges . . . . .	65
5.3.2 Strain transfer in bivergent wedges . . . . .	66
5.3.3 The timing of thrust initiation . . . . .	72
5.3.4 The spacing of thrusts . . . . .	72
5.3.5 Frontal accretion in the retro-wedge . . . . .	73
5.3.6 Parameter combinations . . . . .	75
5.3.7 Self-similar growth . . . . .	76
5.4 Implications and predictions for natural bivergent wedges . . . . .	77
5.5 Implications for erosion experiments . . . . .	82

---

<b>6</b>	<b>The influence of erosion on bivergent wedge evolution</b>	<b>83</b>
6.1	Reference experiment without erosion . . . . .	83
6.2	Experiments with erosion . . . . .	86
6.3	Discussion . . . . .	95
6.3.1	Concepts of bivergent wedge evolution and the accretion cycle . . . . .	95
6.3.2	Discrete erosion versus continuous deformation . . . . .	95
6.3.3	Influence of erosion on bivergent wedge kinematics . . . . .	98
6.4	Implications and predictions for natural orogens . . . . .	100
<b>7</b>	<b>Deformation versus erosion</b>	<b>103</b>
<b>8</b>	<b>Foreland basin evolution and the growth of an orogenic wedge</b>	<b>105</b>
8.1	Introduction . . . . .	105
8.2	Method . . . . .	106
8.3	Results and discussion . . . . .	107
<b>9</b>	<b>Perspectives</b>	<b>111</b>
	<b>Acknowledgements</b>	<b>113</b>
	<b>References</b>	<b>115</b>
	<b>Appendices</b>	<b>129</b>
<b>A</b>	<b>Abbreviations and symbols</b>	<b>131</b>
<b>B</b>	<b>Supplementary data on DVD</b>	<b>133</b>
<b>C</b>	<b>Technical specifications of tested springs</b>	<b>135</b>
<b>D</b>	<b>List of experiments</b>	<b>137</b>
	<b>Curriculum vitae</b>	<b>141</b>

# Summary

Mountain belts result from the interaction between deformation, flexure and surface processes. Previous research has either focused on the mechanics of orogenic evolution and thereby paid special attention to its shape, or on the influence of surface processes on deformation. Thus, both attempts follow the *bird's eye view*. However, conceptual models such as the Critical Coulomb Wedge concept or the forward- and the backward-breaking model of thrust propagation provide only little to no predictive power with respect to the magnitude and location of deformation and surface uplift. We therefore aim to elucidate the spatio-temporal evolution of strain-partitioning within and the associated surface uplift of bivergent wedges. However, such a methodological approach would require the *view from below*.

This challenge is addressed with two series of sandbox experiments, each with a specific purpose. The 1<sup>st</sup> experimental series was designed to analyse the influence of flexure, the mechanic stratigraphy as well as the strength contrast between the lower and the upper plate on the ratio between internal deformation versus foreland-ward propagation of deformation. With the 2<sup>nd</sup> experimental series, special emphasis was devoted to the effect of the location of erosion with respect to the convergence geometry as well as the mode of erosion on the tectonic mass transfer in bivergent wedges.

We introduce a setup, which allows for the first time in sandbox experiments, the simulation of load-driven flexure. Incorporation of Particle Image Velocimetry provided time-series of the incremental displacement field and its derivatives such as horizontal shear-strain. To facilitate interpretation and to successfully communicate results, two new display types, i. e., the surface uplift and the evolution of deformation map are introduced.

Based on the 1<sup>st</sup> experimental series we suggest a four-staged evolutionary model for bivergent orogenic wedges. An initial crustal scaled pop-up (stage I) or backfold is followed by a proto pro-wedge, in which frontal accretion dominates (stage II). Basal accretion commences if a mid-crustal detachment is present (stage III). Frontal accretion within the retro-wedge occurs during stage IV.

We propose the conceptual model of an accretion cycle. Each accretion cycle consists of a thrust initiation, an underthrusting and a re-activation phase, where the first and the third phase of two consecutive accretion cycles are coeval. It follows that strain transfer between thrusts is a gradual process. Furthermore, each accretion cycle initiates a surface uplift and a strain wave at the toe of the pro-wedge and both migrate coevally towards the retro-wedge. Thereby, strain accumulation and surface uplift depend on the phase within the accretion cycle and thus vary predictably in space and time. Although Mohr-Coulomb is time-independent, strain hardening and strain softening processes within fault zones determine the timing and magnitude of slip. We therefore consider the accretion cycle as an internal clock of orogenic deformation.

We strongly emphasise that this conceptual model combines previously unrelated observations, such as the periodicity of thrusting, the topographic evolution of bivergent wedges and the cumulative slip history of thrusts. Additionally, this conceptual model highlights farfield connections between the initiation of a new thrust within the pro-layer (cause) and the resulting “strain- and uplift pulse” at the retro-shear zone (response). However, the degree of “strain communication” between the pro- and the retro-wedge decreases, as the former grows laterally.

Surface uplift of the pro-wedge is highly episodic and reflects individual accretion cycles. Thereby, re-activation of thrusts leads to order-of-magnitude variations in surface uplift. Thus,



changes of the kinematic or mechanic boundary conditions as well as surface processes should not necessarily be invoked to explain the observed variability.

Continuous vertical stacking and retro-ward translation of basally accreted duplexes results in a smooth and dome-like shape of the axial-zone and the retro-wedge. We therefore question the possibility to detect basal accretion episodes within the surface uplift signal.

This conceptual model indicates further that geodetic, paleoseismologic and geologic estimates of fault slip are not necessarily the same. It follows that interpolation of slip rates from different temporal scales and resulting predictions of earthquake recurrence intervals can only be successful if the phase within the accretion cycle is known. In addition, each structure might have its own  $b$ -value, which changes through time as accretion proceeds. We finally explore further implications of the accretion cycle model with respect to kinematic modeling as well as fluid flow and hydrocarbon maturation studies.

Experimental results additionally suggest an end-member scenario in which either thrust spacing or the timing of thrust initiation is constant and the respective other parameter variable. Thus, one should be very careful while deriving one information from the other. This end-member model is thought to resemble the time- and the slip-predictable earthquake model, but on a larger spatial and temporal scale.

Based on the 2<sup>nd</sup> experimental series, we found that retro-wedge erosion amplifies the displacement of the basally accreted material, whereas pro-wedge erosion accelerates and additionally redirects the particle flow of the frontally accreted material. Pro- and retro-wedge erosion retard the propagation of deformation into the foreland. This effect is stronger for pro-wedge erosion. Retro-wedge erosion amplifies vertical growth and leads to increased strain accumulation along the retro shear-zone and the mid-level detachment. Thus,

cause (retro-wedge erosion) and response (deformation within the pro-wedge) are significantly offset in space. Since pro-wedge erosion evokes a complete decoupling of the retro-wedge from the pro-wedge, cause and response are spatially more closely related. Both results highlight the need for orogen-wide climate-tectonics studies. We also found that more focused erosion is associated with a more focused tectonic response.

Experimental results do further indicate that the kinematics of bivergent wedges are robust with respect to erosion. We therefore propose that only if erosion determines the active detachment, erosion has taken the lead.

Peripheral foreland basin systems form in direct response to orogenic loading. We therefore analytically explore the implications of the above results on the spatio-temporal evolution of foreland basin systems. Based on the observation that bivergent wedge growth follows a power law, we propose a kinematic model for the Flysch to Molasse transition. The latter would be thus an emergent result of the imposed kinematic boundary conditions. There would be thus no need to invoke a halt of convergence or a slab break-off.

We also found that retro-wedge erosion influences the spatio-temporal evolution of the proforeland basin system and should be thus taken into account. In addition, forebulge unconformities are preferred sites for Mississippi Valley Type deposits. Their formation might be controlled by an eroding orogen, hundreds of kilometers away.

Finally, boundary conditions do matter. The perception of how nature works commonly guides the setup of simulation studies. The results however, mirror only the interaction between the prescribed boundary conditions and thus influence the way nature is perceived. We therefore strongly suggest to examine the transferability of all boundary conditions to nature and to compare experimental with natural time series.

# Zusammenfassung

Die räumlich-zeitliche Entwicklung von Kollisionsorogenen wird durch das Zusammenwirken von Deformation, Isostasie und Oberflächenprozessen kontrolliert. Bisherige Studien zur orogenen Entwicklung, welche im Wesentlichen auf dem kritischen Keil-Konzept beruhen, untersuchten einerseits den Einfluß der Materialeigenschaften auf die orogene Geometrie und analysierten andererseits den Einfluß von Erosion und Sedimentation auf die Verteilung von Deformation. Trotz der zum Teil sehr weitreichenden Implikationen des kritischen Keil-Konzepts hinsichtlich der Verteilung von Materialpfaden und Metamorphosegraden in orogenen Keilen, besitzt es nur eine begrenzte Vorhersagekraft bezüglich der räumlichen und zeitlichen Verteilung von Deformation und Oberflächenhebung.

Ziel der vorliegenden Arbeit ist es, die räumliche und zeitliche Verteilung von Deformation und Oberflächenhebung in bivergenten Keilen zu analysieren, gegebenenfalls Muster zu erkennen und diese in einen Prozesszusammenhang zu stellen. Letzteres würde nicht nur das Verständnis der geologischen Vergangenheit verbessern, es könnte auch zur genaueren Vorhersagbarkeit von Naturkatastrophen führen.

Dieser Herausforderung soll mit Hilfe zweier Serien skaliert 2D Simulationen begegnet werden. Dabei dient die erste Experimentserie der Klärung des Einflusses von Isostasie, mechanischer Stratigraphie und eines Festigkeitskontrastes zwischen Ober- und Unterplatte auf das Verhältnis von Interndeformation zur Propagation der Deformation. In der zweiten Experimentserie soll der Einfluß des Ortes maximaler Erosion hinsichtlich der Kollisionsgeometrie auf den tektonischen Massenfluß und die daran geknüpfte topographische Entwicklung bei jeweils zwei verschiedenen Erosionsmodi untersucht werden.

Der hierfür notwendige Experimentaufbau greift zum einen bestehende Konstruktionsansätze auf, erlaubt aber auch erstmalig die Simulation von auflastabhängiger Flexur. Der Einsatz von Particle Image Velocimetry ermöglicht die Berechnung des inkrementellen Partikelverschiebungsfeldes und seiner Ableitungen, inklusive der horizontalen Scherdeformation, als auch die Extraktion von Zeitreihen der Oberflächenhebung und der Störungsentwicklung. Diese Daten werden mit Hilfe zweier neu entwickelter Abbildungstypen, der Hebungs- und der Deformationskarte visualisiert.

Resultate der ersten Experimentserie belegen die gute Übereinstimmung mit bereits publizierten Ergebnissen hinsichtlich der generellen Entwicklung bivergenter Keile. Darüber hinausgehend postulieren wir ein Vier-Phasen Modell der orogenen Entwicklung, welches sich am Auftreten bestimmter Akkretionsmodi orientiert. Phase I ist durch die Bildung eines krustalen pop-up gekennzeichnet. In Phase II führt frontale Akkretion zur Herausbildung eines Proto-Prokeiles. Sofern ein interner Abscherhorizont vorhanden ist, kommt es in Phase III zur basalen Akkretion. Frontale Akkretion im Retrokeil markiert den Beginn der Phase IV.

Eines der Hauptresultate dieser Arbeit ist die Entwicklung des konzeptionellen Modelles Akkretionszyklus (*accretion cycle*). Demnach besteht jeder Akkretionszyklus aus einer *thrust initiation*, einer *underthrusting* und einer *re-activation phase*, wobei die letzte und die erste Phase zweier aufeinander folgender Akkretionszyklen zeitgleich sind. Dies belegt, daß der Transfer von Deformation zwischen zwei Überschiebungen ein gradueller und kein abrupter Prozess ist. Des Weiteren wird mit jedem Akkretionszyklus eine Hebungs- und Deformationswelle initiiert, welche sich durch den gesamten bivergenten Keil bis hin zum Retrokeil bewegt. Somit lassen sich Magnitude und Ort von Deformation und Oberflächen-

hebung in Abhängigkeit von der Phase im Akkretionszyklus vorhersagen. Diese Zeitabhängigkeit resultiert aus strain softening und strain hardening Prozessen in den Scherzonen. Der Akkretionszyklus kann somit als internes Metronom orogener Deformation angesehen werden. Es sei ausdrücklich darauf hingewiesen, daß das Akkretionszykluskonzept bisherige Einzelbeobachtungen nicht nur verknüpft sondern auch in einen Prozesszusammenhang stellt. Darunter fallen die Episodizität von Akkretion, die Oberflächenhebung und auch die Versatzentwicklung von Überschiebungen. Weiterhin zeigt dieses konzeptionelle Modell Kausalbeziehungen zwischen räumlich und zeitlich getrennten Phänomenen auf. So erzeugt die Initiierung eines neuen Überschiebungskörpers während der *underthrusting phase* einen Hebungs- und Deformationspuls entlang der Retroscherzone. Der Grad der Deformationspartitionierung zwischen Pro- und Retrokeil nimmt jedoch einer gedämpften Oszillation gleich, mit zunehmender Länge des Prokeils ab.

Die räumlich-zeitliche Entwicklung der Oberflächenhebung im Prokeil trägt einen episodischen Charakter, welcher sich durch die einzelnen Akkretionszyklen ergibt. Dabei kann es durch die Reaktivierung von Überschiebungen zu Änderungen der Hebungsbeträge um eine Größenordnung kommen. Somit müssen Änderungen der kinematischen oder dynamischen Randbedingungen als auch Änderungen im Erosions-Sedimentationsregime nicht notwendigerweise angenommen werden, um diese hohe Variabilität zu erklären. Im Gegensatz dazu erzeugt die kontinuierliche Stapelung basal akkretierter Duplexe in der axialen Zone und im Retrokeil ein eher domähnliches Hebungssignal, wobei sich die Bildung einzelner Duplexe nicht nachweisen ließ.

Weiterhin impliziert das konzeptionelle Modell des Akkretionszyklus, daß geodätisch, paläoseismologisch und geologisch ermittelte Überschiebungsraten nicht zwangsläufig übereinstim-

men müssen. Daraus folgt, daß die Interpolation von Versatzraten zwischen verschiedenen Zeitskalen und die sich daraus ergebenden Wiederkehrintervalle von Erdbeben nur erfolgreich sein kann, wenn die Phase im Akkretionszyklus bekannt ist. Demnach könnte jede Struktur mit einem unterschiedlichen  $b$ -Wert behaftet sein, welcher sich im Laufe des Akkretionszyklus ändert. Des Weiteren werden die oben vorgestellten Ergebnisse hinsichtlich ihrer Implikationen für kinematische Modellierungen, Fluiduntersuchungen als auch Kohlenwasserstoffgenese beleuchtet.

Die Ergebnisse der ersten Experimentreihe deuten außerdem ein Szenario an, in welchem entweder der zeitliche oder der räumliche Abstand zwischen zwei aufeinander folgenden Überschiebungen konstant ist und der jeweils andere Parameter erheblich variiert. Es scheint daher nicht möglich aus der Beobachtung eines Parameters, Schlußfolgerungen hinsichtlich eines anderen Parameters ziehen zu können. Ähnlichkeiten dieses Modells mit Erdbebenmodellen (*time-predictable versus slip-predictable*) sind beabsichtigt und kennzeichnen möglicherweise ähnliche Prozesse auf unterschiedlichen Zeit- und Längenskalen.

Ergebnisse der zweiten Experimentreihe zeigen, daß Prokeilerosion den Massenfluß des frontal akkretierten Materials beschleunigt und zu einer deutlichen Versteilung der Partikelpfade im Prokeil führt. Hingegen beschleunigt Retrokeilerosion den Massenfluß der basalen Akkretion. Sowohl Pro- als auch Retrokeilerosion verzögern die Propagation von Deformation in das Vorland, wobei dieser Effekt verstärkt bei Prokeilerosion auftritt. Retrokeilerosion steigert das vertikale Wachstum bivergenter Keile und führt zu einer erhöhten Akkumulation von Deformation entlang der Retroscherzone und des internen Abscherhorizontes. Somit evoziert Retrokeilerosion eine räumliche Entkoppelung von Ursache (Retrokeilerosion) und Wirkung (Deformation im Prokeil). Da Prokeilerosion

den Prokeil vom Retrokeil entkoppelt, stehen Ursache und Wirkung in einer engeren räumlichen Beziehung. Beide Resultate verdeutlichen, daß Klima-Tektonik-Studien immer das Gesamtsystem „Orogen“ in Betracht ziehen sollten.

Die Resultate deuten aber auch an, daß die Kinematik bivergenter Orogene sehr robust gegenüber der Erosion ist. Wir postulieren, daß ein Orogen nur dann in seiner Kinematik von der Erosion gesteuert wird, wenn letztere in der Lage ist, das aktive Abscherniveau und somit die Größe der Materialzufuhr zu bestimmen.

Periphere Vorlandbecken sind integraler Bestandteil kontinentaler Kollisionszonen. Im letzten Abschnitt werden die Auswirkungen der oben vorgestellten Ergebnisse auf die zeitlich-räumliche Entwicklung von Vorlandbecken untersucht. Basierend auf der Beobachtung, daß bivergente Orogene ein Höhen- und Längenwachstum zeigen, welches einem Potenzgesetz gehorcht, postulieren wir ein kinematisches Modell für den Flysch-Molasse Übergang. Letzterer wäre demnach ein Resultat der kinematischen Randbedingungen und nicht notwendigerweise ein Ergebnis der abklingenden Konvergenz oder eines *slab break off*. Weiterhin zeigen die Berechnungen, daß auch Retrokeilerosion einen erheblichen Einfluß auf die räumlich-zeitliche Entwicklung der Pro-Vorsenke hat. Überlegungen zur tektonostratigraphischen Position von Mississippi Valley Type Lagerstätten schließen sich an.

Ceterum censeo, daß die Vorstellung des Beobachters von der Natur seine Wahl der kinematischen und dynamischen Randbedingungen von physikalischen als auch numerischen Modellstudien beeinflußt. Die gewonnenen Resultate spiegeln jedoch nur das Zusammenwirken der Eingangsparameter wider und werden somit einschließlich ihrer Interpretation indirekt von der Vorstellung des Beobachters beeinflußt. Es scheint daher von großer Bedeutung die Übertragbarkeit aller experimentellen Randbedingungen und Zeitreihen auf die Natur zu prüfen.



# 1 Introduction

Mountain belts have always attracted human attention. They provide shelter against enemies and supply the economy with natural resources such as building materials or precious ores. Mountain belts are also a preferred site for recreation in a beautifully shaped landscape, although they are prone to devastating earthquakes and bedrock landslides. However, and most importantly for this study, mountain belts like the European Alps, the Pyrenees, the Himalayas, the Southern Alps of New Zealand, Taiwan or Borneo are a magnificent and impressive realisation of the probably subtle interplay between endogenic and exogenic geo-processes. Considerable amount of research, focussing on the kinematic and dynamic evolution of mountain belts in the broadest sense, has been carried out during the last two centuries and is still undertaken. Meanwhile our understanding of and our perspective on mountain belts has changed from the opening and closure of geosynclines to the collision of two continental plates and the partial subduction of one beneath the other (Fig. 1.1). The currently held concepts of continental collision zones involve a kinematic and a dynamic assumption. The former proposes that collisional orogens result from the partial subduction of continental lithosphere and accretion of crustal material (e. g., Willett et al., 1993; Storti et al., 2000). The dynamic assumption, which is commonly known as critical taper theory suggests that this subduction-accretion process leads to the formation of an orogenic wedge with a geometry controlled by the basal and internal mechanical properties (e. g., Davis et al., 1983; Willett et al., 2001). The reader is referred to chapter (3) for a more detailed description of both concepts.

With respect to the interplay between tectonics and climate, it has long been recognised that deformation in collisional orogens is a key fac-

tor in controlling the magnitude and location of erosion. Orogenic growth leads to topography, which may enhance monsoonal circulation, provide a rain-shadow and guides or even deflects the drainage pattern or the course of glaciers. Changes in topography may induce the rise or fall of the regional base-level to which rivers and glaciers adjust (Kutzbach et al., 1993; Hay, 1996). Following this view, erosion responds primarily to deformation. In contrast, recent field studies in the Southern Alps of New Zealand (Koons, 1990, 1995; Tippett and Hovius, 2000), in the European Alps (Schlunegger and Willett, 1999), in the Chugach/St. Elias Range of Southern Alaska (Meigs and Sauber, 2000; Sheaf et al., 2003), in the Andes (Horton, 1999; Montgomery et al., 2001), in Taiwan (Lin, 2000), in the Tien Shan (Pavlis et al., 1997; Strecker et al., 2003), and in the Himalayas (Zeitler, 1985; Zeitler et al., 2001; Wobus et al., 2003; Thiede et al., 2004) have shown that “the concentration of erosional energy leads to a similar concentration of mechanical energy” (Koons, 1990). These field studies indicate thus, that erosion influences the distribution of deformation within orogenic belts. This conclusion derives support from the critical taper theory, which links topography and tectonics in a convergent wedge and predicts that deformation should be very sensitive to mass redistributions by surface processes (e. g., Davis et al., 1983). In a more general perspective, mountain building and the influence of surface processes on deformation can also be understood in terms of the minimum work theory (Gutscher et al., 1998; Hardy et al., 1998; Masek and Duncan, 1998; Gerbault and Garcia-Castellanos, 2005). Within this concept, a thrust is either initiated or re-activated, if this process consumes the least gravitational and frictional work to accommodate convergence. Erosion for example decreases the load upon a thrust and reduces thus the gravitational and frictional work, which either promotes prolonged slip along or the re-activation of this thrust. Consequently, the formation of a new thrust within the foreland is retarded.

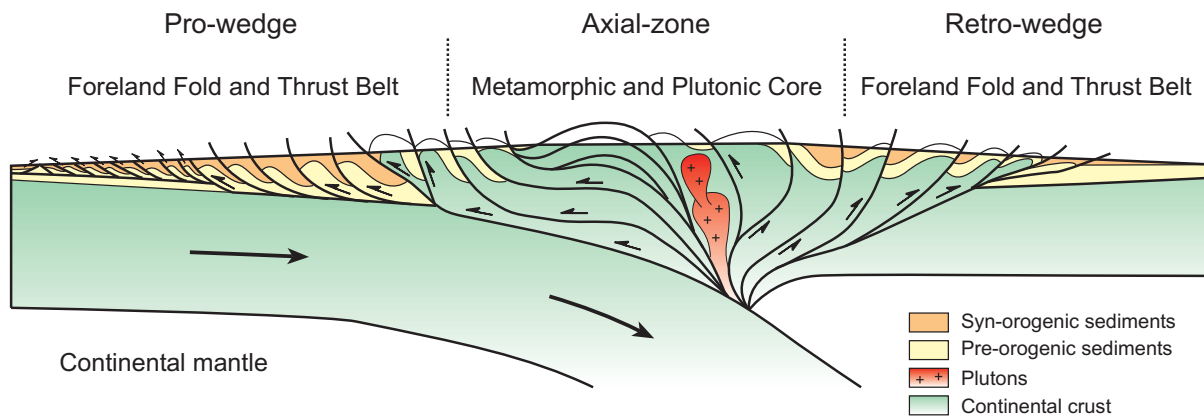


Figure 1.1: Conceptual model of a collisional orogen. Modified after McClay and Whitehouse (2004).

Numerical simulations (Beaumont et al., 1992; Willett et al., 1993; Avouac and Burov, 1996; Willett, 1999; Beaumont et al., 2001), which are based on the kinematic and the dynamic concepts outlined earlier, tested and verified the observations from the above mentioned field studies. The location of erosion with respect to the convergence geometry as a first order parameter controlling orogen-scale deformation has been identified by Beaumont et al. (1992), Willett et al. (1993) and Willett (1999). Accordingly, the asymmetry of erosion would have a profound influence on the distribution of deformation as well as on the amount and location of exhumation within a bivergent orogen (Fig. 1.2).

In addition, results from sandbox simulations suggest that synkinematic erosion promotes out-of-sequence thrusting in the axial-zone and the persistence of retroverging thrusts (Merle and Abidi, 1995; Mugnier et al., 1997; Storti et al., 2000; Marques and Cobbold, 2002; Del Castello et al., 2004; Persson et al., 2004).

Despite this considerable amount of research little is known about the influence of flexure, the mechanic stratigraphy or erosion on the kinematic evolution of bivergent wedges, or more specifically: (i) how is strain partitioned in time and space within a bivergent wedge; (ii) is there a strain pattern either in time or in space or even in

both domains, which can be predicted; (iii) what controls the relative magnitudes of in-sequence, synchronous and out-of-sequence thrusting and can that be predicted as well and (iv) what is the relation between the topographic evolution of and the strain history within a bivergent wedge.

Before these challenges are addressed in later chapters, an account on orogen-scale erosion is given first followed by a summary of concepts, which describe the kinematic and dynamic evolution of bivergent wedges. Based on these observations and concepts, constraints are identified to (i) respectively modify a 2D sandbox setup used in the Geodynamic Laboratory of the GFZ Potsdam and (ii) to generate an erosion model which can be incorporated into the sandbox simulations. Additionally, factors which support and justify the above approach, i. e., the scale invariance of brittle deformation as well as the similarity of the mechanic behaviour between upper crustal rocks in the brittle field and sand are discussed and the limitations of 2D sandbox experiments are indicated. An optical monitoring system, Particle Image Velocimetry, which provides time-series of the displacement field and all its derivatives such as the horizontal shear-strain ( $e_{xy}$ ), is used to employ a quantitative comparison between experiments (section 4.3).

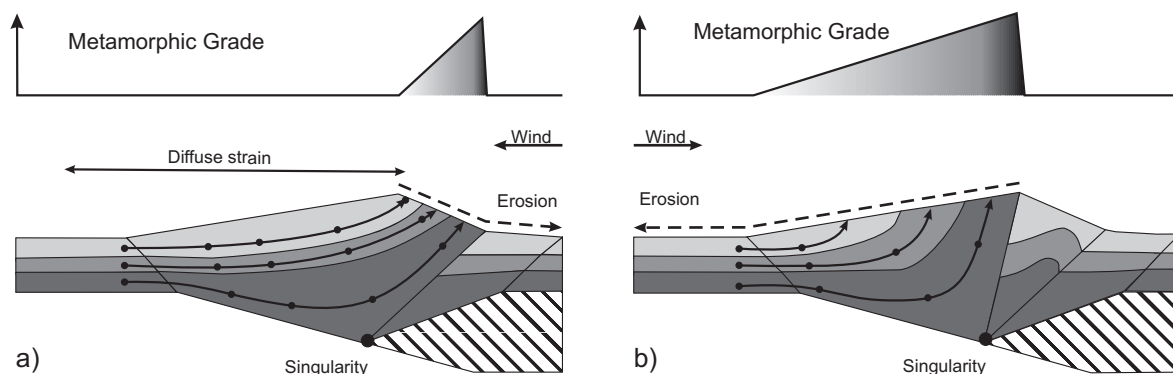


Figure 1.2: Influence of steady-state erosion on the distribution and magnitude of exhumation in a bivergent wedge. (a) Retro-wedge erosion. (b) Pro-wedge erosion. Lines are material trajectories; dots are progressive equal-time positions of points initially aligned vertically. Schematic metamorphic grade is for surface rocks assuming initial equilibrium conditions. Modified after Willett et al. (1993).

In chapter (5) the first set of five experiments aimed at investigating the influence of the imposed boundary conditions on wedge kinematics is presented. Experimental results suggest that the spatio-temporal distribution of deformation follows a distinct pattern, which is referred to as accretion cycle. Thereby, each accretion cycle consists of three phases: the thrust initiation, the underthrusting, and the re-activation phase, which determine the magnitude of strain on any given thrust within the bivergent wedge. Thus, the accretion cycle is considered as an internal clock for wedge-scaled deformation.

Changes of the boundary conditions evoke only minor modifications with respect to the duration and magnitude of individual phases. This underlines the robustness of the accretion cycle and allowed the derivation of a conceptual kinematic model. Thus, the spatio-temporal variability in strain accumulation is an emergent phenomenon of bivergent wedge-growth and there would be no need to invoke plate-kinematic changes or major climatic shifts to explain this variability. It is further highlighted that each accretion cycle is associated with a surface uplift wave. Thus, the strain wave migrating through the wedge is mirrored in a likewise surface uplift wave, which therefore provides a predictive potential.

Experimental results indicate also that boundary conditions, which can be considered as degrees of freedom, determine the relative magnitude of in-sequence, synchronous and out-of-sequence thrusting. Within this respect, I shall demonstrate that an increase of the number of degrees of freedom results in a likewise increase of synchronous and out-of-sequence thrusting. Thus, if the former is known, the latter is predictable. This issue derives its importance from the observation that only a limited number of different setups is in use and that they provide only few degrees of freedom (GeoMod 2004). It has only recently been shown that out-of-sequence thrusting within a forward breaking thrust-sequence is more common than previously assumed (McClay and Whitehouse, 2004). This emphasises, how models can guide one's perception of nature.

The above results are also discussed in the light of the link between geodetic, paleoseismologic and geologic estimates of fault slip (section 5.3). Limiting factors of the prediction of the timing and location of the next slip event are explored as well.

The second set of five experiments is used to investigate the influence of the location of erosion with respect to the convergence geometry on bivergent wedge kinematics. Thereby, special emphasis is devoted to the relative magnitude of in-se-



quence and out-of-sequence thrusting, to the topographic evolution and to the geometry of particle paths (chapter 6). Experimental results reveal that retro-wedge erosion accelerates the existing mass flux through the bivergent wedge and that pro-wedge erosion additionally redirects it. These experiments do also demonstrate that retro-wedge erosion enhances strain accumulation within the pro-wedge, thus pointing to a significant spatial offset of cause and response.

Erosion in mountain belts by rivers, glaciers or bedrock landslides can be considered to be either distributed over a wide area or to be very focused in space. Given the sensitivity of crustal wedges to erosion as outlined above, both erosion modes, which are considered as end-members, should evoke a characteristic deformation style (section 6.3). The respective experiments support the above cited quote from Peter Koons (1990) that the concentration of erosional energy leads to a similar concentration of mechanical energy. These results have been accepted for publication for the GSA Special Paper 398, *Tectonics, Climate and Landscape Evolution*, edited by S. Willett, N. Hovius, M. Brandon and D. Fisher.

It is further evident from the above observations that each erosion scenario is associated with a different orogenic load distribution, which in turn controls the spatio-temporal evolution of the adjacent foreland basins (chapter 8). This bears some implications for their respective facies architecture, especially the Flysch to Molasse transition, and the distribution of natural resources such as base metals or hydrocarbons. Within this respect, it can be noted that the migration of the forebulge and the associated unconformities, which are a preferred site for Mississippi Valley Type Deposits (MVT) is controlled by an eroding orogen hundreds of kilometres away.

Finally, we would like to emphasise two key points of the modelling approach followed during the course of this study. The first key target has been and still is the reduction of the number

of kinematic boundary conditions to allow a more self-organised growth of bivergent sand-wedges. In places where boundary conditions are necessary, explanations are given or natural pendants are provided. While writing these lines, a study is undertaken by Nina Kukowski, Jo Lohrmann and myself, which demonstrates that push and pull experiments with everything else being the same differ significantly with respect to the relative magnitudes of in sequence, synchronous and out-of-sequence thrusting. This observation emphasises again how models can guide one's perceptive of nature.

The second key target of this study is to provide testable predictions of observations to be made in natural orogens. Sandbox simulations are thus understood as an investigative tool to identify process chains, which can either, be proven or disproved in nature. The sandbox simulations presented here with their intermediate spatial scale in terms of their structural resolution may finally help to link results from lithospheric scaled numerical simulations with those from local to regional field studies.

## 2 Orogen-scale erosion

*Definitions.* The term denudation, which is derived from the latin denudare, means to make bare (Ring et al., 1999). In a geological context it refers to the exposure of rocks by erosion, but also involves the processes of weathering and transportation (Allaby and Allaby, 1999; Ring et al., 1999). Erosion, which is derived from the latin erodere, means to gnaw at or to crush something. In a geological context it refers to the physical and chemical breakdown of rocks and also involves the transport of the resulting materials (Allaby and Allaby, 1999). From the above definitions it is evident that they overlap, which leads to a widely synonymous use of both terms (Ring et al., 1999). There is however a tendency to restrict erosion to the local removal of rocks by rivers, glaciers or bedrock landslides. Accordingly, denudation would refer to the large scale exposure of bedrock (Leeder, 1991; Summerfield and Brown, 1998; Ahnert, 1999). On the contrary denudation is often used in the context of tectonic unroofing (Ring et al. (1999) and Sean Willett pers. com., (2004)). Given that there is no clear agreement upon the application of both terms, I follow Sean Willett and use the term erosion, since it is less ambiguous in its reference to physical or chemical surface processes.

Within this respect, the sediment supply system is commonly considered to be a product of the interaction between erosivity and erodibility. The former describes the potential of a river or glacier to remove material from a certain locality, i. e., the amount of abrasive tools transported within either the river, the glacier or even within the air. In contrast, erodibility refers to the resistance of a certain lithology to the work of the erosion agents. Erodibility depends on the physical and chemical composition of the lithology subject to erosion, the mechanic properties of the lithology, the in-

filtration capacity and climatic parameters such as temperature, temperature range, and availability of water (Hovius, 1998).

The term uplift refers to the displacement in the direction opposite to the gravity vector. A displacement is only defined when both, the object displaced and the frame of reference are specified. Accordingly, surface uplift is the displacement of Earth's surface with respect to the geoid (Fig. 2.1). Similarly, rock uplift is defined as the displacement of rocks with respect to the geoid. Displacement of rocks with respect to the surface is referred to as exhumation, where the exhumation rate equals the erosion rate or the rate of removal of overburden by tectonic processes. The above relation can also be written as:

$$\text{surface uplift} = \text{rock uplift} - \text{exhumation}. \quad (2.1)$$

It is emphasised here that the often implicitly made assumption that rock uplift equals surface uplift is equivalent to the assumption that the exhumation is zero – often a difficult assumption to justify (England and Molnar, 1990).

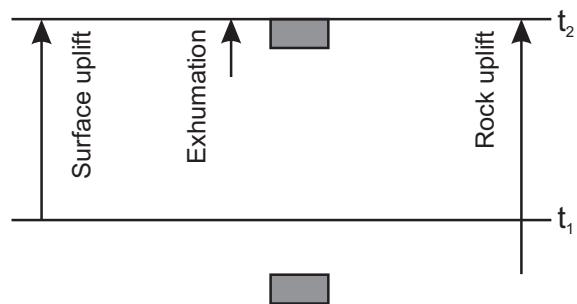


Figure 2.1: Graphic definition of key parameters describing vertical movements within Earth's crust. Taken from Burbank and Anderson (2001).

*Erosion patterns.* One implication of the subduction-accretion process is the tectonic advection of material towards the surface of a collisional orogen. The way of how the resulting topography is counteracted by rivers, glaciers, and bedrock landslides depends on a number of factors. Among

the most important ones are latitude and altitude of an orogen, its position with respect to global atmospheric and oceanic circulation systems, the erosivity of antecedent rivers, channel slope, orientation of topographic slope with respect to geologic structures, water discharge, erodibility, and rate of uplift (Selby, 1982; Seidl and Dietrich, 1992; Howard et al., 1994; Sugai et al., 1994; Hay, 1996; Schmidt and Montgomery, 1995; Hovius, 1998; Meigs and Sauber, 2000; Zeitler et al., 2001).

Given sufficient precipitation, a drainage network will cover the entire orogen up to the channel heads or the snow line. Thereby, the spacing of the transverse streams, which transport most of the material eroded within an orogen, is very regular and is linearly correlated with the half-width of the orogen (Hovius, 1996). This spacing does not differ significantly between young and old orogens and is thus independent of the age or the degree of maturity of an orogen, i. e., the collision stage. Nearly all orogens show at least in parts such a drainage network among them: the Southern Alps of New Zealand, Central Range in Taiwan, the Apennines in Italy, the Peruvian Andes, and the European Alps (Hovius, 1996). This regular organisation of drainage networks and the associated erosion is envisaged to be characteristic for a distributed erosion pattern (Fig. 2.2).

In contrast, monsoon derived precipitation may focus erosion as demonstrated by Wobus et al. (2003), Hodges et al. (2004), and Thiede et al. (2004). According to Thiede et al. (2004), more than 80% of the annual precipitation ( $> 2000 \text{ mm/a}$ ) of the Indian summer monsoon is forced out along the High Himalayan mountain front in NW India at elevations between  $\sim 2$  and  $3.5 \text{ km}$ . This altitudinal band corresponds with an approximately  $50\text{--}70 \text{ km}$  wide zone of high exhumation rates (Fig. 2.3). Furthermore, Thiede et al. (2004) and Bookhagen et al. (2005) showed that where monsoonal circulation reaches major N–S oriented valleys in the High Himalayas,

moisture is channeled farther into the orogen and may lead to higher erosion rates along these valleys. A similar observation is derived from field

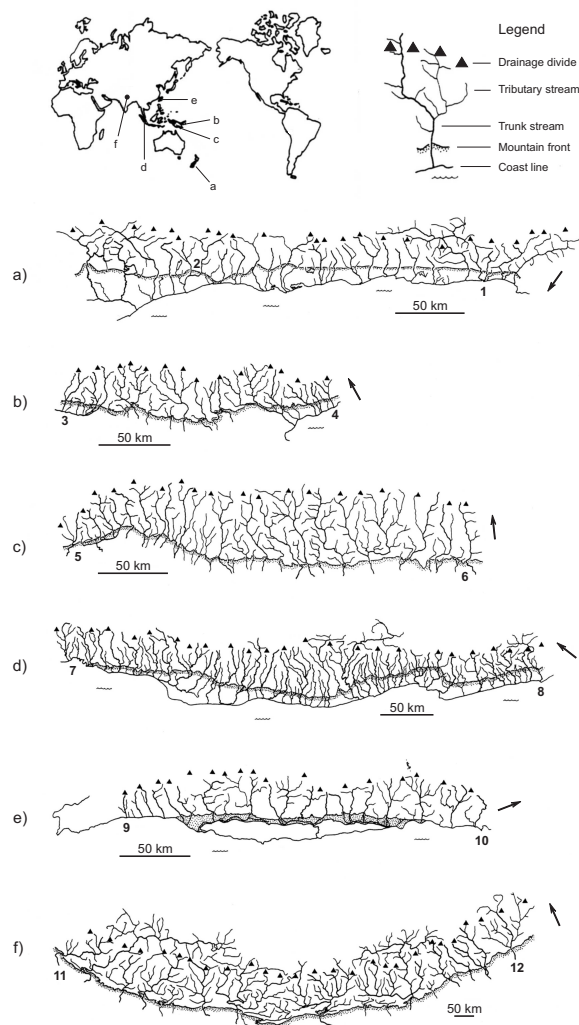


Figure 2.2: Drainage patterns in mountain belts, taken from Hovius (1996). Ranges: (a) Southern Alps, New Zealand; (b) Finisterre Range, Papua New Guinea; (c) Maoke range, Irian Jaya; (d) Barisan Range, Sumatra; (e) Central Range, Taiwan; (f) Himalaya, India/Nepal. Trunk streams: 1 Turnbull; 2 Styx; 3 Surinam; 4 Buham; 5 Ukemupuko; 6 Lorentz; 7 Bajang; 8 Manna; 9 Ta wu; 10 nameless; 11 Beas; 12 Manas. Arrow points to North.

studies in the Toro basin, which belongs to a series of intra-montane basins within the Eastern Cordillera. Hilley and Strecker (2005) pointed

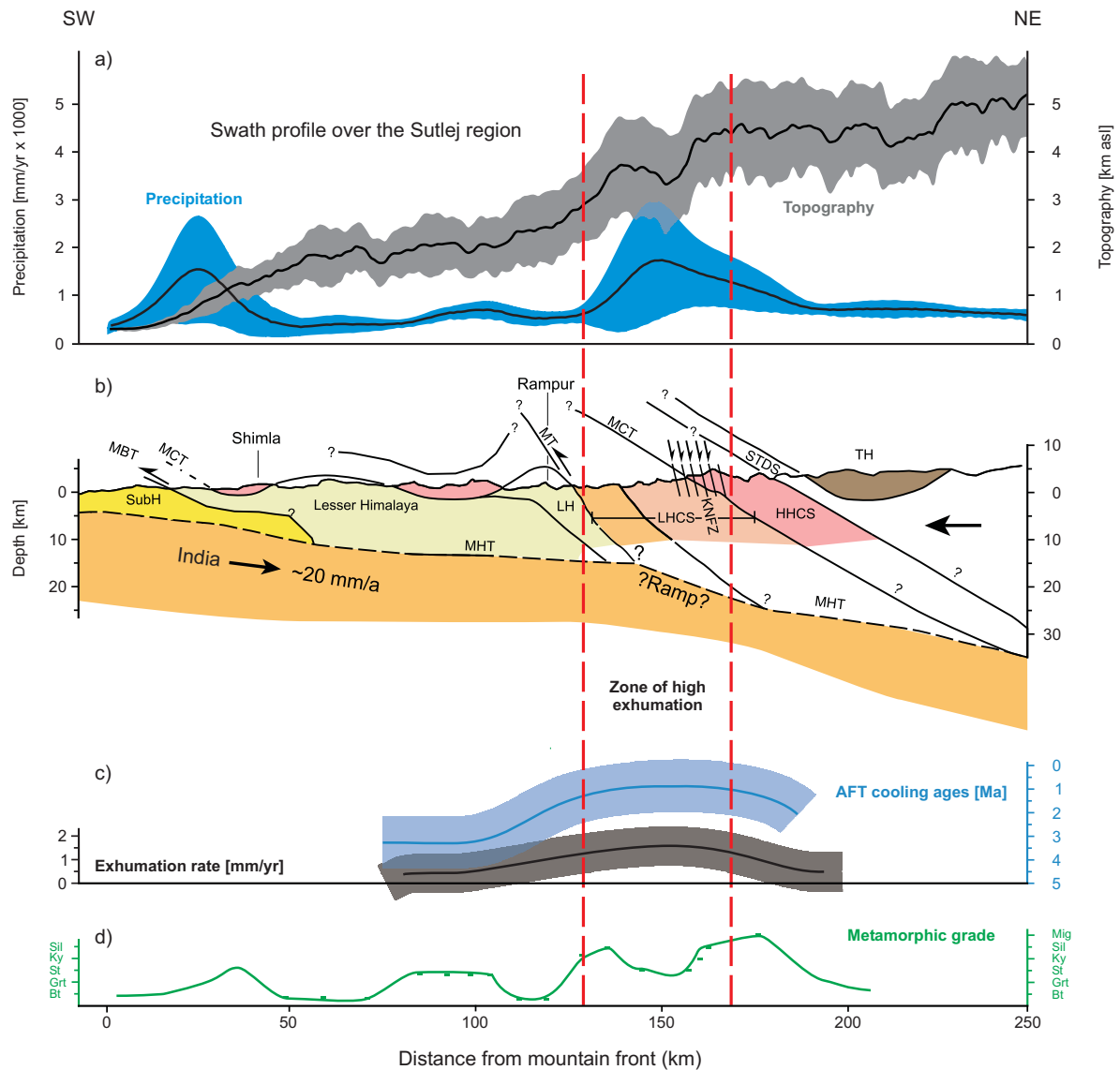


Figure 2.3: Example of focused erosion in the Himalayas. Modified after Thiede et al. (2004). (a) Compiled data illustrate the coupling between surface processes and deformation in the Sutlej Region. Topographic (grey) and precipitation - distribution (blue) swath profiles for the Sutlej area are oriented perpendicular to the SHF. Swath profiles: 250 km long, 100 km wide, thick, lines indicate mean values, shaded areas denote  $\pm 2\sigma$ . Distribution of orographic precipitation is focused between elevations of  $\sim 2-3.5$  km in a  $\sim 50-70$  km-wide zone. (b) Simplified geologic cross-section parallels swath profile. (c) AFT cooling ages (blue) parallel to the geologic cross-section and estimated exhumation rates (black); lines indicate mean values, shaded areas denote  $\pm 2\sigma$ . (d) Metamorphic grade of the rocks along the profile line. Based on AFT cooling ages (c), the coincidence between rapid erosion and exhumation is focused in a  $\sim 50-70$  km-wide sector of the Himalayan orogenic belt. Enhanced and focused orographic precipitation (a) localized erosion and exhumation over geologic time and resulted in exhumation of high-grade metamorphic rocks (d) by motion along a back-stepping thrust to the south (MT) and normal fault zone (KNFZ) to the north (b). TH, Tethyan Himalaya; HHCS, High Himalayan Crystalline Sequence; LHCS, Lesser Himalayan Crystalline Sequence; LH, Lesser Himalaya; SubH, Sub Himalaya; STFS, Southern Tibetan Fault System; MCT, Main Central Thrust; KNFZ, Karcham Normal Fault Zone; MT, Munsiri Thrust; MBT, Main Boundary Thrust; MHT, Main Himalayan Thrust.

out that the meridional orientation of the Eastern Cordillera concentrates moisture along its eastern flank, which leads to a steep precipitation gradient between the humid foreland ( $\sim 1200\text{mm}/a$  mean annual precipitation) and the arid intra-montane Toro basin ( $\sim 260\text{mm}/a$  mean annual precipitation). However, the outlet of the Rio Toro in the foreland allows penetration of moisture into the respective gorge and ultimately into the Toro basin itself (Hilley and Strecker, 2005).

In a likewise manner, the Southern Alps of New Zealand form an orographic barrier to the moisture laden, north-westerly winds moving off the Tasman Sea. Mean annual precipitation rates reach as much as  $15\text{m}$  on the steep western flank of the orogen and resulted in erosion rates by landslides of up to  $9\text{mm}/a$  and of likewise high rock uplift rates approaching  $7\text{mm}/a$  (Hovius et al., 1997).

Antecedent rivers with high erosivity, which cross an orogen, might also focus erosion. Both the Indus and the Tsangpo river were capable of cutting steep gorges with several thousand meters relief into the massifs of Nanga Parbat and Namche Barwa, respectively (Zeitler et al., 2001; Koons et al., 2002). This focused erosion lead to the rapid exhumation of Quaternary metamorphic rocks and granites (Zeitler et al., 2001) and may also have attracted channel flow within the middle to lower crust (Zeitler et al., 2001; Beaumont et al., 2001). A further example of an antecedent river focussing deformation is provided by the Surkhob river (Pavlis et al., 1997). Since Late Miocene to Pliocene times the Surkhob river takes its course right above the northern deformation front of the Pamir and removed nearly all material delivered to this deformation front. According to Pavlis et al. (1997) this has lead to a halt in deformation front advance, to a build up of excess topography along the deformation front and to backthrusting as well as out-of-sequence thrusting.

Orogen-scale glacial erosion can also be considered as focused. Glacial erosion is at its maximum along the mean position of the Equilibrium Line

Altitude (ELA), where the net mass balance of glaciers is equal to zero (i. e., accumulation equals ablation), the sliding velocity of glaciers is highest and so is the erosion rate. Below the ELA, glacial erosion decreases and fluvial processes start to dominate (Fig. 2.4). Due to the transition from warm-based to cold-based glaciers, the latter are frozen to their beds, at higher altitudes, glacial erosion decreases above the ELA (Meigs and Sauber, 2000; Burbank, 2002). One prominent example for this scenario is the Chugach/St. Elias Range in Southern Alaska, where high deformation and exhumation rates are confined to an altitudinal band spanned by the ELA (Meigs and Sauber, 2000; Sheaf et al., 2003; Spotila et al., 2004).

Based on the above observations we propose that orogen-scale erosion can either be envisaged as distributed or focused. These modes are considered as two alternatives of the spatial distribution of erosion. Given the sensitivity of crustal wedges to erosion as outlined in the preceding chapter, both erosion modes should evoke a characteristic deformation pattern.

*Simulation of orogen-scale erosion.* Several methods have been suggested to incorporate erosion into either numerical or physical simulations (e. g., Koons, 1995; Mugnier et al., 1997; Willett, 1999; Persson et al., 2004). In essence four classes of orogen-scale erosion models can be distinguished:

- i. Erosion rate is constant through time and space (Fig. 2.5a)

$$v_{er} = -\frac{dH}{dt} = \text{constant} \quad (2.2)$$

where  $v_{er}$  is the erosion rate,  $H$  is the elevation and  $t$  is time.

- ii. Erosion rate is proportional to elevation (Fig. 2.5b)

$$v_{er} = -\frac{dH}{dt} = -\frac{H}{t_E} \quad (2.3)$$

where the erosion parameter  $t_E$  (in units of time) describes how long it takes to erode a mountain of the elevation  $H$ .

- iii. Erosion rate is proportional to slope (Fig. 2.5c)

$$v_{er} = -\frac{dH}{dt} = -\frac{u dH}{dx} \quad (2.4)$$

where  $x$  is a horizontal spatial coordinate and  $dH/dx$  is the topographic gradient, i. e., the slope. The proportionality constant  $u$  is the horizontal rate of displacement of the slope.

- iv. Erosion rate is proportional to surface curvature (Fig. 2.5d)

$$q = -\frac{D dH}{dx} \quad (2.5)$$

where  $q$  is the rate of down slope transport of mass (mass flux),  $dH/dx$  is the topographic gradient, the slope and  $D$  is the erosional diffusivity.

The constant erosion approach (Eq. 2.2) is the most dramatic simplification of real erosion processes, but has been very successfully used to explain the clockwise shape of metamorphic PT paths (Stüwe, 2000). In sandbox simulations this model was applied by Mugnier et al. (1997), Leturmy et al. (2000), and Persson and Sokoutis (2002), who did not distinguish between pro- and retro-wedge erosion.

The elevation dependent erosion model (Eq. 2.3) is a variant of an assumption made by Ahnert (1970), which states that erosion rates increase with increasing local relief and that the latter is in turn positively correlated with elevation (Milliman and Syvitski (1992), Summerfield and Hulton (1994), Fig. 2.6). From a causal perspective this relation is generally invalid, since it is incompatible with fluvial incision laws. Also elevation by itself cannot be a determining factor (Peter Koons pers. com., (2004)). Additionally,

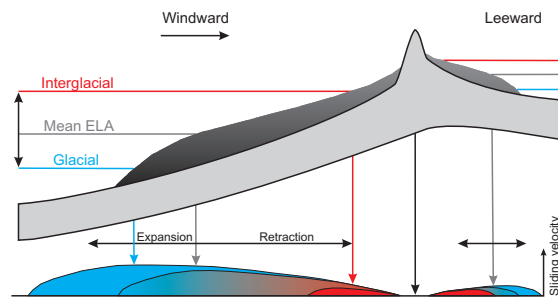


Figure 2.4: Model illustrating relationship between sliding velocity and the ELA across an orogenic belt. An orographically induced rise in ELA leads to a higher mean ELA (solid black line). Smaller amplitude fluctuations of the ELA between glacial (blue) and interglacial (red) are shown schematically. Assuming that bedrock erosion rate scales with basal sliding velocity (Hallet et al., 1996), the model suggests concentration of erosion in a topographic band whose height is dictated by glacial/interglacial altitudinal limits to the ELA and whose width is a function of the concomitant glacial expansion/retraction in the landscape. The windward band width and height are likely to be greater than those of the leeward flank. The range crest is defined by a topographic peak that corresponds spatially with a zone of low glacial erosion. Modified after Meigs and Sauber (2000).

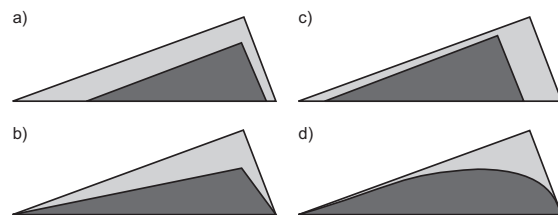


Figure 2.5: Influence of different erosion models on the shape of an asymmetric mountain belt. The light shaded area shows the mountain belt before, the dark shaded area after erosion. (a) Constant erosion rate. (b) Erosion rate proportional to elevation. (c) Erosion rate proportional to slope. (d) Erosion rate proportional to surface curvature. Note that the highest point of the topography remains laterally fixed in erosion models (a) and (b). Modified after Stüwe (2000).

an elevation dependent erosion model does not take other parameters like uplift or precipitation rates into account and thus contradicts with observations from recent field studies. Dadson et al. (2003) showed that the highest erosion rates in Taiwan are found where rapid deformation, high storm frequency and weak substrates coincide, despite low topographic relief. Nevertheless, an

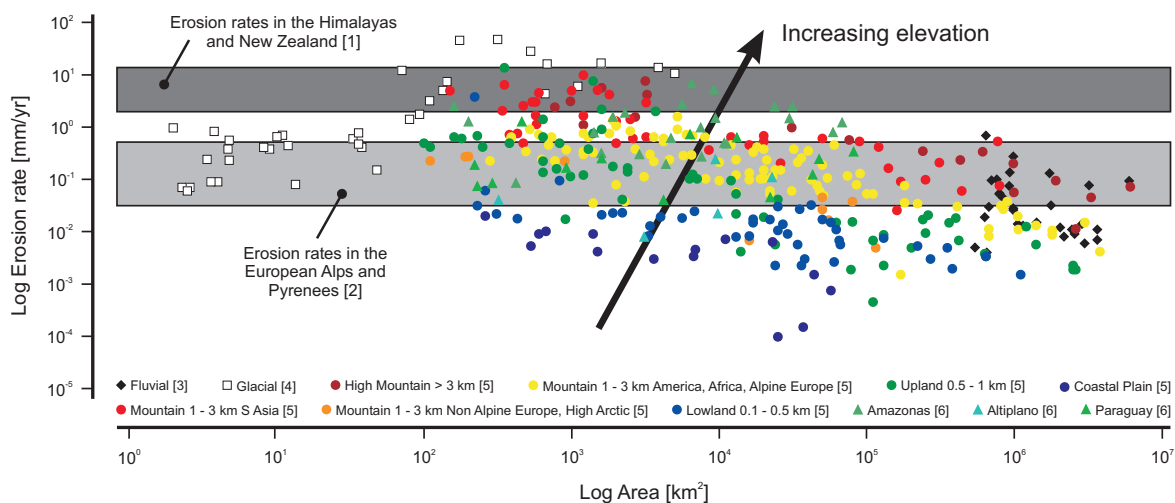


Figure 2.6: Relation between catchment area, erosion rate, and altitude (arrow). Note different trends for fluvial and glacial erosion rates. The latter are highest along the ELA and a larger catchment area implies a larger area covered by the ELA. A larger catchment area in fluvial terrains is often associated with low local relief, which hampers fluvial erosion. Data sources: [1] Adams (1980), Hovius et al. (1997), Lavé and Avouac (2001), Zeitler et al. (2001), White et al. (2002), Dadson et al. (2003), Willett et al. (2003), Barnard et al. (2004); [2] Morris et al. (1998), Fitzgerald et al. (1999), Schlunegger et al. (2001); [3] Summerfield and Hulton (1994); [4] Hallet et al. (1996); [5] Milliman and Syvitski (1992); [6] Filizola et al. (2002).

elevation dependent erosion model is a closer approximation of nature when compared with the constant erosion model (Stüwe, 2000).

The model, which states that erosion rates are proportional to slope (Eq. 2.4) was used to describe many landforms such as the geomorphic evolution of passive margins (Stüwe, 2000).

The diffusion model (Eq. 2.5) assumes proportionality between temporal change and spatial curvature. Despite its simple form, it summarises a range of physical processes such as fluvial incision, hillslope creep and even bedrock landslides. The diffusion model has been very successfully applied in a variety of numerical simulations concerned with the interaction of deformation and erosion (Koons, 1995; Tucker and Slingerland, 1996; Densmore et al., 1998; Willett, 1999; Simpson and Schlunegger, 2003; Simpson, 2004). Persson et al. (2004) used a combination of numerical and sandbox simulations to investigate the topographic evolution of bivergent sand-wedges.

From the above erosion models the elevation dependent erosion law was chosen and imple-

mented to simulate erosion during the sandbox experiments presented in this study. As a second order approach (Stüwe, 2000) it allows to account for results from Willett et al. (1993), who suggested that the location of erosion with respect to the convergence geometry has a significant influence on the distribution and propagation of deformation as well as on the outcrop pattern of metamorphic facies belts. Also, it is emphasised that it was not intended to model the process of erosion itself. Instead, this study is aimed at simulating the effect of erosion on orogenic belts, i. e., unloading with a certain distribution perpendicular to orogenic strike.

Furthermore, an elevation dependent erosion scheme provides a minimum estimate of erosion rates, since Montgomery and Brandon (2002) pointed out that the relation between relief and erosion rate might be better described by a power law. A higher than a minimum estimate of the erosion rates might have exaggerated the effect of erosion on deformation, which was not intended. In addition, an elevation dependent erosion model

has also been successfully applied to (i) numerically simulate the kinematic evolution of bivergent orogens (Pfiffner et al., 2000); (ii) to investigate the effect of erosion on forebulge unconformities (Crampton and Allen, 1995) and (iii) to calculate particle paths trajectories in either bivergent orogens or accretionary wedges (Dahlen and Suppe, 1988; Dahlen and Barr, 1989; Dahlen, 1990; Whipple and Meade, 2004).

The constant erosion model would have been simpler to simulate and considerable experience within sandbox simulations exists. However, this model does not account for the gradient dependence inherent in erosion which should find an expression in the model. Both the slope and the surface curvature dependent erosion models are at present beyond the resolution of this work. At this stage sandbox simulations might be limited by human determined accuracy. We speculate that it would be a key challenge to find a compromise between erosion model (Eq. 2.3) and (Eq. 2.5) to incorporate it in sandbox simulations.





## 3 Continental collision zones

The following chapter provides a summary of concepts and models thought to describe bivergent wedges. Thereby, special emphasis is devoted to the ability of these models to predict the spatio-temporal distribution of deformation and surface uplift.

### 3.1 Kinematic concepts of bivergent orogens

Lithosphere-scaled profiles across natural bivergent orogens such as the European Alps, the Pyrenees or Taiwan (Fig. 3.1) have several phenomena in common, which result from the asymmetry associated with the convergence geometry, i. e., the presence of a downgoing and an overriding plate. This asymmetry forms the basis for the key kinematic assumption that collisional orogens result from the partial subduction of continental lithosphere and accretion of crustal material (Willett et al., 1993; Ellis et al., 1995; Ellis, 1996). According to Willett et al. (1993) a velocity discontinuity (singularity) separates the subducting (lower) plate from the overriding (upper) plate and forms thus the lower limit of accretion (Fig. 1.2). The asymmetry of the subduction process evokes a polarity in the resulting crustal mass transfer, i. e., all crustal mass moving into an orogen is derived from the subducting plate and moves towards the overriding plate. This in turn leads to the formation of two crustal sub-wedges. The pro-wedge located upstream of the singularity grows by frontal and basal accretion of lower plate material. In contrast, the retro-wedge located downstream of the singularity develops by translation of pro-wedge material towards the upper plate. The axial-zone is defined as the topographic culmination of the

bivergent wedge and changes its position with respect to the singularity through time. Furthermore, both the pro- and the retro-wedge differ also with respect to their topographic gradients. Thereby, the former has a lower and the latter a higher topographic gradient (Willett et al., 1993; Beaumont et al., 1996).

The asymmetry of the convergence geometry evokes also a distinct temporal distribution of deformation. During early stages of collision, deformation is dominantly located within the pro-wedge, but migrates towards the upper plate during a late collisional-stage (Willett et al., 1993; Beaumont et al., 1996). A further key observation, which emerges from the above cross-sections, is the flexural downbending of the involved lithospheres during continental collision. Thus, a successful simulation of bivergent wedges should provide the key characteristics indicated above.

### 3.2 Kinematic models of fold and thrust belts

One of the critical issues in the analysis of fold and thrust belts, is the timing of thrusting and several models have been put forward to explain the variability found in nature (Storti et al., 2000; Butler, 2004). These are:

- i. Forward breaking piggy-back thrusting (Boyer and Elliott, 1982), where displacement is transferred onto a new thrust initiated in the footwall of the previously active thrust (Fig. 3.2a). The latter is abandoned and passively carried in the hangingwall of the former (Butler, 1987). Thus, deformation propagates systematically from the hinterland towards the foreland.
- ii. Break-back thrusting (Butler, 1987), where a sole thrust propagates into the foreland, followed by the formation of major thrusts

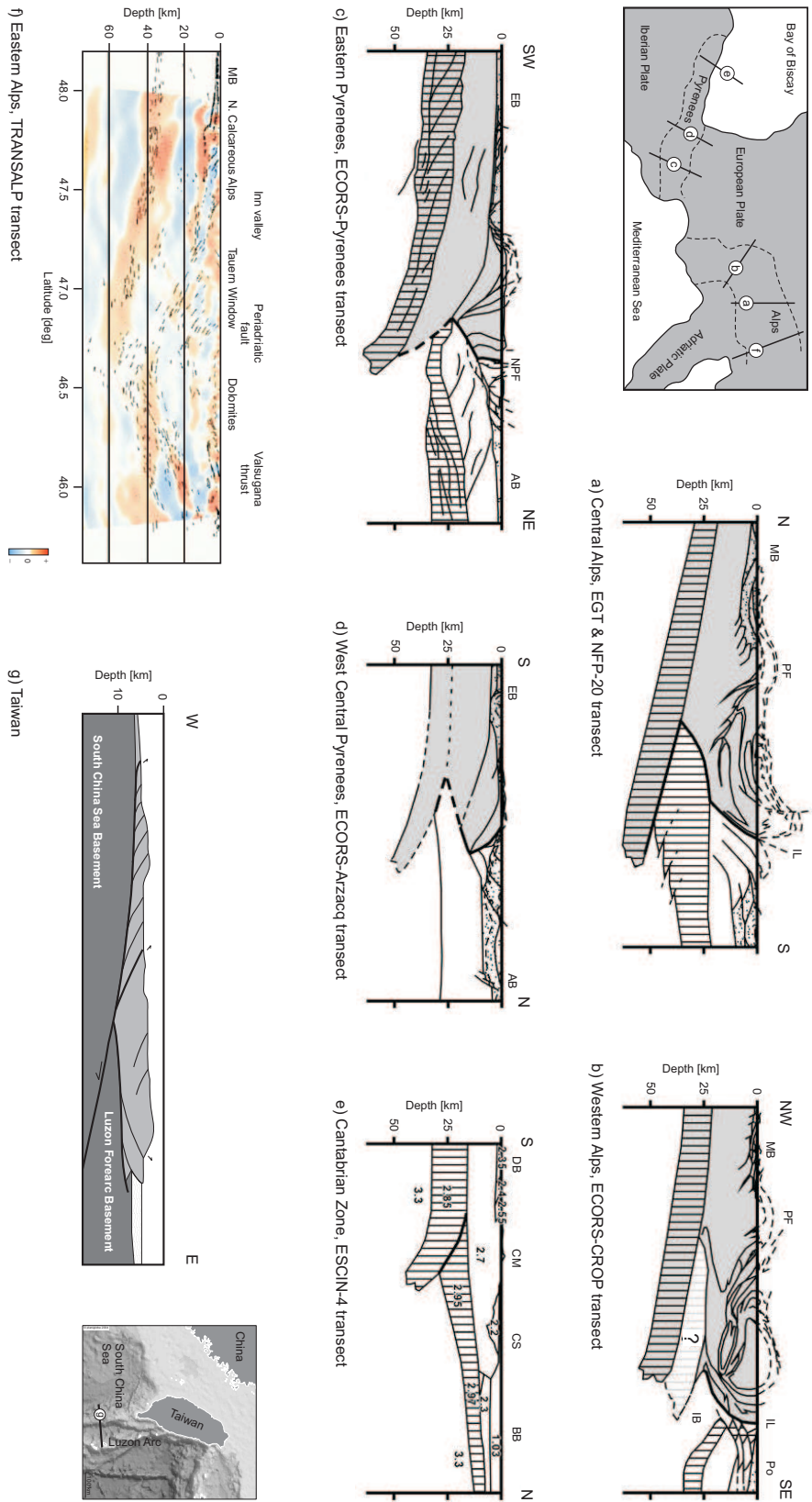


Figure 3.1: Crustal scaled cross-sections of divergent orogens: (a) Central Alps; (b) Western Alps. The area with gray vertical ruling represents imbricated European lower crust; (c) Eastern Pyrenees; (d) West Central Pyrenees; (e) Cantabrian Zone, densities are listed in  $g/cm^3$ ; (f) Eastern Alps; (g) Taiwan. Cross sections (a) - (e) are based on deep seismic reflection, refraction and gravity. Cross section (f) is based on seismic reflection and receiver functions, cross section (g) on seismic reflection. No vertical exaggeration. Gray represents the downgoing and white the overriding plate. Vertical ruling in (a) - (e) indicates a reflective and high velocity or density (e.g.,  $> 6.5 km/s$ ;  $2900 kg/m^3$ ) layer commonly associated with the mafic lower crust. Dot pattern represents foreland sedimentary deposits. Dashed lines indicate eroded features or lack of control. AB, Aquitaine basin; BB, Bay of Biscay; CM, Cantabrian mountains; CS, Cantabrian shelf; DB, Duero basin; EB, Ebro basin; IB, Ivrea Body; IL, Insubric Line; MB, Molasse basin; PF, Penninic front; Po, Po basin. (a) - (e) modified after Moore and Witschko (2004), (f) after Kummerow et al. (2004) and (g) after Malavieille et al. (2002). Taiwan map created with [www.planiglobe.com](http://www.planiglobe.com).

above it (Fig. 3.2b). Thereby, successively younger thrusts are formed towards the hinterland (Morley, 1988).

- iii. In-sequence thrusting, where a thrust sequence has formed progressively in one direction, which can either be a forward- or a break-back sequence (McClay, 1992).
- iv. Out-of-sequence thrusting (Morley, 1988; McClay, 1992), where the sequence of thrusting does not conform with either a progressive forward- or break-back sequence. Morley (1988) distinguished three modes of out-of-sequence thrusting: the re-activation of an older thrust (Fig. 3.2c), synchronous thrusting (Boyer, 1992; Storti et al., 2000), where two or more thrusts accumulate displacement at the same time (Fig. 3.2d) and the formation of a new thrust which cuts through and displaces pre-existing thrusts (Fig. 3.2e).

Whether forward breaking, break-back, in sequence or out-of-sequence thrusting occurs is commonly attributed to local factors such as mechanical stratigraphy, syntectonic erosion, sedimentation or basement fabrics (Storti et al., 2000). Storti et al. (2000) showed also that several of the above “thrust-modes” can act at the same time. This is thought to result from the complex mechanical balance, which varies through time.

Although, not clearly stated, the above conceptual models involve some predictions of how displacement is partitioned in space and time. Henry Cadell (1888) was probably the first to note that the slip along the deformation front depends on the phase within the accretion cycle, a term not known in his days. Cadell (1888) showed that *at one point, the brittle strata snapped, i. e., a thrust was formed, and all the movement was concentrated along the line of weakness thus produced. The whole mass above this thrust-plane moved obliquely upwards and forwards, and all interstitial movement ceased.* Similarly, Mulugeta and

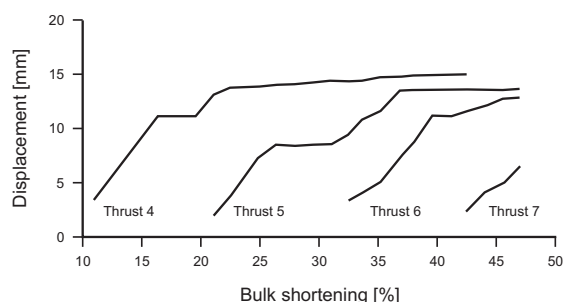
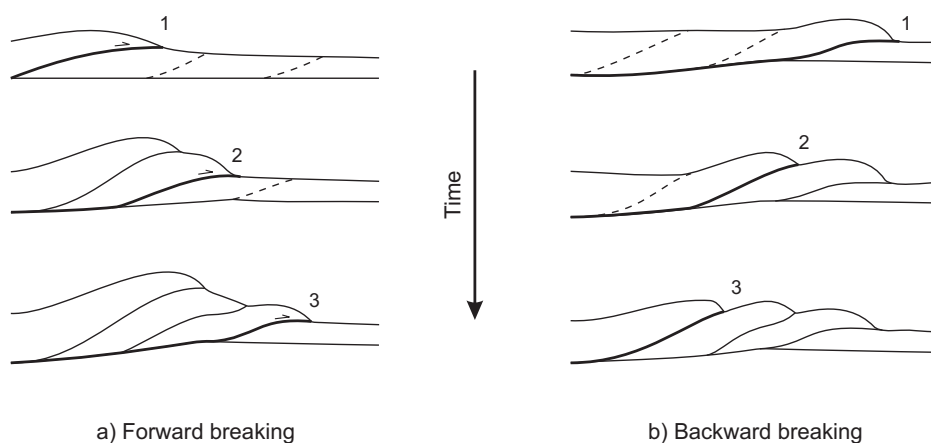


Figure 3.3: Displacement versus bulk shortening of four thrusts taken from Koyi (1995). Evolution of displacement of all imbricates follows a similar pattern; starting with a sharp increase as the imbricate begins to form, followed by little or no additional displacement before the formation of a new imbricate in front of the former. This in turn is followed by a gentler increase in displacement that decreases significantly with progressive deformation.

Koyi (1992) found that lateral growth of an accretionary wedge is episodic and Koyi (1995) suggested that each accretion episode is predated by a stepwise increase of the height of the wedge. Furthermore, Koyi (1995) demonstrated that displacement rate along thrusts is not constant through time and that three phases can be distinguished. During the first phase, i. e., the initiation of an imbricate, displacement rate is high, followed by a period of quiescence, during which a new thrust is formed in the foreland. In the third phase a slight increase of the displacement rate, which is lower than the one in the first phase can be observed. Finally, displacement rate approaches zero with continued convergence (Fig. 3.3). This result suggests thus that displacement is partitioned in space and time. Experimental observations and minimum work calculations by Gutscher et al. (1998) provided additional support for the cyclic nature of accretion. Similar to Koyi (1995) they found that (i) the maximum uplift migrates systematically backwards during an accretion cycle and that (ii) the main backthrust accommodates most of its slip at the end of each accretion cycle, which lead Gutscher et al. (1998) to conclude that each accretion cycle consists of two phases: the thrust initiation and the underthrust-

## End-member modes of thrust sequences



## Modes of out-of-sequence thrusting

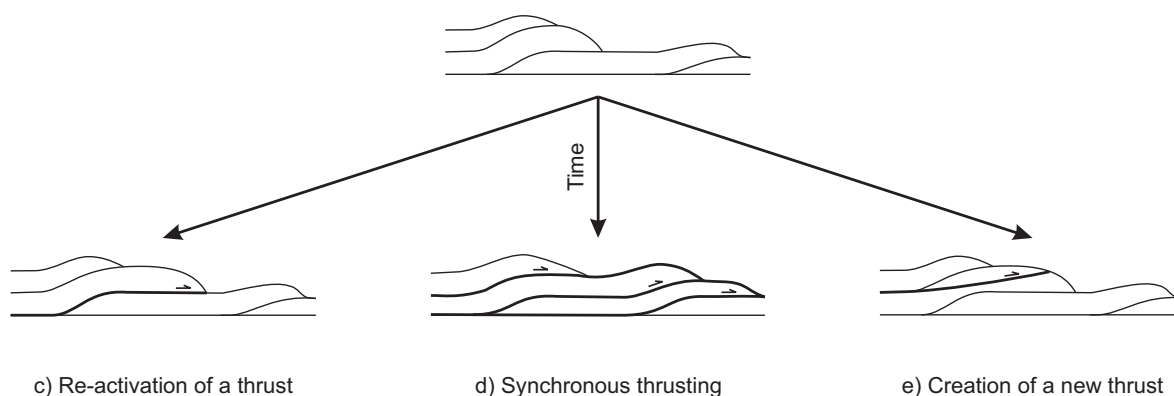


Figure 3.2: End-member modes of thrust sequences, modified after Morley (1988). (a) Forward or piggy-back breaking sequence, where deformation propagates toward the foreland with time. (b) Break-back sequence, where deformation propagates toward the hinterland with time, numbers indicate sequence of activity. Modes of out-of-sequence thrusting: (c) Re-activation of an older thrust located within the wedge. (d) Synchronous thrusting of two or more thrusts. (e) Creation of a new thrust, which cuts across and displaces older ones.

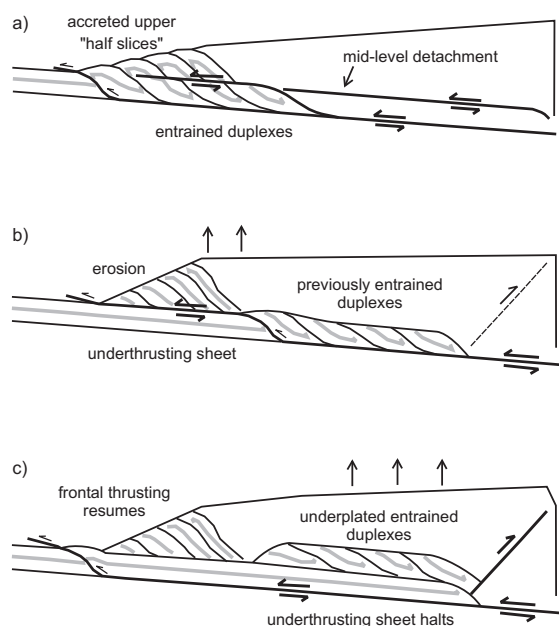


Figure 3.4: Bipartite evolution of an accretion cycle, taken from Gutscher et al. (1998). (a) Frontal accretion with shearing of imbricate slices at a mid-level detachment. (b) Underthrusting with frontal uplift. (c) Underplating of entrained duplexes associated with backthrusting and uplift at the rear of the wedge (vertical arrows indicate maximum uplift). Gutscher et al. (1998) used a high basal friction, i. e.,  $\mu_b = 0.5$ , which is similar to the one used in this study  $\mu_{dynamic} = 0.54$ .

ing phase respectively (Fig. 3.4). Such a bipartite evolution has also been documented from sandbox experiments, which simulate oblique convergence (Hoffmann-Rothe et al., 2004). Therefore, both terms, i. e., the thrust initiation phase and the underthrusting phase are adopted in this study.

### 3.3 The Critical Coulomb Wedge concept

The fundamental dynamic assumption is that a subduction-accretion process leads to the formation of an orogenic wedge with a geometry governed by the relative magnitude of the frictional resistance along the base and the compressive strength of the wedge material (Dahlen, 1990).

Although, considerable natural variations exist among crustal wedges, they exhibit several common properties in cross section. Chapple (1978) pointed out that accretionary wedges as well as fold-and-thrust belts show: (i) a basal detachment or décollement, which dips towards the interior of the mountain belt; (ii) large horizontal compression in the material above and little deformation within the material below the detachment and (iii) a characteristic wedge shape of the deformed material, tapering towards the foreland of the mountain belt. These observations in conjunction with sandbox experiments formed the basis for the critical taper theory (Davis et al., 1983), which was later adopted by various physical and numerical simulation studies for accretionary wedges (Byrne et al., 1993; Kukowski et al., 1994; Lallemand et al., 1994; Gutscher et al., 1996, 1998; Lohrmann et al., 2003), for fold-and-thrust belts (Storti and McClay, 1995; Nieuwland et al., 2000; Cobbold et al., 2001), as well as for doubly vergent wedges (Malavieille, 1984; Wang and Davis, 1996; Willett, 1999; Storti et al., 2000, 2001; Persson et al., 2004; Hoth et al., 2006). In principle, provided crustal deformation is driven by convergence and basal shear stresses are significant, the deforming crust attains a ‘critical’ balance between gravitational stresses, basal shear stresses and the strength of the crust at the scale of the entire crust, thus resulting in the formation of an ‘orogenic wedge’ (Platt, 1986).

The overall mechanics of critical Coulomb wedges are commonly considered to be analogous to the mechanics of wedges that form in front of a moving bulldozer or snow plow (Davis et al., 1983) and both models are often cited for intuitive understanding. Accordingly, if a snow plow starts to move through a fresh layer of snow two scenarios can be envisaged. Given that the internal strength of the snow is higher than the friction with the road, e. g., if the snow is icy and the road is warm, then the snow will be moved as an undeformed slab in front of the plow. If

however, the internal strength is smaller than the friction with the road, which is usually the case, then the snow deforms internally and its surface will become inclined. According to the Mohr-Coulomb failure criterion, the strength of the snow will increase as the thickness of the snow wedge increases until a critical taper between the surface slope and the basal detachment (i. e., the road) is reached. At this stage, the strength of the snow is exactly as large as the basal traction and the snow wedge can now move along its base without internal deformation. It follows that a critically tapered snow wedge is the thinnest body that can be thrust over its detachment without internal deformation. While sliding over its base, accretion of new material to a critically tapered snow wedge promotes internal deformation to accommodate the respective influx and to restore the critical taper.

From the above analogy it is evident that the parameters, which determine the failure criterion of the wedge material and its base, control the shape of the wedge. Thus, a failure law must be specified both within the wedge and along its base in order to solve for the state of stress within and for the critical taper of the respective wedge (Dahlen and Suppe, 1988). Generally, stress within the lithosphere is thought to be limited by frictional sliding (Byerlee, 1978) at low confining pressures and by thermally activated processes, especially dislocation creep (Brace and Kohlstedt, 1980) at high temperatures. Therefore, brittle behaviour is thought to be satisfactorily described by the Mohr-Coulomb failure criterion and is considered as the stress-limiting factor (Davis et al., 1983; Dahlen and Suppe, 1988). It can be written as:

$$\tau = \mu(\sigma_N - p_f) + C_0 \quad (3.1)$$

where  $\tau$  is the shear strength,  $C_0$  the cohesive strength,  $\mu$  is the coefficient of internal friction, which relates to the angle of internal friction ( $\phi$ ) by  $\mu = \tan \phi$ ,  $\sigma_N$  is the normal stress and  $p_f$  the fluid pressure. The form  $(\sigma_N - p_f)$  describes the effective normal stress (Hubbert and Rubey,

1959). It follows from equation (3.1) that the Mohr-Coulomb failure criterion is strongly (fluid) pressure-dependent but is largely independent of temperature or strain rate (Byerlee, 1978).

The effect of cohesion on the magnitude of the resulting shear strength and finally on the geometry of the wedge depends on the vertical and horizontal position within the wedge under consideration. At depths on the order of a few kilometers, the effect of cohesion, which is in the order of 1 to 150 MPa (Dahlen and Suppe, 1988), is negligible in comparison with the pressure-dependent term in the failure equation (3.1). According to Davis et al. (1983) the main effects of cohesion on wedge geometry will be observed near the toe of the wedge, where cohesion can add significantly to the total strength and produce a critical taper smaller than the corresponding cohesionless taper. Farther from the toe where the wedge is thicker, the pressure-dependent term dominates, and the critical taper will asymptotically approach the cohesionless value (Davis et al., 1983).

Furthermore, Byerlee (1978) demonstrated that  $\mu$  is largely independent of lithology but depends on the magnitude of normal stresses. For normal stresses below 200 MPa, the shear stress required to induce sliding is given by  $\tau = 0.85 \sigma_N$ ; above 200 MPa,  $\tau = 0.6 \sigma_N$  (Byerlee, 1978).

As indicated above, fluid pressures play a crucial role in controlling the mechanics of thrust faulting. Fluids cannot support shear stresses and their respective pressure has the same magnitude in all directions. Therefore, fluid pressure reduces the magnitude of the principal stresses, but the deviatoric stress remains constant. It follows that the Mohr circle is shifted towards the origin – brittle failure sets in at lower shear stresses. The corresponding angle between  $\sigma_1$  (highest normal stress) and the failure plane is reduced with respect to the case, where no fluid pressure was present.

From the above description of the controlling failure law it is evident that the lower limit of the

Critical Coulomb wedge (CCW) theory is the middle to lower crust, where pressure and temperature become sufficiently high that common rocks begin to display a temperature-dependent plastic behaviour (Davis et al., 1983). Although the CCW concept was originally formulated for a non-cohesive Mohr-Coulomb type rheology (Davis et al., 1983; Dahlen et al., 1984) presented a solution involving cohesion and Platt (1993) extended this theory to involve perfectly plastic materials.

In the following a short derivation of the critical taper equation is provided. A Cartesian coordinate system is employed, where  $x$  is parallel to the base of the wedge and  $z$  increases upward (Fig. 3.5). The local thickness of the wedge is given by  $H_w$ , measured along the  $z$ -axis. Neglecting along-strike variations and assuming plane strain, Davis et al. (1983) proposed that the critical taper of a compressive wedge is controlled by the balance of four forces in the  $x$  direction:

The gravitational body force which is given by:

$$F_g = -\rho g H_w dx \sin \beta \quad (3.2)$$

where  $\rho$ , assumed constant, is the density of rocks,  $g$  is the acceleration due to gravity,  $H_w$  is the height of the wedge and  $\beta$  is the dip of the base with respect to the horizontal.  $F_g$  is negative, since it resists movement of the material uphill.

The  $x$ -component of the pressure of the water overburden, which resists sliding:

$$F_w = -\rho_w g D dx \sin(\alpha + \beta) \quad (3.3)$$

where  $\rho_w$  is the density of water,  $D$  is the height of the water column at  $x$  and  $\alpha$  is the local angle of topographic relief of the wedge.

The basal shear traction  $\tau_b$  is negative as well, since it resists sliding and is given by:

$$\tau_b = -\mu_b (1 - \lambda_b) \rho g D H_w \quad (3.4)$$

where  $\mu_b$  is the basal coefficient of friction and  $\lambda_b$  is the Hubbert and Rubey pore fluid ratio for

the basal detachment. While introducing  $\mu_b$  and  $\lambda_b$  one allows explicitly for the fact that the basal detachment is a zone of weakness either because of a lower intrinsic strength with respect to the internal strength ( $\mu_0$ ), or because of elevated fluid pressures. For a through-going basal detachment to operate the condition

$$(1 - \lambda_b) \mu_b = (1 - \lambda_0) \mu_0 \quad (3.5)$$

must be satisfied. Thereby,  $\lambda_0$  is the internal pore fluid ratio (Davis et al., 1983).

Let  $\sigma_x(x, z)$  be the normal traction, which acts across any face perpendicular to the  $x$ -axis. Integration of this term with respect to  $dz$  at position  $x$  delivers the work needed to push the face at position  $x$ . However, this is counteracted (actio = re-actio) by a force at  $x + dx$  which is somewhat smaller, since  $z$  is lower and the respective work resulting from integration is smaller as well. Thus, the difference in work between the position  $x$  and  $x + dx$ , which can be considered as the gradient or the first derivation, is the resultant compressive push in positive  $x$  direction. In case  $dx > 0$  the above gradient belongs to a secant. Therefore, the limit of  $dx \rightarrow 0$  is needed to calculate the gradient of the tangent at position  $x$ , which is thus the resultant compressive force at position  $x$  (Fig. 3.6).

$$F_s = \frac{d}{dx} \int_0^H \sigma_x dz \quad (3.6)$$

Balancing the above four forces to find the condition at which the wedge can be pushed over its base without internal deformation, results in:

$$0 = F_g + F_w + \tau_b + F_s. \quad (3.7)$$

Equation (3.7) implies that a critically tapered wedge is at the verge of shear failure everywhere, which is the key physical assumption made in the CCW concept. In order to solve for the state of stress within and for the critical taper of the respective wedge, the only remaining unknown quantity is  $\sigma_x$ , which can be determined by using



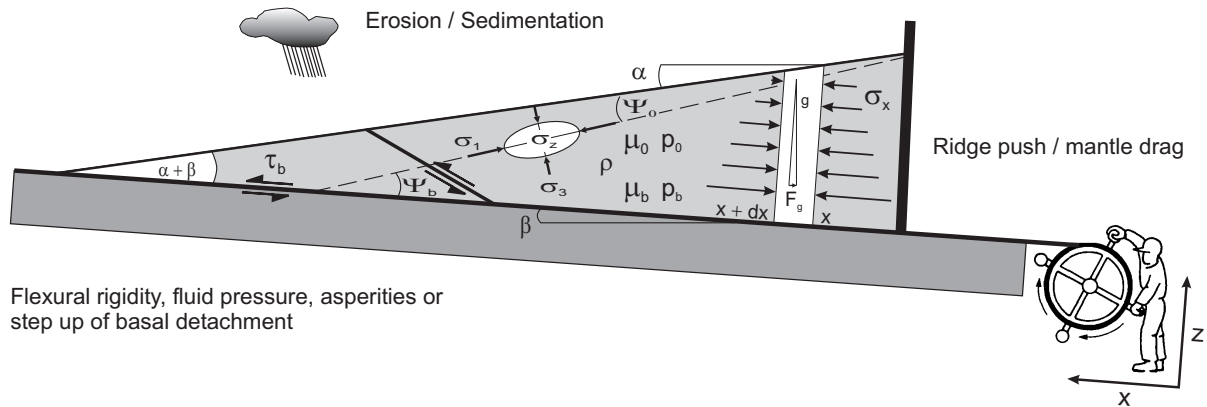


Figure 3.5: Schematic diagram of a subaerial wedge subject to horizontal compression. Terminology used to describe the critical taper equation is provided:  $\alpha$  surface slope;  $\beta$  basal dip;  $\mu_0$  coefficient of internal friction;  $\mu_b$  coefficient of basal friction;  $p_0$  internal fluid pressure;  $p_b$  basal fluid pressure;  $\rho$  density of rocks;  $\sigma_1$  maximum,  $\sigma_3$  minimum principal stress;  $\Psi_0$  angle between  $\sigma_1$  and surface slope;  $\Psi_b$  angle between  $\sigma_3$  and wedge base. The three forces, acting upon an arbitrary wedge-column of width  $dx$  are: the gravitational body force and the basal traction resist movement of the material up hill and the push from the rear. For stable sliding of the whole wedge to occur, the force balance has to equate to zero, i. e., a critically tapered wedge is the thinnest body of material, which can slide over its base without internal deformation. Additionally, external processes thought to influence the shape and growth of wedge are indicated. Figure in cap (Dan Davis) not shown to scale. Modified after Davis et al. (1983), Dahlen (1990) and Lohrmann et al. (2003).

a Mohr circle (Davis et al., 1983). After several rearrangements of equation (3.7), small angle approximations as well as the simplifying assumption that  $\lambda_0 = \lambda_b$ , one finally arrives at the following equation for a submarine wedge:

$$\alpha + \beta = \frac{(1 - \lambda_b)\mu_b + (1 - \rho_w/\rho)\beta}{(1 - \rho_w/\rho) + (1 - \lambda)K}. \quad (3.8)$$

In case of a subaerial wedge  $\rho_w$  is set to 0 in equation (3.8). It follows:

$$\alpha + \beta = \frac{(1 - \lambda_b)\mu_b + \beta}{1 + (1 - \lambda)K}. \quad (3.9)$$

In case of sandbox experiments where the sand is dry, i. e.,  $\lambda = 0$  and assuming that  $\lambda_b = 0$  as well, one obtains:

$$\alpha + \beta = \frac{\mu_b + \beta}{1 + K} \quad (3.10)$$

where  $K$  describes the push from the rear.

*Implications and predictions of the CCW concept.* The CCW concept predicts that a high ratio between basal and internal friction increases,

whereas a low ratio decreases the critical taper. Similarly, a high fluid pressure inside the wedge decreases its strength and increases thus the critical taper, while a high fluid pressure along the basal detachment decreases the basal strength and thus decreases the critical taper.

A taper stability field ( $\alpha - \beta$  space) is defined by the basal and internal coefficients of friction (Dahlen, 1984), whereby cohesion and fluid pressure are neglected. Wedges in region I and III fail by thrusting or by a combination of thrusting and normal faulting because the frictional traction on their base is too great (Fig. 3.7). The resulting deformation acts to increase the taper of wedges in region I and to decrease it in region III. Wedges in regions II and IV are unstable as well, since the friction on their bases is too weak. They both fail by normal faulting, decreasing their taper in region II by gravity spreading and increasing it in region IV. Any wedge in the stability field is stable as long as the basal friction remains constant. An increase of the magnitude of basal friction causes regions I and III to grow and regions II and IV to

shrink in size. It follows that the stable regions decreases in size and ultimately disappears as the limit  $\mu_b = \mu_0$  is approached (Dahlen, 1984).

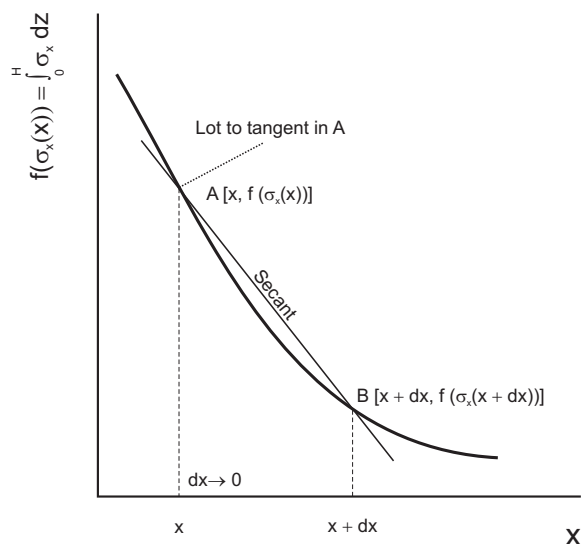


Figure 3.6: Relation between  $x$  position and a hypothetical solution of  $f(\sigma_x(x)) = \int_0^H \sigma_x dz$ , which is the work needed to push a plane perpendicular to  $x$ -axis at position  $x$ . This work is counteracted by forces acting on the plane at position  $x + dx$ . However, the latter is somewhat smaller than the former, since the push is coming from the thick end and the  $x$ -face is larger in area at  $x$  than at  $x + dx$ . The resultant force pushing the wedge towards the thin end, can be thus considered as the gradient of the secant (between A and B). If  $dx \rightarrow 0$  is given, one obtains the gradient of the tangent at A and thus the push from the thick end at position  $x$ .

Surface processes tend to perturb the critical topographic form and may thus control the propagation and distribution of deformation within an orogenic wedge (Fig. 3.7). Outward propagation of deformation towards the foreland is more likely to occur in regions where erosion cannot maintain the surface gradient at or below a critical taper, or where enhanced sedimentation within intramontane basins adds to the thickness of the orogenic wedge (Schlunegger, 1999; Hovius, 2000). In contrast, erosion decreases the thickness of the wedge, which is equivalent to a decrease in the strength of crustal faults and thus drives continued internal deformation until the critical taper is restored (Davis et al., 1983; Dahlen and

Suppe, 1988; Willett, 1999). Correction of the perturbed topographic shape back to its critical state may also lead to changes in the pre-existing morphology, the pre-existing drainage pattern and the erosion rates which may finally trigger different modes of deformation.

The CCW concept has also been employed to predict the distribution and magnitude of fluid pressures, the velocity field and the distribution of metamorphic facies within accretionary wedges as well as their thermal structure (Dahlen and Barr, 1989; Barr and Dahlen, 1989; Barr et al., 1991). Furthermore, Hilley et al. (2004) and Hilley and Strecker (2004) used the CCW concept in conjunction with fluvial incision laws to show how a critically tapered orogenic wedge, which is in an erosional equilibrium, evolves through time. Probably the most important implication of the CCW concept is based on the fact that it does not depend on the across-strike position  $x$ , which means that critical wedges are scale invariant, i. e.,  $\alpha + \beta = \text{constant}$  (Davis et al., 1983; Dahlen and Suppe, 1988). The mechanics of orogenic wedges can thus be explained with the same concept used for snow or sand wedges. The above relation also indicates that critical wedges remain constant in shape but grow in size. A direct link between wedge shape and the orientation of the principle stresses is provided by:

$$\alpha + \beta = \Psi_b - \Psi_0 \quad (3.11)$$

where the angle between the maximum principle stress  $\sigma_1$  and the rigid base or the surface slope is denoted by  $\Psi_b$  for the former and by  $\Psi_0$  for the latter (Davis et al., 1983).

A self-similar evolution of a crustal wedge implies also that the depth to the basal detachment increases with time. Such a scenario has been proposed for Taiwan by Davis et al. (1983). Based on the above result Dahlen and Suppe (1988) showed that the width and the height of critically tapered wedges grow proportional to convergence or time  $t$  by  $t^{0.5}$  (Dahlen, 1990).

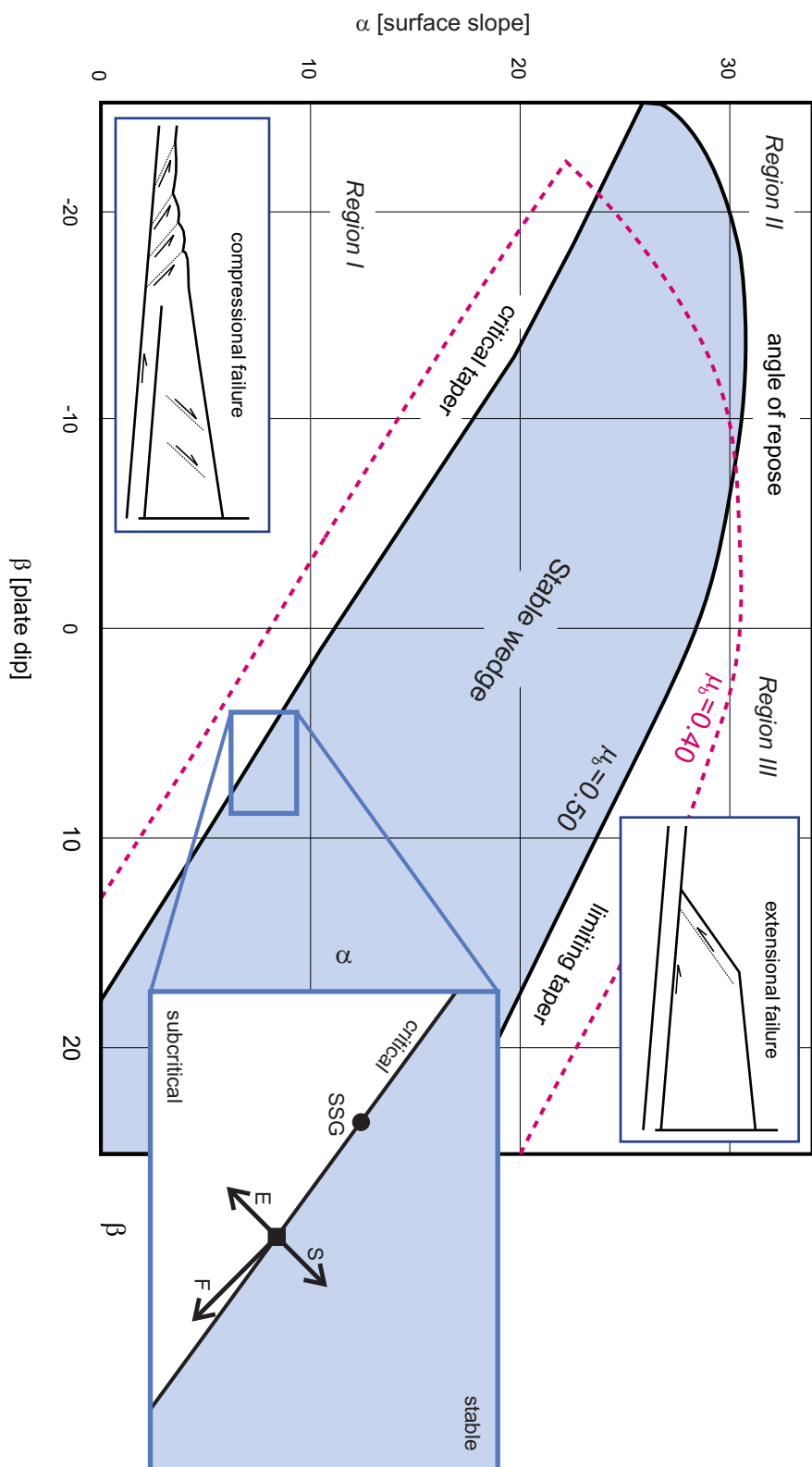


Figure 3.7: Taper stability field for two wedges with  $\mu_b = 0.5$  and  $\mu_b = 0.4$  and the four regions of non-stability. See text for explanation (page 21). Region IV not shown is located in the lower left corner. Modified after Dahlen (1984). Inset depicts influence of some key parameters: erosion of upper surface ( $E$ ), Sedimentation or increased resistance to erosion ( $S$ ) and flexural subsidence ( $F$ ). Self-similar growth (SSG) of a certain wedge is shown as well. Modified after Horton (1999).

Although the predictive power and generality of the CCW concept is evident, it “only” provides quasi-static solutions for the geometry and stress states of wedges, but does not make any predictions about the deformation or the kinematics within deforming wedges (Willet and Pope, 2004). Thus, the often cited modes of internal thickening such as synchronous and out-of-sequence thrusting as well as basal accretion or back rotation may or may not be a consequence of the CCW concept (Boyer, 1995). As outlined above, the CCW concept assumes a linear Mohr-Coulomb failure criterion, which seems to be an oversimplification since rocks exhibit pre-failure strain-hardening and post-failure strain-softening (e. g., Mandl et al., 1977; Lohrmann et al., 2003), which promotes the re-activation of thrusts. It might follow, that the CCW concept should only be applied to the frontal part of a wedge (Lohrmann et al., 2003).

### 3.4 The minimum work concept of mountain building

The minimum work concept provides an alternative view on mountain building. Its conceptual simplicity in combination with its potential to predict the spatial and temporal distribution of deformation, an issue, which cannot be resolved with the CCW concept, has attracted many workers (Masek and Duncan, 1998). This concept assumes that the combined gravitational and frictional work associated with each slip increment along a set of faults is minimised. Thus, the fault which consumes the least work to accommodate slip is “chosen” (Fig. 3.8). Prolonged slip along a fault induces a negative feedback, since the gravitational load increases with every new slip increment. At a certain stage, the initiation of a thrust within the foreland would consume less gravitational and frictional work to accommodate further convergence. Thereby, the magnitude of work needed to initiate a fault depends on

the depth to its detachment, the internal and basal properties of the material and finally on the fluid-pressure (Davis et al., 1983; Hardy et al., 1998).

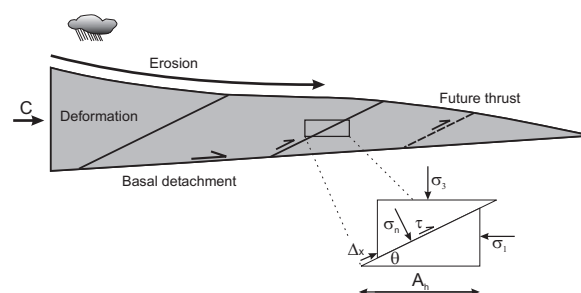


Figure 3.8: Schematic diagram of the minimum work concept and the parameters used to calculate the gravitational and frictional work. Modified after Hardy et al. (1998).  $C$ , external displacement rate;  $\theta$ , local dip of the fault;  $\Delta x$ , fault parallel displacement;  $A_h$ , area of the fault plane projected onto the horizontal plane;  $\sigma_1$ , maximum;  $\sigma_3$ , minimum principal stress;  $\tau$ , critical shear stress across the fault surface and  $\sigma_N$ , normal stress acting on this fault.

Although it is not appropriate to invoke a priori a minimisation principle to justify geological modelling, several studies have successfully demonstrated that the minimum work concept provides good approximations for specific aspects of mountain building; among them: the evolution of foreland duplexes (Mitra and Boyer, 1986), the lateral expansion of plateaus (Molnar and Lyon, 1988), the formation of triangle zones in fold and thrust belts (Jamison, 1993), the evolution of fold and thrust belts subject to erosion/sedimentation (Hardy et al., 1998), the initiation of thrusts within an accretionary wedge (Gutscher et al., 1998) and the interaction between erosion and plateau formation (Gerbault and Garcia-Castellanos, 2005).



## 4 Experimental method

The application of analogues to understand nature might be as old as man. One prominent example is the use of balls, instead of apples or cars to study the laws of conservation of either energy or momentum. The simplification of natural processes inherent in analogues enables the identification of the principles and the quantification of parameters that control nature and as such geodynamics. More specifically, mountain building is thought to depend on a multitude of parameters. Among the most important are deformation, erosion, sedimentation, and flexure, which may act on various time- and length-scales. Non-linear feedback processes are therefore likely to occur. As noted earlier, considerable amount of research on mountain building by either physical or numerical simulations has been carried out during the last decades and the respective parameter space has been extensively explored. These simulation techniques require that the overwhelming wealth of possible parameters, as they emerge from field studies, is simplified and that those parameters are investigated in accordance to their expected importance within the geodynamic framework. It is emphasised here that such a simplification is implicitly based on several model assumptions outlined in previous chapters. The resulting setup, i. e., the kinematic boundary conditions, may guide not only the interpretation of experimentally derived results, but also one's perception of natural processes, which might finally evoke circular reasoning. However, a fixed reference frame in conjunction with known boundary conditions, which can only be inferred in nature, might also help to interpret experimentally derived results. Despite these epistemological challenges, physical forward modelling techniques such as sandbox simulations have been successfully applied and provided detailed insight into the parameters controlling mountain building: basal fric-

tion (Mulugeta, 1988; Liu et al., 1992; Calassou et al., 1993; Nieuwland and Walters, 1993; Luján et al., 2003); presence of several décollements (Kukowski et al., 2002; Couzens-Schultz et al., 2003); thickness of the incoming layer (Calassou et al., 1993; Nieuwland and Walters, 1993; Gutscher et al., 1998; Soto et al., 2002); back-stop geometry and material (Davis et al., 1983; Malavieille, 1984; Byrne et al., 1988, 1993; Wang and Davis, 1996; Bonini et al., 1999; Storti et al., 2001); pore fluids (Cobbold et al., 2001); erosion and sedimentation (Merle and Abidi, 1995; Storti and McClay, 1995; Mugnier et al., 1997; Barrier et al., 2002; Persson et al., 2004; Hoth et al., 2006); topography (Dominguez et al., 1998; Marques and Cobbold, 2002; Del Castello et al., 2004); obliquity of convergence (Burbidge and Braun, 1998; Martinez et al., 2002; McClay et al., 2004; Hoffmann-Rothe et al., 2004). The above list does not claim to be complete.

The justification of the application of sandbox simulations to the brittle deforming part within orogenic wedges is derived from the fundamental observation that sand is characterised by similar mechanic properties as the upper brittle crust (section 4.1) and that brittle behaviour is scale-independent. The latter has been intuitively known from the earliest days of geology and led to the rule to always include a scale in drawings or maps. In later days, the scale independence has been more quantitatively shown by the Gutenberg-Richter-Law or by the length-displacement ratio of faults (e. g., Turcotte and Malamud, 2004). Also, a key prediction of the CCW concept, as outlined in section (3.3), is that the mechanics of mountain building are scale independent and can thus be understood while studying the mechanics of sand-wedges. Thus, the analysis of the spatio-temporal evolution of bivergent sand-wedges may provide predictions for natural observations which can be used in turn to constrain the former. In this study, emphasis is laid upon those predictions that are testable.

Two additional factors supported the use of 2D sandbox experiments. First, this method allows large magnitudes of convergence to be simulated. Second, a direct observation of strain localisation and fault propagation with a high temporal and spatial resolution, especially if monitoring techniques such as Particle Image Velocimetry (section 4.3) are applied, is possible.

Despite these advantages, sandbox simulations are like every other method associated with limitations, some with a more general and others with a more specific character. The former comprise the observation that subtle parameter variations, which can be easily explored with numerical simulations, are more difficult to test on their respective influence with sandbox simulations. However, the latter might provide trends, which can either be tested in numerical simulations or within field studies. Additionally, certain parameters such as erosion, sedimentation, fluid flow or phase transitions cannot be described or implemented in a physically correct way. In the case of erosion, sandbox experiments are “only” capable of simulating the effect, i. e., unloading of a structure, and not the process of erosion itself. Although, this limits the transfer of experimentally derived predictions to nature, we did not intend to rebuild a certain natural structure or geomorphologic feature and aimed at broader implications. Limitations, which are considered to be specific of the setup or the experimental implementation, are outlined were appropriate (section 4.2).

All sandbox simulations presented in this study were carried out at the Geodynamic Laboratory of the GFZ Potsdam, Germany. A short visit of the Tectonics Analogue Modelling Laboratory at the Vrije Universiteit Amsterdam, Netherlands was aimed at measuring the in-situ stress evolution in front of a propagating thrust. However, technical difficulties such as an insufficient shielding against external currents hindered success.

## 4.1 Physical properties of analogue materials

As indicated in the previous section, the knowledge of the physical properties of analogue materials is crucial for the justification of the sandbox simulation approach, to model upper crustal processes as well as the application of the CCW concept to laboratory sand-wedges. Since brittle behaviour is thought to be scale-invariant, the physical properties of the analogue materials were measured to compare experimental results with nature. Within this respect Hubbert (1937) noted that a change of the size of a given body is associated with a change of its physical properties. Therefore, sandbox-simulations do only unfold their full wealth of information if they are “properly” scaled with respect to their natural pendants.

The sand in this study, is derived from a Quaternary fluvio-glacial quartz sand deposit near Königsutter, Germany and shows a unimodal grain size distribution (Fig. 4.1). Grains are well to moderately rounded. Glass-beads (300–400  $\mu\text{m}$ ) and mortar were used as well, whereas the latter is characterised by a unimodal distribution with a slight negative skewness (Fig. 4.1).

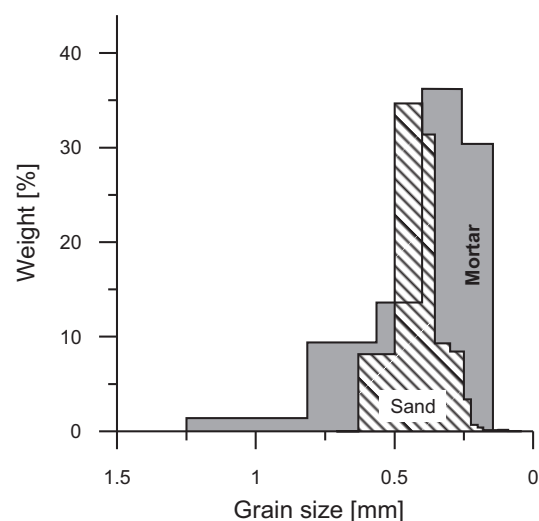


Figure 4.1: Grain size distributions of sand and mortar.

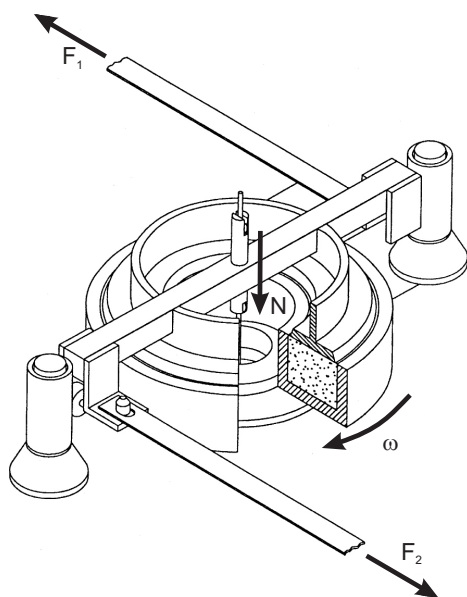


Figure 4.2: Ring-shear tester used to measure the mechanical properties of the analogue materials.  $N$  is normal load;  $\omega$  is angular velocity;  $F_1$  and  $F_2$  are the measured shear forces. Modified after Schulze (1994).

A ring-shear tester (Schulze, 1994) was utilized to measure the internal and the basal mechanic properties of the above analogue materials (Fig. 4.2). To determine the internal mechanic properties, either sand, glass-beads or mortar was sieved into a shear box (Fig. 4.2), which was subsequently loaded with a range of normal loads (1–12 kg). This range is similar to those normal loads, found in experiments. While the shear box rotated with a constant velocity, the associated shear force was measured. After an unloading phase during which the direction of rotation was reversed until the shear force dropped to zero, a new loading cycle was applied, i. e., the direction of rotation was again reversed. According to Byerlee (1978), this procedure allows the measurement of the frictional strength of the undeformed material (peak friction), the strength of the previously deformed material (static-stable friction) and the strength of active shear zones (dynamic-stable friction). A schematic stress-strain curve is shown in (Fig. 4.3). To assess the error associated

with the above procedure, all measurements were carried out three times. The raw data in conjunction with REM images of the granular materials are provided in (Fig. 4.4) and are summarised in table (4.1).

With respect to the derivation of cohesion values from ring-shear measurements, Schellart (2000) demonstrated that for very small normal stresses ( $< 400 Pa$ ) the Mohr envelope is characterised by a convex-outward shape which converges to a straight line with increasing normal stresses. Since the lowest normal stress applied during measurements at the GFZ Laboratory is  $500 Pa$ , it is justified to derive the respective cohesion values from linear extrapolation of the Mohr envelope. Both the coefficient of internal friction and the cohesion obtained for the above materials agree with Lohrmann et al. (2003), who found that granular flow of sieved, dry quartz sand is characterised by a strain-dependent deformation behaviour with pre-failure strain hardening and post-failure strain softening and is therefore similar to the non-linear deformation behaviour of crustal rocks in the brittle field. Based on the S30T sand, Lohrmann et al. (2003) tested different grain-size distributions and found that the similarity between the mechanic properties of brittle upper-crustal rocks and the sand is highest for sieved sand with a grain-size distribution, ranging from 20–630 mm, which is therefore used in this study.

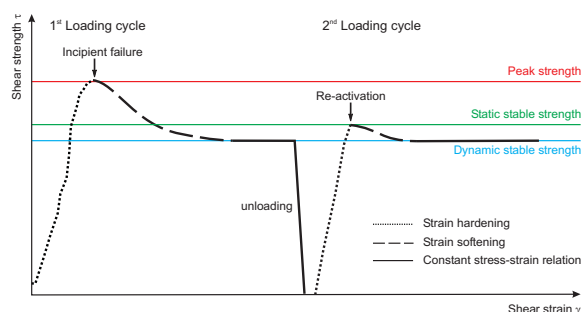


Figure 4.3: Characteristic stress-strain curve for the used sand as a function of angular shear ( $\gamma$ ). Two loading cycles are shown. See text for explanations.



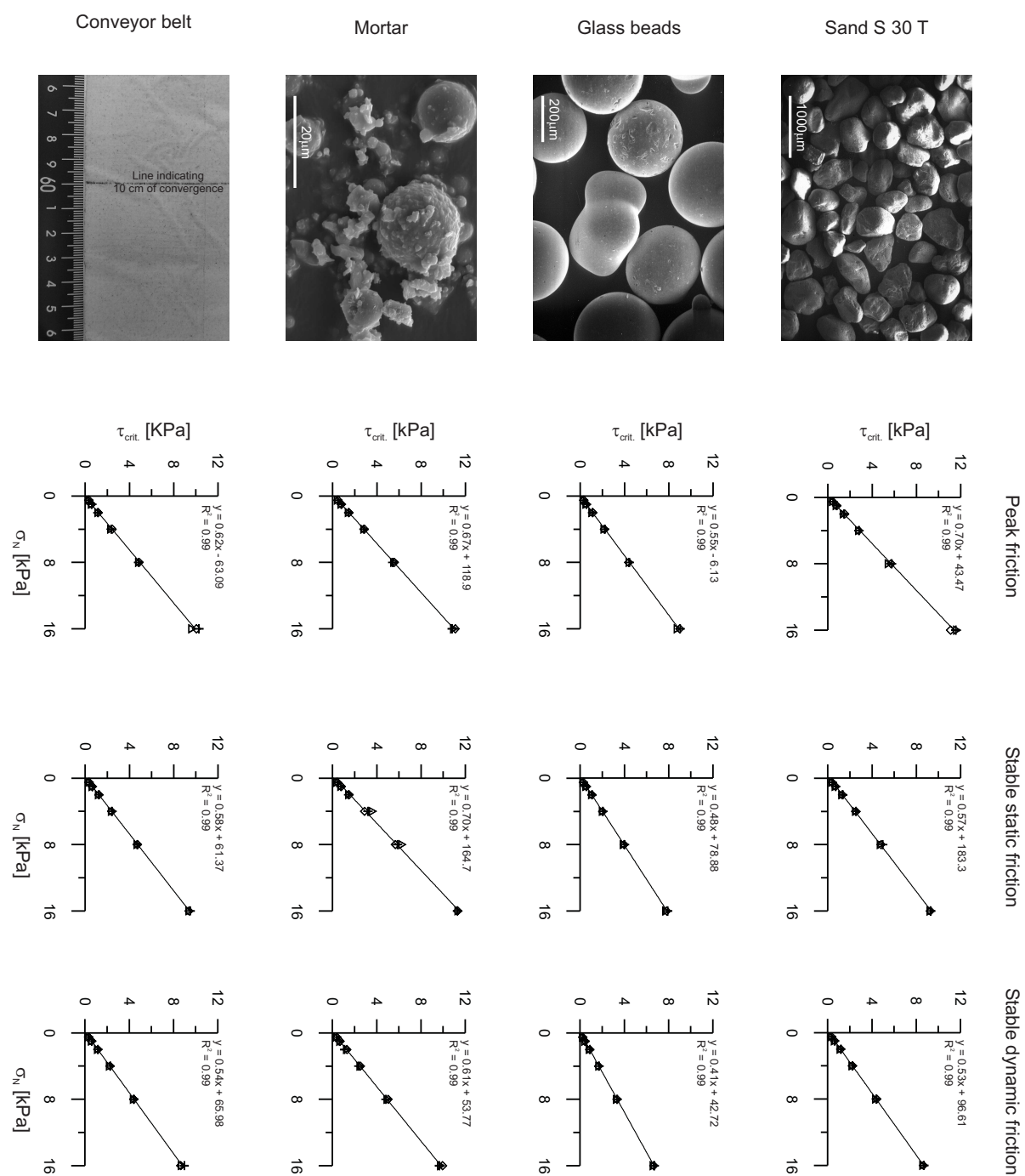


Figure 4.4: Results of ring-shear measurements. Shear stress  $\tau$  is a function of the normal stress  $\sigma_N$ . Columns from left to right, if page is turned: REM images of granular analogue materials and photo from sandpaper, measured peak friction, stable static friction and stable dynamic friction. All measurements were repeated three-times. Respective angles of internal and basal friction as well as cohesion were derived from linear regression. Basal properties of the conveyor belt were measured with respect to the used sand. Note 10 cm mark on conveyor belt, which was used to determine the duration of 10 cm convergence.

Material	Type	Grainsize [ $\mu m$ ]	Density [ $g/cm^3$ ]	$\phi_{peak}^*$ [ $^\circ$ ]	$C_{peak}$ [ $Pa$ ]	$\phi_{static}^\dagger$ [ $^\circ$ ]	$C_{static}$ [ $Pa$ ]	$\phi_{dyn}^\S$ [ $^\circ$ ]	$C_{dyn}$ [ $Pa$ ]	Strain soft. $^\ddagger$ [%]
Sand	Internal	20 – 630	1.74 $\pm 0.01$	35.36 $\pm 0.34$	43.47 $\pm 44.34$	29.82 $\pm 0.19$	176.38 $\pm 24.80$	28.20 $\pm 0.05$	94.66 $\pm 6.53$	20.24
Glass beads	Internal	300 – 400	1.59 $\pm 0.01$	29.14 $\pm 0.14$	-6.13 $\pm 18.82$	25.91 $\pm 0.09$	78.89 $\pm 11.56$	22.51 $\pm 0.04$	42.71 $\pm 5.15$	13.63
Mortar	Internal	145 – 1250	1.82 $\pm 0.03$	34.09 $\pm 0.15$	118.89 $\pm 20.54$	35.18 $\pm 0.59$	164.71 $\pm 77.27$	31.38 $\pm 0.22$	53.77 $\pm 28.95$	7.95
Sand paper	Basal	< 400	–	32.02 $\pm 0.32$	-63.09 $\pm 42.49$	30.34 $\pm 0.07$	61.37 $\pm 8.73$	28.62 $\pm 0.15$	65.98 $\pm 19.77$	–

Data are derived from ring shear tests. Internal properties were measured with sieved materials, basal properties were determined relative to sieved sand. Interpolation of the Mohr envelopes was used to calculate cohesion. The sand - S30T in industry standards - was washed and dried at high temperature by the mining company before delivery to the laboratory.

\* Peak friction provides the strength of undeformed material.

† Static-stable friction provides the strength of previously deformed material.

§ Dynamic-stable friction provides the strength of active shear-zones (Byerlee, 1978).

‡ Strain softening is expressed as the percentage difference between peak friction and dynamic stable friction.

Table 4.1: Physical properties of analogue materials used in experiments

In the second measurement set, which followed the same procedure as the one described above, the basal properties of the sand with respect to the conveyor belt were determined. The latter is made of linen covered with an adhesive tape which in turn is sprinkled with sand (20–400 mm), providing a high friction interface (Table 4.1). Based on these results, a geometric scaling factor, following Ramberg (1981) was calculated:

$$S = \frac{C\rho_m a}{C_m \rho g} \quad (4.1)$$

where the index  $m$  denotes the analogue model,  $S$  is the scaling factor,  $C$  is the cohesion,  $\rho$  is the density,  $g$  is the acceleration due to gravity in nature ( $9.81 m/s^2$ ) and  $a$  the one in the model. If all experiment are carried out under normal gravity conditions, equation (4.1) reduces to:

$$S = \frac{C\rho_m}{C_m \rho}. \quad (4.2)$$

Given that the density of sedimentary or upper crustal rocks ranges between  $2000 - 3000 kg/m^3$  (Landolt-Börnstein, vol. I "Physical properties of rocks" available at [www.springerlink.com](http://www.springerlink.com)), analogue materials:  $1500 - 1800 kg/m^3$  and provided that the respective cohesion values are in the order

of  $0.7 - 105 MPa$  (Landolt-Börnstein), analogue materials:  $20 - 240 Pa$ . Consequently,  $S$  equates to a range ( $10^3 - 10^6$ ), whereas  $10^5$  is the commonly used value. Consequently,  $1 cm$  in the model corresponds to  $\sim 1 km$  in nature. This scaling approach has been successfully used by a multitude of authors, among them Malavieille (1984), McClay (1996), Storti et al. (2000), Kukowski et al. (2002) and Del Castello et al. (2004). It is finally concluded that the theoretical considerations made in section (3.3), the measured mechanic properties of the analogue materials as well as the scale invariance of brittle failure, justify the approach of 2D sandbox experiments.

## 4.2 Experimental setup

Bivergent sand-wedges have been successfully simulated with two setups:

*The mantle subduction model.* Within an Eulerian reference frame, i. e., the material moves relative to the coordinate system, this model assumes that the mechanical energy delivered into an orogen is derived from the basal pull or drag of the subducting plate (Silver and Reed, 1988), since the crust is strongly coupled to the mantle lithosphere (Ellis et al., 1995; Ellis, 1996). This model was first

used in sandbox simulations by Malavieille (1984) and later adopted by Storti et al. (2000). These authors used the same material on both sides of the singularity. Within this scenario (Fig. 4.5a), upper plate material acts as a dynamic backstop sensu Kopp and Kukowski (2003). A rigid backstop (Fig. 4.5b) was used by Wang and Davis (1996), Bonini et al. (1999) and Storti et al. (2001) and their setups thus mediate between the mantle subduction and the indenter model, given below.

The *indenter model* assumes a strength contrast between the involved lithospheric plates and a weak coupling between the crust and the lithospheric mantle (Ellis et al., 1995; Ellis, 1996). Thus, the mechanical energy delivered into an orogen is derived from the push from the rear, which was also assumed in the CCW concept (Fig. 4.5c). This approach (Lagrangian reference frame, i. e., the coordinate system moves with the material) was applied in sandbox simulations by Merle and Abidi (1995), Persson and Sokoutis (2002) and Persson et al. (2004).

Both types may provide end-member scenarios since Ellis (1996) pointed out that an orogen initially dominated by mantle subduction mechanics may, with continued convergence, evolve into an orogen dominated by indenter-style mechanics. If slab pull is considered as the most important force driving the plates (Conrad and Lithgow Bertelloni, 2004), the basal pull model was chosen. This bears also the advantage that the results drawn from this study can be easily compared with those from numerical simulations, which successfully simulated bivergent orogens with the basal pull approach (Batt and Braun, 1999; Willett, 1999; Beaumont et al., 2000; Pfiffner et al., 2000).

To study the most general case, collision of material with the same mechanical properties on both sides of the singularity was simulated (e. g., Storti et al., 2000). The respective upper plate material forms thus a dynamic backstop (Kopp and Kukowski, 2003). A strength contrast across the singularity was only simulated in one experiment.

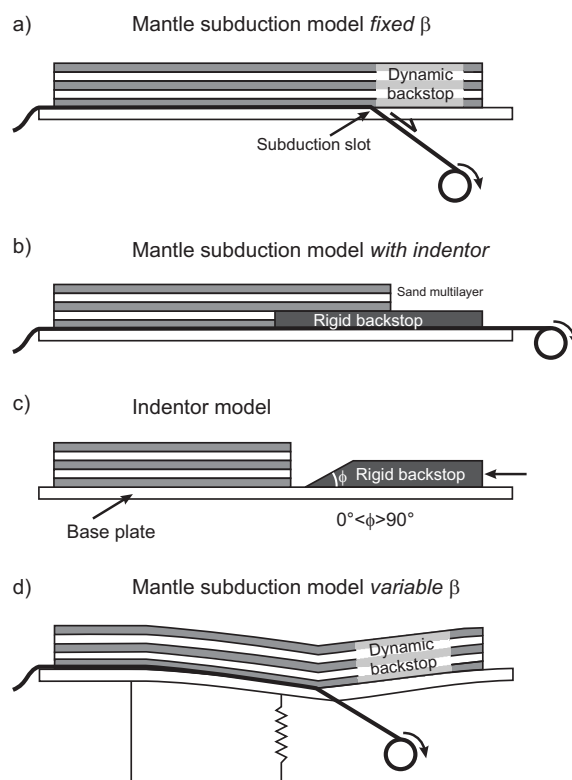


Figure 4.5: Summary of setups, which have been used to simulate bivergent sand-wedges. Two end-member models, i. e., the mantle subduction and the indenter type model have been put forward. (a) Mantle subduction model with a fixed  $\beta$ . (b) Mantle subduction model with an indenter. (c) Indenter model. (d) Mantle subduction model with a variable  $\beta$  as used in this study. See figure (4.6) for a technical sketch.

As indicated in chapter (1), the evolution of bivergent orogens is controlled by deformation, erosion/sedimentation, and flexure. To date, flexure has not been incorporated in sandbox-simulations, although it is commonly involved in numerical models (Willett, 1999; Pfiffner et al., 2000). Flexure is considered to be important, since the flexural rigidity of the involved plates controls the lateral and vertical distribution of tectonic loads (Allen and Allen, 2005), which in turn influences the spatial distribution of deformation (Boyer, 1995). Therefore, a new setup which allows for load-driven flexure was invented, i. e., the singularity migrates vertically and the dip angle  $\beta$  changes through time (Fig. 4.5d).

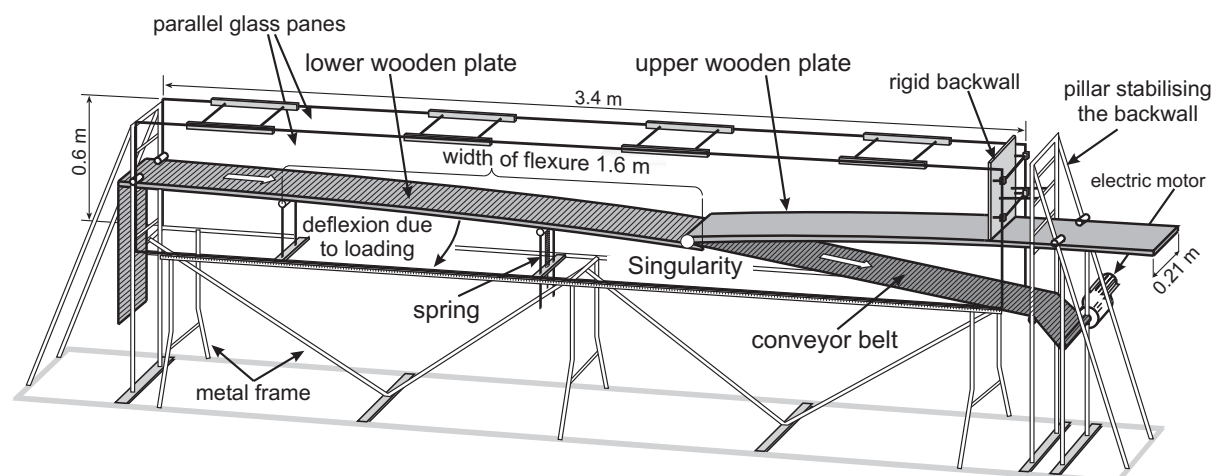


Figure 4.6: Technical sketch of sandbox, which allows for load-driven flexure.

The sandbox simulations were run in a glass-sided deformation apparatus with internal dimensions (length, width, height) of  $340 \times 21 \times 60$  cm (Fig. 4.6). It consists of an upper and a lower elastic wooden plate (referred to as upper and lower plate base), which overlap in the center. They are only fixed at their respective outward sides to allow for load-driven flexure. In order to minimise the influence of the boundary conditions imposed by the experimental device, the singularity is located sufficiently away from the rigid back-wall. The lower plate is supported by a spring to adjust its stiffness. Several test experiments were carried out to find an appropriate plate-spring combination, which ensures a constant increase of the dip angle  $\beta$  as well as a plausible magnitude for the latter. Thereby, four parameters were tested: (i) the distance between the free end and the point, where flexure is zero; (ii) the position of the spring with respect to the free end; (iii) the spring constant and (iv) the material of the plate bases. In order to find a plate-spring combination, which satisfies the above requirements, the free end of the lower plate was incrementally loaded with  $2\text{ kg}$  (maximum was  $20\text{ kg}$ ) and the vertical deflection was measured (Fig. 4.7). This was carried out for all parameter combinations listed in table (4.2). Finally, a plate-spring combination was chosen,

for which  $\beta$  changes from  $\sim 5^\circ$  to  $\sim 7^\circ$  during experiments. The scaling factor between experimental and natural flexure is unknown because Young's modulus of the setup could not be determined.

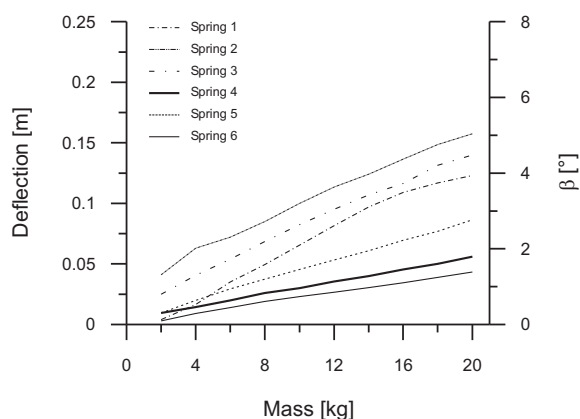


Figure 4.7: Load dependent deflection and basal dip  $\beta$  of lower plate. Length between the free and the point, where the deflection is zero, is  $1.6\text{ m}$ , length between the free end and the spring is  $0.3\text{ m}$ . Graph shows six springs, which differ with respect to their spring constants (see appendix). The above geometry together with spring 4 was chosen for experiment. During experiments load may reach up to  $80\text{ kg}$  and  $\beta$  changes correspondingly from about  $5^\circ$  to about  $7^\circ$ .

However, two disadvantages are associated with this new setup. First, the curvature of the plates hampers the preparation of the sand multilayer

Distance from free end and the point, where flexure is 0 [m]	Distance from spring to free end [m]				
	0.2	0.3	0.5	0.7	0.8
1.5	✓		✓	✓	
1.6		✓	✓		✓
1.9		✓	✓		✓

The thickness of the plywood was chosen to be 20.7 mm. A thicker or thinner plate would have provided either too little or too much deflection, respectively. The above parameter combinations were tested for six different springs. See appendix C for spring specifications.

Table 4.2: Parameters tested to find an appropriate plate-spring combination for the lower plate.

with a constant thickness, which is accounted for, by normalising all experimentally derived values with respect to the thickness of the incoming layer ( $H_0$ ). Second, the glass panels had to be tangent to the base plates. Otherwise, sand grains would have fallen inbetween and would have resulted in a blurred profile view. It follows, that with respect to the above test experiments, the downward movement is retarded, whereas the upward movement is significantly delayed. Both features are not critical as long as the kinematic interpretation is not tightly linked with the magnitude of flexure, which is not intended and a net mass-gain of the bivergent sand-wedges is observed. The latter condition is satisfied for all, but one experiment. Additionally, reproducibility was successfully tested.

Lower-plate subduction and basal shear is simulated by a conveyor belt, which only covers the lower plate and is drawn by a motor ( $\sim 9 \text{ cm/min}$ ) beneath the tip of the upper plate. In order to ensure a strong mechanical coupling between the conveyor belt and the sand layer, a sand paper with a grain size  $< 0.4 \text{ cm}$  was chosen. The resulting basal friction (Table 4.1) is in the same range as published values for similar experimental devices (Wang and Davis, 1996; Kukowski et al., 2002). A lower basal friction would have resulted in a bivergent sand-wedge, which is wider and shows a lower  $\alpha$ . In order to study the most general and simplest scenario, a 6 cm thick sand layer covers the upper and lower plate base equally. We therefore did not account for (i) the variety of materials with differing frictional properties found in continental collision zones; (ii) the progressive fore-

landward decrease of the thickness of the sedimentary succession and (iii) inherited zones of weakness commonly found in orogenic forelands. The influence of the latter two factors on model results would have been a change in the spacing of thrusts (Bombolakis, 1986; Boyer, 1995; Hardy et al., 1998; Macedo and Marshak, 1999).

Most orogens, e. g., Pyrenees and European Alps, show a variety of possible detachment horizons, which can lead to orogen-scale frontal and basal accretion (e. g., Beaumont et al., 2000; Pfiffner et al., 2000). Such weak layers are simulated with dry glass-beads, which are characterised by a Mohr-Coulomb type rheology, but show significantly lower frictional properties as sand (Fig. 4.8, Table 4.1). In addition, Kukowski et al. (2002) found that an internal weak layer serves only as a detachment if its internal friction is significantly lower than the friction of the basal detachment. This imposed another constraint to use a high basal friction interface.

In order to promote frontal accretion within the retro-wedge, a basal glass-bead layer was placed above the upper plate base. Such an approach is in accordance with numerical simulations of bivergent wedges (e. g., Pfiffner et al., 2000).

Convergence is  $\sim 150 \text{ cm}$ , i. e.,  $\sim 150 \text{ km}$  in nature and is therefore similar to medium-sized orogens like the European Alps or the Pyrenees. Thus, the applied kinematic boundary conditions resemble those in numerical and other physical simulations (Willett, 1999; Beaumont et al., 2000; Pfiffner et al., 2000; Storti et al., 2000;

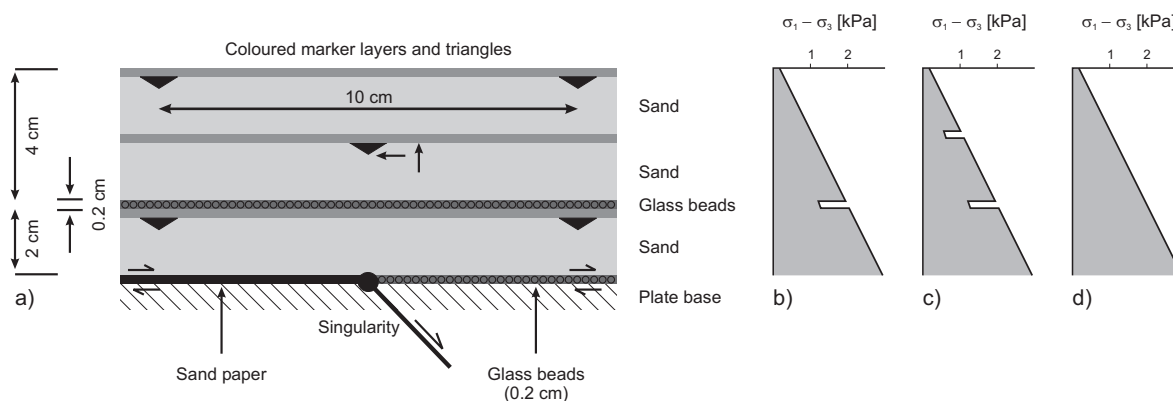


Figure 4.8: (a) Detailed mechanic stratigraphy with one internal glass-bead layer. The sand above is frontally, the sand below is basally accreted. (b) Calculated strength profile for mechanic stratigraphy in (a). (c) Calculated strength profile for a mechanic stratigraphy with two glass-bead layers. (d) Calculated strength profile for a mechanic stratigraphy with no glass-bead layer. (d) was used as the reference experiment for the 1<sup>st</sup>, (a) as the reference experiment for the 2<sup>nd</sup> experimental series. Strength profiles were calculated after Corti et al. (2003):  $\sigma_1 - \sigma_3 = [2(C + \mu \rho g z)] / [(\mu^2 - 1)^{1/2} - \mu]$ , where  $C$  is cohesion,  $\mu$  is the coefficient of internal friction,  $\rho$  is the density,  $g$  is the acceleration due to gravity, and  $z$  is the depth.

Del Castello et al., 2004) and mimic the geometry of numerous published sections through small orogens (Beaumont et al., 2000; Pfiffner et al., 2000; Schäfer et al., 2000; Kummerow et al., 2004).

In erosion experiments, the sand wedge was allowed to produce an initial topography during the first 40 cm of convergence before incremental erosion was simulated. The convergence prior to erosion ensured that the bivergent sand-wedge was fully established. In order to unequivocally detect the influence of the location and the mode of erosion on the kinematics of bivergent sand-wedges, five simplifying assumptions were made:

- i. Either the pro- or the retro-wedge is eroded.
- ii. To ensure comparison between experiments, erosion was simulated at a constant interval (10 cm of convergence). The reader is referred to section (6.3.2) for a detailed discussion on the continuous deformation versus discrete erosion challenge.
- iii. Both erosion modes were investigated separately despite the observation that most natural bivergent orogens undergo distributed and focused erosion at the same time.

- iv. During experiments all eroded material left the model system and sedimentation either in the foreland or in piggy-back basins was neglected. This procedure is justified by the following observations: Morris et al. (1998) showed that along-strike variations in sediment discharge, calculated from apatite fission track ages, may reach up to 500% between drainage basins in the Pyrenees. They further pointed out that temporal variations of sediment discharge from individual drainage basins are greater than 300%.

A similar observation was made by Kuhlmann (2000) for the European Alps. Based on mass budget calculations, he pointed out that since the Oligocene, the temporal variations of sediment supply are in the order of 550% for the Swiss and Western Alps and up to 1000% for the Eastern Alps. His data do also suggest that only ~50% of the debris derived from the European Alps were deposited in the peripheral foreland basins. The remaining ~50% were shed either into the Gulf of Lyon (Rhône fan), the Adriatic and Ionian basins or in the Pannonian basin. Results from balanced crustal-scale cross-

sections from the Eastern Pyrenees (Vergés et al., 1995) and the Swiss Alps (Adrian Pfiffner pers. com., (2003)) suggest that one half to two thirds of the eroded material was either shed into the Atlantic during middle Lutetian to late Oligocene times (Eastern Pyrenees) or into the Gulf of Lyon (Swiss Alps), which agrees thus well with Kuhle-mann (2000).

- v. The key assumption made for the experiments involving erosion is that erosion rate is positively correlated with elevation (chapter 2). Accordingly, distributed erosion is simulated as follows. Erosion increases linearly from the toe of either the pro- or the retro-wedge towards the top of the bivergent sand-wedge, where it reaches its maximum of  $1\text{ cm}$  per  $10\text{ cm}$  of convergence (Fig. 4.9). Erosion in the focused mode reaches its maximum of  $1\text{ cm}$  per  $10\text{ cm}$  of convergence at the middle of either the pro- or the retro-wedge slope and decreased toward zero at the respective tops and toes.

In order to compare the magnitude of erosion with natural examples we calculated the erosion efficiency parameter  $r = v_e/v_c$ , where  $v_e$  is the erosion rate, i. e.,  $1\text{ cm}$  of erosion per  $10\text{ cm}$  of convergence and  $v_c$  is the convergence velocity, i. e.,  $10\text{ cm}$  of material input per  $10\text{ cm}$  of convergence. It is highlighted here that the velocity with which the conveyor belt is drawn ( $\sim 9\text{ cm}/\text{min}$ ) is of no importance for the above calculation since deformation of a Mohr-Coulomb material like sand is not time-dependent. We further assume that the instantaneous removal of sand, as simulated, reflects a continuous removal of  $1\text{ cm}$  per  $10\text{ cm}$  of convergence. The resulting value  $r = 0.1$  is thus well in the range of natural values obtained from currently deforming orogenic wedges such as Taiwan:  $0.03 - 0.18$  (Dadson et al., 2003), New Zealand:  $0.5 - 1.3$  (Hovius et al., 1997; Koons et al., 2003), Southern Alaska:  $0.02 - 0.94$

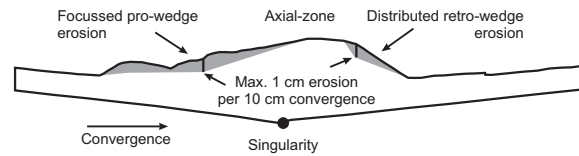


Figure 4.9: Distribution of incremental erosion, either distributed or focused.

(Meigs and Sauber, 2000), and the Himalayas:  $0.07 - 0.25$  (Bilham et al., 1997; Thiede et al., 2004). It is emphasised again, that it was not intended to accurately simulate the process of either distributed or focused erosion. Instead, the differing magnitudinal distributions across orogenic strike of both erosion modes, as they emerge from field studies (chapter 2), were used.

Finally, during all experiments either with or without erosion, the internal and basal mechanic properties were held constant. Examination of both cross sections during and after each experiment revealed that the plane strain assumption is valid. Reproducibility is justified by the repetition of experiments and the comparison of emerging trends and mutual relations of different data sets such as the propagation of deformation, particle paths and the amount of erosion, with the ones derived from similar experimental series.

### 4.3 Data acquisition and processing with Particle Image Velocimetry

Particle Image Velocimetry (PIV) is based on an adaptive cross correlation algorithm, which compares successive images and enables thus the calculation of the incremental displacement field within sand-wedges, the corresponding horizontal and vertical components as well as the incremental shear-strain (Adam et al., 2005).

The PIV system at the Geodynamic Laboratory of the GFZ Potsdam, Germany is made up of two high speed, digital cameras ( $2000 \times 2000$  pixels), which were used to monitor all experiments. The resolution of both cameras is sufficiently high to

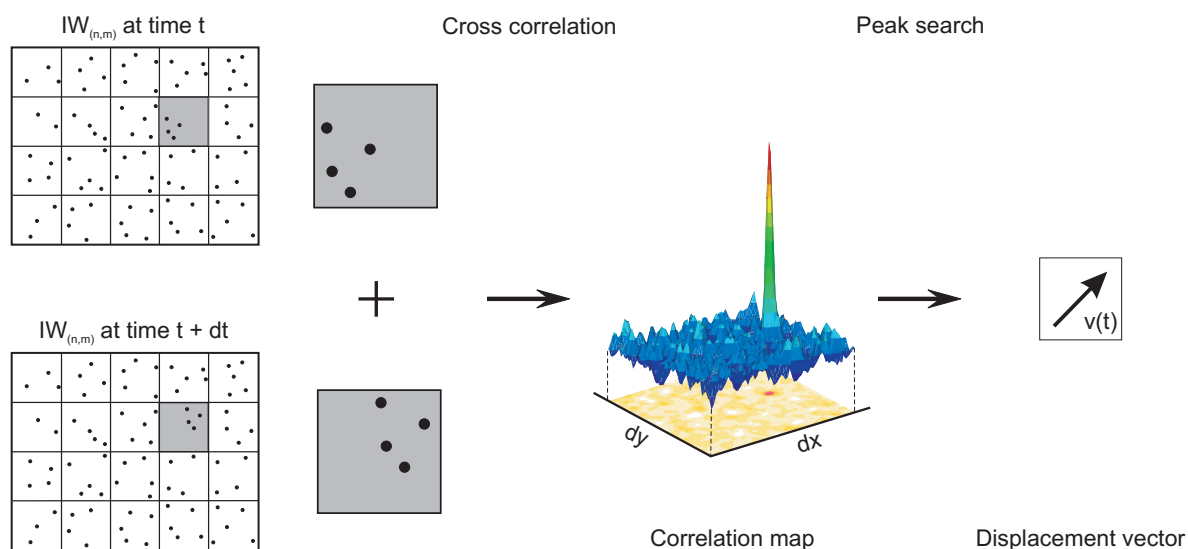


Figure 4.10: PIV workflow. Every image is divided into interrogation windows (IW), which are associated with an intensity value. During cross-correlation  $IW_{(n,m)}$  at time  $t + dt$  is shifted incrementally by  $dx$  and  $dy$  with respect to  $IW_{(n,m)}$  at time  $t$ . For each position a correlation coefficient between both intensities is calculated with Fast Fourier Transformation. Respective results are stored in a correlation map. The coordinates of the maximum correlation peak reveal the most likely position of the local displacement vector to match the pattern of  $IW_{(n,m)}$  at  $t + dt$  to  $IW_{(n,m)}$  at  $t$ . Modified after LaVision Göttingen.

image individual sand-grains. Images were taken every 2 s during experiments with erosion and with one exception at every 1 s for experiments without erosion. The higher temporal resolution of the latter was chosen to ease comparison with other standard experiments carried out within the laboratory. The software DaVis developed by LaVision GmbH, Göttingen, Germany was used to operate both digital cameras and to finally process and analyse the respective images. Acquisition and processing of the images involves four steps:

- i. Prior to image acquisition both cameras are calibrated and a mapping function is calculated to correct the images for distortions, resulting from the view angle of the cameras.
- ii. According to the mapping function the images are corrected during acquisition.
- iii. Both images are stitched together and the scale of the images [pixel] is converted to millimeter using again the mapping function.

- iv. Based on an adaptive cross correlation algorithm, successive images are compared and the incremental displacement field is calculated as explained below (Fig. 4.10).

Cross correlation of successive images (image 1 at time  $t$ , image 2 at time  $t + dt$ ) involves the division of each image into interrogation windows (IW 1, IW 2), which were assigned an intensity value. With respect to IW 1, the second interrogation window is now shifted incrementally by  $dx$  and  $dy$  in both  $x$  and  $y$  direction. For each position a correlation between both intensities is calculated with Fast Fourier Transformation and results are stored in a correlation map (Fig. 4.10). The coordinates of the maximum correlation peak reveal the most likely position of the local displacement vector of this sub-sample to match the pattern of IW 1 to IW 2 (Adam et al., 2005). It follows that the local displacement vector is a spatial average for the entire interrogation window. The corresponding spatial resolution can be improved by using adaptive multi-pass correlation



(Flow Master<sup>®</sup> Manual by LaVision; Adam et al. (2005) and references therein). This algorithm calculates a vector field based on a large interrogation window size. In the next step the size of the interrogation window is half the previous size and the first vector field is now used as a reference. Thus, the shift of the interrogation windows is adaptively improved and the calculated vectors become more reliable. Accuracy of the displacement measurement is  $\sim 0.5\text{ mm}$  and is thus equal to  $\sim 50m$  in nature (Adam et al., 2005).

The incremental vector field forms the basis for the calculation of its derivatives such as its horizontal and vertical components and the associated components of the strain tensor, e. g.,  $e_{xy}$ . Thereby,  $e_{xy}$  denotes the change of the  $x$ -component of the velocity vector in the  $y$ -direction and is thus referred to as horizontal shear strain. However, a complete description of the state of plane strain within the bivergent sand-wedges would require the calculation and analysis of horizontal and vertical shortening ( $e_{xx}$  and  $e_{yy}$ ). Given that the strain field in orogenic wedges results from the lateral shortening and vertical thickening (Ranalli, 1995),  $e_{xy}$  is thus considered as a good measure of bivergent wedge deformation.

#### 4.4 Data mining and its limitations

The digital images recorded by PIV provide an excellent possibility to extract time series data for several geometric features such as the propagation of deformation, the height above the singularity or the length of thrusts (Fig. 4.11). These geometric features are commonly thought to be indicative for the kinematic evolution of bivergent sand-wedges. They also allow a quantitative comparison between experiments and may finally provide a link to data from natural bivergent orogens.

All geometric data derived from PIV analysis were normalised with respect to  $H_0$ , the height of the undeformed multilayer, to account for slight variations in its thickness. These geometric data

were taken at every fifth image which corresponds to a convergence interval of  $1.5\text{ cm}$ . Since the geometric data were collected in the time domain [s], they had to be transferred to the convergence domain [cm] to ensure comparability between experiments. The respective conversion procedure bears some error as indicated below. During experiments marks drawn at every  $10\text{ cm}$  on the conveyor belt passed an external reference frame, while the corresponding PIV image number, which provides the time in [s] was taken. Although the motor runs at a constant velocity ( $9\text{ cm/min}$ ), the velocity of the conveyor belt increases with time, as the radius of the engine shaft plus the winded conveyor belt increases. However, significant deviations from this linear trend occurred (Fig. 4.12). As a first-order approach the linear increase was used to convert time to convergence and the associated error is  $\sim 5\%$ . The accuracy of measured lengths within PIV images is in the order of four to six pixels, which are  $\sim 2 - 3\text{ mm}$ .

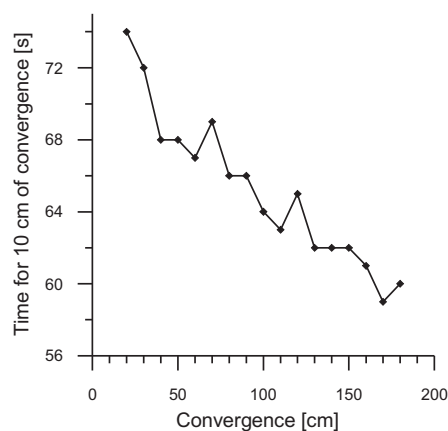


Figure 4.12: Change of the duration of  $10\text{ cm}$  of convergence during the reference experiment. Deviations from linear decrease (see text) may either result from human error or from wedge kinematics, but no relation could be established.

In order to elucidate the spatio-temporal evolution of deformation within, and of the associated surface uplift of a bivergent wedge, three new display-types were invented. To ensure successful communication the reader is provided with a how to read guide:

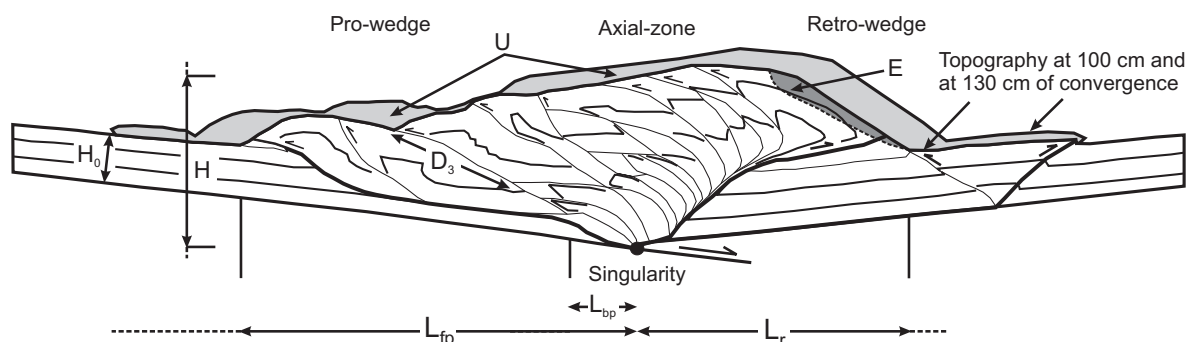


Figure 4.11: Measured parameters, which describe bivergent wedge evolution. (i) Propagation of the deformation front of frontal accretion in the pro-wedge [ $L_{fp}$ ], (ii) Propagation of the deformation front of basal accretion in the pro-wedge [ $L_{bp}$ ], (iii) Topographic height above the singularity [ $H$ ], (iv) propagation of the deformation front of the retro-wedge [ $L_r$ ], (v) Length of individual thrusts [ $D_{1...8}$ ], (vi) Erosion [ $E$ ] and (vii) Incremental surface uplift [ $U$ ]. Index  $p$  relates to the pro-wedge, index  $r$  to the retro-wedge, index  $f$  to frontal accretion and index  $b$  to basal accretion.  $H_0$  is the height of the undeformed multilayer. All geometric features are normalised with respect to  $H_0$  to account for slight variations in the thickness of the multilayer.

*Topographic envelopes.* Every pixel in a PIV image is assigned with an intensity value (counts). Pixels of the background or the setup are set to 0, pixels of the sand-wedge are set to 1 count. This leads to a black (background and setup) and white (sand-wedge) image, which forms the basis for all later calculations (Fig. 4.13a, b). At this stage two sources of error may occur. First, the PIV cameras have a perspective view on the sand wedge, i. e., they image the third dimension, which can result in an overestimation of the wedge area. Second, the definition of background and sand wedge is ambiguous with respect to the number of counts, since a certain cut off had to be chosen. This may also lead to an over- or an underestimation of the wedge area. The respective black and white image is exported as a bitmap (another source of error) and is finally automatically digitised. Especially the latter procedure can lead to an over- or an underestimation of the wedge area. Thus, some care should be taken while analysing the topographic envelopes (Fig. 4.13c). Nevertheless, they show first and second order features, thought to be valid [see section 5.1] but may have some inconsistencies, especially with respect to the thickness of the incoming layer. Topographic envelopes were generated at every 10 cm of convergence.

*Incremental Surface Uplift (ISU) maps.* To calculate ISU, an increment is 10 cm of convergence, the area of a sand wedge at time  $t$  is subtracted from the area of a sand wedge at time  $t + 10$  cm of convergence. This results in secondary black and white image, which shows the spatial distribution of ISU (Fig. 4.13d). Its magnitude is measured at the scale of a pixel and an uplift curve is generated. Finally, all uplift curves are grided and displayed as a map, which indicates the spatial and temporal distribution of ISU in an Eulerian reference frame (Fig. 4.13e, f). The sources of error associated with ISU maps are similar to the ones determined during the derivation of the topographic envelopes. But again, ISU maps are thought to indicate first and second order phenomena. Therefore, subtle variations of ISU were not interpreted. Nevertheless, ISU maps provide a wealth of information and can be read at least in two ways. Timelines (horizontal) indicate the spatial distribution of ISU for a certain stage during wedge evolution. Location lines (vertical) provide the change of ISU through time at a given position. The spatial resolution of ISU maps depends on the mapping function, but is generally around 0.5 mm. The temporal resolution is 10 cm of convergence. Narrower intervals have not provided more information.

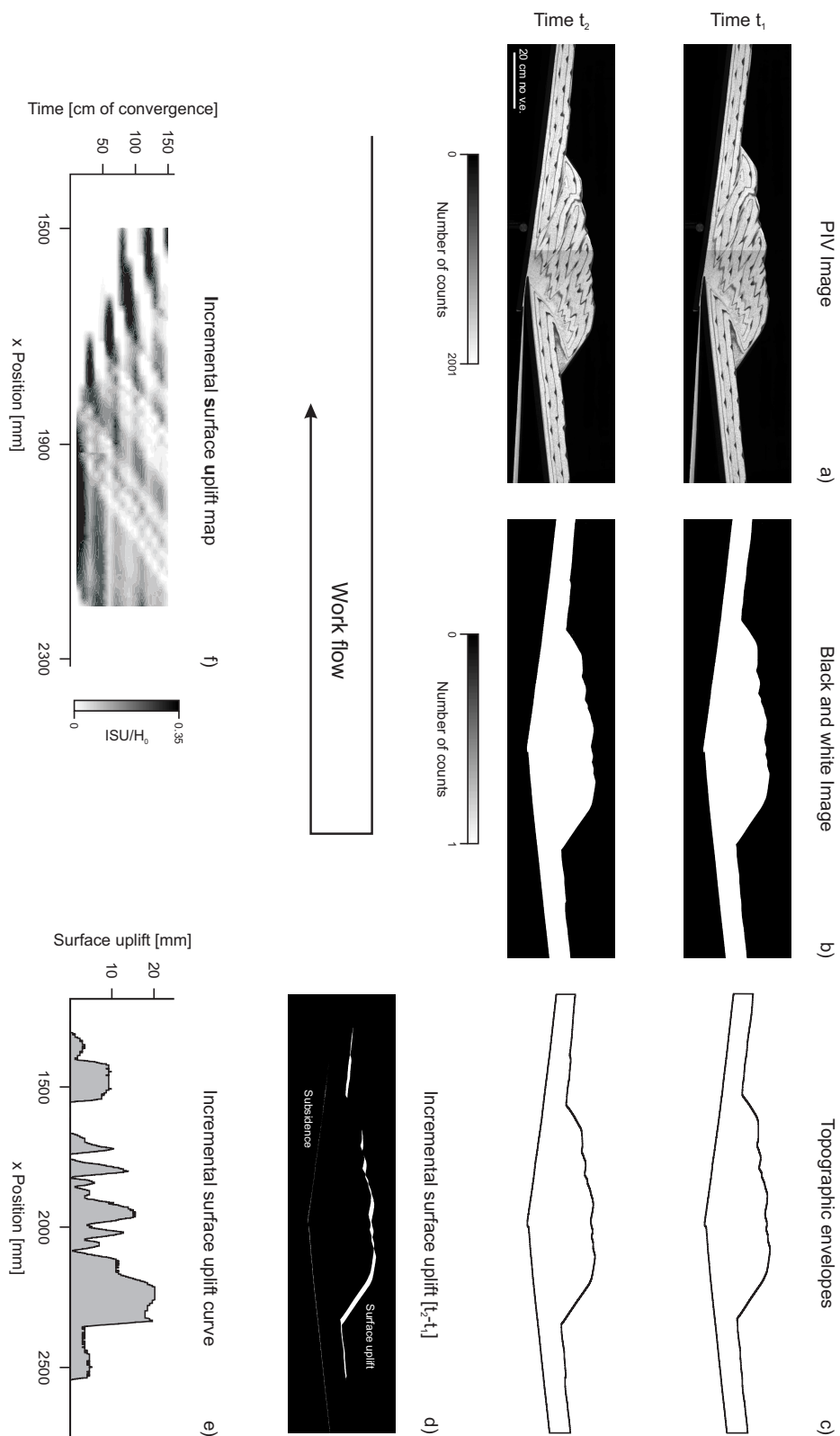


Figure 4.13: Generation of topographic envelopes and of ISU maps. (a) Original PIV images. (b) Converted PIV images. (c) Topographic envelopes of divergent sand-wedge at  $t_1$  and  $t_2$  derived from automatic digitisation of (b). (d) Subtraction of converted PIV images (b) results in incremental surface uplift. Increments correspond to 10 cm of convergence. (e) Incremental surface uplift is measured and displayed as a curve. (f) Map display of all incremental surface uplift curves.

*Evolution of Deformation Maps (EDM).* The incorporation of PIV into sandbox simulations resulted in an overwhelming wealth of data with respect to the spatio-temporal distribution of incremental strain. Therefore, the need emerged to display these data in a way that facilitates the detection of trends or patterns. In a first step the scalar of  $e_{xy}$  was extracted. In a second step,  $e_{xy}$  is measured along a profile parallel to the base plates (Fig. 4.14a). A likewise processing of all images results in  $e_{xy}$  profiles, which are finally displayed (Fig. 4.14b). The EDM provides thus the spatio-temporal distribution of  $e_{xy}$  in an Eulerian reference frame and allows the analysis of strain transfer patterns. Since material moves through the profile line and the angle between the latter and the ramp segments is not constant due to continued accretion and flexure, several EDM were calculated for different positions of the profile line. The resulting  $e_{xy}$  pattern was similar, although the magnitudes differed. Note that the position of the profile line determines the visibility of the back-thrusts associated with the major thrust imbricates.

*Strain histories for individual thrusts.* First, the finite Lagrangian  $e_{xy}$  after 140 cm of convergence is calculated (Fig. 4.4a). Then, all particles and their associated finite  $e_{xy}$  magnitude are restored back to their original position prior to convergence (Fig. 4.4b). Similar to the procedure described above the scalar of  $e_{xy}$  is extracted from every image and  $e_{xy}$  is measured along a profile line, parallel to the base plates. The resulting map indicates thus the accumulation of finite strain through time for every position along the profile line (Fig. 4.4c). Now, the finite  $e_{xy}$  history is derived for a point, located within a ramp segment through a vertical profile (Fig. 4.4d). If this is done for all ramp segments, strain transfer patterns can be identified. They compare well with the ones recognised in the EDM. In the final stage incremental  $e_{xy}$  histories for a certain point located within a ramp segment are derived from the finite ones (Fig. 4.4d, e).

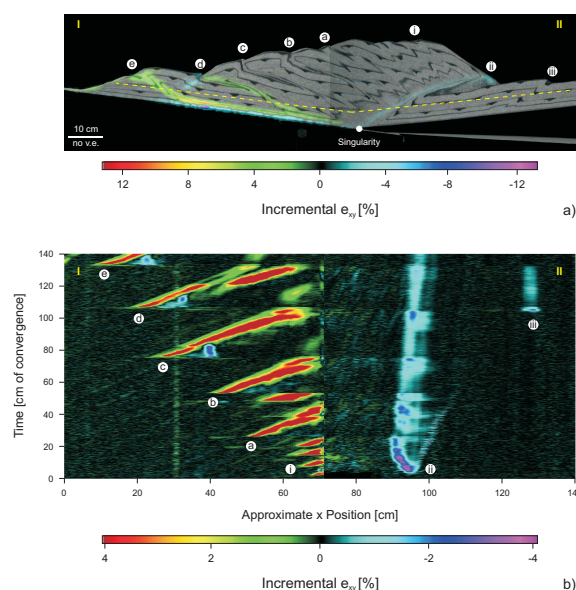


Figure 4.14: Derivation of EDM. Incremental  $e_{xy}$  is extracted along profile I - II (a) for every image and is finally displayed as a map (b). Labels (a) to (c) refer to forethrusts within the pro-wedge. (i) denotes the pro-shear of the initial pop-up, (ii) the respective retro-shear and (iii) the accretion within the retro-wedge. Only the approximate x position is given, since the raw data are enlarged during extraction from PIV.

Finally, four conventions are made. The term *pro-shear* is used for all shear zones, which dip towards the upper plate, whereas shear zones with *retro-shear* dip towards the lower plate. In  $e_{xy}$  images, the former is coloured in green to red, the latter in blue to purple. The term *retro shear-zone* is taken only for the shear zone bounding the retro-side of the initial pop up (section 3.1). The term *incremental* refers to a convergence interval of 10 cm, if used to describe the topographic evolution of the bivergent wedges. If however *incremental* is used in conjunction with strain information, than this term describes the time between two successive PIV images.

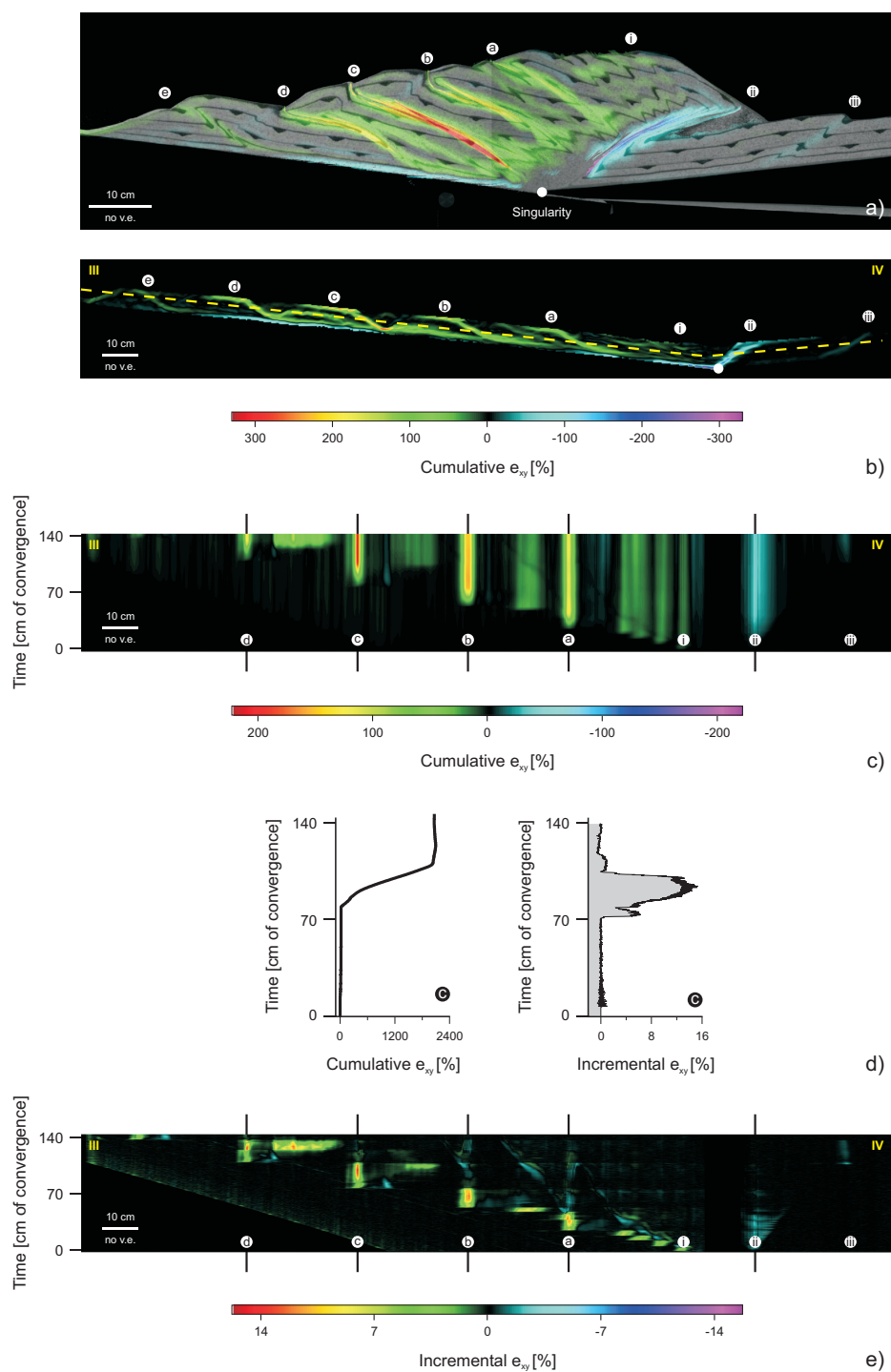


Figure 4.15: Derivation of  $e_{xy}$  profiles for ramp segments of the forethrusts and the retro-shear zone. (a) Finite  $e_{xy}$ , i. e., after 140 cm of convergence. Annotations are the same as in figure (4.14). (b) Restoration of original particle position. (c) Cumulative  $e_{xy}$  values are extracted from profile III – IV in (b) for every image and are displayed as a map. (d) Extraction of cumulative  $e_{xy}$  values from a vertical profile. (e) Shows the incremental  $e_{xy}$  accumulation for each location along profile III – IV in (b). Vertical profile in (e) provides  $e_{xy}$  history of points within ramp segments of the forethrusts and is shown in (d).

## 5 Kinematic boundary conditions and their influence on bivergent wedge evolution

The following chapter intends to elucidate the influence of imposed kinematic boundary conditions such as a strength contrast across the singularity, different mechanic stratigraphies, and the degree of flexure on the kinematic evolution of bivergent sand-wedges. Special emphasis shall be laid upon the strain transfer between the pro- and the retro-wedge as well as the timing and magnitude of strain accumulation within the pro-wedge. An account on the kinematic evolution of the reference experiment is provided first, followed by a description of four other experiments which differ with respect to their kinematic boundary conditions (Fig. 5.1).

### 5.1 Reference experiment

*Kinematic evolution of a bivergent sand-wedge.* Based on visual inspection of the reference experiment, the kinematic evolution of a bivergent sand-wedge is divided into four stages. In stage I, initial layer parallel shortening leads to the formation of two conjugate shear zones, which nucleate at the singularity and define thus a symmetric pop-up (Fig. 5.2a). Further convergence leads to rapid surface uplift associated with progressive back tilting of this pop-up towards the upper plate. During stage II, three narrowly spaced thrust faults form successively within the pro-layer (Fig. 5.2b, c). They nucleate as well at the velocity discontinuity and are carried passively back- and upwards in the hangingwall of the retro shear-zone throughout the remaining experiment. Stage II marks thus

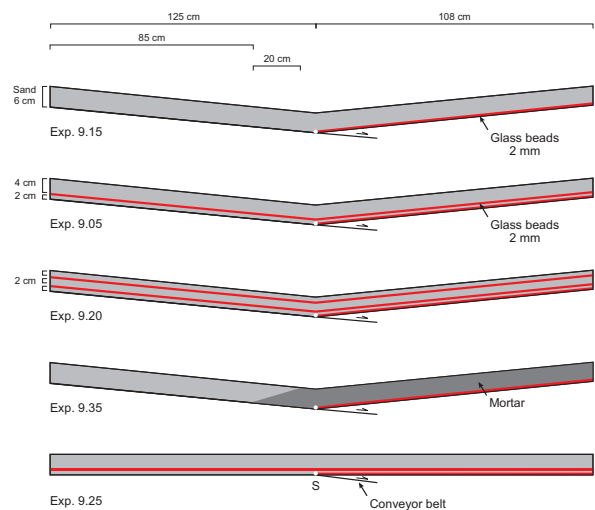


Figure 5.1: Kinematic boundary conditions of 1<sup>st</sup> experimental series. Sand and glass-beads for all experiments were taken from one charge. Basal friction was the same in all experiments. Flexure was not simulated in experiment 9.25. Experiment number is used in text.

the transition from a symmetric to an asymmetric topographic and kinematic state. At this stage surface uplift rates of the axial-zone and the retro-wedge are still high but start to decrease (Fig. 5.3), while rates of thrusting along the retro shear-zone remain constant. With continued convergence, the topographic load of the axial-zone and the retro-wedge increases until a critical height is reached. At this point, i. e., after  $\sim 30\text{ cm}$  of convergence (Fig. 5.2d, e), the axial-zone and the retro-wedge provide a sufficient load to initiate a basal detachment, which ramps up through the pro-layer to finally form a flat-topped box anticline – stage III commences. Lateral growth of the pro-wedge is now attained by a forward-breaking sequence of flat-topped box anticlines, which is hereafter referred to as frontal accretion. The respective basal detachment is located within the lowermost part of the pro-layer and thus a few millimeters above the conveyor belt. During stage III, rates of thrusting along the retro shear-zone remain fairly constant (Fig. 5.3). However, rates of the lateral growth of the pro-wedge, as well as surface uplift rates of both the axial-zone and the retro-wedge do fur-

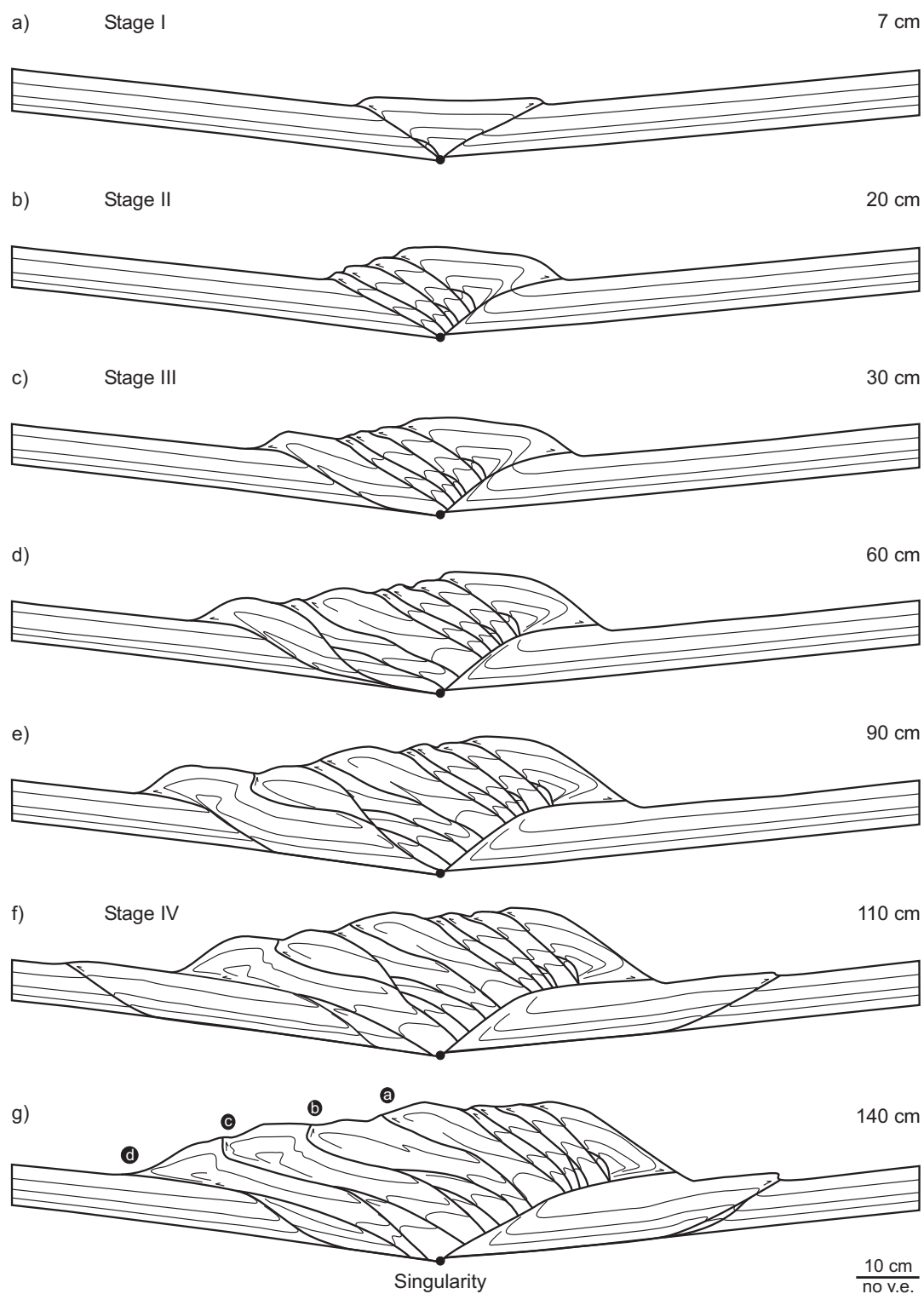


Figure 5.2: Line drawings of sequential stages of the reference experiment (9.15). Numbers on the right are *cm* of convergence. Frontal accretion within the retro-wedge occurs after  $\sim 100$  *cm* of convergence (stage IV). Label ① to ④ denote thrusts.

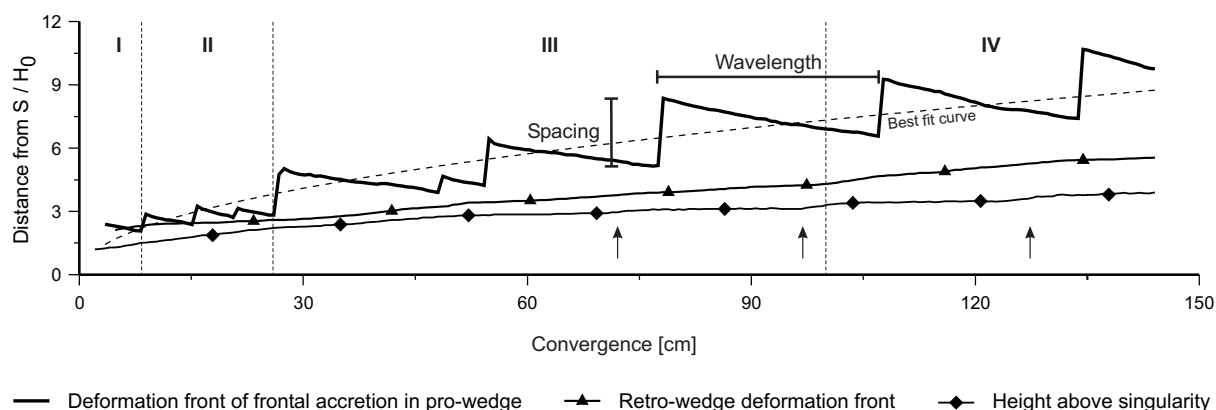


Figure 5.3: Evolution of geometric parameters as defined in figure (4.11), taken from the PIV images at every  $1.5\text{ cm}$  of convergence. Arrows point to times of accelerated vertical growth, which predate the formation of a new thrust within the pro-layer. Dashed line is the best fit curve for the propagation of deformation of frontal accretion within the pro-wedge:  $y = 0.79t^{0.48}$  with  $R^2 = 0.88$ ;  $y$  is the normalised distance between the deformation front of frontal accretion within the pro-wedge and the singularity and  $t$  is convergence [ $\text{cm}$ ]. Roman letters and vertical dotted lines indicate duration of the four stages of bivergent wedge evolution. Graphic definition of spacing as the horizontal distance between the previous and the newly formed deformation front; and wavelength as the time in  $\text{cm}$  convergence between two successive thrust initiations.

ther decrease. Additionally, the latter is disturbed by discrete, short-lived accelerations, which predate the formation of a new thrust within the pro-layer. After  $\sim 100\text{ cm}$  of convergence, frontal accretion within the retro-wedge commences and marks thus the onset of stage IV. Continued convergence is now taken up by two frontal accretion systems (Fig. 5.2f, g), indicating that the wedge starts to regain its initial symmetric conditions. This results in a further slowdown of the lateral growth rate of the pro-wedge (Fig. 5.3). It follows from the above description that the propagation of deformation within the pro-wedge, i. e., its lateral growth, is attained by the cyclic formation of flat-topped box anticlines at its toe. The resulting overall trend is best described by a power law (Fig. 5.3). Accordingly, the pro-wedge grows proportional to the convergence ( $t$ ) by  $t^{0.48}$  ( $R^2 = 0.88$ ), which is close to the theoretically predicted value of  $t^{0.5}$  (Dahlen, 1990).

*Topographic evolution.* Given an Eulerian reference frame, two domains of the spatio-temporal distribution of incremental surface uplift are distinguished within the bivergent sand-wedge. One

comprises the pro-wedge and one includes the axial-zone and the retro-wedge. ISU in the former is highly variable and shows discrete accelerations, while the latter is characterised by an almost concentric growth (Fig. 5.4, Fig. 5.5). As noted in section (4.4), several ways to read ISU maps exist:

Time- and location-lines indicate the high spatial or temporal variability of ISU for a given time interval or position in a Eulerian reference frame. The initiation of individual flat-topped box anticlines is associated with a maximum ISU right above the respective ramp segment. Thus, propagation of these ISU maxima through time and space reflects the propagation of deformation within the pro-wedge. While convergence proceeds, new thrust faults are formed and older ones are abandoned. This is coeval with a decay of ISU for a given ramp segment. However, almost all ramp segments identified in figure (5.5) show a renewed increase in ISU, which suggests their re-activation. The respective increase can gain an order of magnitude without any modifications of the imposed kinematic boundary conditions (Fig. 5.5). Therefore, lines which follow individual ramp segments are referred to as thrust



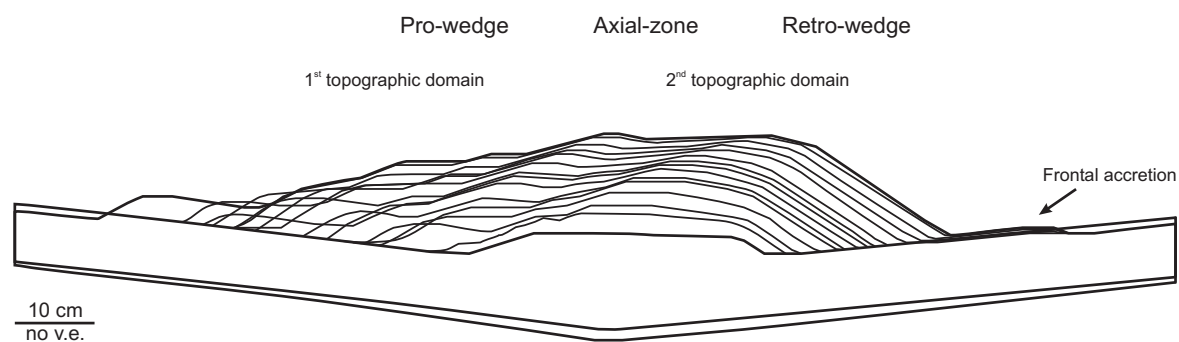


Figure 5.4: Topographic evolution of reference experiment. Outlines were taken at every 10 cm of convergence. The first, i. e., after 10 cm and the last, i. e., after 150 cm of convergence are given in complete form, to indicate the magnitude of flexure. Two topographic domains mirroring two different growth modes can be distinguished. Cyclic accretion within the pro-wedge results in distinct steps in topography, whereas continuous addition of pro-wedge derived material to the axial-zone and the retro-wedge leads to a nearly concentric growth.

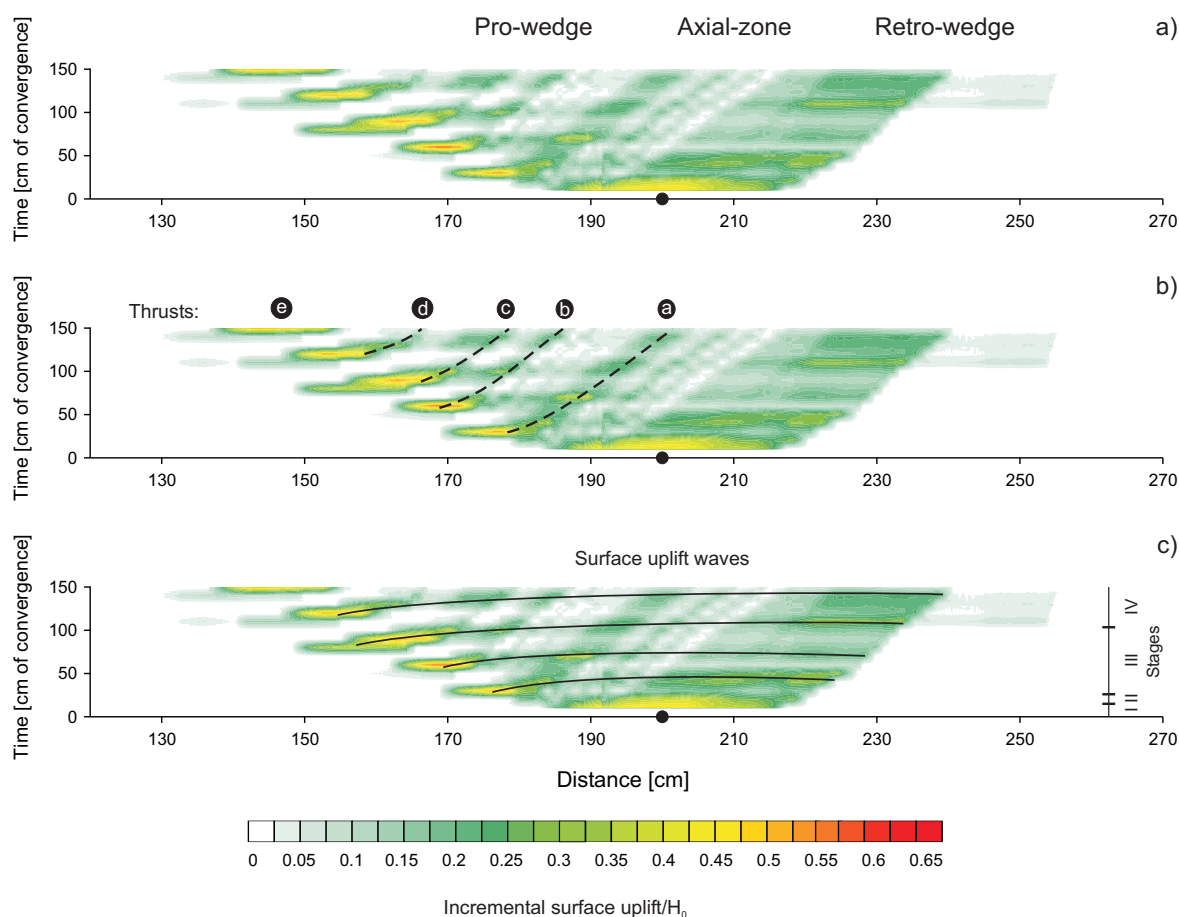


Figure 5.5: Incremental surface uplift of reference experiment. (a) Raw data, see figure (4.13) for derivation. (b) Dashed lines follow surface uplift traces of ramp segments of forethrusts. Re-activation of thrusts can result in an increase of ISU by one order of magnitude. For location of thrusts ① to ⑤ see figure (5.2g). (c) Bold lines follow surface uplift waves, which are tightly linked with the accretion cycle.

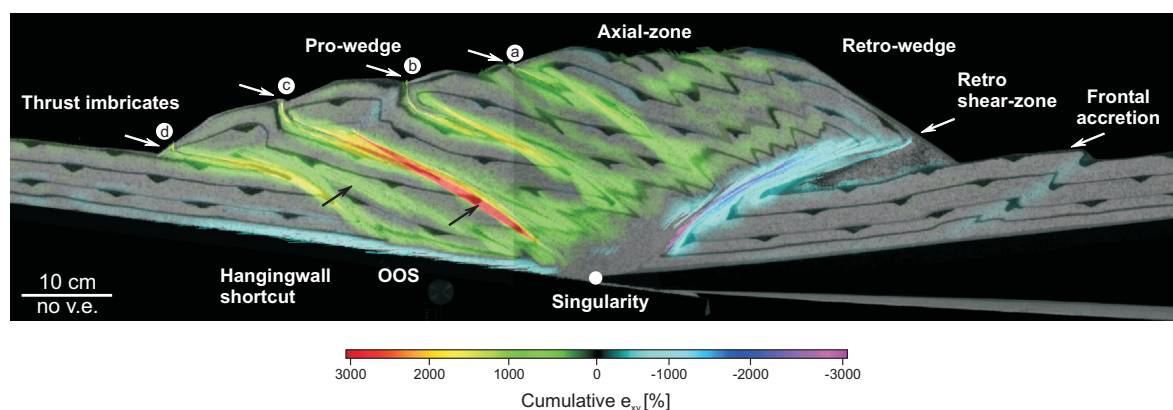


Figure 5.6: Distribution of finite  $e_{xy}$  for the reference experiment after 140 cm of convergence.

traces. It is furthermore pointed out, that at times of maximum ISU within the pro-wedge the respective magnitudes of ISU within the axial-zone and the retro-wedge are at their minimum. This observation led to the discovery of very subtle surface uplift waves, which are intimately linked to the accretion cycle. Thereby, the initiation of each thrust within the pro-layer is associated with maximum ISU. With ongoing convergence, this maximum migrates as a wave, with decreasing magnitude through the entire wedge until it has reached the tip of the retro-wedge deformation front. At this stage a new thrust in the pro-layer is formed, which again is followed by a similar surface uplift wave. This observation agrees well with the finding that the height above the singularity shows discrete accelerations just before a new thrust within the pro-layer is formed (Fig. 5.3).

Finally, ISU mirrors the four stages of bivergent-wedge evolution, as outlined above. In stage I ISU is symmetrically distributed above the singularity, while during stage II the location of maximum ISU shifts towards the lower plate and results thus in a topographic asymmetry. The former is further magnified during stage III, especially, if the ISU maxima associated with the initiation of the thrusts, are considered. Frontal accretion within the retro-wedge (stage IV) marks the transition to a more symmetric wedge-topography.

*Strain accumulation.* Based on the displacement field derived from PIV analysis, finite strain after 140 cm of convergence was calculated, to obtain a wedge-scaled view on strain accumulation (Fig. 5.6). The distribution of finite strain clearly images the main structural elements such as the basal detachment, the retro shear-zone and individual thrust imbricates. Within the pro-wedge a systematic distribution of finite strain was recognised: thrusts located at either the toe or the rear of the pro-wedge show only minor magnitudes of finite strain. In turn, thrusts positioned close to the prominent topographic break within the pro-wedge show significantly higher finite strain magnitudes. It is also pointed out that the magnitude of retro shear is highest at the retro shear-zone which separates lower plate from upper plate material and is thus interpreted as long-lived.

A more detailed insight to strain accumulation at the thrust-scale is derived from the EDM. Based on the EDM, the main structural elements such as the initial pop-up, the retro shear-zone, individual thrust imbricates within the pro- and the retro-wedge as well as subtle features like back-thrusts, footwall shortcuts and out-of-sequence reactivation of thrusts can be identified (Fig. 5.7).

The proposed four stages in bivergent-wedge evolution can be deduced from figure (5.7) as well. The transition from stage I to stage II can be iden-

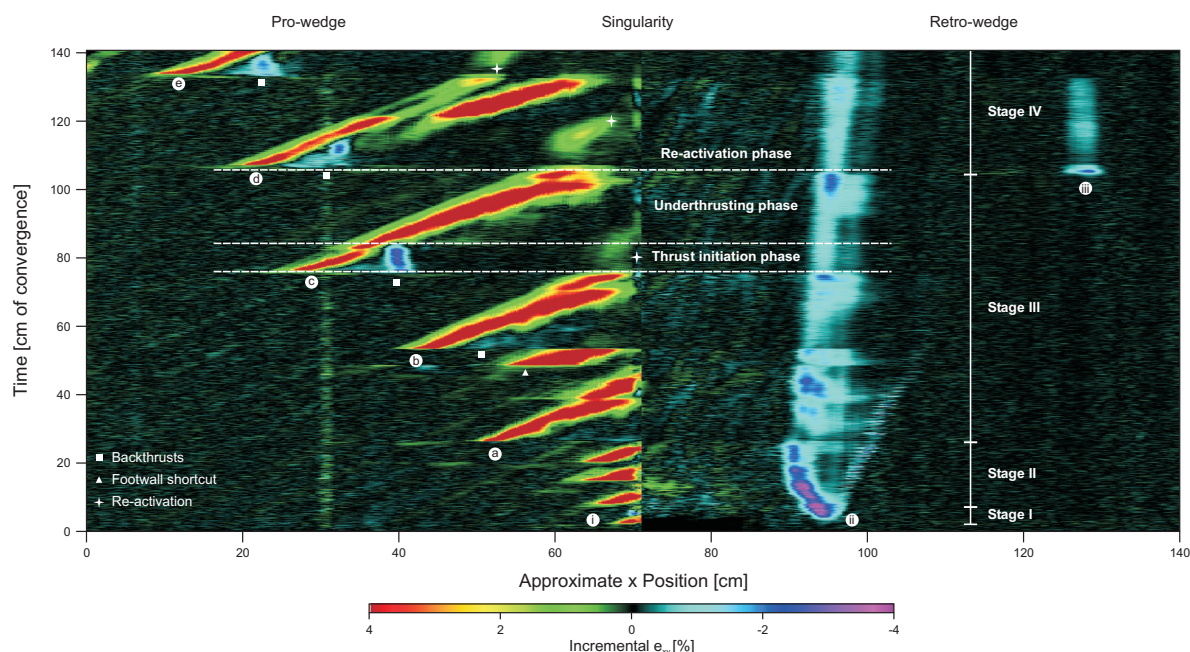


Figure 5.7: Evolution of deformation for the reference experiment. Labels (a) to (e) refer to forethrusts within the pro-wedge. See figure (5.2g) for location and figure (4.14) for derivation. (i) denotes the pro-shear of the initial pop-up, (ii) the respective retro-shear and (iii) denotes the frontal accretion within the retro-wedge. Four stages of bivergent wedge evolution as well as phases of accretion cycle are explained graphically. Note, pulsating but decreasing activity of retro-shear zone.

tified, since the life-span of the three narrowly spaced thrusts is significantly longer, than the life-span of the fore-thrust bounding the initial pop-up. The transition from stage II to stage III is more pronounced, since the flat-topped box anticlines have a significantly longer life-span than the three fore-thrusts. Incremental  $e_{xy}$  along the retro shear-zone decreases markedly as well, but shows pulses, which predate the formation of a new thrust within the pro-layer. These strain pulses agree well with the ISU waves described above. The onset of stage IV is marked by the emergence of frontal accretion within the retro-wedge. Coevally, re-activated thrusts accumulate more, the retro shear-zone less incremental  $e_{xy}$ , whereby the latter still shows incremental  $e_{xy}$  pulses.

*The accretion cycle.* Further analysis of the EDM revealed a regular, incremental  $e_{xy}$  pattern, which is referred to as the accretion cycle. Al-

though  $e_{xy}$  was calculated from the velocity field,  $e_{xy}$  is considered to be better suited for the description of an accretion cycle than the horizontal ( $v_x$ ) or the vertical ( $v_y$ ) component of the velocity field. However, key observations concerning either  $v_x$  or  $v_y$  are indicated where appropriate. Each accretion cycle is thought to consist of three phases: a thrust initiation phase, which in turn is divided into three sub-phases; an underthrusting phase; and a re-activation phase, where the latter is coeval with the thrust initiation phase of the following accretion cycle. The nomenclature of the first two phases follows Gutscher et al. (1998) and Hoffmann-Rothe et al. (2004), whereas the term re-activation phase is introduced here.

During the first sub-phase of the thrust initiation phase, deformation propagates outward along the basal detachment and finally steps up to form a symmetric pop-up. The respective backthrust terminates right at the tip of the previous deforma-

tion front (Fig. 5.8b). Although, not very well localised, this pop-up evokes a significant decrease of  $v_x$  within the pro-layer (Fig. 5.8h). Interestingly, this pop-up has no topographic expression, but it clearly stands out in the diagram showing the vertical component of the velocity field (Fig. 5.8n).

During the second sub-phase of the thrust initiation phase, the basal detachment and the forethrust of the pop-up form a continuous shear-zone with a flat-ramp geometry. Coevally, the backthrust associated with the pop-up and the previous deformation front cease in activity (Fig. 5.8c).

In the third sub-phase of the thrust initiation phase, the initial pop-up evolves into a flat-topped box anticline, which is associated with the formation of a backthrust. Convergence is now taken up by the newly formed forethrust, its backthrust, the previous forethrust, and the retro shear-zone (Fig. 5.8d). With respect to the first sub-phase, no significant change of the components of the velocity field occurred during the latter two sub-phases.

In the following underthrusting phase, the backthrust and the previous deformation front are abandoned and the pro-layer is considerably overthrust by the pro-wedge. Convergence is now taken up by two conjugate shear-zones, which define a wedge-scaled, symmetric pop-up (Fig. 5.8e). Thereby, the frontally accreted material is continuously transferred towards the axial-zone, rotated back and finally passively uplifted in the hangingwall of the retro shear-zone. Consequently,  $v_x$  is at its maximum within the axial-zone and decreases towards the pro- and the retro-wedge (Fig. 5.8m, q). It follows that the location of maximum  $v_y$  has moved from the flat-topped box anticline at the toe of the pro-wedge towards the axial-zone. This observation agrees well with the ISU wave documented earlier. However, the location of maximum  $v_y$  during subsequent underthrusting phases is systematically shifted from the axial-zone during early accretion cycles towards the center of the pro-wedge during later accretion cycles (Fig. 5.8m, q).

The underthrusting phase is terminated by the thrust initiation phase of the next accretion cycle. Note again, that prior to the formation of a new thrust imbricate within the pro-layer, strain accumulation increases significantly along the retro shear-zone (5.7). During the second sub-phase of the thrust initiation phase, incremental  $e_{xy}$  ceases to accumulate along the previous deformation front, but is re-activated during the respective third sub-phase (Fig. 5.8f). The previous deformation front remains active until the next underthrusting phase commences. Note, that during the underthrusting phase, the difference between both velocity components, i. e.,  $v_x - v_y$  remains nearly constant, but is highly variable during the thrust initiation and the re-activation phase (Fig. 5.9, Fig. 5.8a).

The evolution of incremental  $e_{xy}$  at points located within individual ramp segments of either the fore-thrusts or the retro shear-zone shows one absolute and two local maxima which can be linked with the three phases of the accretion cycle identified above (Fig. 5.10). Within this respect, the two local maxima correspond to the thrust initiation phase and the re-activation phase respectively, whereby the former attains higher magnitudes than the latter. The absolute maximum is linked with the underthrusting phase. These observations suggest that each phase within an accretion cycle is associated with different magnitudes and rates of strain accumulation. In addition, the strain history of the retro shear-zone follows a pattern, which can be best described by a damped oscillation. Thereby, local  $e_{xy}$  maxima predate the formation of a new thrust imbricate within the pro-layer, which is concordant with the information deduced from the EDM. It follows that the communication or the ability to transfer strain between fore-thrusts within the pro-wedge and the retro shear-zone decreases with increasing distance between them. It is finally emphasised that the EDM and the strain histories of ramp segments provide complementary information and have to be viewed as such.

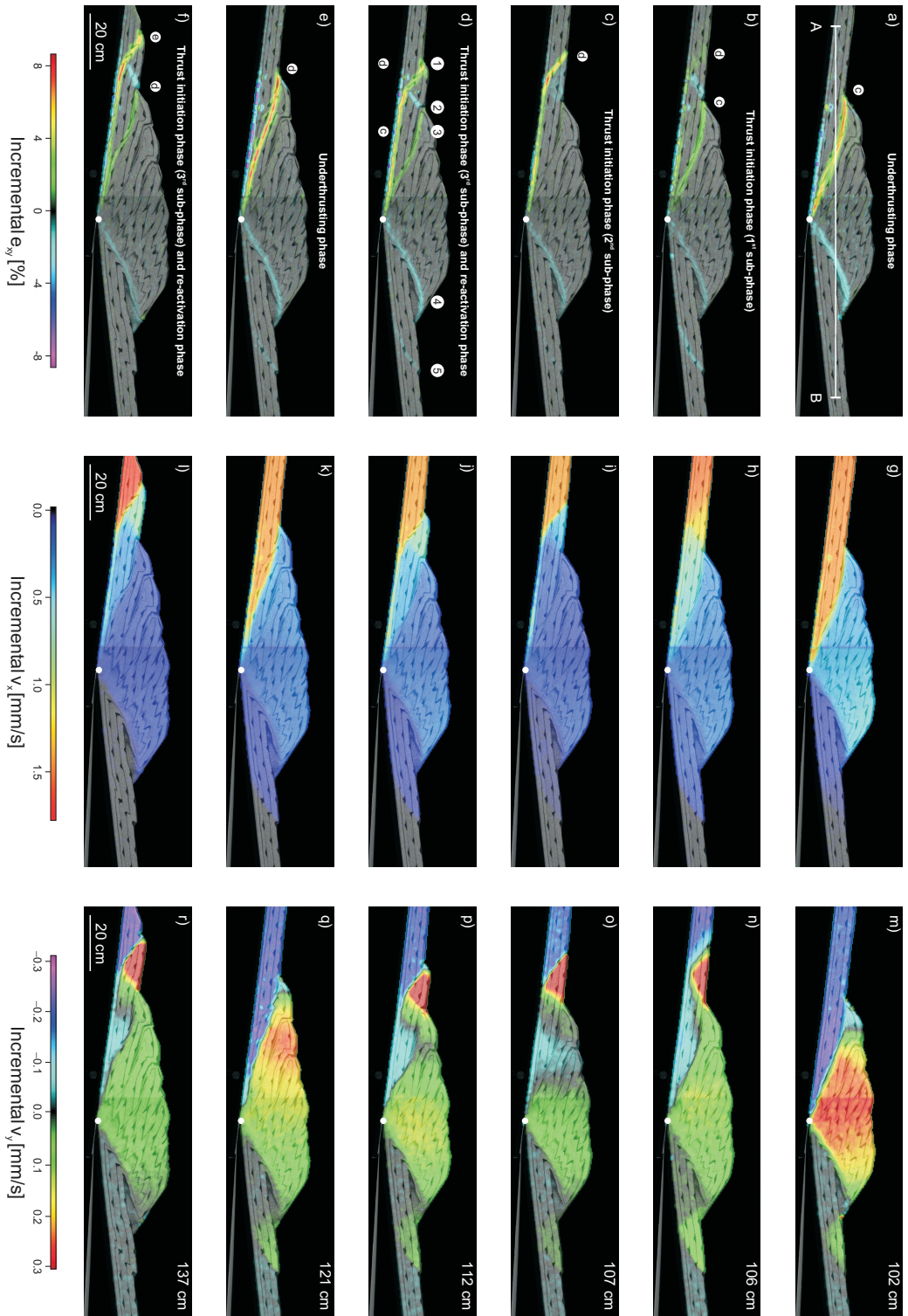


Figure 5.8: Sequential development of an accretion cycle. Columns from left to right show incremental  $e_{xy}$  and the respective horizontal and vertical component of the velocity field. Numbers on the right indicate *cm* of convergence. Interpretation of the  $e_{xy}$  pattern in terms of the accretion cycle is given. Evolution of profile AB in (a) is shown in figure (5.9). Labels ① to ⑤ in (d) refer to different thrusts and are explained in figure (5.9). Labels ① to ⑤ denote successive thrust imbricates.

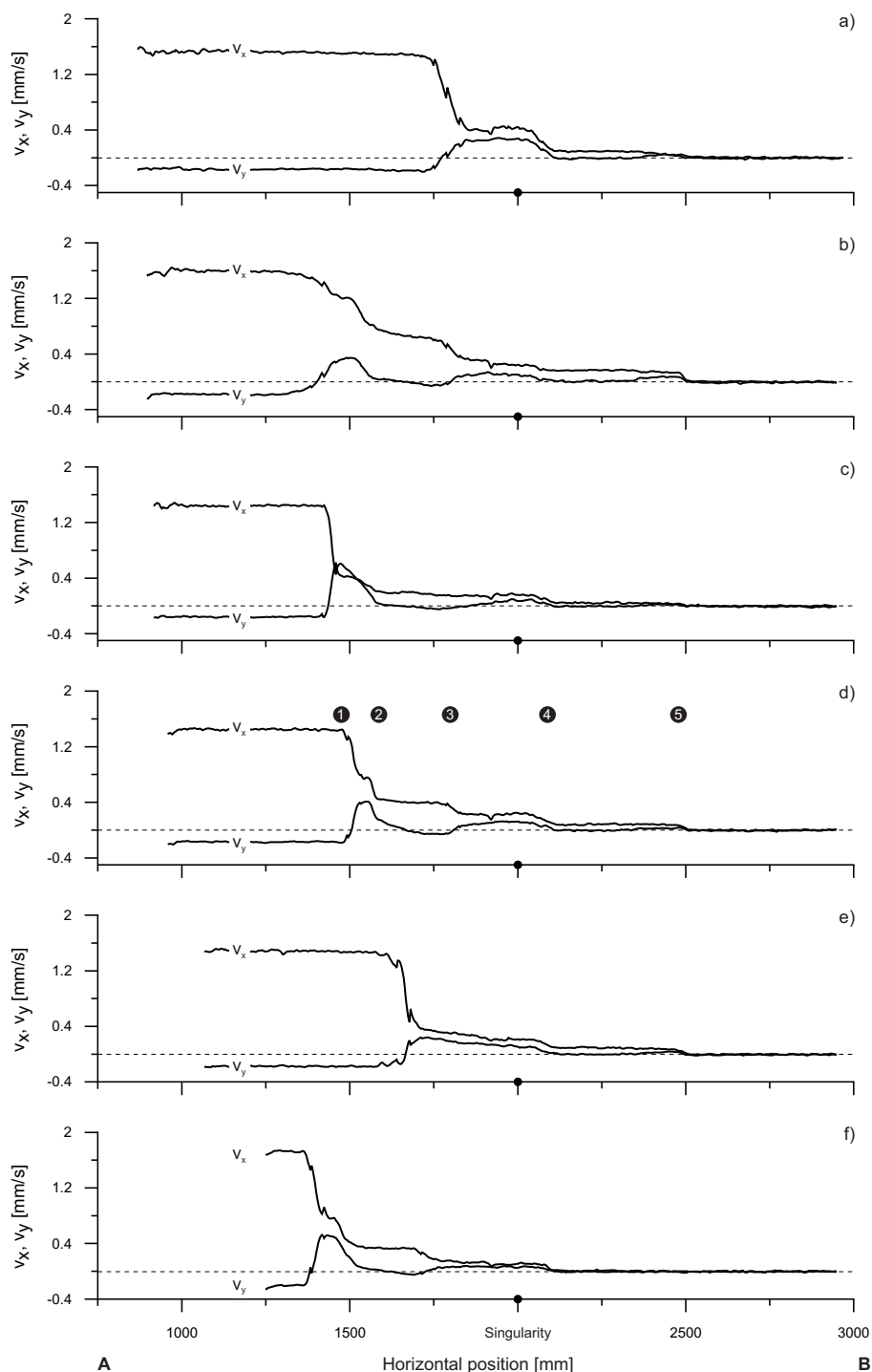


Figure 5.9: Evolution of the vertical and the horizontal component of the velocity field during an accretion cycle as derived from figure (5.8a). The initial plateau of  $v_x$  at  $1.5\text{ mm/s}$  is due to the velocity of the undeformed incoming layer, the negative values of  $v_y$  ( $-0.3\text{ mm/s}$ ) derives from the experimental setup, i. e., the sand-layer moves first downwards, as a response to the flexural deflection and is then tectonically uplifted. Note changes of either  $v_x$  or  $v_y$  across thrusts. Labels: ① Forethrust within the pro-wedge, ② The respective backthrust, ③ Internal thrust, ④ Retro-shear zone and ⑤ Forethrust within the retro-wedge.

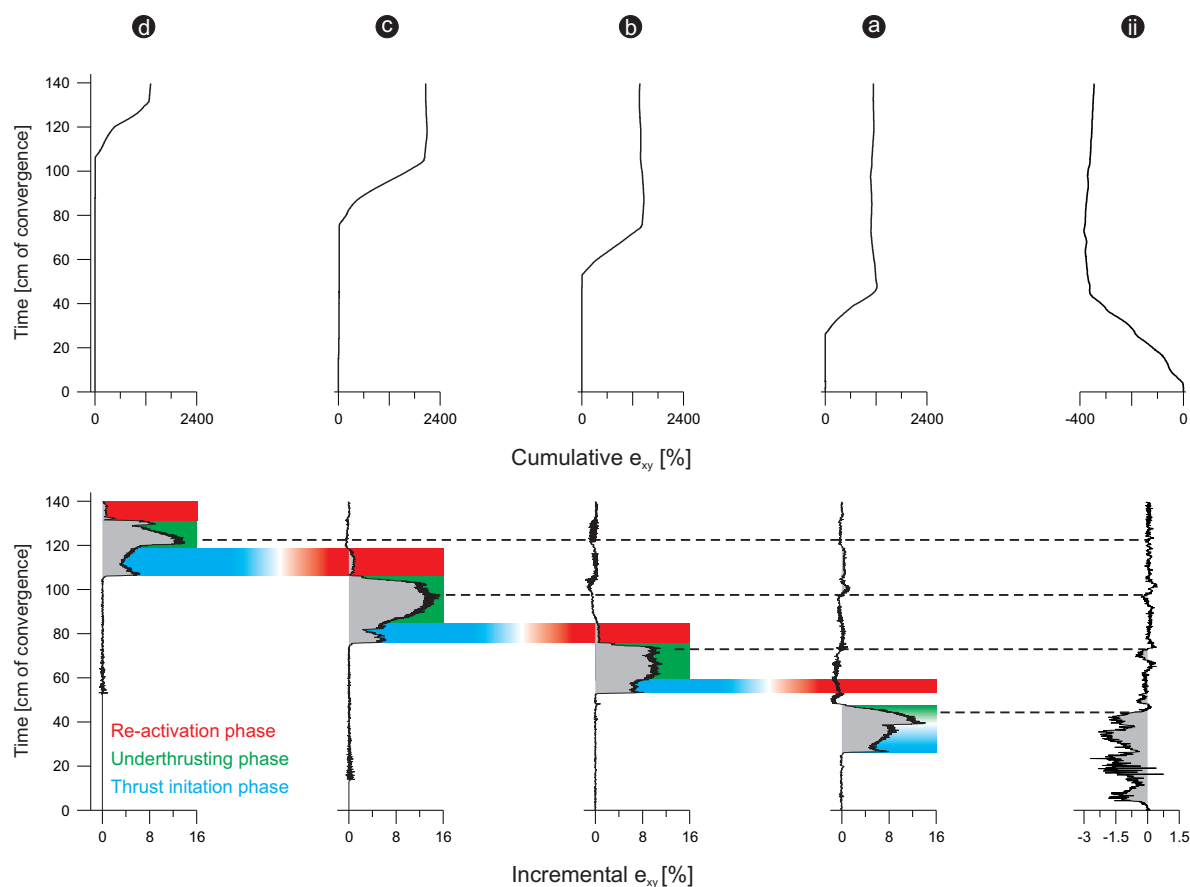


Figure 5.10:  $e_{xy}$  accumulation of forethrusts (a) to (d) and the retro-shear zone (ii). The phases of the accretion cycle are marked in coloured to visualise strain transfer. Note that the “communication” of the pro-wedge with the retro-shear zone follows a damped oscillation. Information in this figure is complementary to figure (5.7).

## 5.2 Experiments with other kinematic boundary conditions

A key observation is that neither changes of the mechanic stratigraphy nor the absence of flexure did inhibit the segmentation of the sand-wedges into a pro-wedge, an axial-zone and a retro-wedge (Fig. 5.11). With one exception all four bivergent sand-wedges showed the first three stages out of the four staged evolutionary pathway found for the reference experiment. Experiment 9.35, where the upper plate was made up of mortar, lacks stage II. The kinematic similarity between these four experiments is also evident from the time series data (Fig. 5.12). However, differences with respect to

the accumulation and propagation of strain as well as the topographic evolution of the bivergent sand-wedges do exist and are outlined below.

*Frontal accretion.* Similar to the reference experiment, time series data from all four experiments show that the propagation of frontal accretion is composed of individual accretion cycles and to a lesser degree of footwall shortcuts (Fig. 5.12). The resulting overall trend of the lateral growth of the pro-wedge, is again best described by a power law. However, significant differences between the respective power law coefficients are observed (Table 5.1). The closest approximation between the experimentally derived

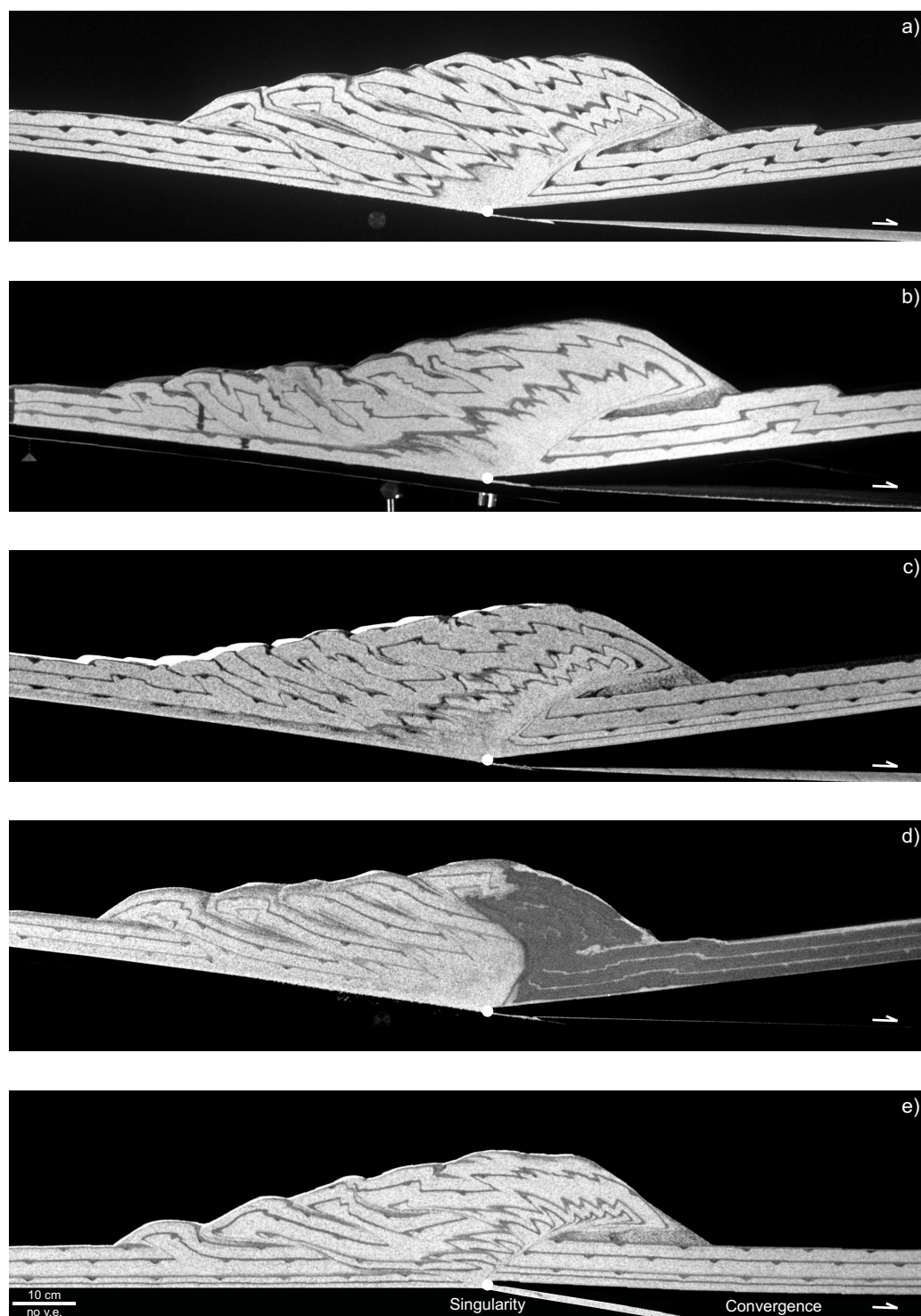


Figure 5.11: Photographic images of final stages of experiments: (a) Reference experiment 9.15; (b) Experiment 9.05; (c) Experiment 9.20; (d) Experiment 9.35; (e) Experiment 9.25; after 140 *cm* of convergence, except experiment (e), where convergence was 120 *cm*.



power law coefficients and the theoretically predicted value of 0.5 (Dahlen, 1990) is found in experiments, where two conditions are met. First, the respective mechanic stratigraphy is symmetric with regard to a horizontal symmetry plane. Second, no changes of the mechanic stratigraphy across the singularity do occur (vertical symmetry plane). Both conditions are satisfied in experiment 9.15 and 9.20. In the remaining experiments (9.05, 9.25, 9.35), where only one boundary condition is given, significant deviations of the respective power law coefficients from the theoretically predicted value are observed (Table 5.1). However, the largest difference between the theoretical value and the experimentally derived one was found for experiment 9.35, where the upper plate was made up of mortar. This might indicate that a strength contrast across the singularity has a stronger influence on the propagation of deformation within the pro-wedge, than changes of the mechanic stratigraphy with respect to the number and vertical distribution of weak layers. An experiment, in which both boundary conditions are not provided, has not been carried out but would be due to be done.

The depth to the detachment determines the number of thrust imbricates (Table 5.1). Experiments without an internal detachment, i. e., the depth to detachment is 6 cm show five imbricates (9.15, 9.35) whereas experiments with an internal detachment, i. e., the depth to detachment is 4 cm result in eight imbricates (9.05, 9.20). In experiment 9.25 a cyclic change of the position of the detachment was observed. The detachment was first initiated as a basal detachment, i. e., above the conveyor belt and jumped during the following accretion cycle to the internal weak-layer.

The spacing of frontal accretion, which describes how far deformation propagates into the foreland (Fig. 5.12), remains fairly constant throughout the experiments. If however, the depth to the detachment decreases as in experiment 9.20 and 9.25, the respective spacing decreases accordingly (Fig. 5.12). Interestingly, experiments where

the basal detachment of frontal accretion is located above the conveyor belt show a higher variability in spacing, than those where the respective detachment is located in the glass-bead layer (Table 5.1).

Contrary, the wavelength, which is the time expressed in convergence between two consecutive thrust initiation events, varies within and between experiments and is thus more sensitive to the parameters tested. As a measure of this variability, the sample standard deviation of the wavelength of frontal accretion ( $s_{fw}$ ) was calculated for all experiments. It is highest for experiment 9.25, which agrees with the observation of a changing depth to the detachment.  $s_{fw}$  is significantly lower for the remaining three experiments and shows a positive correlation with the number of weak layers (Table 5.1). Experiment 9.35 deviates from this trend and illustrates thus the influence of a strength contrast across the singularity on the propagation of deformation within the pro-wedge.

*Basal accretion.* During experiments, with either one or two internal glass-bead layers, decoupling of the upper from the lower sand-unit initiated after  $\sim 40$  cm of convergence. Coeval to frontal accretion above the glass bead-layer the sand layer beneath it was detached from the one above and transferred towards the axial-zone. Here beneath the base of the pro-wedge duplexes were formed, continuously stacked, and finally uplifted in the hangingwall of the retro shear-zone. The initiation, formation, stacking and translation of these duplexes is referred to as basal accretion. In contrast to the very regular propagation of frontal accretion, basal accretion is more irregular in terms of its wavelength and its spacing (Fig. 5.12). The respective variability expressed in the sample standard deviation of the wavelength ( $s_{bw}$ ) was as well calculated for all experiments. It emerges that  $s_{bw}$  is generally higher than  $s_{fw}$ . Also, the range of the latter (0.37) is nearly a third of the former (0.97) and suggests that basal accretion, as opposed to frontal accretion, is more sensi-

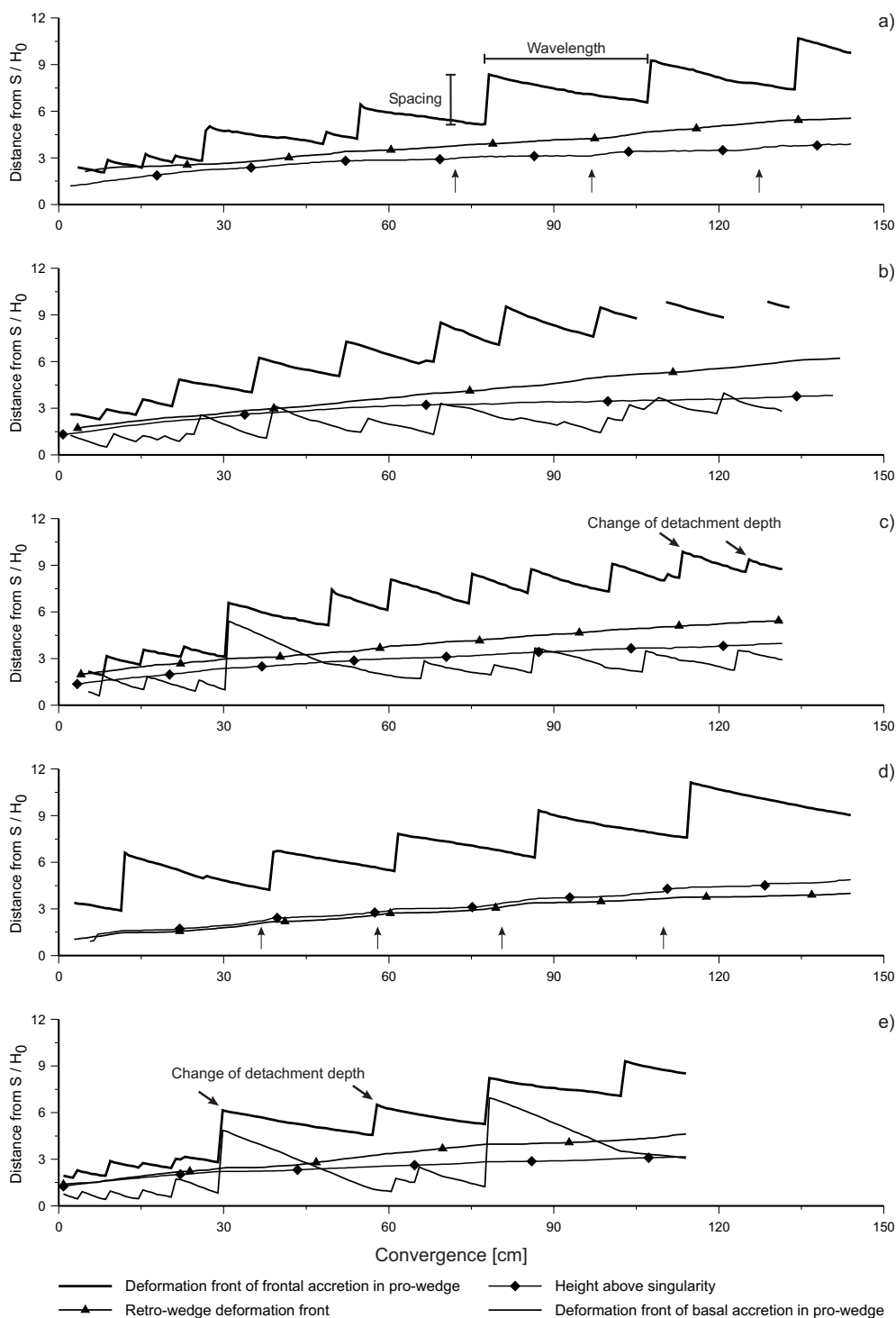


Figure 5.12: Evolution of geometric parameters taken from the digital images at every 1.5 cm of convergence. (a) Reference experiment 9.15; (b) Experiment 9.05; (c) Experiment 9.20; (d) Experiment 9.35; (e) Experiment 9.25. Arrows in (a) point to times of accelerated vertical growth, which predate the formation of a new thrust imbricate within the pro-layer. Arrows in (c) and (e) indicate changes of the depth to the detachment. Note the associated change of the thrust spacing.

Experiment Observations	9.15	9.35	9.05	9.20	9.25 *
Flexure	✓	✓	✓	✓	∅
Number of weak layers	0	0	1	2	1
Frontal accretion in retro-wedge	✓	✓	✓	∅	∅
Number of thrusts in pro-wedge after 140 cm of convergence	5	5	8	8	4
Sample standard deviation of wavelength of frontal accretion <sup>†</sup> $s_{fw}$	0.13	0.19	0.15	0.30	0.50
Sample standard deviation of spacing of frontal accretion <sup>†</sup> $s_{fs}$	0.15	0.15	0.07	0.09	§
Sample standard deviation of wavelength of basal accretion $s_{bw}$			0.47	0.90	1.44
Power law equation of lateral growth of pro-wedge $y_L =$	$0.79t^{0.48}$	$1.80t^{0.32}$	$1.06t^{0.44}$	$0.80t^{0.50}$	$0.97t^{0.43}$
Coefficient of determination $R_L^2 =$	0.88	0.76	0.89	0.90	0.82
Power law equation of height above singularity $y_H =$	$0.85t^{0.29}$	$0.48t^{0.42}$	$1.03t^{0.26}$	$0.76t^{0.33}$	$1.00t^{0.23}$
Coefficient of determination $R_H^2 =$	0.97	0.96	0.97	0.99	0.97
Out-of-sequence displacement (OOSD) index	0.62	3.95	3.73	8.1	0.46
Length ratio of pro-/ retro-wedge	2.82	2.47	3.03	2.75	1.82

\* Only 120 cm of convergence.  
† Without footwall shortcuts.  
§ Not determined because of cyclic change of detachment depth.

Table 5.1: Summary of experimentally derived results – 1<sup>st</sup> experimental series.

tive to the parameters tested (Table 5.1). Convergence intervals, where both accretion modes are either in or out of phase, are too short to be correlated over longer distances. It is finally pointed out that the height above the singularity provides a geometric envelope for basal accretion (Fig. 5.12).

*Topographic evolution.* Similar to the reference experiment, the topography of all four experiments consists of two domains: the first that comprises the pro-wedge and shows discrete steps and the second that encompasses the axial-zone and the retro-wedge with a concentric growth pattern (Fig. 5.13). Despite this first order similarity, the shape and evolution of both domains differ between experiments. For three experiments (9.05, 9.25, 9.35) examination of the topographic envelopes revealed a distinct topographic low within the respective pro-wedges. Accordingly, experiments which lack this topographic depression have a smoother topographic envelope. This is in agreement with a previous observation that the power law exponents of the lateral growth of the latter experiments are closer to the theoretically predicted value, than it is the case for the other three experiments (Table 5.1).

A closer analysis of the concentric growth pattern found within the second topographic domain shows that during experiments with basal accretion, this growth is nearly equidistant (Fig. 5.13). In experiments without basal accretion, the concentric growth pattern can be divided into periods of accelerated and slowed growth, whereas the latter are linked with the initiation of individual frontal accretion cycles (Fig. 5.13a, d). The relation between basal accretion and equidistant concentric growth of the second topographic domain can be tested with experiment 9.25. If the detachment is located above the conveyor belt, topographic outlines start to merge. A more equidistant growth pattern can be recognised during phases, where the detachment is located within the internal weak layer (Fig. 5.13e).

Incremental surface uplift of the four experiments shows a high spatio-temporal variability, similar to the reference experiment. Nevertheless, the key features identified previously can be clearly recognised: (i) two uplift domains; (ii) thrust traces, i. e., different phases of thrust activity associated with the accretion cycle; (iii) the temporal coincidence between maximum ISU within the pro-wedge and significantly

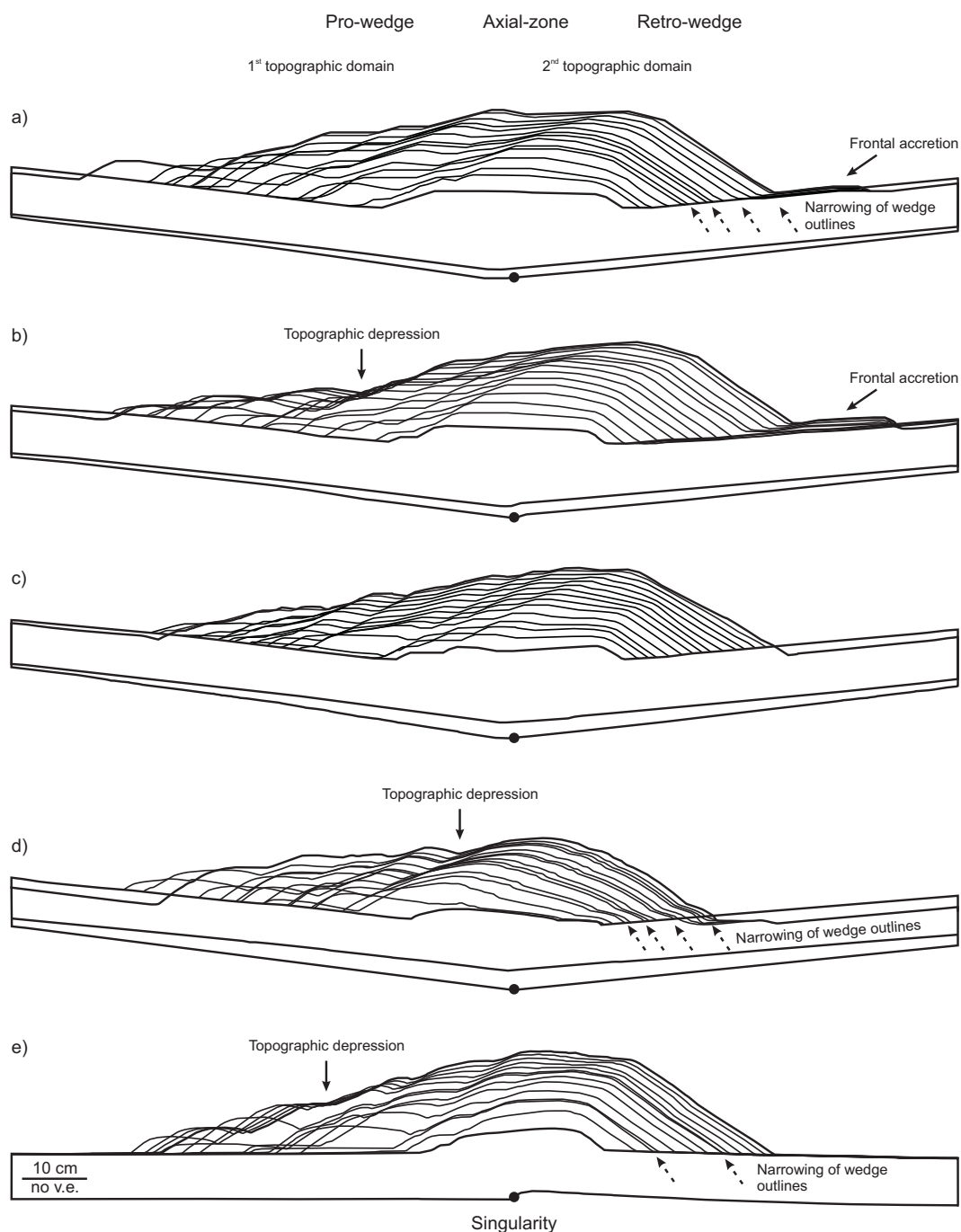


Figure 5.13: Topographic evolution of all experiments of the 1<sup>st</sup> series. Outlines were taken at every 10 cm of convergence. The first, i.e., after 10 cm and the last, i.e., after 150 cm of convergence outline are given in complete form, to indicate the magnitude of flexure. (a) Reference experiment 9.15; (b) Experiment 9.05; (c) Experiment 9.20; (d) Experiment 9.35; (e) Experiment 9.25. All experiments show two topographic domains: cyclic accretion within the pro-wedge results in distinct steps in topography, whereas continuous addition of pro-wedge derived material to the axial-zone and the retro-wedge leads to a nearly concentric growth. Experiments with an asymmetric mechanic stratigraphy show a marked topographic low within the pro-wedge. Dashed arrows indicate narrowing of wedge outlines, which are linked with thrust initiation phases.

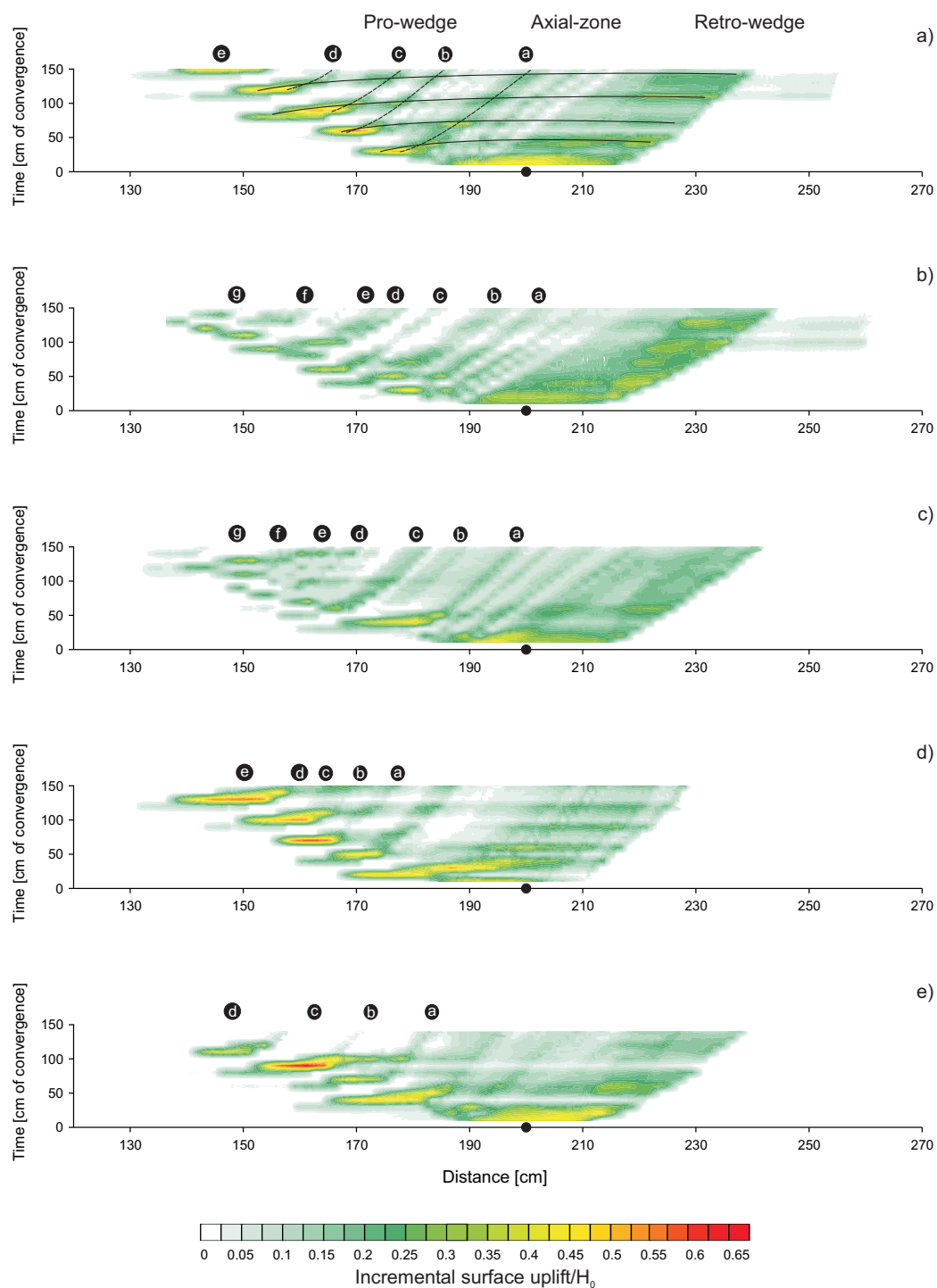


Figure 5.14: Incremental surface uplift map for all experiments of the 1<sup>st</sup> series. (a) Reference experiment 9.15; (b) Experiment 9.05; (c) Experiment 9.20; (d) Experiment 9.35; (e) Experiment 9.25. Interpretation of thrust traces (dashed lines) as well as surface uplift waves (bold lines) is only provided for (a), but can be recognised in all experiments. Labels (a) to (g) refer to forethrusts within the pro-wedge of (a), but can be recognised in all experiments. Higher magnitudes of ISU within the pro-wedge of (a), (d) and (e) result from a deeper detachment level, i. e., 6 cm.

lowered ISU within the axial-zone and the retro-wedge and (iv) surface uplift waves associated with the accretion cycle (Fig. 5.14). The latter are most pronounced in experiment 9.35, which lacks basal accretion (Fig. 5.14d). In experiments with basal accretion (9.05, 9.20) ISU waves remain a very subtle feature (Fig. 5.14b, c). Both observations are thus concordant with the findings from experiment 9.25. If the detachment is located above the conveyor belt, i. e., only frontal accretion operates, a consecutive ISU wave can be traced. However, if the detachment is positioned within the internal weak layer, a respective surface uplift wave is hard to detect (Fig. 5.14e). It is finally highlighted that the ISU pattern does not mirror the accretion of individual duplexes.

*Strain accumulation.* Similar to the reference experiment, finite strain was calculated for each experiment (Fig. 5.15). The main structural elements such as the basal and the internal detachment, the retro shear-zone, individual thrust imbricates, duplexes as well as hangingwall short-cuts can be clearly identified. As recognised in the reference experiment the magnitude of retro shear is highest at the retro shear-zone, which separates lower plate from upper plate material and is thus again interpreted as long-lived. Back-thrusts intimately linked with the initiation of the flat-topped box anticlines accumulated only minor magnitudes of incremental strain and are therefore difficult to recognise in the finite strain images. A similar distribution of finite strain, as observed in the pro-wedge of the reference experiment, is found in all four experiments, i. e., cumulative  $e_{xy}$  magnitudes are highest for thrust imbricates located within the central part of the pro-wedge close to the topographic break, if present. On the other hand thrusts positioned either at the toe or at the top of the pro-wedge show significantly lower cumulative  $e_{xy}$  magnitudes (Fig. 5.15). Based on these observations a first order similarity in terms of strain accumulation and distribution between

the reference and the experiments with varied kinematic boundary conditions is postulated.

However, if similar structures are compared between experiments, it emerges that different magnitudes of finite strain were accommodated. This is assigned to the respective kinematic boundary conditions and examples are provided below. Thrusts, which have a common depth to the detachment are characterised by similar finite strain magnitudes. In experiment 9.15 and 9.35, where this depth is 6 cm, the finite strain magnitudes are generally higher (Fig. 5.15a, d) than in experiment 9.05 and 9.20, where the depth to the detachment is only 4 cm (Fig. 5.15b, c). This trend can also be recognised in experiment 9.25 (Fig. 5.15e). Here, finite strain magnitudes of thrust imbricates, which detach just above the conveyor belt (6 cm) are higher than the respective magnitudes of thrust imbricates with an internal detachment level (4 cm). The former magnitudes compare well with the ones derived from experiment 9.15 and 9.35, whereas the latter magnitudes are in a similar range as the ones from experiment 9.05 and 9.20. This dependence of finite strain magnitude on the depth to the detachment was found to be independent of the relative position of individual thrust imbricates within the pro-wedge.

Finite strain at the retro shear-zone is highest in experiment 9.05 and lowest in experiment 9.35. Interestingly, finite strain at the internal detachment is also highest for experiment 9.05 (Fig. 5.15b). In experiment 9.20 and 9.25 however, this internal detachment is difficult to recognise within the finite strain image (Fig. 5.15c, e).

*Strain propagation and the thrust cycle.* Similar to the reference experiment, the EDM provide a detailed insight in the spatio-temporal distribution of incremental  $e_{xy}$  for the experiments described in this section and the main structural elements such as: the initial pop-up, the retro shear-zone, individual thrust imbricates within the pro- and the

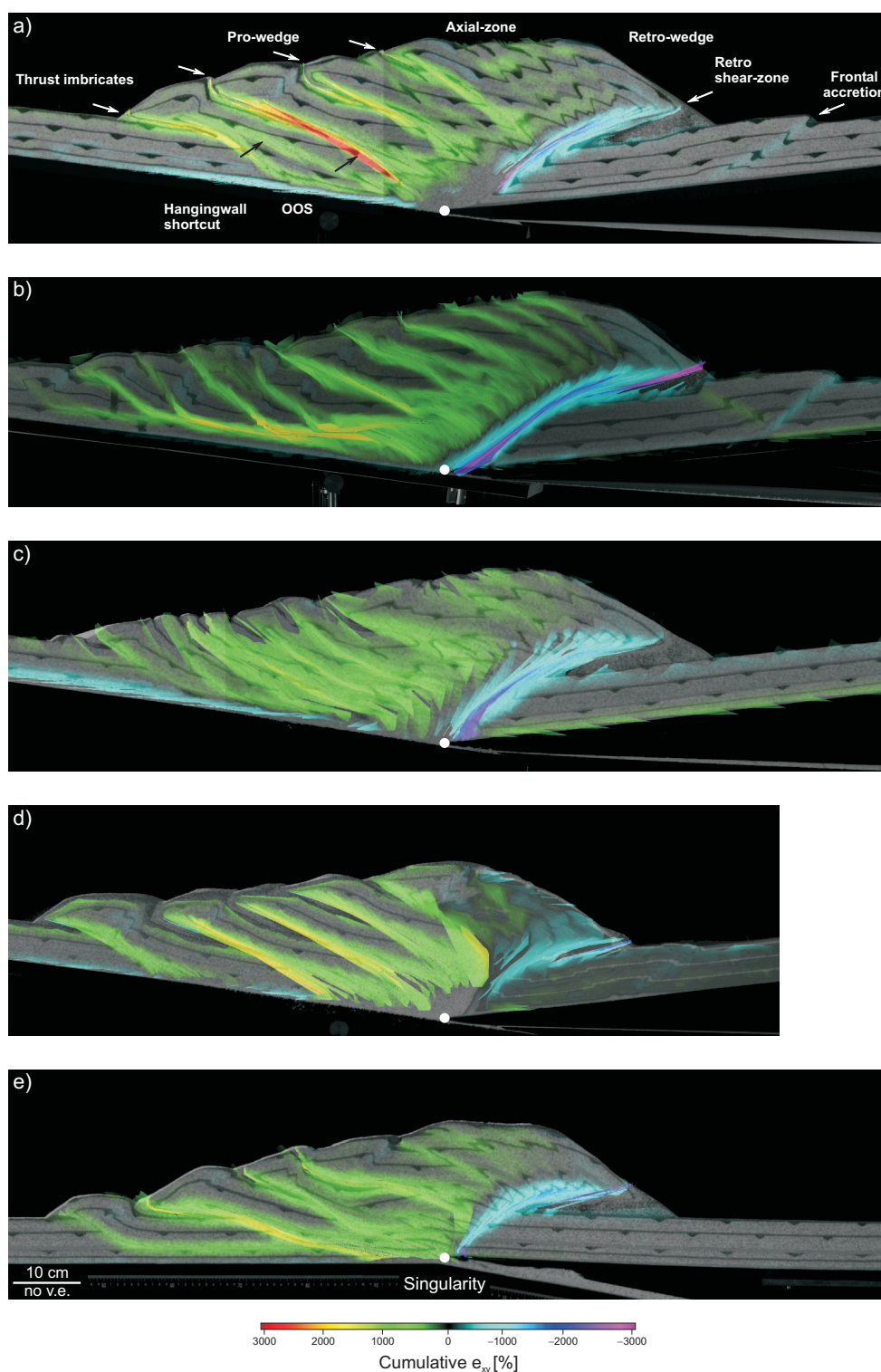


Figure 5.15: Finite  $e_{xy}$  after 140 cm of convergence. (a) Reference experiment 9.15; (b) Experiment 9.05; (c) Experiment 9.20; (d) Experiment 9.35; (e) Experiment 9.25 with only 120 cm of convergence.

retro-wedge as well as subtle features like back-thrusts, footwall, and hangingwall shortcuts and out-of-sequence re-activation of thrust imbricates are clearly recognisable (Fig. 5.16). Even the late stage frontal accretion within the retro-wedge in experiment 9.35, which is not recognised in the finite strain image, leaves a very subtle trace in the EDM (Fig. 5.16c).

Furthermore, and most importantly, the regular strain pattern identified within the reference experiment and referred to as the accretion cycle, can be clearly observed for all experiments, although variations do exist. The latter can be related to the number of active backthrusts and the longevity of major thrusts. Especially, the time span and magnitude of out-of-sequence strain accumulation along thrusts varies between experiments. It is highest for the experiment 9.05 and 9.20 and is lowest for the experiments 9.25 and 9.35. Thus, in the former experiments, several structures accommodate  $e_{xy}$  at the same time, resulting in a smoothed EDM for which experiment 9.20 is a good example (Fig. 5.16b). Oppositely, the temporal overlap of  $e_{xy}$  accommodation by several structures is restricted to short episodes in experiment 9.25 and 9.35 (Fig. 5.16c, d). Note, that all experiments, except 9.20, show a pulsating  $e_{xy}$  accumulation along the retro shear-zone.

Similar to the reference experiment, the above observations are reflected in the  $e_{xy}$  histories of individual ramp segments of the fore-thrusts and the retro shear-zone (Fig. 5.17). Again, all three phases of the accretion cycle can be linked with the three maxima of incremental  $e_{xy}$ . The varying degrees of contemporaneous  $e_{xy}$  accumulation along several structures noted earlier can be clearly recognised as well. Within this respect, experiment 9.05 and 9.20 show the highest degree of overlap (Fig. 5.17a, b). It is furthermore evident from these graphs that the activity of the retro shear-zone within all experiments follows a pattern, similar to a damped oscillation. Inspection by eye of (Fig. 5.17) reveals that the magni-

tude of damping differs significantly between experiments and is assumed to be highest in experiment 9.20 (Fig. 5.17b) and lowest in experiment 9.25 (Fig. 5.17 d).  $e_{xy}$  maxima, which predate the formation of a new thrust imbricate within the pro-layer show a shape, which are similar to a funnel, while using the terminology of well log analysis (Rider, 2000). Interestingly, the response of the retro shear-zone in terms of  $e_{xy}$  accumulation differs in dependence on the depth to the detachment (Fig. 5.17d). As outlined above, experiment 9.25 shows two cycles, where each cycle is composed of two accretion cycles, one with 6cm and one with 4cm detachment depth. During the former, the response of the retro shear-zone is similar to a funnel, during the latter, a box-like shape is found.

*Out-of-sequence displacement.* Frontal accretion in all experiments shows a pure forward-breaking or piggy-back thrust-sequence, although the corresponding displacement along each individual thrust is accumulated at several stages during wedge evolution. The result of this re-activation of older thrusts is termed out-of-sequence displacement. Based on the cumulative length evolution of individual thrusts, two end-member kinematic scenarios can be identified, between which all transitions are possible (Fig. 5.18). Thrusts, with only one phase of activity, are found in the reference experiment as well as in experiment 9.25 and 9.35 (Fig. 5.18a, e, d). However, careful examination of this figure reveals that the cumulative thrust length curves are made up of three segments. While the first segment is characterised by a gentle slope, the second segment shows a significantly steeper slope. The slope of the third segment approaches almost zero. This observation agrees with results derived from the analysis of the spatio-temporal distribution of  $e_{xy}$  (Fig. 5.17). Within this scenario, the first segment correlates with the postulated thrust initiation phase and the second segment with the underthrusting and the re-activation phase.



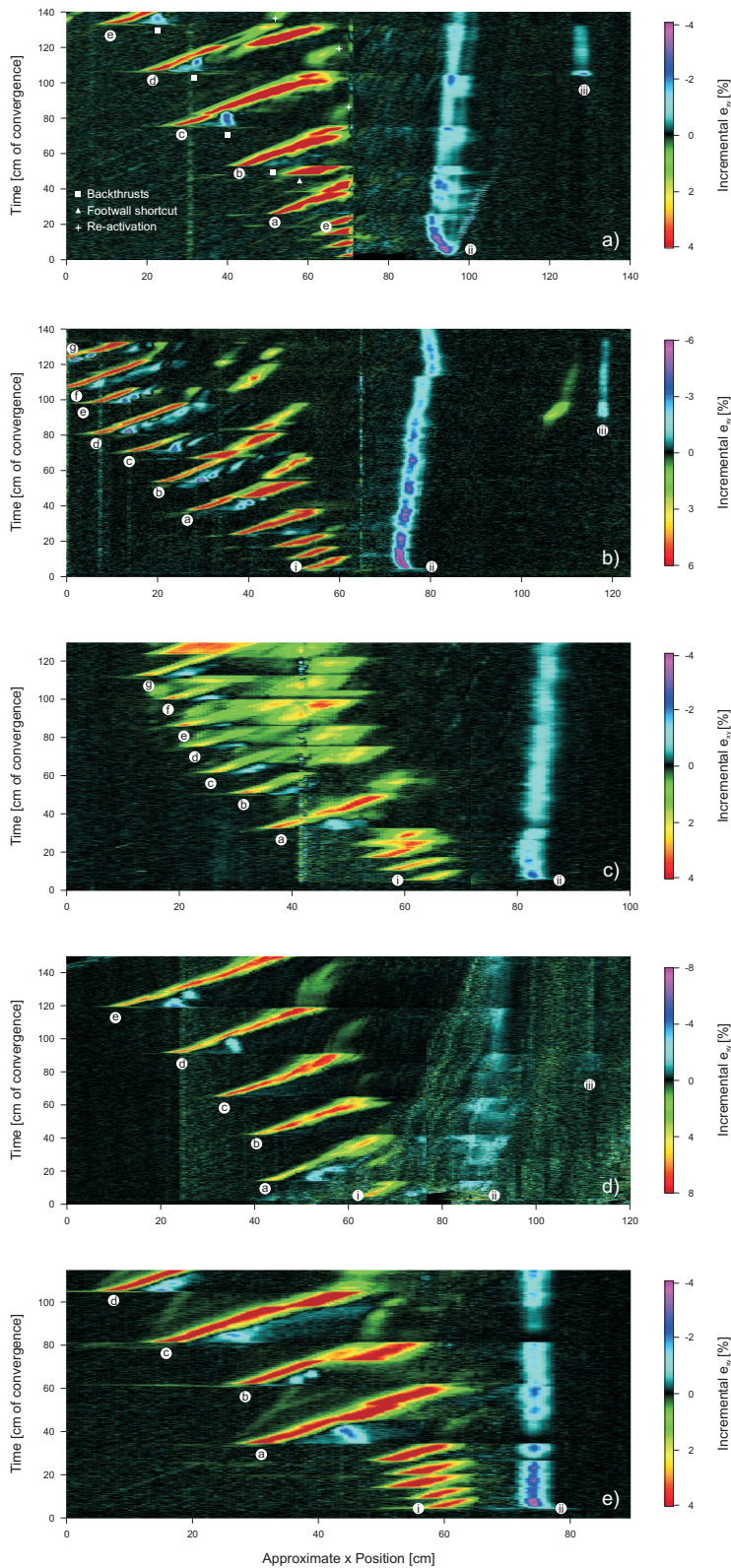
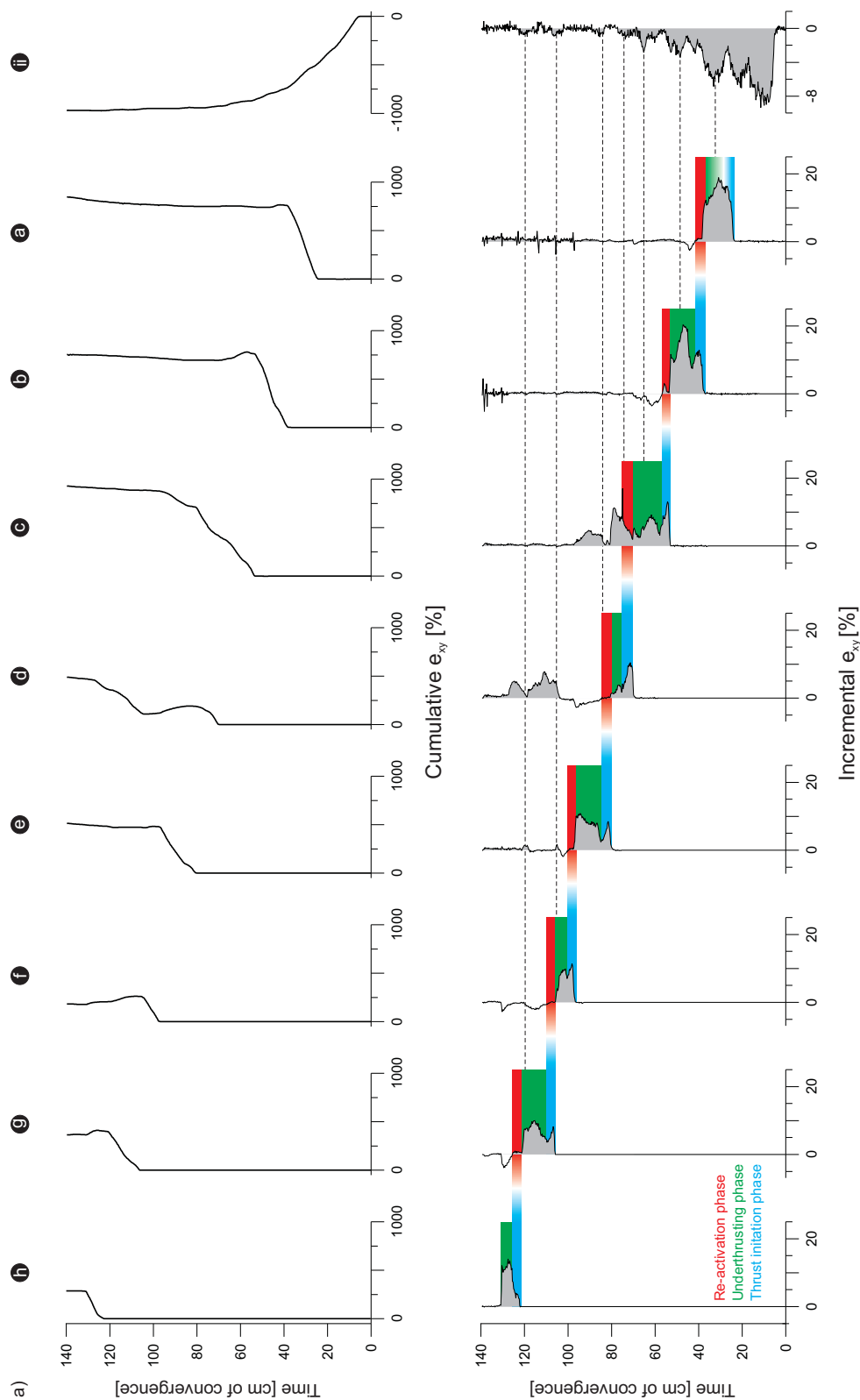
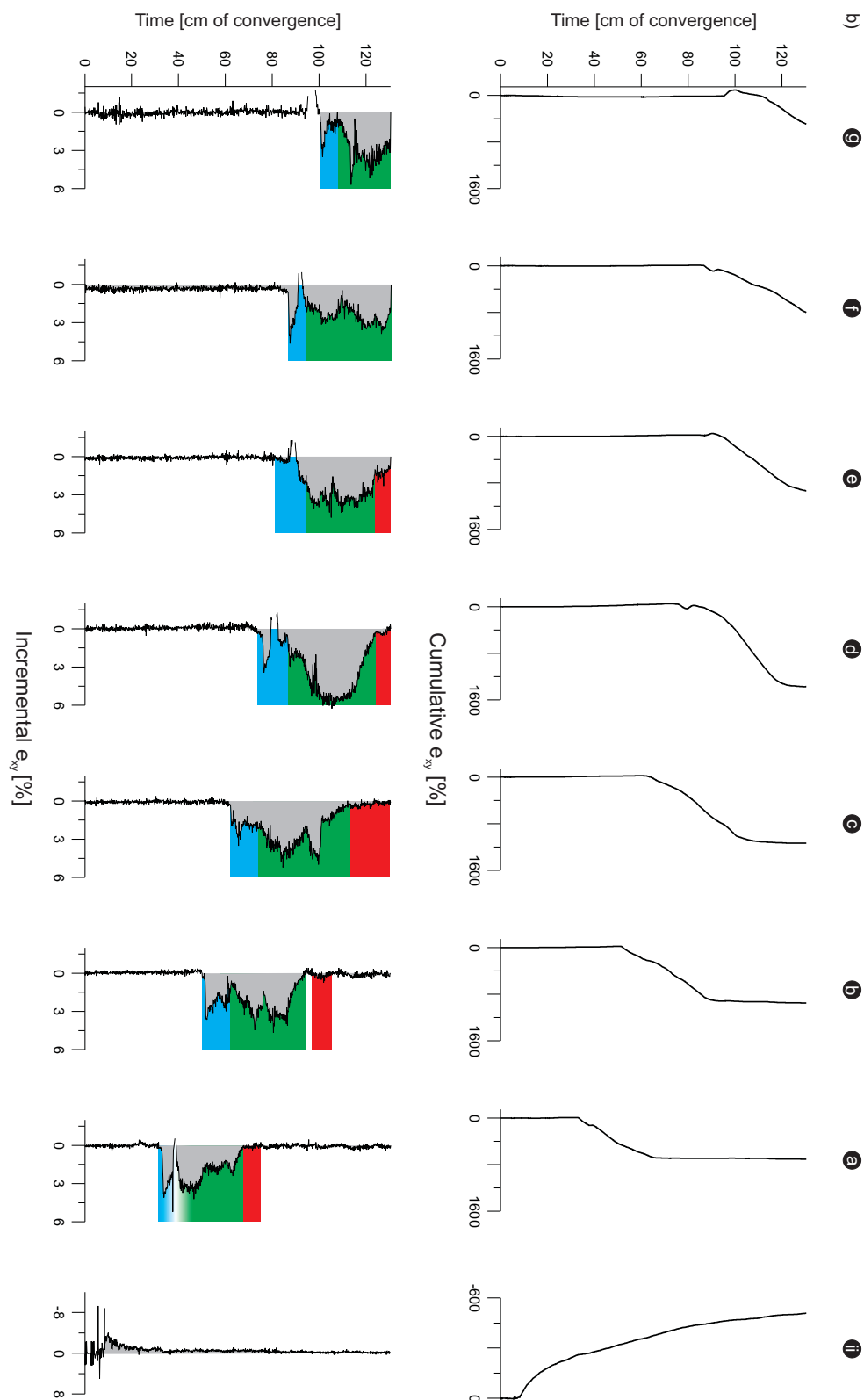
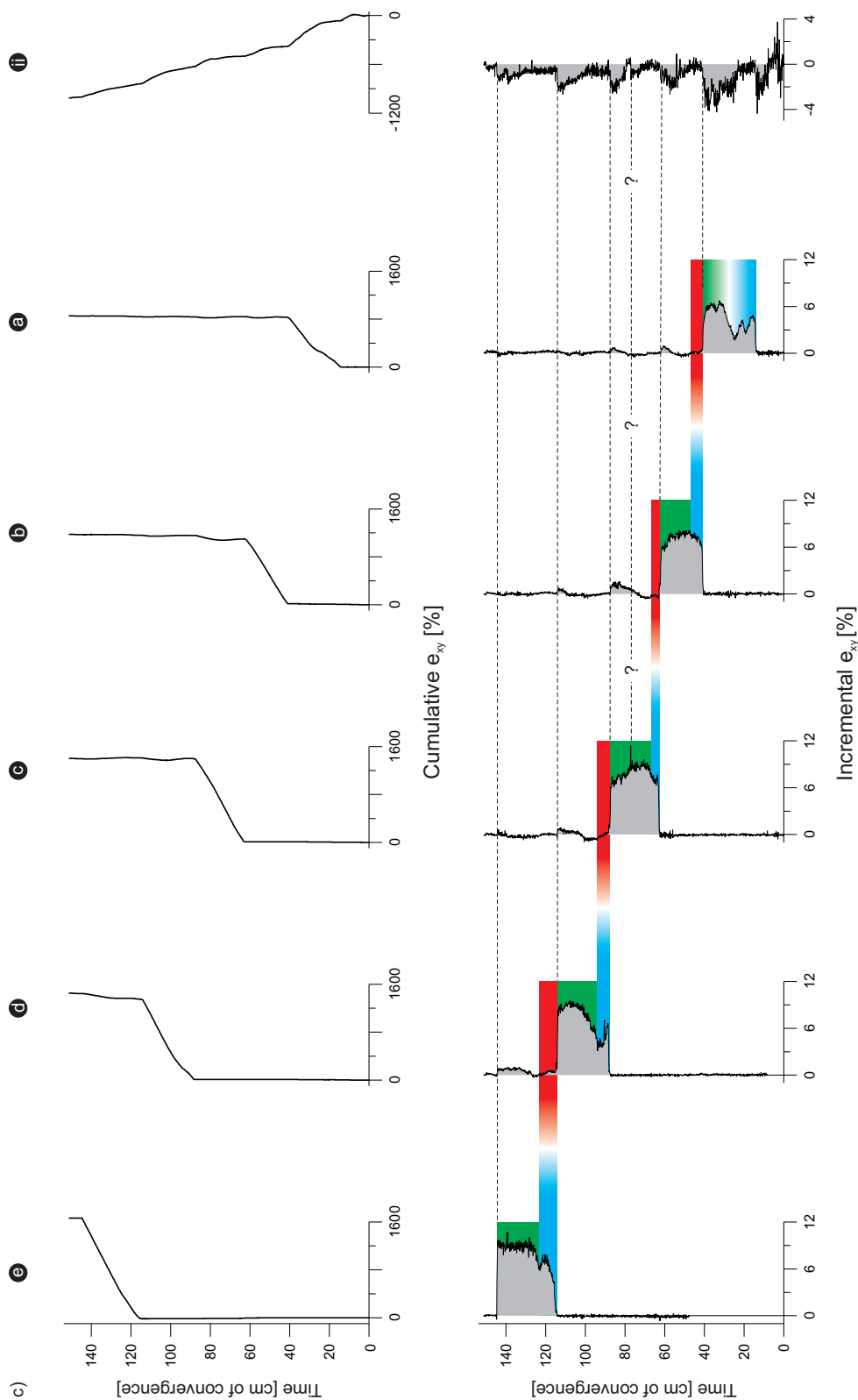


Figure 5.16: EDM for all experiments of the 1<sup>st</sup> series. (a) Reference experiment 9.15; (b) Experiment 9.05; (c) Experiment 9.20; (d) Experiment 9.35; (e) Experiment 9.25. Labels (a) to (g) refer to forethrusts within the pro-wedge. (i) denotes the pro-shear of the initial pop-up, (ii) the respective retro-shear and (iii) denotes the frontal accretion within the retro-wedge. The accretion cycle with its three phases can be recognised in all experiments. This figure is aimed at showing maximum details. Therefore strain magnitudes are not the same but similar. Positions of profile line with respect to the ramp segments of the forethrusts may vary within and between experiments. Changes of the magnitude may result, but the overall pattern is not affected. This figure provides complementary information to the following figure.







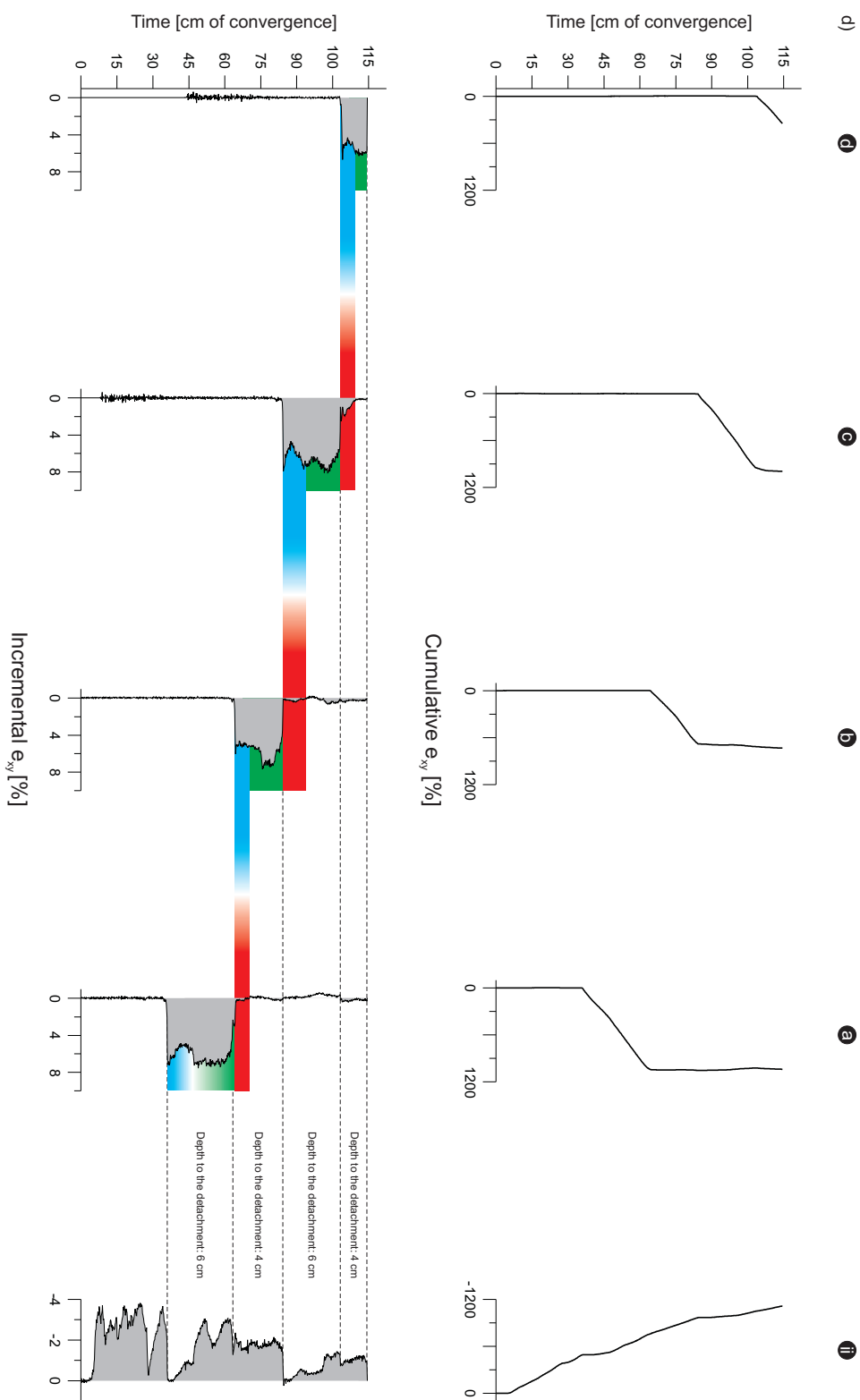


Figure 5.17: Strain accumulation of forethrusts within the pro-wedge (a) to (d) and the retro-shear zone (i) to (iv). (a) Experiment 9.05; (b) Experiment 9.20; (c) Experiment 9.35; (d) Experiment 9.25. Letters in circles refer to forethrusts within the pro-wedge. Roman ii denotes the retro-shear zone of the initial pop-up. Coloured areas mark times of the three phases of an accretion cycle: blue – thrust initiation phase, green – underthrusting phase and red – re-activation phase. Each phase is associated with different peak values of  $e_{xy}$ . Dashed lines link pro-wedge deformation with the one of the retro-shear zone. Such a link is difficult to establish for experiment 9.20 (b), given the low amplitude accumulation of  $e_{xy}$  at the retro-shear zone. Magnitude of  $e_{xy}$  along the retro-shear zone decreases with increasing length of the pro-wedge and can be described by a damped oscillation. Experiment 9.25 (d) indicates that the response of the retro-shear zone depends on the depth to the detachment.

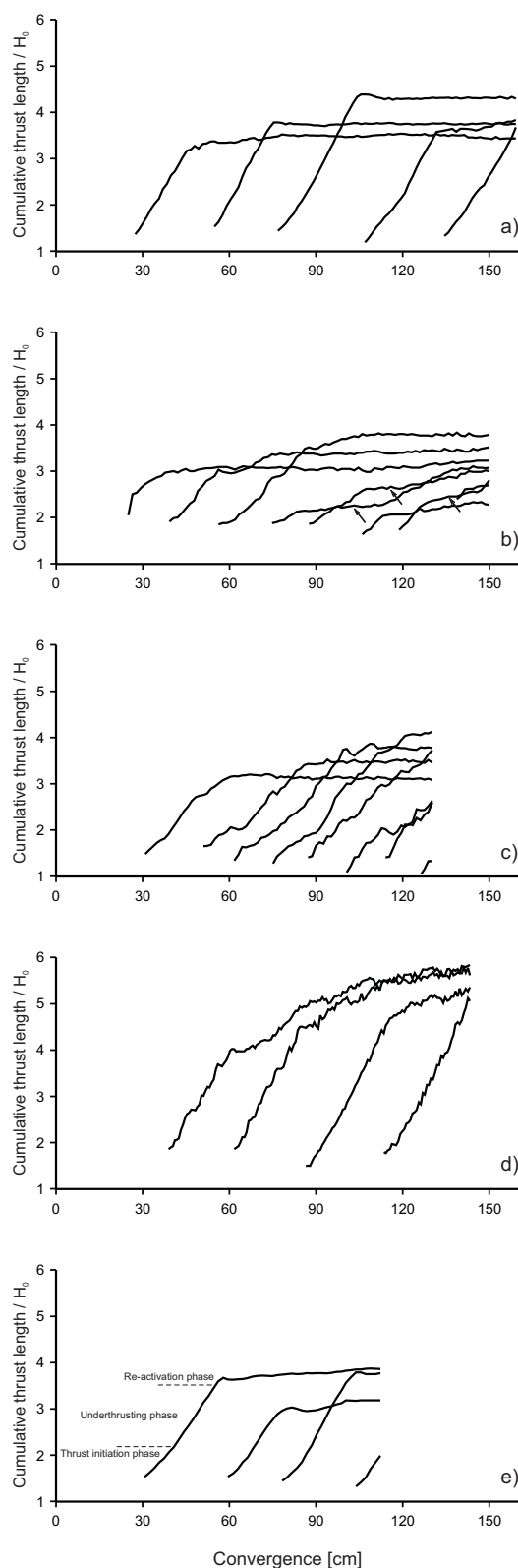
Figure 5.18: Cumulative thrust lengths of each thrust within the pro-wedge, taken at every 1.5 cm of convergence. (a) Reference experiment 9.15; (b) Experiment 9.05; (c) Experiment 9.20; (d) Experiment 9.35; (e) Experiment 9.25. Each curve consists of three segments, each with a different gradient. They correlate with the three phases of the accretion cycle. Note that some thrusts in (b) show a temporal offset between the underthrusting phase and the re-activation phase (arrow).

A slight difference of the cumulative length evolution is recognised for thrusts from experiment 9.05 and 9.20. They are characterised by two distinct phases of activity, separated by a period of quiescence. This is consistent with observations from the  $e_{xy}$  profiles (Fig. 5.17a, b), which indicate that the re-activation phase is temporally offset from the underthrusting phase. To quantify out-of-sequence activity, an out-of-sequence displacement index (OOSD) was derived, which is based on the magnitude of slip accumulated out-of-sequence. This OOSD index is highest for experiment 9.20 and lowest for the reference experiment (Table 5.1). The reader's attention is finally drawn to the observation that in experiment 9.05, 9.15, and 9.20 the third thrust accumulates the maximum finite displacement. Thus, finite displacement increases from thrust one to thrust three and decreases with later thrusts.

## 5.3 Discussion

### 5.3.1 Four-staged evolutionary model for bivergent sand-wedges

Deciphering the influence of kinematic boundary conditions, such as different mechanic stratigraphies and the degree of flexure on bivergent-wedge evolution was one of the key targets of this study. In order to address this issue, scaled 2D sandbox simulations were chosen. Confidence about the appropriateness of the selected setup is derived from the observation that all six key features of natural bivergent wedges (section 3.1)



were observed during experiments: (i) the asymmetry of the convergence geometry; (ii) the polarity of the mass-transfer; (iii) the bivergence of structures; (iv) the emergence of two sub-wedges, the pro-wedge with a low and the retro-wedge with a higher topographic gradient; (v) the dominance of deformation in the pro-wedge during early stages and migration of deformation into the upper plate during later stages of collision and (vi) the flexural downbending of the plates (Fig. 5.11).

All conducted experiments followed a similar four-staged evolutionary pathway: (I) initiation of a symmetric pop-up; (II) formation of a proto pro-wedge; (III) growth of the pro-wedge by frontal accretion and, in case an internal detachment layer was available, basal accretion and (IV) emergence of frontal accretion within the retro-wedge (Fig. 5.11, movies on DVD). The associated evolution of the lateral and vertical growth of the pro- and the retro-wedge is summarised in table (5.2) and agrees well with results from other sandbox and numerical simulations (Malavieille, 1984; Wang and Davis, 1996; Storti et al., 2000; McClay and Whitehouse, 2004; Willett et al., 1993; Beaumont et al., 1996; Naylor et al., 2005) and suggests thus reproducibility despite different setups and methodological approaches.

The proposed four-staged evolutionary model is also supported by observations from natural orogens. Uplift, folding and retoward translation of the initial pop-up might be envisaged as a crustal-scale backfold (Adrian Pfiffner pers. com., (2003)). In the case of the Swiss Alps this backfold is marked by the Austroalpine nappes and is coeval with the onset of frontal accretion but remains active throughout the collisional history (Pfiffner et al., 2000). Based on balanced cross sections, Pfiffner et al. (2000) showed that frontal accretion preceded basal accretion, after collision started during the Late Eocene. This has also been documented for the Pyrenees (Beaumont et al., 2000) and for Taiwan (Lacombe and Mouthereau, 2002). Therefore, similar to the transition from

stage II to stage III, as evidenced by experiments of this study, a certain load was needed to facilitate slip along deeper lying detachments. A late stage frontal accretion within the retro-wedge (transition from stage III to stage IV) is observed in the Pyrenees (Beaumont et al., 2000), the European Alps (Pfiffner et al., 2000), the German Variscides (Schäfer et al., 2000), and the Sunda Arc (Silver and Reed, 1988).

### 5.3.2 Strain transfer in bivergent wedges

Although we found that bivergent wedge evolution is very similar despite different kinematic boundary conditions, a likewise similarity with respect to the spatio-temporal distribution of strain was not expected, but observed. Indeed experimental results indicate that the accretion cycle with its three phases is a very robust process (Fig. 5.17). Therefore, a conceptual model of an accretion cycle is proposed (Fig. 5.19), which can be viewed as an extension of the one postulated by Gutscher et al. (1998) and Hoffmann-Rothe et al. (2004).

In addition, this conceptual model integrates and explains previously unrelated observations such as (i) the periodicity of thrusting (Cadell, 1888; Mulugeta and Koyi, 1992); (ii) the topographic evolution, especially the significant increase of the vertical growth rate at the rear of a wedge prior to the formation of a new thrust (Koyi, 1995; Storti et al., 2000; Naylor et al., 2005) and (iii) the cumulative slip evolution of thrusts (Storti et al., 2000; McClay and Whitehouse, 2004).

An exemplified accretion cycle might evolve as follows: during the thrust initiation phase, convergence is taken up by four thrusts, i. e., the forethrust, which defines the deformation front; the associated backthrust; an internal thrust, i. e., the previous deformation front and the retro shear-zone. The resultant incremental surface uplift is highest above the ramp segment of the forethrust and lowest above the retro shear-zone.

Stage	Distribution of deformation	Uplift of axial-zone and retro-wedge	Symmetry of bivergent sand-wedge
I*	Pop up	High	Symmetric
II <sup>†</sup>	Pro-wedge: high frequency thrust nucleation close to the singularity	High, but starts to decrease	Asymmetric
III <sup>§</sup>	Pro-wedge: low frequency thrust nucleation far from the singularity	low	Increase of asymmetry
IV <sup>‡</sup>	Pro-wedge: low frequency thrust nucleation far from the singularity Retro-wedge: frontal accretion	low	Asymmetric, but symmetry increases

Note: Bivergent wedge evolution has been described with different sequences of stages as indicated below.

\* Corresponds to stage 1 in Storti et al. (2000) and stage 1 in Willett et al. (1993).

† Corresponds to stage 1 in Storti et al. (2000) and stage 2 in Willett et al. (1993).

§ Corresponds to stage 2 in Storti et al. (2000) and stage 2 in Willett et al. (1993).

‡ Corresponds to stage 3 in Willett et al. (1993).

Table 5.2: Summary of key characteristics of bivergent wedge evolution (Inspired by Storti et al. (2000)).

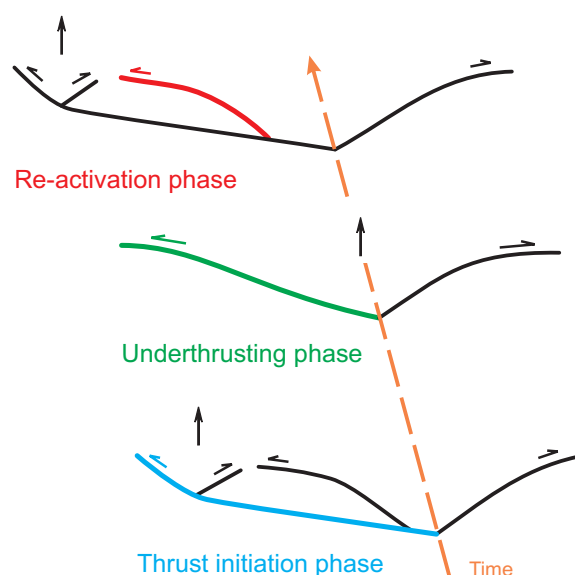


Figure 5.19: Conceptual model of an accretion cycle. The three phases thrust initiation, underthrusting and re-activation phase are colourcoded with respect to the forethrust. Vertical arrows indicate locations of maximum ISU. The accretion cycle is associated with a strain and a ISU wave. Both are initiated at the toe of the pro-wedge and migrate through the entire bivergent wedge until the retro-shear zone is reached. The phase within an accretion cycle controls thus the timing, location and magnitude of deformation and surface uplift.

In the following underthrusting phase, the forethrust evolves from a flat-ramp, via a ramp toward a ramp-flat geometry. The latter geometry

is therefore similar to the one of the retro shear-zone (Fig. 5.14). Thus, the asymmetry associated with the thrust initiation phase is abandoned in favour of a more symmetric geometry during the late stages of the underthrusting phase. Thereby, the entire sand-wedge shortens horizontally and grows vertically. At the same time, a surface uplift wave, which mirrors locations of high  $e_{xy}$  accumulation, migrates through the entire wedge until it reaches the retro shear-zone.

During the third phase, i. e., the re-activation phase, deformation propagates outward into the pro-layer to form a flat-topped box anticline and a new accretion cycle commences. The forethrust under consideration is now located in the hangingwall of the newly formed forethrust. This implies that the third phase of an accretion cycle is coeval with the first phase of the following accretion cycle. Strain transfer between two successive forethrusts can therefore not be considered as abrupt, i. e., one thrust is “switched” off while the other is “switched” on. Instead, strain is transferred gradually, i. e., the decay in activity of a forethrust is simultaneous with the increasing activity of the newly formed one (Fig. 5.16, Fig. 5.17). Thus,  $e_{xy}$  is not only partitioned in space but also in time. Thereby, the magnitude of



$e_{xy}$  taken up by each thrust depends on its relative strength, which changes predictably through time, as outlined below (Fig. 5.20).

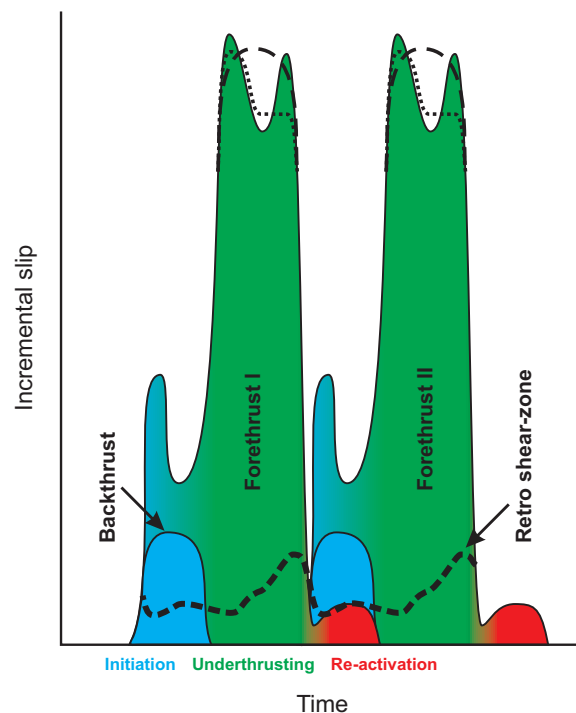


Figure 5.20: Incremental  $e_{xy}$  (slip) accumulation for all thrust, which are active during two accretion cycles. Magnitudes were taken from experiment 9.15. Phase within accretion cycle determines thus the location and magnitude of strain and slip accumulation. Therefore, strain and slip are partitioned in time and space. Note different peak scenarios for the underthrusting phase of two consecutive forethrusts.

Initiation of a thrust is associated with the successive formation and growth of isolated precursor structures, i. e., small-scaled shear zones (Nicol et al., 2002; Crider and Peacock, 2004). At the same time individual grains re-arrange and the porosity decreases significantly as evidenced by ring-shear measurements (Mandl et al., 1977; Lohrmann et al., 2003; Adam et al., 2005). This leads to an increase of the resistance to slip, since more grain boundaries are in contact with each other (strain hardening). The resultant strain accumulation is low. Coalescence of these small-scaled shear zones during the underthrusting phase

results in a thoroughgoing shear zone with a flat-ramp geometry. Grains are now decompacted and more preferentially orientated with respect to the shear direction and slip accumulation is promoted (strain softening). However, the continuous transfer of the thrust under consideration towards the singularity, in conjunction with an increasing load upon this thrust, leads to its final locking during the re-activation phase. The respective  $e_{xy}$  magnitudes are low.

Given that  $e_{xy}$  accumulation along the retro-shear zones mirrors this evolution (Fig. 5.17) we postulate that the entire bivergent wedge is subjected to a strain hardening – strain softening cycle. Thus, during the thrust-initiation phase the wedge is “strain softest”, but with continued convergence successively strengthened. At the very final stage of the underthrusting phase, the wedge is assumed to be “strain hardest”. This results in a temporal dependence of the magnitude of strain accumulation for individual thrusts, although brittle failure by itself is independent of time (Byerlee, 1978). The accretion cycle is therefore considered as an internal clock of wedge-scaled deformation.

Differences between experiments with respect to the duration and magnitude of individual phases relate either to (i) the exact position of the profile line from which  $e_{xy}$  data were taken; (ii) the depth to the detachment and (iii) the number of degrees of freedom (section 5.3.3). It is emphasised that the change of the geometry of the deformation front from a flat-ramp, via a ramp toward a ramp-flat, mirrors the tripartite evolution of the accretion cycles (Fig. 5.8). This relation has lead Hoffmann-Rothe et al. (2004) to propose that the southern Chilean margin at  $36^\circ$  S is in a thrust initiation phase, but at  $39^\circ$  S it is in an underthrusting phase. Additionally, we have shown that the cumulative length evolution of thrusts reflects the three phases of the accretion cycle as well and can thus be used to constrain the latter, if strain monitoring techniques, such as PIV, are not available (Fig. 5.18, section 5.2).

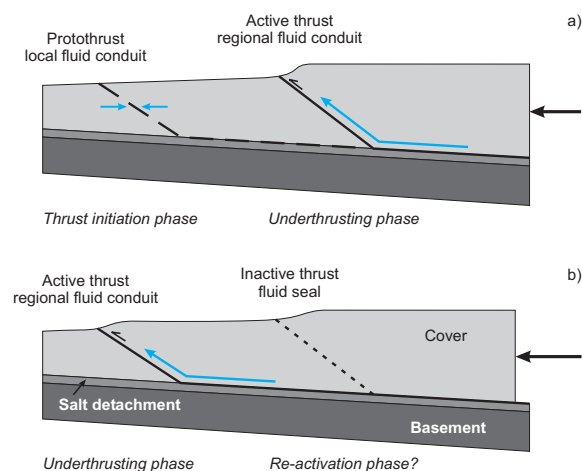


Figure 5.21: Relation of microfracture phase 1 (a) and 2 (b) with thrust development and main fluid-source (blue arrows). Interpretation with respect to the conceptual model of an accretion cycle is given. Modified after Travé et al. (2000).

The above postulated kinematic model of an accretion cycle derives further support from a variety of field studies. Micro-structural work in the Appalachian fold and thrust belt has led Wojtal and Mitra (1986) to conclude that the emplacement of a thrust sheet generates an array of mesoscopic faults beneath it. These fault-bounded blocks are displaced relative to one another and may be viewed as mesoscopic “grain boundary” sliding. The latter however occurs at least in two phases, the first associated with strain hardening, the second accompanied with strain softening.

Similarly, Travé et al. (2000) reported two microfracture phases in the El Guix anticline (South-Pyrenees). During the first stage, a network of discontinuous microfractures developed, which allowed only local meteoric fluids to circulate (Fig. 5.21a). In the second stage, a continuous thrust fault formed, facilitating now regional fluids to migrate (Fig. 5.21b). With respect to the terminology of this study, the first microfracture stage could correspond to the thrust initiation phase, whereas the second microfracture stage could be linked with the underthrusting phase.

Based on micro-structural work in the Char treuse district of the French Alps Butler and Bowler (1995) concluded that thrusts evolve through a strain- or displacement-rate cycle (Fig. 5.22). During the first phase thrust 1 is active at high rates whereas, thrust zone 2 deforms at significantly lower rates through an array of minor thrusts (Fig. 5.22a). In the second phase, displacement is transferred to thrust zone 2 (Fig. 5.22b). While thrust 2 has fully developed and deforms at a high rate, thrust 1 has moved into a slow strain rate field (Fig. 5.22c). This evolution is consistent with the conceptual model of an accretion cycle, which predicts low strain rates during the thrust initiation and the re-activation phase (Fig. 5.22a, c) and high strain rates during the underthrusting phase (Fig. 5.22b).

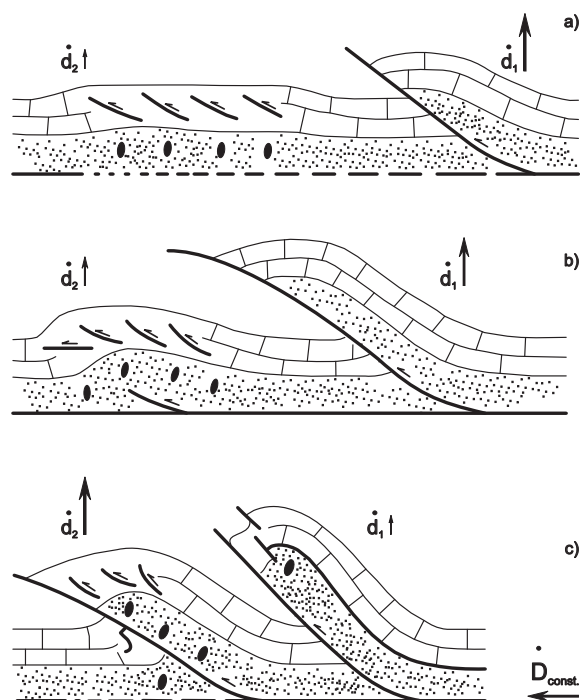


Figure 5.22: Strain (displacement) rate cycle of thrusts. The bulk displacement rate  $D$  is assumed to be constant. See text for explanation. Modified after Butler and Bowler (1995).

Meigs et al. (1996) reconstructed the displacement evolution of the South-Pyrenean Sierras Marginales thrust, which is very similar to the

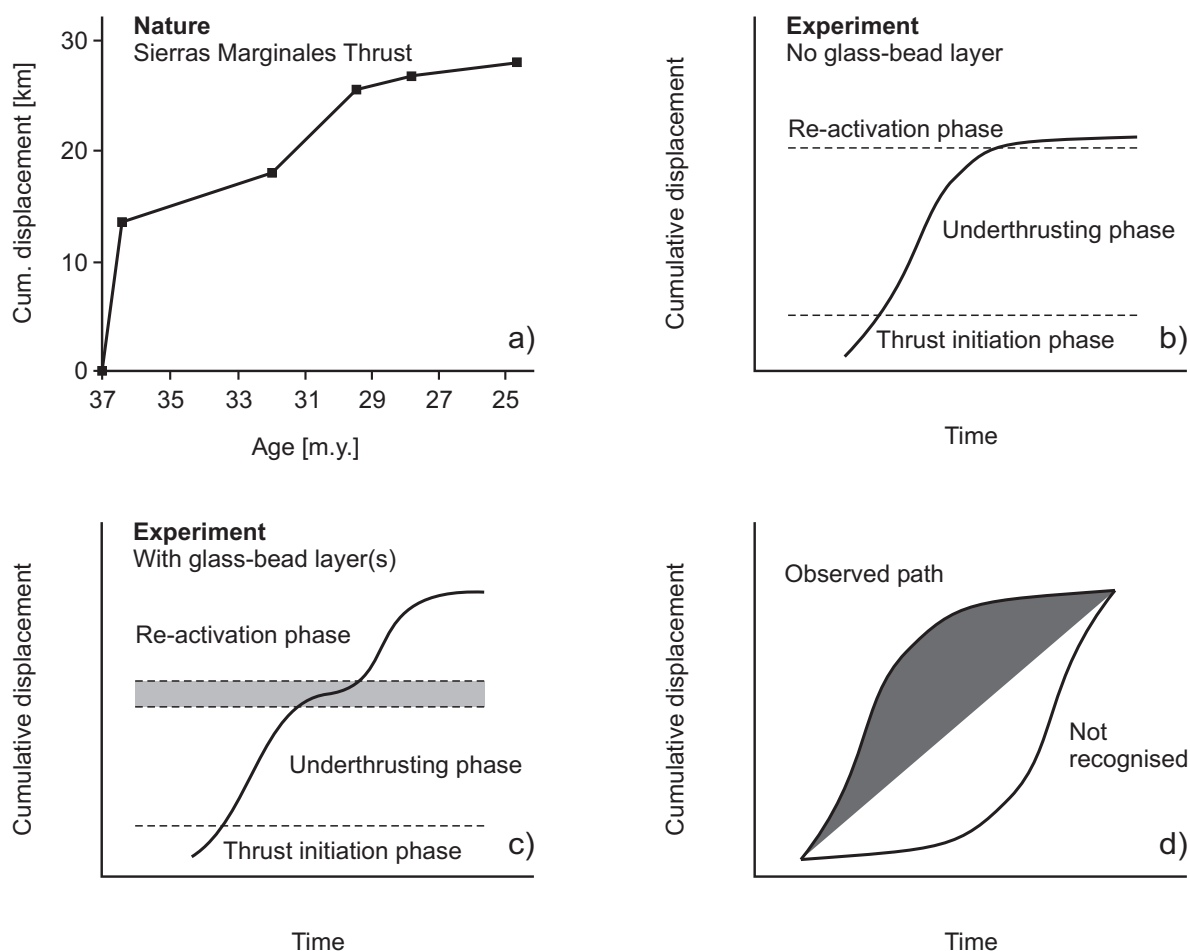


Figure 5.23: (a) Cumulative displacement of the Sierras Marginales Thrust, Southern Pyrenees. Modified after Meigs et al. (1996). Solid squares indicate data points. (b) and (c) show cumulative displacement of thrusts derived from sandbox experiments. Dashed lines in (b) and (c) mark phase boundaries. Gray line in (c) indicates temporal offset between underthrusting and re-activation phase. Note similarity between experimentally derived thrust length evolution and natural pendant. (d) Cumulative deformations paths may indicate that only paths within the dark shaded area are realised by deformation. This in turn might suggest that deformation through time follows a diffusion law, similar to erosion.

displacement histories observed in the bivergent sand-wedges (Fig. 5.23). They further proposed that the displacement transfer from internal to external thrusts is a continuous process, rather than a step-wise sequence of formation, displacement, and de-activation of thrusts. This conclusion is consistent with the one derived from the experiments. Therefore, box-functions of the displacement through time (Jordan et al., 2001) should be invoked with care.

Based on balanced cross-sections Jones et al. (2004) investigated the Eocene to Oligocene Catalan fold and thrust belt. They proposed a thrust sequence, which is concordant with the conceptual model of an accretion cycle (Fig. 5.24).

There are thus several lines of evidence from a variety of methodological approaches as well as from field studies, which provide direct and indirect support for the postulated conceptual model of an accretion cycle. Implications of this model shall be addressed in section (5.4).

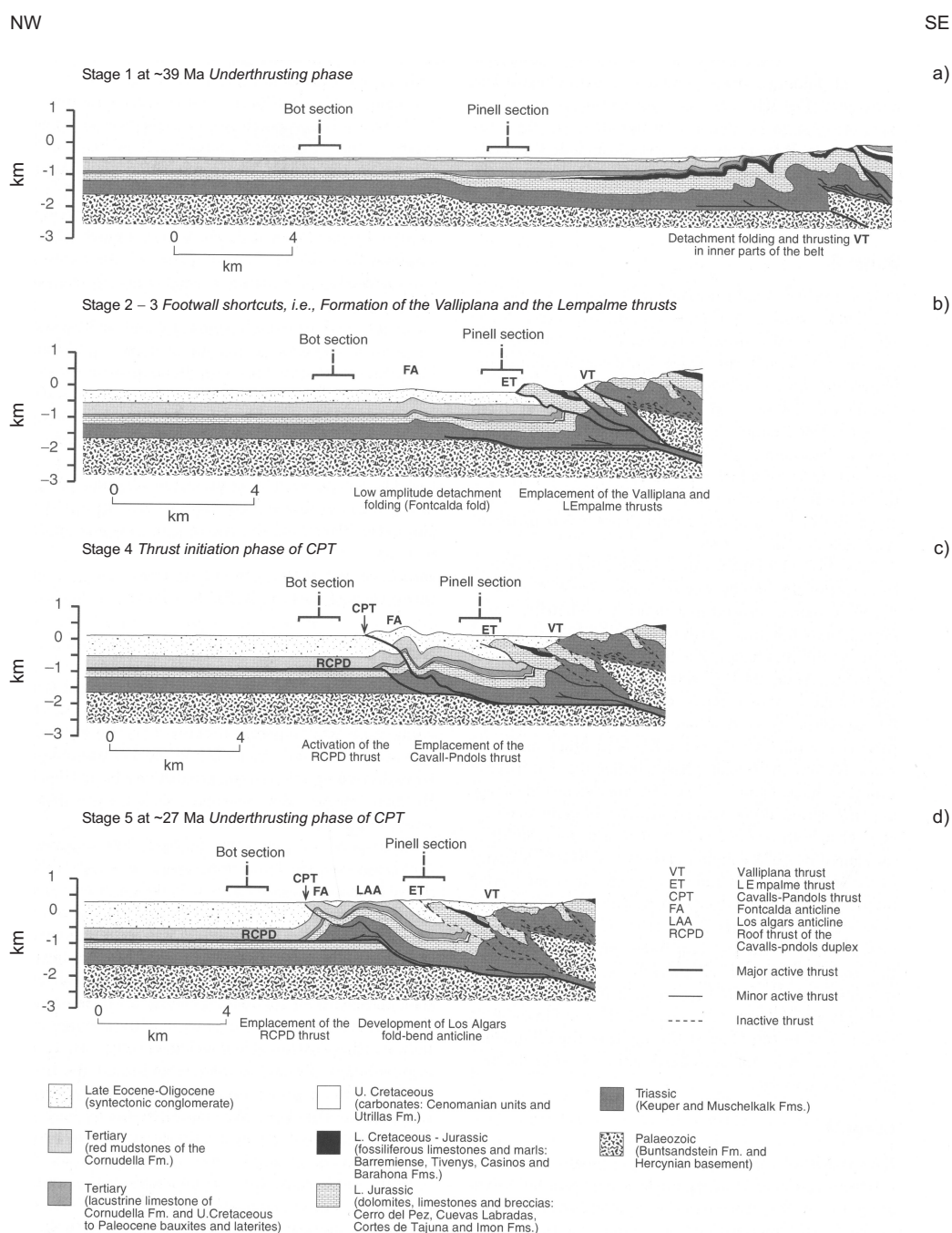


Figure 5.24: Sequential evolution of the central part of the Catalan Coastal Range derived from balanced cross-sections. Time interval is  $\sim 10Ma$ . Stages 1 to 5 are based on provenance analysis and other sedimentological data of syntectonic strata, taken at the Bot and at the Pinell section. Own interpretation with respect to the phase within the accretion cycle is given in italics. (a) Probably underthrusting phase. (b) Footwall shortcuts, i.e., the formation of the Valliplana and Lempalme thrusts. Thereby the basal detachment propagates towards the foreland. (c) Thrust initiation phase of the Cavalls-Pandols Thrust, whereby the previous deformation front is still active, i.e., Lempalme thrust. (d) Underthrusting phase of the Cavalls-Pandols Thrust. Note that the hinterland lacks any thrust activity. Modified after Jones et al. (2004).

### 5.3.3 The timing of thrust initiation

In the previous section the accretion cycle was considered as an internal clock of bivergent-wedge deformation. However, what controls the duration of each accretion cycle and is it predictable? We therefore introduced the sample standard deviation of the wavelength of frontal accretion  $s_{fw}$ , which is thought to measure the temporal regularity of the initiation of forethrusts within the pro-layer (Table 5.1).  $s_{fw}$  provides thus an estimate of the variability of the time span taken up by individual underthrusting phases. Consequently the term wavelength is used (Fig. 5.3). This method puts more emphasis on the timing of thrust initiation rather than the horizontal distance between two successive ramp segments, commonly referred to as thrust spacing (Marshak and Wilkerson, 1992). A constant timing, i. e., a low  $s_{fw}$  value indicates that the wedge response to accretion by internal deformation is similar for every accretion cycle, as outlined in the previous section. High  $s_{fw}$  values suggest that this response varies with each accretion cycle. In terms of the minimum work theory this means that internal deformation is favoured until the initiation of a new thrust within the pro-layer would consume less work (section 3.4).

Introduction of one or more weak layers or the simulation of erosion (chapter 6) reduces the internal strength of the pro-wedge and may thus lead to prolonged internal deformation and finally to higher  $s_{fw}$  values. This is supported by experimental observations since  $s_{fw}$  increases as the number of glass-bead layers increases as well (Table 5.1). Experiment 9.25 deviates only apparently from this trend, since the basal and the internal detachment are both activated twice, which results in a high  $s_{fw}$  value. Further support for this interpretation is derived from the OOSD index (Table 5.1). A high OOSD index indicates more internal deformation, i. e., more thrusts are synchronously active (Fig. 5.18). Again, experimental data suggest that the OOSD index increases if the number of glass-bead layers increases as well (Table 5.1).

If one considers flexure and each glass-bead layer as degrees of freedom, then a further interpretation emerges. Experiment 9.15 and 9.25 with one degree of freedom have the lowest, experiment 9.05 and 9.35 with two degrees of freedom have higher and experiment 9.20 with three degrees of freedom attains the highest OOSD index. A similar trend can be recognised for  $s_{fw}$ .

It follows from the above discussion that the variability of the duration of each accretion cycle does strongly depend on the boundary conditions, i. e., the numbers of degrees of freedom. Thus, with a given setup, one prescribes the relative magnitude of piggy-back, synchronous, and out-of-sequence thrusting. If the number of degrees of freedom is low, then piggy-back thrusting dominates, while more degrees of freedom promote synchronous and out-of-sequence thrusting. This conceptual model of degrees of freedom might explain the high variability found in natural fold and thrust belts (Butler, 1987; Morley, 1988; Boyer, 1992; Butler, 2004), puts emphasis on boundary conditions in nature and in modelling techniques and finally sheds light onto what is often considered as “local conditions”.

### 5.3.4 The spacing of thrusts

The spacing of thrusts as defined by Marshak and Wilkerson (1992) is fairly constant throughout the experiments (Fig. 5.12). Its dependence on the depth to the detachment is evidenced in experiment 9.20 and 9.25. This agrees with results from field studies (Soto et al., 2002; Morellato et al., 2003; Marshak, 2004), analytical considerations (Bombolakis, 1986; Mitra and Boyer, 1986; Goff and Wiltshko, 1992; Panian and Wiltshko, 2004) as well as analogue simulations (Liu et al., 1992; Marshak and Wilkerson, 1992; Mulugeta and Koyi, 1992; Boyer, 1995; Koyi, 1995; Corrado et al., 1998; Gutscher et al., 1998; Soto et al., 2002) that thrust spacing depends on the thickness of the incoming layer, its internal and basal properties as well as on the surface slope of the wedge.

Furthermore, figure (5.3) indicates that the aspect ratio of the thrusts, i. e., length (spacing) of a thrust divided by the thickness of the incoming layer is approximately 3, which is very similar to values observed in fold and thrust belts (Onno Oncken pers. com., (2005)). This finding provides additional support for the correct scaling of the mechanics of sand-wedges.

The variability of thrust spacing in the experiments is highest for those, where the basal detachment of the thrusts is located above the conveyor belt and lowest, where this detachment is located within the internal glass-bead layer (Table 5.1). The difference in peak friction between glass-beads and sand is significantly higher (6.2° or 17.6%) than the difference in peak friction between the sand and the conveyor belt (3.3° or 9.5%). Thus, the glass-bead layer provides always the weakest zone in the incoming layer and is thus prone to be used as a detachment. Additionally, a glass-bead layer is spatially better defined, if sieved carefully, than the sand – conveyor belt interface. The resulting shear zone is more or less straight in the former and shows an anatomising pattern in the latter case (Jürgen Adam pers. com., (2002)). Such irregularities of a detachment surface have been observed along the Barbados Ridge décollement, which crosscuts other stratigraphic levels, but remains within a 10m to 20m wide zone of significantly increased porosity and fluid content (Bangs et al., 1999; DiLeonardo et al., 2002). From a broader perspective, topographic irregularities of the basement surface upon which a wedge is thrust can focus the nucleation of thrusts and thus influence their respective spacing (Wiltschko and Eastman, 1983; Bombolakis, 1986). On the other hand, Dixon (1982) noted that the regular spacing of thrusts in the Idaho-Wyoming-Utah thrust belt developed over a featureless basement surface. Similarly, Sean Willett (pers. com., (2005)) suggested that thrust spacing is more similar, if basal friction is low.

Interestingly, experiment 9.15 shows a low variability with respect to the temporal regularity of forethrust formation, but shows at the same time a high variability of thrust spacing (Table 5.1). The opposite holds true for experiment 9.20. We therefore hypothesise: (i) that thrust spacing is dominantly controlled by the mechanical properties of the incoming layer and its detachment, which agrees with previous studies (e. g., Marshak and Wilkerson, 1992), and (ii) that the timing of thrust initiation is controlled by wedge internal deformation, which in turn depends on the number and orientation of weak zones, the degree of flexure or erosion (section 6.3.3), i. e., the degrees of freedom as postulated earlier. This would further imply that no direct link between the spatial regularity of the spacing and the temporal regularity of the timing exists. Therefore, neither observation can be used to infer the other and may finally point to end-member behaviour, i. e., time predictable and spacing predictable. A similarity with earthquake models might appear (Fig. 5.25). However, the latter assumes a constant slip rate, whereas the end-member scenarios derived from the experiments does not. Accordingly, both models would describe similar observations, but at different spatial and temporal scales.

### 5.3.5 Frontal accretion in the retro-wedge

One of the critical issues associated with the strain transfer in bivergent wedges is the occurrence of frontal accretion within the retro-wedge (stage IV). Factors thought to control this phenomenon, include the geometry of the backstop (Davis et al., 1983; Byrne et al., 1988; Lallemand et al., 1994; Wang and Davis, 1996), the strength of the backstop (Byrne et al., 1993), the strength of the backstop base (Pfiffner et al., 2000), and finally a subduction reversal (Del Castello et al., 2004). However, based on experimental results we propose that additional factors have to be taken into account. As demonstrated in section (5.2), we found that strain accumulation along the retro-shear zone

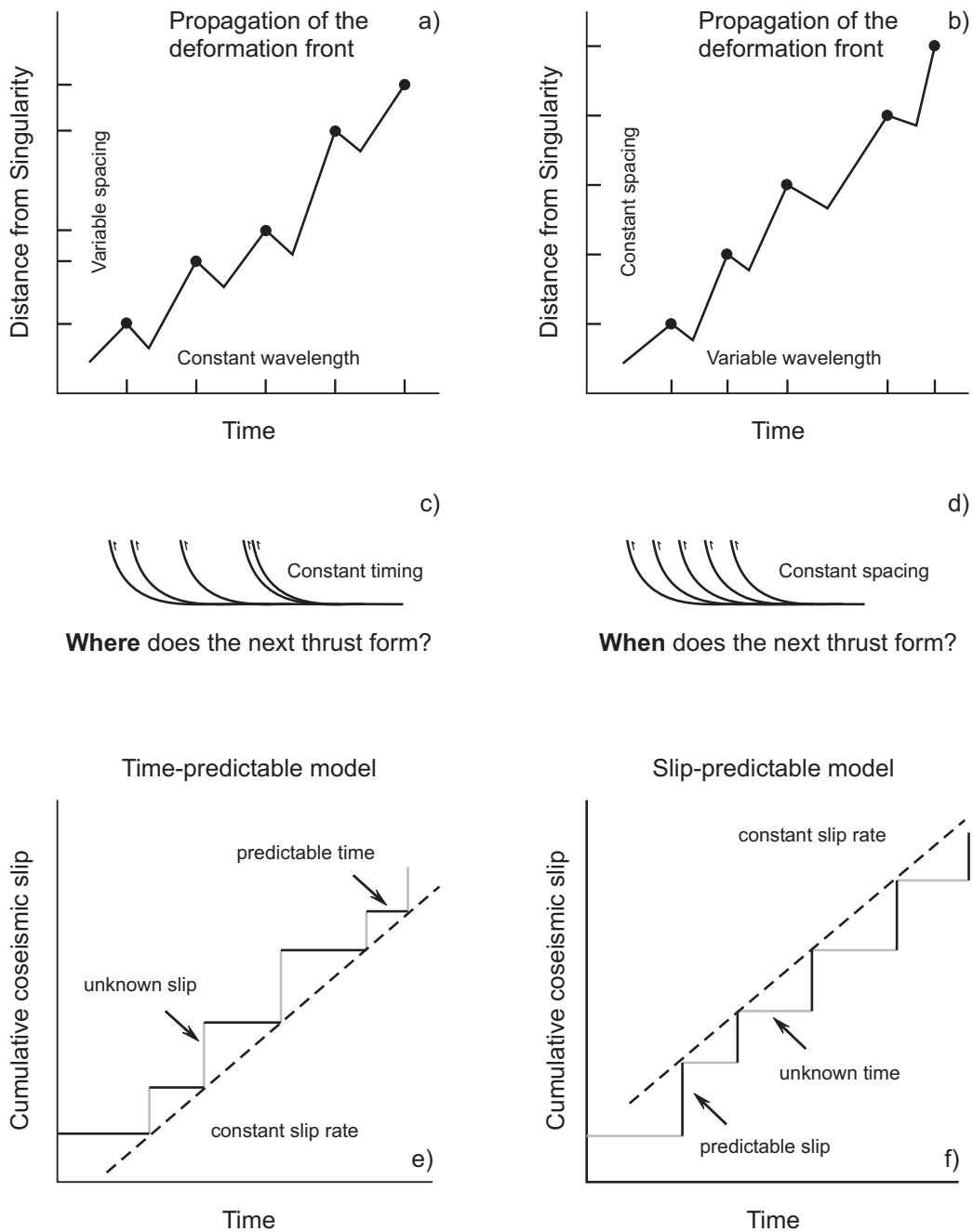


Figure 5.25: Postulated end-member behaviour: (a) Timing of thrust initiation is constant but not its spacing. (b) Thrust spacing is constant but not its timing. (c) and (d) are schematic imbricate fans, which may result from (a) and (b) respectively. It follows that a regular geometry does not necessarily indicate a constant timing, which suggests that one cannot use geometry to unequivocally infer a temporal regularity of thrust initiation. Both end-members bear some similarity to earthquake models: (e) Time-predictable model is based on a constant stress level at which failure occurs. Stress drop and slip magnitude are unpredictable, but given previous slip, time until the next earthquake with unknown slip is predictable. (f) Slip-predictable model is based on a constant stress level at the end of an earthquake. Given time since the last rupture, magnitude of slip is predictable. Both earthquake models assume a constant slip rate, which is not the case or only for very short time increments within the end-member scenarios derived from the experiments. (e) and (f) are redrawn from Burbank and Anderson (2001).

does not only depend on the phase within the accretion cycle, but also on:

- i. *Length of the pro-wedge.* The strain history of all monitored retro-shear zones (section 5.2) follows a damped oscillation, which can be correlated with the lateral growth of the pro-wedge (Fig. 5.17). The latter in turn leads to an increasing number of weak zones, i. e., thrusts, between the deformation front and the retro-shear zone. As noted earlier, these thrusts have to be strain-hardened first, before the entire pro-wedge and the axial-zone can slip upon the retro-shear zone. We therefore hypothesise that a growing pro-wedge evokes strain dissipation.
- ii. *Strength of the pro-wedge.* Among all experiments, experiment 9.20, with its two glass-bead layers, shows the lowest magnitude of incremental  $e_{xy}$  at the retro-shear zone (Fig. 5.16, Fig. 5.17). Additionally, experiment 9.20 has the highest OOSD as well as the highest  $s_{fw}$  index (Table 5.1) among all experiments and shows a rather distributed pattern of finite  $e_{xy}$  (Fig. 5.15). These observations in conjunction with the strength profile (Fig. 4.8) are therefore thought to indicate that the respective pro-wedge has a significantly lowered integrated strength.
- iii. *Mechanical properties of the detachment of frontal accretion within the pro-wedge.* Figure (5.17d) reveals that the mechanical properties of the basal detachment of the flat-topped box-anticlines within the pro-wedge exert an influence on the respective response of the retro-shear zone. Thus, the latter “knows” the mechanical properties of the former.

It follows that a force balance approach sensu Gutscher et al. (1998), to calculate the width and the height of the axial-zone/retro-wedge necessary

to initiate frontal accretion within the retro-wedge, would have to invoke (i) those thrust, i. e., at least four, which are active during an accretion cycle, (ii) a measure of the length of the pro-wedge, (iii) a measure of the integrated strength of the pro-wedge, and (iv) if erosion is simulated (chapter 6), a measure of the topography/load through time. This is at present not possible and it is left for future studies to explore solutions.

It is finally pointed out, that the surface slope of all retro-wedges remained rather uniform throughout the entire wedge evolution and was always at or close to the angle of repose. A lower-tapered retro-wedge sensu Willett et al. (1993) could not be observed since frontal accretion within the retro-wedge started late during experiments.

### 5.3.6 Parameter combinations

The observation of frontal accretion within the retro-wedge has been made for three out of five experiments considered at this stage. In the previous section, we proposed that a decrease of the integrated strength of the pro-wedge has at least retarded if not inhibited this process to occur. A similar effect is observed, if  $\beta$  is zero. To start with, this observation agrees well with published results from experiments with similar kinematic boundary conditions, e. g., Storti et al. (2000) and McClay and Whitehouse (2004). Although, experiment 9.25 has only 120 cm of convergence, a similar experiment by U. Schönrock (experiment 11.7, GFZ Laboratory 2004) with 150 cm of convergence revealed the same result – no frontal accretion within the retro-wedge. Given that the only difference between experiment 9.25 and 9.05 is flexure, we conclude that flexure might promote frontal accretion within the retro-wedge. Experimental evolution reveals that flexure leads to a rotation of the already steep retro shear-zone towards the pro-wedge. At the same time, the glass-bead layer, located at the base of the upper plate, rotates as well, attaining a more inclined orientation. It follows from Mohr-circle considerations,



Parameter	Promoting upper plate failure	Retarding upper plate failure
Flexure [9.15; 9.25]	✓	
Integrated strength of upper plate [*]	If low	If high
Upper plate thickness [4.06 <sup>†</sup> ]	If thick	If thin
Basal detachment [9.04 <sup>§</sup> ]	If weak	If strong
Integrated strength of lower plate [9.20]	If similar to upper plate or higher	If low
Amount of material addition via convergence [4.03 <sup>‡</sup> ]	If high	If low
Retro-wedge erosion [9.06]	✓	
Pro-wedge erosion [9.09]		✓

\* Numerical simulations by Beaumont et al. (2000) show that increased retro-crust strength reduces retro-thrusting.  
<sup>†</sup> Upper plate is two times thicker than the lower plate.  
<sup>§</sup> Experiment 9.04 is similar to experiment 9.05 but lacks the basal glass bead-layer and also frontal accretion within the retro-wedge. Results from Wang and Davis (1996) indicate a coincidence between a flat lying backstop covered with a plastic sheet ( $\mu_b = 0.43$ ) and frontal accretion within the retro-wedge. In contrast, a flat lying backstop covered with sandpaper ( $\mu_b > 0.65$ ) prohibited frontal accretion within the retro-wedge.  
<sup>‡</sup> Experiment by Jürgen Adam (1999). Setup mediates between 9.05 and 9.25. Frontal accretion within the retro-wedge emerged after 210 cm of convergence.

Table 5.3: Parameters, which either promote or retard frontal accretion within the retro-wedge.

that a higher differential stress is required to keep the steeper retro-shear zone active, whereas it is the opposite for the glass-bead layer. Within this respect, Boyer (1995) found that a higher  $\beta$ , which results from increased flexure, requires less internal shortening to attain a critical taper, and a larger percentage of tectonic shortening translates into frontal advance of a thrust belt. It is highlighted that the role of flexure in controlling the kinematics of bivergent orogens has not been addressed (Teresa Jordan pers. com., (2004)).

The above considerations as well as the ones from section (5.3.5) indicate that the initiation of the frontal accretion within the retro-wedge cannot be assigned to a unique parameter combination. For example, the absence of flexure retards frontal accretion within the retro-wedge, whereas prolonged convergence promotes it (Table 5.3). Similarly, increased flexure in combination with a higher basal friction of the upper plate base evokes frontal accretion within the retro-wedge, above the glass bead-layer (Experiment 9.02, Fig. 5.26), which is consistent with the observations of Wang and Davis (1996).

These results do further indicate that some parameters tend to promote, others tend to retard frontal accretion in the retro-wedge (Table 5.3).

Whether frontal accretion within the retro-wedge occurs, depends finally on the combination of the above mentioned and other parameters such as fluid flow, cementation processes, sedimentation or a polarity reversal of the convergence geometry. Thus, the observation “frontal accretion within the retro-wedge” can be imagined as a cloud in multi-dimensional parameter-space, where several combinations of parameters lead to the same result. This might indicate that a hierarchical order of parameters does not exist.

The only condition for frontal accretion within the retro-wedge to occur is that the strength of the initiation of a thrust within the upper plate is lower than the re-activation of the retro shear-zone, provided that a sufficient stress transfer into the upper plate takes place. How to achieve this condition is a question of parameter combination.

### 5.3.7 Self-similar growth

The CCW concept predicts that only critically tapered wedges grow in width and height proportional to the convergence ( $t$ ) by  $t^{0.5}$  (Dahlen, 1990). However, none of the bivergent sandwedges showed such a self-similar growth. Only the lateral growth of two pro-wedges (Experiments 9.15, 9.20) was proportional to the conver-

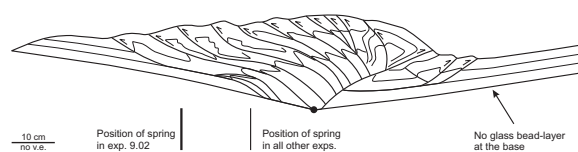


Figure 5.26: Experiment 9.02 has the same mechanic stratigraphy as experiment 9.05, but has a 50% higher deflection of the lower plate. The latter results from a longer distance between the free end of the lower plate and the spring (44 cm), compared to 30 cm in all other experiments. Note, that the internal glass-bead layer within the upper plate acts as a detachment, which was not observed in the other experiments.

gence ( $t$ ) by  $t^{0.5}$  (Table 5.1). This would indicate that all studied bivergent sand-wedges grew not self-similar but self-affine, which agrees with observations from Koyi (1995).

Given that a self-similar growth results from the critical state only, we suggest that the bivergent sand-wedges within this study are not critical. Interestingly, a self-similar growth of sand-wedges has, to our knowledge never been reported from any sandbox simulations, nor from natural orogens. Further support for the postulation that the bivergent sand-wedges are not critical, is derived from critical taper considerations. Given that a basal shear-zone is active throughout the experiment, its mechanical properties are thought to be best described by the stable-dynamic friction. Additionally, we follow Lohrmann et al. (2003) and suggest that the internal mechanic properties of the pro-wedge are as well best described by stable-dynamic friction.

Based on these assumptions we find that the pro-wedge of experiment 9.15 is in the stable field throughout its evolution (Fig. 5.27), which agrees very well with the above observations. Other assumptions with respect to the material properties would lead to the postulation that the pro-wedge is over-critical and should fail by extension, which was not observed. These calculations were only made for experiment 9.15, since the knowledge about the internal material properties of a pro-wedge, which contains one or two glass-bead layers, is not adequate. The above observations how-

ever, could also indicate that the CCW concept, which assumes an ideal Mohr-Coulomb material is not sufficiently appropriate to describe the mechanics of a sand-wedge, which clearly shows strain hardening and strain softening processes.

## 5.4 Implications and predictions for natural bivergent wedges

In this study we have investigated the influence of the imposed kinematic boundary conditions such as different mechanic stratigraphies or the degree of flexure on the kinematic evolution of bivergent sand-wedges. Given the scale invariance of brittle behaviour, we propose that the obtained results are applicable to (i) bivergent orogens, e. g., the European Alps, the Pyrenees; to (ii) fold and thrust belts, e. g., the Western Altiplano Thrust Belt (Elger et al., 2005) and to (iii) accretionary prisms, e. g., the Sunda Arc (Silver and Reed, 1988), and the Mediterranean Ridge (Le Pichon et al., 2002). Accordingly, the implications derived from the experiments bear no specific spatial scale and may be tested upon their validity in all three settings. However, some caution must be taken while transferring and applying our results to bivergent orogens, since we focus only on lower temperature orogens, where brittle behaviour prevails. High exhumation rates may finally lead to the removal of the highest strength part of the continental crust, which significantly reduces its integral strength. At this stage ductile processes might start to dominate (Zeitler et al., 2001; Koons et al., 2002).

*Four staged evolution of bivergent wedges.* Based on the assumption that one continental plate descends beneath the other during orthogonal continent-continent collision, we suggest a four-staged evolutionary model for the growth of bivergent orogens. An initial symmetric, crustal scaled pop-up (stage I) or backfold is followed by the formation of a proto pro-wedge, where frontal ac-

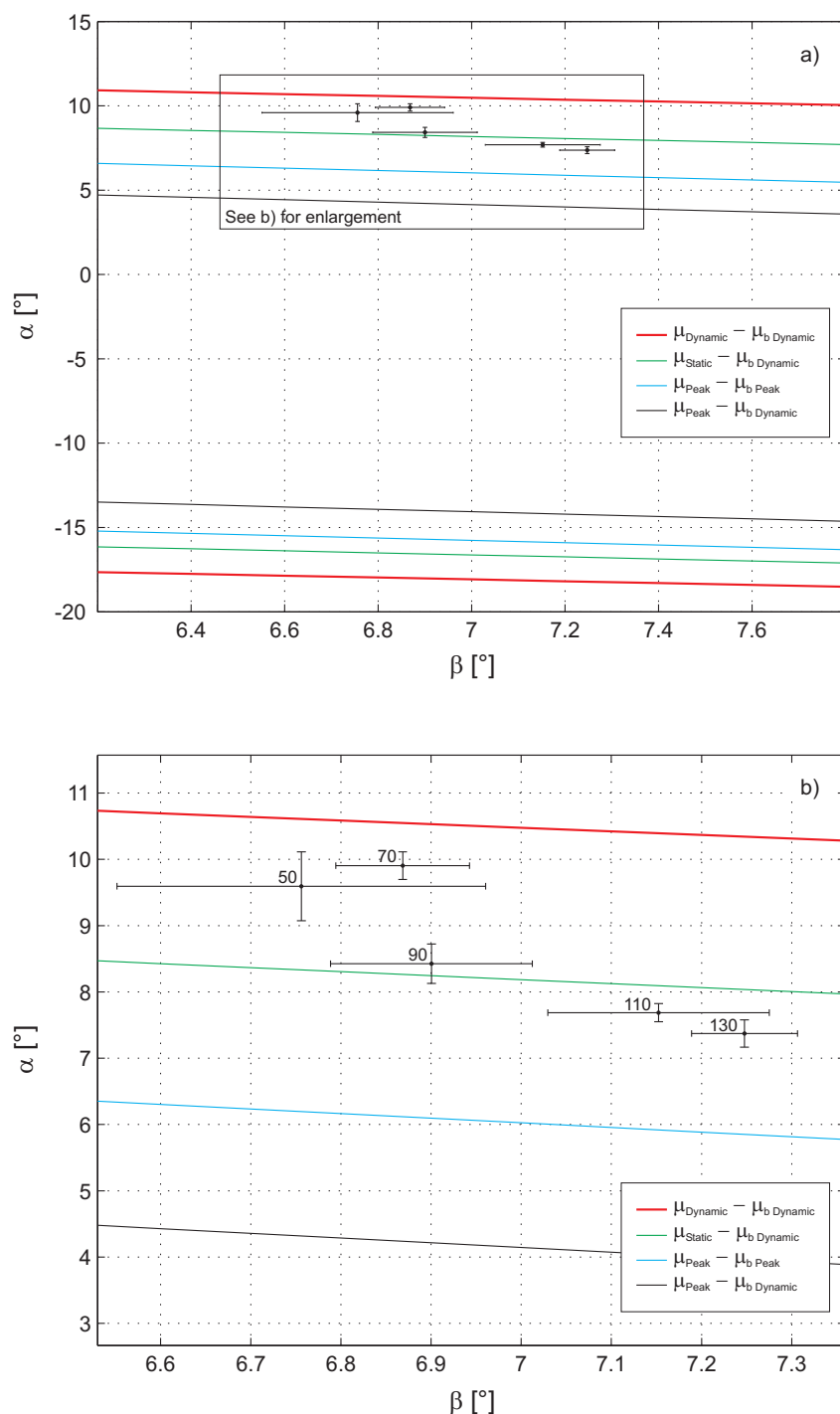


Figure 5.27: (a) Theoretical stability fields, using equation (3.10), for four combinations of frictional properties of the wedge interior and its base. Data are taken from ring-shear measurements.  $\mu$  denotes the coefficient of internal and  $\mu_b$  denotes the coefficient of basal friction respectively. (b) Enlargement of (a). Numbers associated with data points are *cm* of convergence (Experiment 9.15). If one assumes that  $\mu$  and  $\mu_b$  are best described by the dynamic stable friction, than the entire pro-wedge of experiment 9.15 is within the stable field throughout its evolution.

cretion dominates (stage II). Further convergence leads to an increase of the kinematic and topographic asymmetry. Basal accretion commences, if a mid-crustal detachment is present (stage III). During stage IV, frontal accretion within the retro-wedge occurs, which may drive the orogen back to more symmetric conditions. This model can be tested against balanced orogen-scale cross-sections and we suggest that the transition from stage II to stage III, i. e., onset of basal accretion as well as the transition from stage III to stage IV, i. e., onset of frontal accretion within the retro-wedge, should be identifiable. The latter is explained in terms of the strength contrast between the upper plate and the retro-shear zone. Thus, neither a reversal of the convergence geometry nor specific backstop geometries are necessary for frontal accretion within the retro-wedge to occur.

*Self-similar growth.* A self-similar growth was neither observed in this study, nor has been reported from any sandbox experiment. This agrees with Lohrmann et al. (2003), who proposed that only the frontal part of a sand-wedge is in a critical state. Additionally, based on balanced cross-sections from the South Pyrenean fold and thrust belt, Meigs and Burbank (1997) showed that the spatio-temporal distribution of deformation, as well as the magnitude of  $\alpha$  and  $\beta$  through time are decoupled and not simply related. Thus, the assumption that an entire orogen is in a critical mechanic state should be made with great care if at all. We therefore propose that orogen-scaled mass-budget calculations, which focus on erosion and assume a self-similar growth, should be limited to the most frontal part of an orogenic wedge.

*Accretion cycle.* The proposed conceptual model of an accretion cycle integrates previously unrelated observations such as the periodicity of thrusting, the associated topographic evolution, and the cumulative slip evolution of thrusts. In addition this model predicts:

The occurrence of a thrust initiation, an underthrusting and a re-activation phase. Thereby, the latter phase is coeval with the thrust initiation phase of the following accretion cycle. Depending on the kinematic boundary conditions, the re-activation phase maybe temporally offset from the underthrusting phase.

We found that the magnitude of strain accumulated at any given structure within a bivergent wedge systematically varies with the accretion cycle. The accretion cycle is therefore considered as an internal clock of wedge-scaled deformation and resulting surface uplift. Such a mechanism could explain the irregular earthquake cycle along the Aksu thrust, Tien-Shan (Hubert-Ferrari et al., 2005) and the irregular initiation and re-activation of thrusts within the southern Pyrenees (Meigs, 1997). It follows that geodetic, paleoseismologic, and geologic estimates of fault slip must not necessarily be the same, as found, e. g., in the Tien-Shan (Coutand et al., 2002). Thus, interpolation of slip rates from different temporal scales and resultant predictions of recurrence intervals of earthquakes can only be successful, if the phase within the accretion cycle is known. Accordingly, the ability to differentiate between individual events (earthquakes) or phases within an accretion cycle will guide our perception on how deformation is distributed in space and time. We therefore suggest that an accretion cycle should be sampled with  $\frac{1}{4}$  of its duration, to resolve its three-partite evolution (Fig. 5.28). Also, each structure might have its own b-value (seismicity), which changes through time, as accretion proceeds. Since a thrust is not necessarily in the same phase within the accretion cycle along its strike, differences in seismicity may result. We therefore propose that such along strike changes should be taken into account, if seismic hazard potential is evaluated. It follows that changes of kinematic boundary conditions or of the climate/erosion scheme do not need to be invoked to explain the spatio-temporal variability of strain accumulation.

Observed strain histories of thrusts do not resemble box-functions. The former however, would overestimate strain accumulation during the thrust initiation and during the re-activation phase, but underestimate strain accumulation during the underthrusting phase. Thus, the temporal dependence of strain-partitioning on the phase within the accretion cycle should be taken into account, while restoring deformed sections and simulating hydrocarbon maturity in fold and thrust belts, which commonly assume that only one structure is active for a certain time (Rouré et al., 2004).

Based on the cumulative strain histories of thrusts either within sand-wedges or within fold and thrust belts (sections 5.1, 5.2), we further hypothesise that strain accumulation follows a diffusion law (Fig. 5.23). Such a behaviour would be very similar to the one predicted for erosion (Burbank and Beck, 1991).

Spatial and temporal offset of cause and response. We observed a temporal offset between the initiation of a new thrust within the pro-layer (cause) and the resulting “strain-pulse” at the retro-shear zone (response). This could be one explanation for the temporal offset of  $\sim 5\text{ Ma}$  between the emplacement of the Helvetic nappes above the Aar massif and enhanced rates of back-thrusting along the Insubric Line (Schlunegger and Willett, 1999). However, the magnitude of strain transfer between the pro- and the retro-wedge decreases while the former grows laterally. Thus, during later stages of orogenic evolution this strain transfer might not be detectable.

Fluid flow. Depending on their permeability and porosity evolution, thrust faults may either provide important fluid conduits or act as barriers (Travé et al., 2000; Badertscher et al., 2002). While the former can promote the formation of precious ore deposits, such as the mesothermal gold mineralisations in the Southern Alps of New Zealand (Craw et al., 2002; Upton et al., 2003; Craw and Campbell, 2004), the latter can lead to compartmentalisation of a fold and thrust belt,

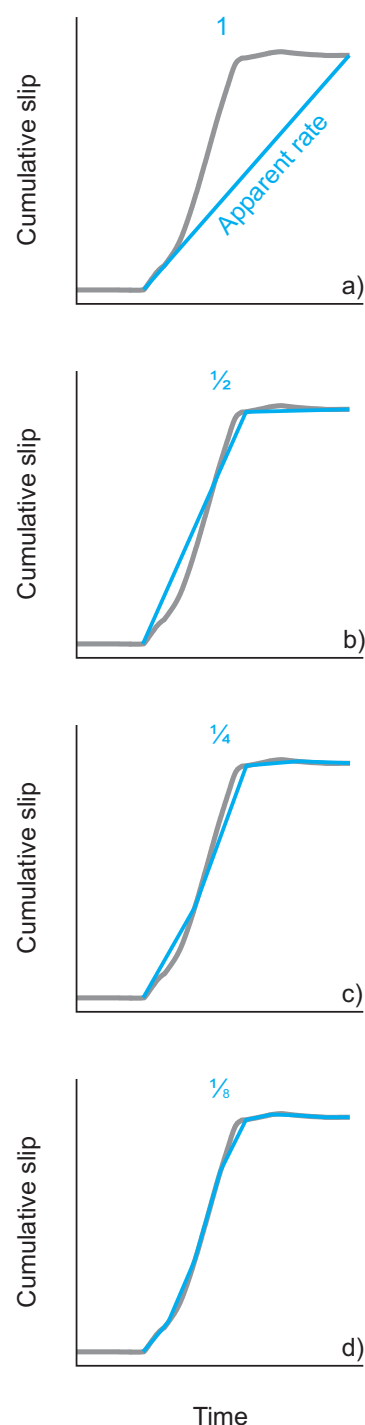


Figure 5.28: Sampling interval controls estimates of cumulative slip. Original data in grey; (a) Resulting rate, if only pre- and post-tectonic strata are dated; (b-d) Increasing resolution approaches “real data”, given that age constrains are equally distributed in time.

which may aid the accumulation of hydrocarbons (Moretti et al., 2000). In addition, and probably most importantly, we documented that the phase within the accretion cycle determines the degree of connectivity between thrusts and their maximum incremental  $e_{xy}$ . We therefore speculate that the source and the availability of fluids may vary with the accretion cycle as well. Observations from the El Guix anticline in the Southern Pyrenean foreland basin (Travé et al., 2000) would support such a prediction (section 5.3.2). Within this context, it is interesting to note that Muir-Wood (1994) linked the secondary migration of hydrocarbons with seismic pumping (Sibson, 1994). Thus, the former may be enhanced during phases of accelerated seismicity, i. e., the underthrusting phase. It follows that the accretion cycle concept may help to constrain hydrocarbon exploration strategies.

*Topographic evolution.* The distribution of surface uplift within orogens should indicate at least two domains, one that comprises the pro-wedge and one that includes the axial-zone and the retro-wedge. Topography in the former is highly segmented and reflects individual accretion cycles. On the contrary, continuous vertical stacking and retro-ward translation of basally accreted duplexes results in a smooth and dome-like shape of the second topographic domain. Thus, care should be taken, while interpreting surface uplift rates from different parts of an orogen. We additionally highlight that basal accretion episodes have not led to a detectable trace within the ISU and we speculate that this might be similar in nature. However, basal accretion leads to the bending of the upper surface, resulting in extension. The respective faults and syntectonic sediments might finally provide indirect insight into the timing and magnitude of basal accretion. Thereby, other processes, e. g., late orogenic collapse have to be ruled out.

Each accretion cycle is associated with a surface uplift wave, which decreases in magnitude with increasing distance from the deformation front.

Nevertheless, the increase in ISU observed in the second topographic domain, may reach up to 400% and takes place between a thrust initiation phase and the late stages of the respective underthrusting phase. Such an increase in ISU should be therefore detectable in natural systems.

A surface uplift wave would also successively rejuvenate the relief of more internal parts of an orogen. We therefore propose that a detailed provenance analysis might detect the successive unroofing and erosion of a certain suite of hinterland lithologies and may thus trace a surface uplift wave. Results from a field study within the Catalan Coastal Range (Jones et al., 2004) indicate that the detection of such a surface uplift wave is possible. In addition, a certain lag time between relief rejuvenation and the appearance of the respective clasts within the foreland is expected and has been also proposed by Tucker and Slingerland (1996). These authors invoked this mechanism to explain the apparent delay between uplift of the Tibetan Plateau ( $\sim 14 + Ma$ ) and the onset of rapid sedimentation in the northern Indian Ocean ( $\sim 12 Ma$ ).

ISU above a ramp segment of a forethrust does not increase linearly with time and a thrust re-activation can lead to a tenfold increase of the respective ISU. Therefore, changes of the kinematic boundary conditions or of the climate/erosion scheme do not need to be invoked to explain such variability. A similar non-linear growth has been reported from a late Quaternary anticline in New Zealand (Jackson et al., 2002) and from numerical simulations (Bernal et al., 2004). Additionally, Masferro et al. (2002) concluded that the Neogene-Quaternary growth of the Santaren anticline (Cuban fold and thrust belt) was characterized by several tectonic uplift pulses of different duration and intensity, interrupted by periods of variable duration in which no fold growth occurred. We therefore suggest that a self-similar growth assumption for thrust induced topography should be treated with care.

*Heisenberg's principle of uncertainty?* Experiments show that the mechanical properties of the detachment control the variability of the spacing of thrusts, whereas the number of degrees of freedom such as flexure, weak zones and erosion determine the relative magnitude of internal deformation versus propagation of deformation and thus the timing of thrust initiation and its variability. We therefore envisage an end-member scenario, where the spacing is constant but not the timing and vice versa. In the former, one would know the location of thrust initiation but not its timing, in the latter one would know the timing of thrust initiation but not its location. It follows, that a spatial regularity is not necessarily associated with a temporal regularity. One should be therefore very careful, while deriving one information from the other. A similar model has been put forward for earthquakes, i. e., time-predictable versus slip-predictable. Although these processes are entirely deterministic as opposed to quantum mechanics, the uncertainty associated with the prediction of the timing and location of the next slip event results from the incomplete knowledge of the mechanic state of each grain or fault.

We found that an observation like frontal accretion within the retro-wedge can be explained with several parameter-combinations and a parameter-hierarchy may not exist. This raises the challenge to decide whether two observations are coincidentally or if a causal relation exists between them.

## 5.5 Implications for erosion experiments

The results derived from the first experimental series are now used to constrain the kinematic boundary conditions of the second experimental series, which is aimed at investigating the influence of the location of erosion with respect to the convergence geometry and the mode of erosion (distributed or focused) on the kinematics of bivergent sand-wedges. Two arguments can be

raised in favour of incorporating flexure. First, as shown in chapter (3), flexure is besides deformation and surface processes one of the major controlling processes of mountain building. Second, natural orogens show a distinct ratio of 2 to 3 between the length of the pro- and the length of the retro-wedge (Silver and Reed, 1988; Vietor and Oncken, 2005). Sandbox models of bivergent wedges without flexure reveal ratios that are lower than two (Malavieille (1984) and our own experiment 9.25). Those experiments with flexure show ratios between 2.5 and 3 (Table 5.1) and are thus similar to the ones observed in nature. The contemporaneous occurrence of frontal and basal accretion is a common observation in natural bivergent wedges, e. g., Pyrenees, European Alps (Beaumont et al., 2000; Pfiffner et al., 2000). Thus, experiment 9.05 is used as a reference for all "erosion" experiments (chapter 6).

## 6 The influence of erosion on bivergent wedge evolution

The following chapter intends to elucidate the influence of the location of erosion with respect to the convergence geometry and the mode of erosion, i. e., distributed or focused on the kinematic evolution of bivergent sand-wedges. Thereby, special emphasis is devoted to finite strain accumulation, the topographic evolution and to the geometry of particle paths. A summary of experiment 9.05, which is used as reference, is provided first, followed by a description of four experiments which differ only with respect to the mode and location of erosion (Fig. 6.1).

### 6.1 Reference experiment without erosion

The following section summarises the results obtained from experiment 9.05 and the reader is referred to section (5.2), where a detailed account on this experiment is provided.

Visual inspection of experiment 9.05 reveals, as previously noted, a four staged evolution. During stage I initial layer parallel shortening leads to the formation of two conjugate shear zones, which nucleated at the singularity. They define a symmetric pop-up (Fig. 6.2a). Further convergence leads to a rapid uplift associated with progressive back tilting of the pop-up towards the upper plate. In stage II, three narrowly spaced thrust faults are formed within the pro-layer (Fig. 6.2b, c) and result in an increasing asymmetry of wedge topography and kinematics. At this stage rates of thrusting along the retro shear-zone and uplift rates of the axial-zone and the retro-wedge are high but start to decrease (Fig. 6.3a). Stage III commences after

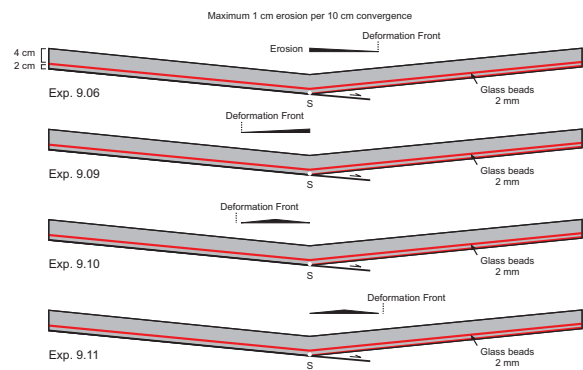


Figure 6.1: Kinematic boundary conditions and erosion modes of 2<sup>nd</sup> experimental series. Distributed erosion of: (a) Retro-wedge, (b) Pro-wedge; Focused erosion of: (c) Pro-wedge, (d) Retro-wedge.

40 cm of convergence (Fig. 6.2d, e). The initial pro-wedge provides now sufficient load to activate the internal glass bead-layer, which facilitates the coeval formation of thrust imbricates above and duplexes below it. Lateral growth of the pro-wedge is now attained by cyclic formation of flat-topped box anticlines at its toe. Coeval to frontal accretion, the sand layer beneath the glass bead-layer is detached from the one above and is as well transferred towards the axial-zone. Beneath the base of the pro-wedge, duplexes are formed, stacked, and finally uplifted in the hangingwall of the retro shear-zone. Thus, compared to the pro-wedge, which grows by discrete steps, the axial-zone and the retro-wedge are continuously fed with pro-wedge derived material. Thereby, the axial-zone and the retro-wedge grow in width and height. These two modes of addition of new material to the respective sub-wedges further amplify the existing topographic and kinematic asymmetry of the bivergent sand-wedge.

While the rates of the lateral growth of the pro-wedge increase during stage III, a further decrease of the rates of thrusting along the retro shear-zone and the uplift rates of both the axial-zone and the retro-wedge is observed (Fig. 6.3a). After  $\sim 90$  cm of convergence, frontal accretion within the retro-wedge emerges and marks thus the onset



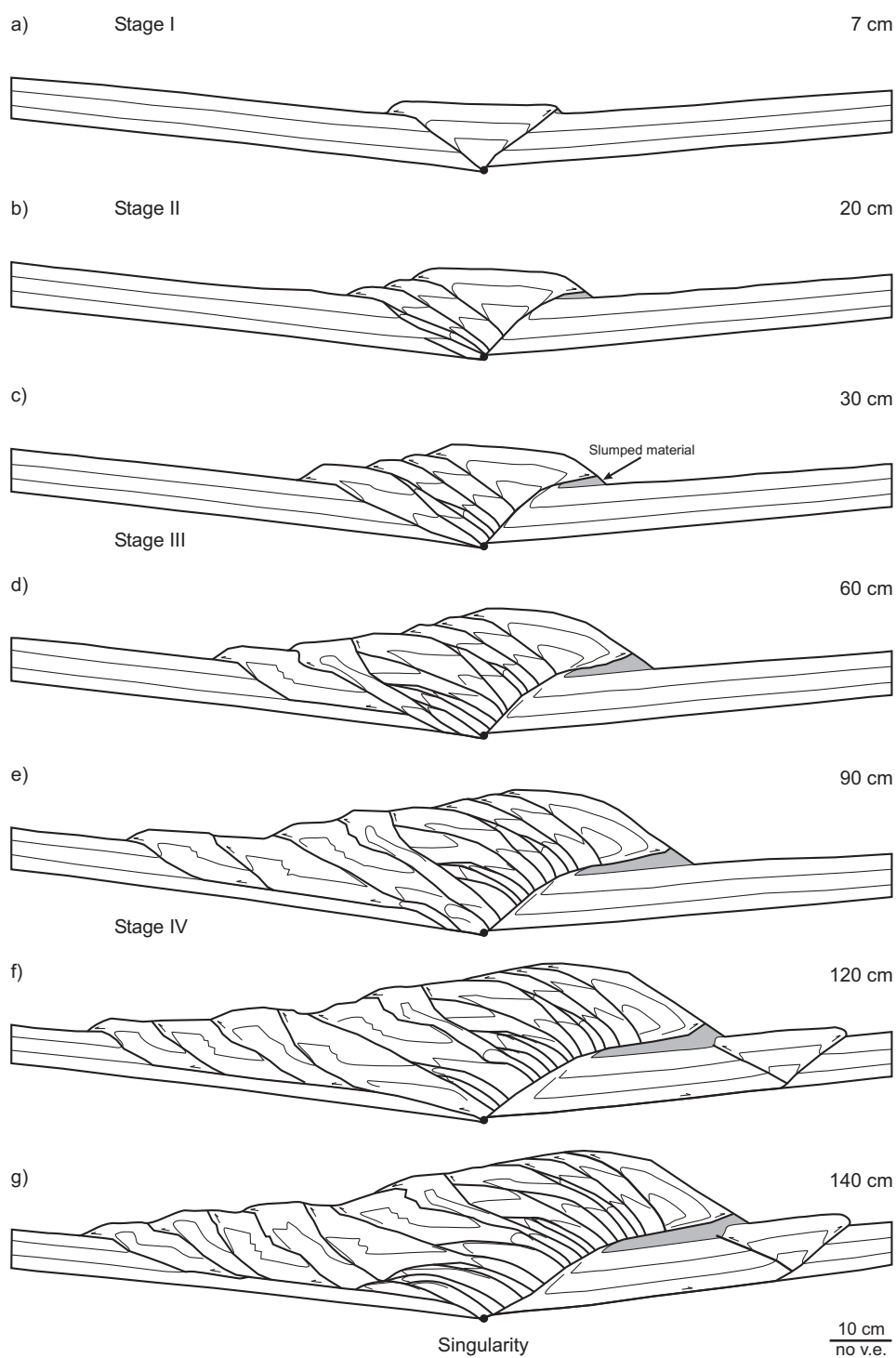


Figure 6.2: Line drawings of sequential stages of experiment (9.05), used as reference for the experiments involving erosion. Numbers on the right are *cm* of convergence. A footwall shortcut can be observed in (c) before deformation propagates far into the undeformed pro-layer and stage (III) begins, i. e., after 40 *cm* of convergence. Frontal accretion within the upper plate emerges after  $\sim 90$  *cm* of convergence, i. e., stage IV commences.

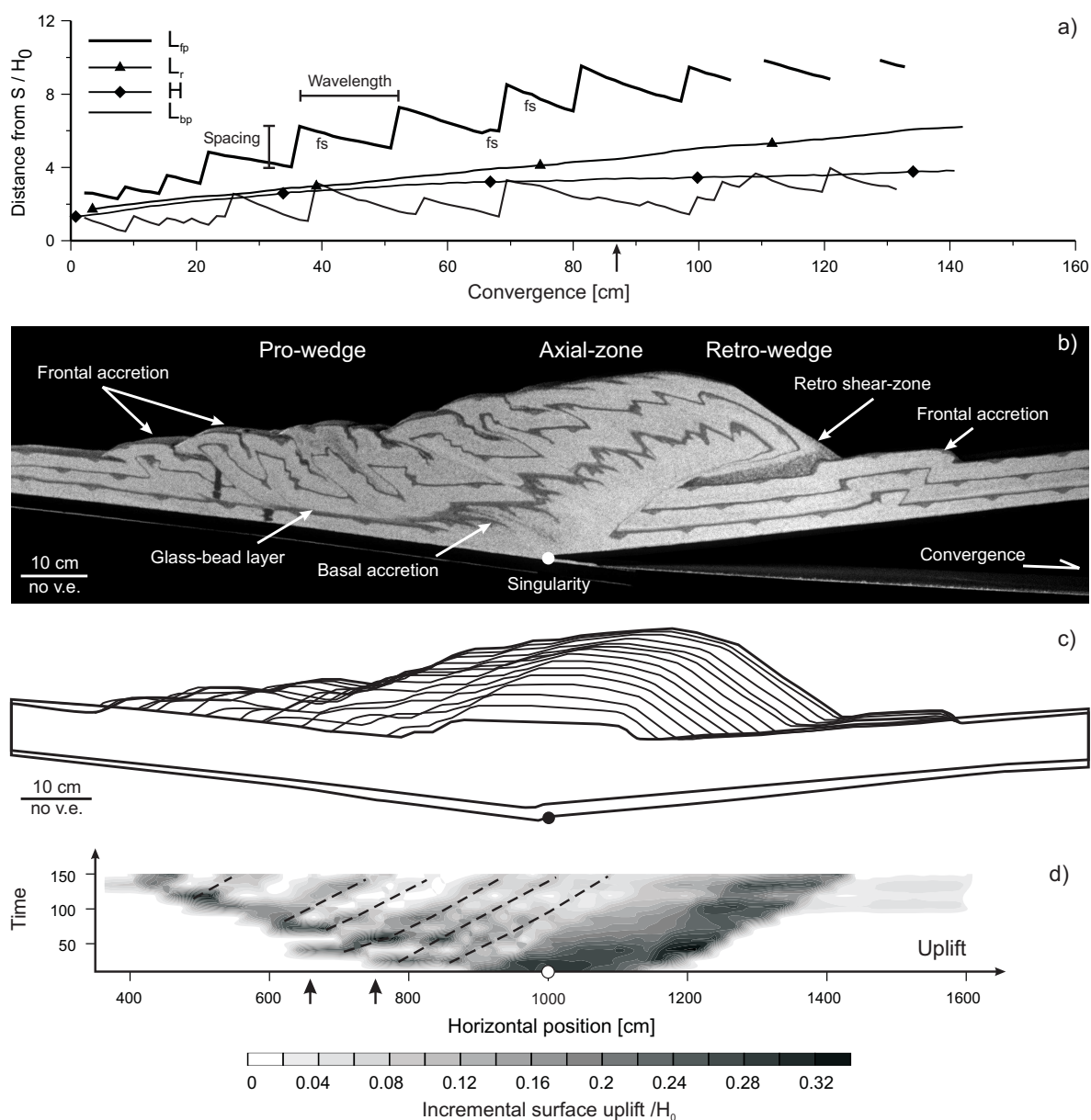


Figure 6.3: Synopsis of reference experiment. (a) Evolution of geometric parameters as defined in figure (4.11), taken from the digital images at every 1.5 cm of convergence. Arrow indicates onset of upper plate accretion. fs shows footwall shortcuts. (b) Photograph after 140 cm of convergence. (c) Topographic evolution. Outlines were taken at every 10 cm. of convergence. The first, i.e., after 10 cm and the last, i.e., after 150 cm of convergence outline are given in complete form, to indicate the magnitude of flexure. Two growth modes can be distinguished: cyclic accretion within the pro-wedge results in distinct steps in topography, whereas continuous addition of pro-wedge derived material to the axial-zone and the retro-wedge leads to near concentric growth pattern. (d) ISU with high spatial and temporal variability. Arrows indicate positions, where ISU changes by 10 during the evolution of the bivergent sand-wedge. Dashed lines trace activity of ramp segments. (e) From PIV extracted particle paths after 140 cm of convergence.

of stage IV. Continued convergence and resulting deformation is now taken up by two frontal and one basal accretion system (Fig. 6.2f, g, Fig. 6.3b). This results in a slowdown of the rate with which the pro-wedge grows laterally (Fig. 6.3a). Key characteristics of the topography and its evolution include: (i) the existence of two uplift domains (Fig. 6.3c); (ii) the uplift trace of the different phases of thrust activity, i. e. the life-cycle of a thrust; (iii) the correlation between maximum ISU within the pro-wedge and significantly lowered ISU within the axial-zone and the retro-wedge for a given time-slice and (iv) the surface uplift waves associated with the accretion cycles (Fig. 6.3d). Also, the onset of frontal accretion within the retro-wedge results in a significant reduction of ISU within the pro-wedge.

## 6.2 Experiments with erosion

A summary of the similarities between the reference experiment and the experiments involving erosion is provided first, followed by an analysis of the differences between these experiments.

One of the key observations which emerged from the analysis of the PIV images is that despite the differences in the location and the mode of erosion, all sand-wedges evolved into a bivergent state with a pro-wedge, an axial-zone and a retro-wedge (Fig. 6.4). All four bivergent sand-wedges subjected to erosion showed at least the first three phases out of the four stage evolutionary model proposed in section (5.1). Finally, all experiments showed a simultaneous occurrence of frontal and basal accretion and no activation of the internal upper plate glass-bead layer.

*Particle paths.* For each experiment two triangular markers were traced, which started at approximately the same position. One marker was located above and one below the internal glass-bead layer, as a representation for frontal and basal accretion,

respectively. The spatial distribution of both markers after 140 cm of convergence indicates:

- i. Different magnitudes of displacement between both accretion modes must have occurred, since the distance between both markers varies between experiments (Fig. 6.4a, e). They are closest in the distributed pro-wedge erosion and farthest in the reference experiment (Fig. 6.4a, c).
- ii. The markers for frontal accretion reached a similar position in the reference as well as in the retro-wedge erosion experiments (Fig. 6.4a, b, e). However, the markers for basal accretion show a larger displacement, but are located in the same region as the respective marker in the reference experiment (Fig. 6.4a, b, e).
- iii. During pro-wedge erosion the markers being representative for frontal accretion indicate a higher displacement and a change in the direction of the particle flow. The markers for basal accretion attained a similar position as observed in the reference experiment (Fig. 6.4a, c, d).

Additionally, up to 120 particles were traced for each experiment (Fig. 6.5). The respective particle path geometries show a flat-ramp-flat geometry and no distinction can be made between frontally and basally accreted particles. Only those particles, derived from the upper or the lower plate can be distinguished. In pro-wedge erosion experiments, particle paths within the axial-zone are slightly steeper than in the retro-wedge erosion or within the reference experiment (Fig. 6.5). This agrees with the previous observation, that pro-wedge erosion redirects particle-flow.

Visual inspection of the photographs (Fig. 6.4) indicates that the internal glass-bead layer was exposed at the surface of the pro-wedge during focused pro-wedge erosion, which did not occur in

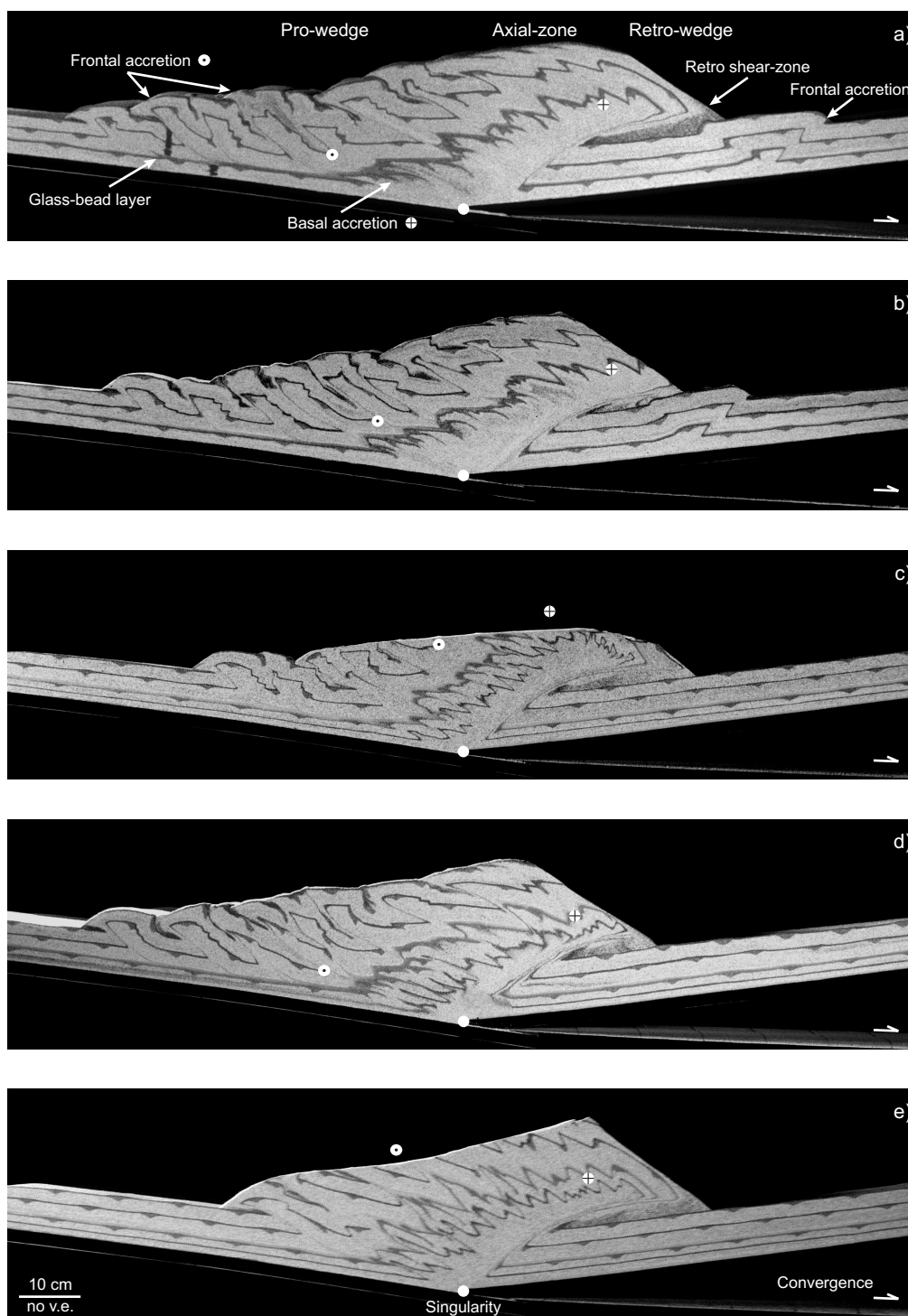


Figure 6.4: Photographic images of each experiment after 140 cm of convergence. (a) Reference experiment; Distributed erosion of: (b) Retro-wedge, (c) Pro-wedge; Focused erosion of: (d) Retro-wedge, (e) Pro-wedge. The main structural elements are highlighted. Two markers, one being indicative for the frontal accretion (black dot), the other being indicative for the basal accretion (black cross) are given to show different amount of exhumation.

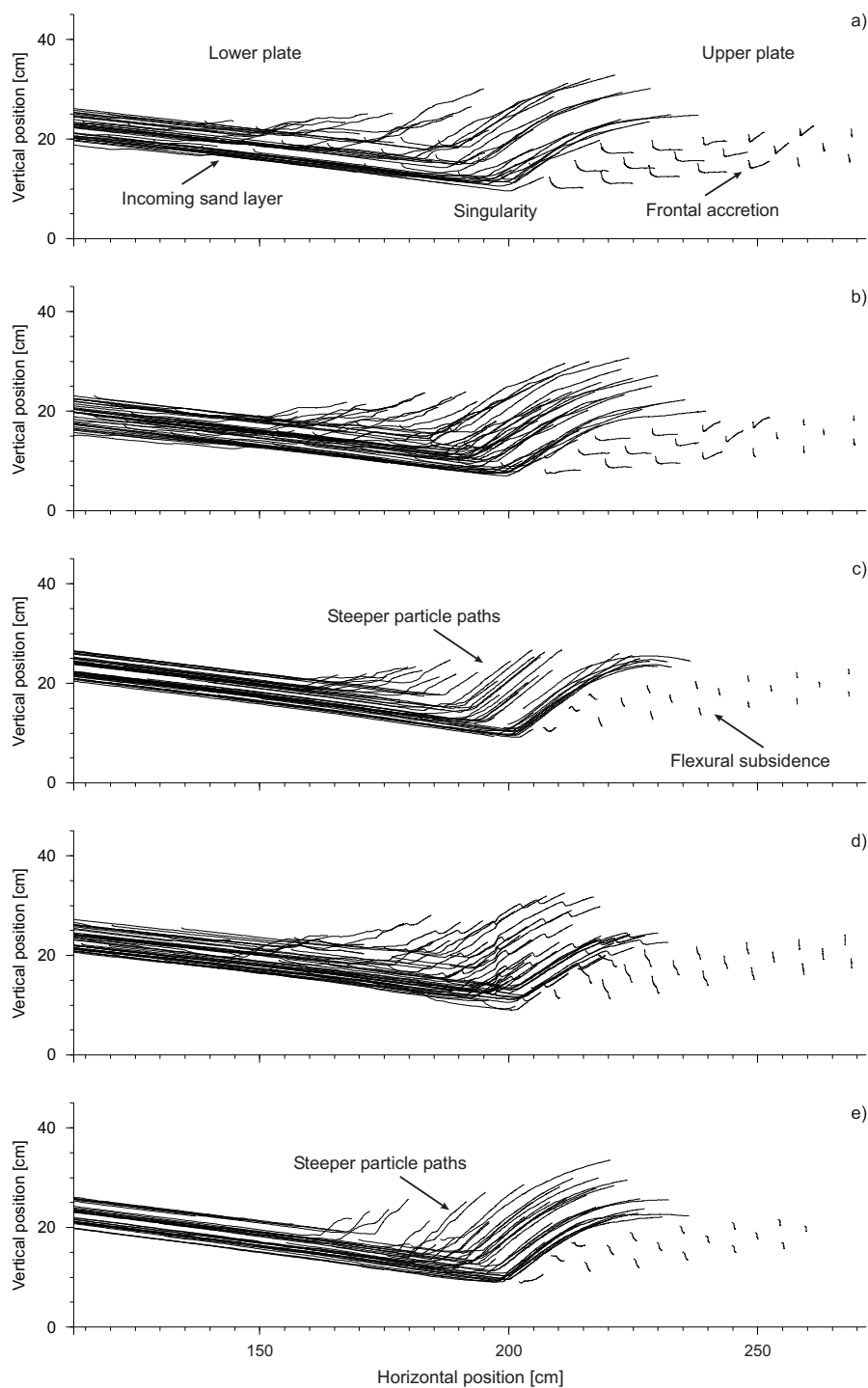


Figure 6.5: Particle paths calculated for  $\sim 120$  particles for each experiment. (a) Reference experiment; Distributed erosion of: (b) Retro-wedge, (c) Pro-wedge; Focused erosion of: (d) Retro-wedge, (e) Pro-wedge. All particle paths show a flat-ramp-flat geometry. There is no difference in particle path geometry between frontally and basally accreted particles. Particle paths within the axial-zone are slightly steeper in pro-wedge erosion experiments (c, e), which indicates that pro-wedge erosion tends to redirect the tectonic mass flux.

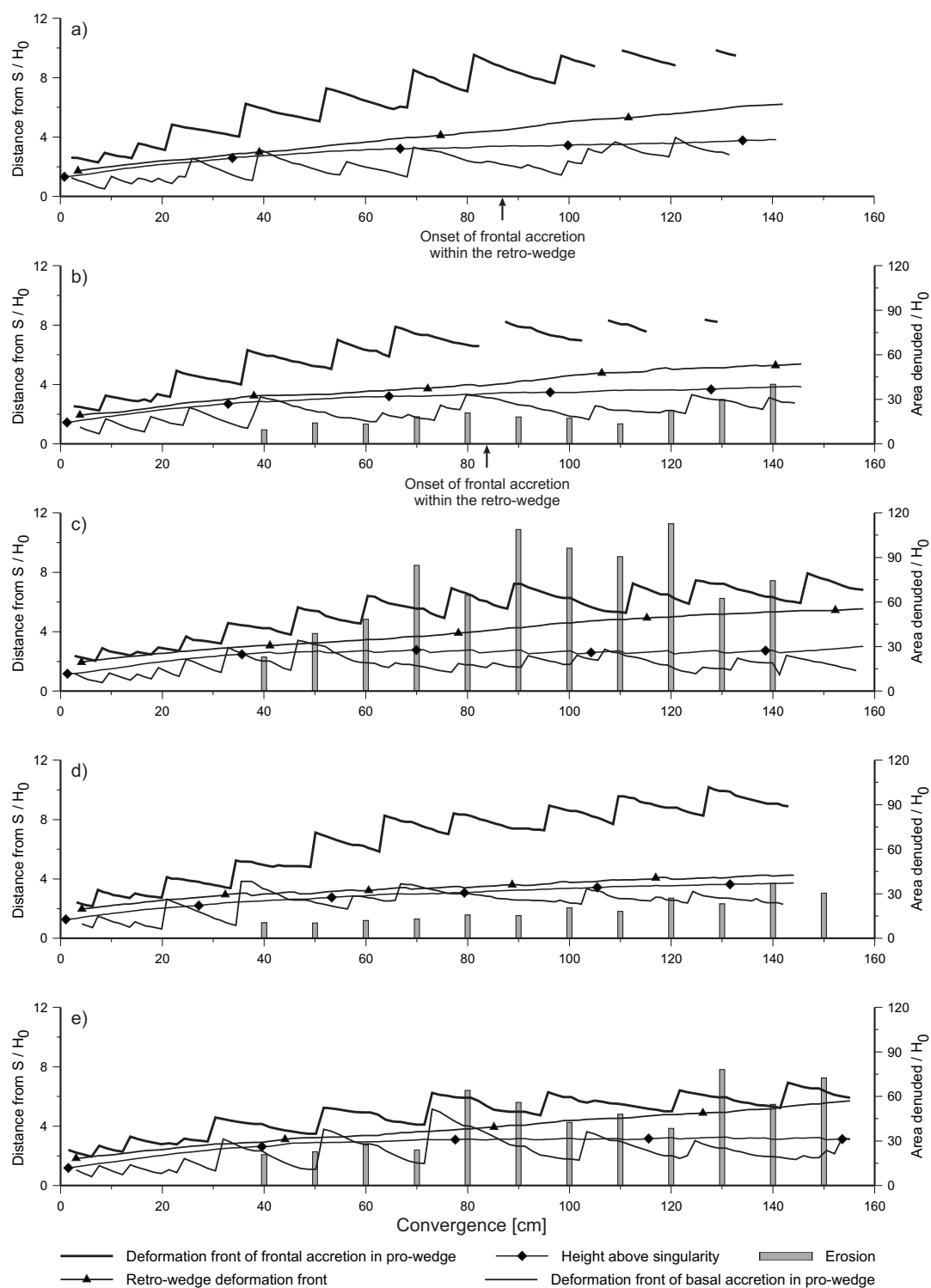


Figure 6.6: Evolution of geometric parameters derived from the PIV images at every 1.5 cm of convergence. The amount of eroded material at every 10 cm of convergence is given as well. (a) Reference experiment; Distributed erosion of: (b) Retro-wedge, (c) Pro-wedge; Focused erosion of: (d) Retro-wedge, (e) Pro-wedge.

any of the other experiments. Distributed pro-wedge erosion however removed nearly the entire upper sand-unit and thus lead to a dominance of stacked duplexes within the pro-wedge. Only four out of eight thrusts are completely preserved at the final stage of this experiment (Fig. 5.11a, e). This agrees well with the observation that distributed pro-wedge erosion leads to the maximum amount of mass denuded in any of the four erosion experiments (Fig. 6.6, Table 6.1). Also, a mass flux steady state (tectonic advection equals erosion) is reached at two convergence intervals only during this experiment (Fig. 6.6). This is consistent with the observation that the experiment with distributed pro-wedge erosion shows the least flexural deflection (Fig. 6.4). The more general observation derived from figure (6.6), is that the amount of incrementally denuded material increases through time as a consequence of the increase in length of either the pro- or the retro-wedge. It has to be emphasised that the simulated erosion modes assume an ideal-shaped bivergent wedge with a smooth topographic gradient. This however is perturbed by frontal and basal accretion. Thus, the amount of material taken away at any increment of convergence depends on the state within the accretion cycle, i. e., during thrust initiation phases, topography is build up far away from the pro-wedge toe, which results in an overestimation of the material to be denuded. In contrast, during underthrusting phases the envelope of the pro-wedge is much smoother and adjustment of the simulated erosion law to this envelope is more accurate.

*Frontal and basal accretion.* Similar to the reference experiment time series show that the propagation of frontal accretion is composed of individual accretion cycles (Fig. 6.6). The lateral growth of the pro-wedge as well as the height above the singularity is again best described by power laws. However, the respective power law coefficients are significantly lower than the theoretically predicted value (Table 6.1). Whereas the spacing of

frontal accretion, sensu Marshak and Wilkerson (1992), remains fairly constant, the wavelength varies within and between experiments and is thus more sensitive to the parameters tested. The sample standard deviation ( $s_{fw}$ ) is highest for the experiment with distributed and lowest for the experiment with focused pro-wedge erosion (Table 6.1).

Basal accretion is, in contrast to the very regular propagation of frontal accretion, more irregular in terms of its wavelength and its spacing (Fig. 6.6). The variability expressed in the sample standard deviation of the wavelength ( $s_{bw}$ ) was calculated for all experiments. It emerges that  $s_{bw}$  always exceeds  $s_{fw}$ . Also, the range of the latter (0.3) is nearly half the value of the former (0.72) and suggests that basal accretion is more sensitive to the parameters tested (Table 6.1). Convergence intervals, during which both accretion modes are either in or out of phase, are always too short to be correlated over longer distances. There is however, a prominent exception. In the experiment with focused pro-wedge erosion both accretion modes are in phase throughout the entire experiment, which suggests that basal and frontal accretion are not decoupled in time (Fig. 6.6). The respective wavelength of basal accretion remains fairly constant, which is evidenced by the lowest  $s_{bw}$ -value among all experiments.

After the first erosion increment, basal accretion propagated towards the foreland in pro-wedge erosion experiments, whereas it stepped back in retro-wedge erosion experiments (Fig. 6.6). The further evolution of basal accretion shows that retro-wedge erosion tends to reduce shorter wavelength activity as compared to the reference or the distributed pro-wedge erosion experiment. During the latter experiment, basal accretion remained nearly stationary with respect to the singularity. It is further pointed out that the height above the singularity can be considered as an envelope for basal accretion (Fig. 6.6). In addition, figure (6.6) reveals that the rate of lateral growth of the pro-wedge during stage III and stage IV is higher for the ref-

Experiment	9.05	9.09	9.10	9.06	9.11
		Pro-wedge Distributed	Focused	Retro-wedge Distributed	Focused
Location of erosion					
Mode of erosion					
Observations					
Flexure	✓	✓	✓	✓	✓
Number of weak layers	1	1	1	1	1
Frontal accretion in retro-wedge	✓	∅	∅	✓	∅
Number of thrusts in pro-wedge after 140 cm of convergence	8	8	6	8	8
Cumulative amount of erosion/ $H_0$	0	804	549	217	233
Sample standard deviation of wavelength of frontal accretion $s_{fw}$	0.15	0.45	0.18	0.29	0.24
Sample standard deviation of wavelength of basal accretion $s_{bw}$	0.47	0.48	0.39	0.78	1.11
Power law equation of lateral growth of pro-wedge $y_L =$	$1.06t^{0.44}$	$1.08t^{0.37}$	$1.34t^{0.30}$	$1.17t^{0.40}$	$0.90t^{0.47}$
Coefficient of determination $R_L^2 =$	0.89	0.87	0.83	0.89	0.90
Power law equation of height above singularity $y_H =$	$1.03t^{0.26}$	$1.10t^{0.19}$	$1.00t^{0.24}$	$1.12t^{0.24}$	$0.92t^{0.27}$
Coefficient of determination $R_H^2 =$	0.97	0.83	0.93	0.98	0.98
Out-of-sequence displacement (OOSD) index	3.73	4.16	0.97	3.42	3.16
Propagation of frontal accretion	0*	—	—	-	-
Propagation of basal accretion		-	0	-	-
Height above singularity		-	-	+	+
Exhumation of frontally accreted material		+	+	0	0
Exhumation of basally accreted material		0	0	+	+
Finite $e_{xy}$ at retro-shear zone		-	0	0	+
Finite $e_{xy}$ at mid-level detachment		-	-	-	+

\* Reference level derived from experiment without denudation. - less, + more than reference level.

Table 6.1: Summary of experimentally derived results - 2<sup>nd</sup> experimental series.

erence and both retro-wedge erosion experiments when compared to both pro-wedge erosion experiments. Lateral pro-wedge growth within the latter is nearly stationary. A summary of the relative magnitudes of the propagation of frontal and basal accretion is given in table (6.1).

*Topographic evolution.* Similar to the reference experiment, the topography of all erosion experiments consists of two domains, one that comprises the pro-wedge and grows by discrete steps and one that encompasses the axial-zone and the retro-wedge which grow more concentrically (Fig. 6.7). In both retro-wedge erosion experiments this equidistant concentric growth pattern as observed in the reference experiment is perturbed. Lines representing incremental stages of wedge evolution merge at an earlier stage, i. e., after the first erosion increment at 40 cm of convergence, than it is the case for the reference experiment, i. e., after 120 cm of convergence. Parts of the axial-zone and the retro-wedge, which were

not subject to the backstepping pro-wedge erosion, tend to retain their equidistant concentric growth in both pro-wedge erosion experiments. The respective pro-wedge slopes are stationary after  $\sim 60$  cm of convergence (Fig. 6.7).

Both topographic domains are mirrored, similar to the reference experiment, in the corresponding distribution of ISU (Fig. 6.8). The overall evolution of ISU in the retro-wedge erosion experiments and the reference experiment is similar. Thereby, maximum ISU is confined to either initiated or re-activated ramp segments and to the retro-wedge. A change of ISU by one order of magnitude due to thrust re-activation, as shown in section (5.1), can be recognised in both retro-wedge erosion experiments (Fig. 6.8). The experiment with distributed retro-wedge erosion shows a peak in incremental surface uplift at  $\sim 90$  cm of convergence (Fig. 6.8), which is higher than in the reference experiment. After frontal accretion within the retro-wedge has set in, a significant decrease of ISU within the pro-wedge is observed.



This has been as well observed in the reference experiment. A similar feature, with a lower magnitude and without frontal accretion within the retro-wedge is recognised in the focused retro-wedge erosion experiment. Finally, the surface uplift waves, associated with each accretion cycle were found in both retro-wedge erosion experiments.

Both pro-wedge erosion experiments differ significantly with respect to the spatio-temporal distribution of ISU, from the reference and both retro-wedge erosion experiments. In the distributed erosion scenario nearly the entire pro-wedge is heavily denuded, which corresponds to an equally sized area of low magnitude incremental surface uplift within the pro-wedge. Only minor magnitudinal variations are observed. This general pattern is also found in the focused pro-wedge erosion experiment. However, maximum incremental erosion and surface uplift is highest at the toe of the pro-wedge and decrease towards the axial-zone (Fig. 6.8).

*Out-of-sequence displacement.* Frontal accretion in all experiments shows a pure forward-breaking or piggy-back thrust sequence although the corresponding displacement along each individual thrust is accumulated at several stages during wedge evolution (Fig. 6.9). The resulting out-of-sequence displacement index (section 5.2) is highest for the distributed pro-wedge erosion experiment and lowest for the focused pro-wedge erosion experiment (Table 6.1). In addition, the cumulative thrust length curves are made up of three segments, which can be linked with the three phases of the accretion cycle (section 5.2).

*Strain accumulation.* Based on the displacement fields derived from PIV analysis, finite strain after 140 cm of convergence was calculated for each experiment (Fig. 6.10). The main structural elements such as the basal and the internal detachment, the retro shear-zone and each thrust imbrication

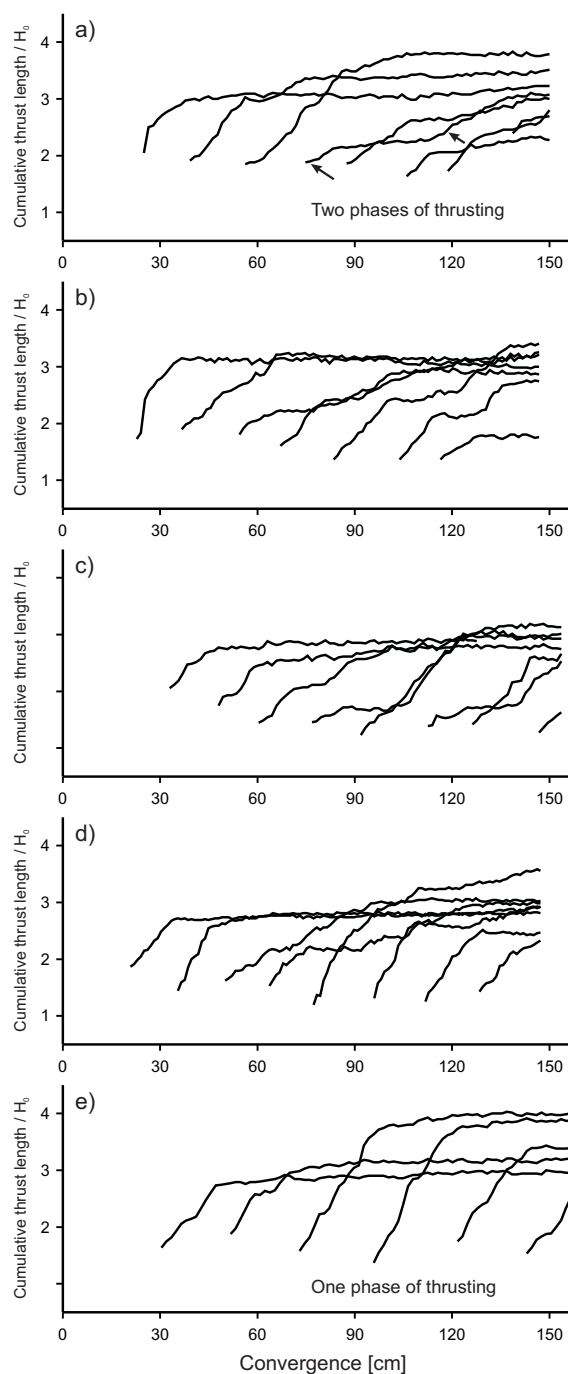


Figure 6.9: Cumulative thrust lengths of each thrust within the pro-wedge, taken at every 1.5 cm of convergence. (a) Reference experiment, arrows indicate first and second phase of thrusting; Distributed erosion of: (b) Retro-wedge, (c) Pro-wedge; Focused erosion of: (d) Retro-wedge, (e) Pro-wedge. Experiments (d) and (e) have the least OOSD index.

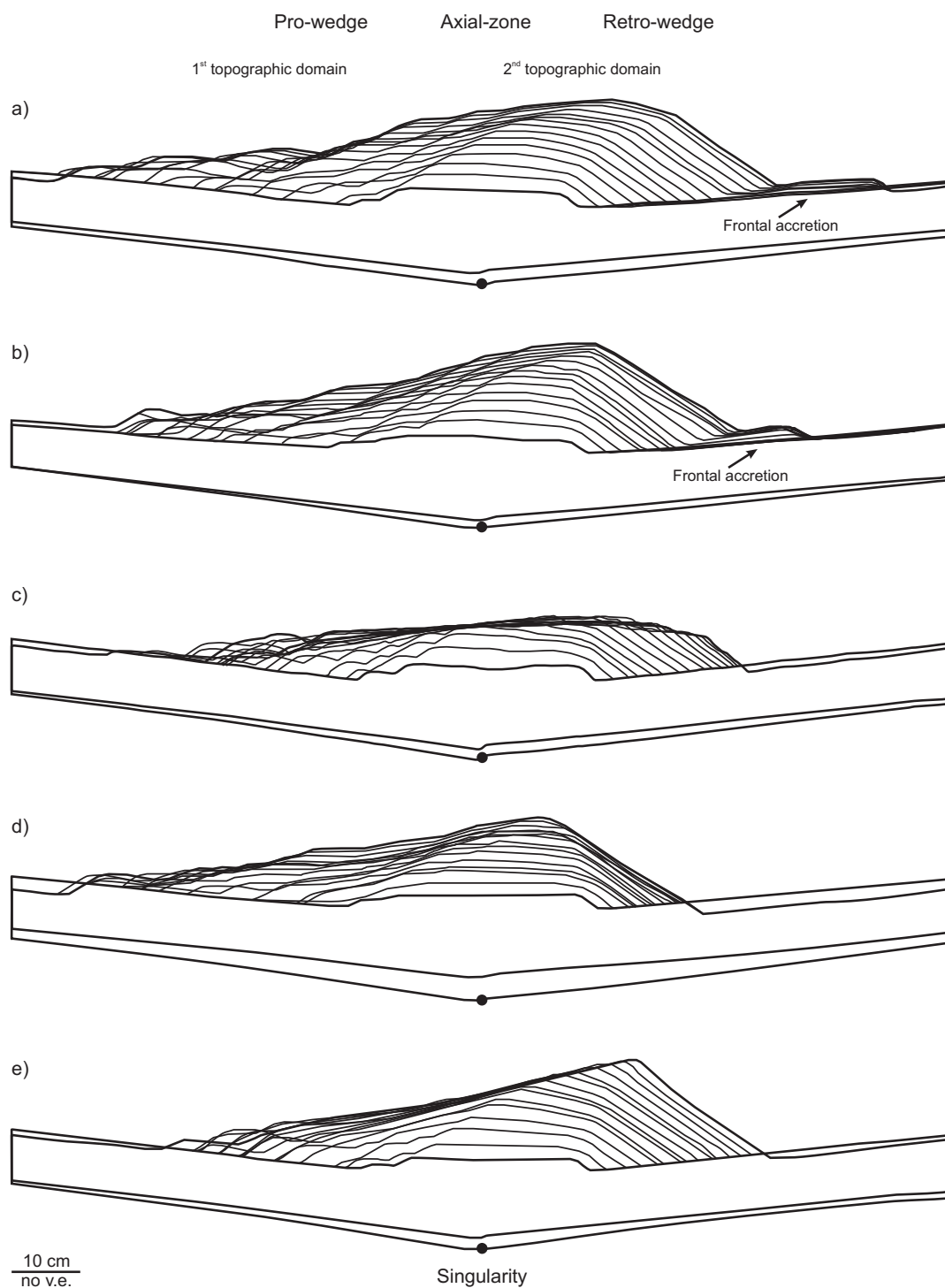


Figure 6.7: Topographic evolution of all experiments of the 2<sup>nd</sup> series. Outlines were taken at every 10 cm of convergence. The first, i. e., after 10 cm and the last, i. e., after 150 cm of convergence outline are given in complete form, to indicate the magnitude of flexure. (a) Reference experiment; Distributed erosion of: (b) Retro-wedge, (c) Pro-wedge; Focused erosion of: (d) Retro-wedge, (e) Pro-wedge. Pro-wedge slopes in both pro-wedge erosion experiments (c and e) are nearly stationary.

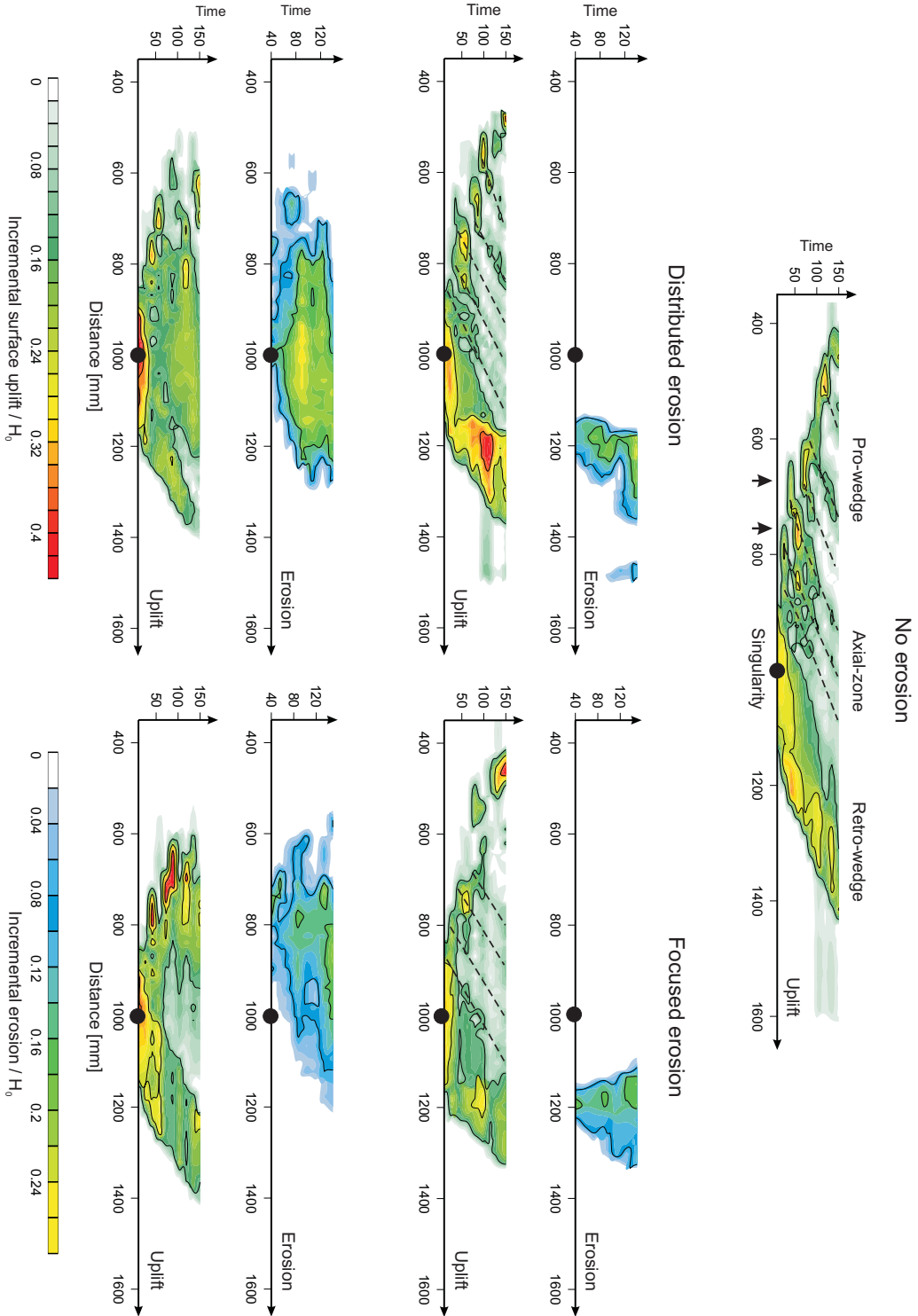


Figure 6.8: ISU and incremental erosion are mapped at every 0.5 mm along the experiment (abscissa) and are displayed as a function of time (ordinate). Time is expressed in cm of convergence. Data were taken at every 10 cm of convergence. Dashed lines trace the initiation and re-activation positions of thrust ramps. Re-activation can lead to a temporary increase of ISU by one order of magnitude for a given position. Two examples are highlighted by arrows.

cate as well as the duplexes can be clearly identified for each experiment. A systematic distribution of finite strain accumulated by each individual thrust imbricate can be observed as well. Finite strain is lowest within imbricates closest to the toe of the pro-wedge, and highest in the central part and decreases towards the top. Finally, it is pointed out that the magnitude of retro-shear is highest at the retro shear-zone which separates lower-plate from upper-plate material and is thus interpreted as long-lived.

However, if similar structures are compared between experiments, it can be shown that different magnitudes of finite strain were accommodated in dependence on the location and the mode of erosion. In the experiment with focused retro-wedge erosion the long-lived retro shear-zone accommodated most finite strain relative to all other experiments. This structure accommodated the least magnitude of finite strain in the experiment with distributed pro-wedge erosion. The long-lived retro shear-zones within the remaining three experiments accumulated similar magnitudes of finite strain (Table 6.1). A likewise pattern is found with respect to the magnitude of finite strain accumulated by the internal glass-bead layer. There, finite strain is highest in the experiment with focused retro-wedge erosion and lowest in both pro-wedge erosion experiments (Table 6.1). The accretion cycle with its three phases was observed in all experiments and is thus concordant with the documented surface uplift waves and the cumulative evolution of thrust lengths (Fig. 6.11).

## 6.3 Discussion

The purpose of this study has been to demonstrate the influence of the location of erosion with respect to the convergence geometry and the mode of erosion, i. e., distributed or focused, on the upper crustal kinematics of bivergent orogenic wedges. Scaled sandbox simulations were chosen to address this issue. Again, we intended to reduce

the number of kinematic boundary conditions and to study the most general case, in order to allow a more self-organised growth of the bivergent sand-wedge. It is highlighted here that this study was not aimed at reproducing the geometry of a certain structure or geomorphologic feature. Since the four-staged evolutionary model as well as the accretion cycle have been extensively dealt with in chapter (5), we focus our discussion on the sensitivity of model results with respect to the simulated erosion intervals and on the influence of both tested parameters on bivergent wedge evolution.

### 6.3.1 Concepts of bivergent wedge evolution and the accretion cycle

The evolution of experiments carried out during the second experimental series supports the postulation of a four-staged evolutionary pathway for bivergent wedges (Fig. 6.6, Fig. 6.4) and the reader is referred back to chapter (5) for further details. In addition, surface uplift waves (Fig. 6.8) in conjunction with the cumulative length evolution of thrusts (Fig. 6.9) and finally the EDM (Fig. 6.11) bear strong evidence that the accretion cycle with its three phases operates in all experiments. This lends additional support to the notion that the first two observations can be used to infer the phase within an accretion cycle, if strain-monitoring techniques such as PIV are not available. As shown in section (5.3.2) this may also hold for “natural” data.

### 6.3.2 Discrete erosion versus continuous deformation

The simulation of erosion within sandbox experiments remains one of the key challenges to be addressed in the future. At present it is only possible to simulate the effect of erosion, i. e., the distribution of unloading across an orogen and not the process of erosion either by rivers, glaciers or bedrock landslides. Due to practical limitations erosion can only be simulated at discrete time in-

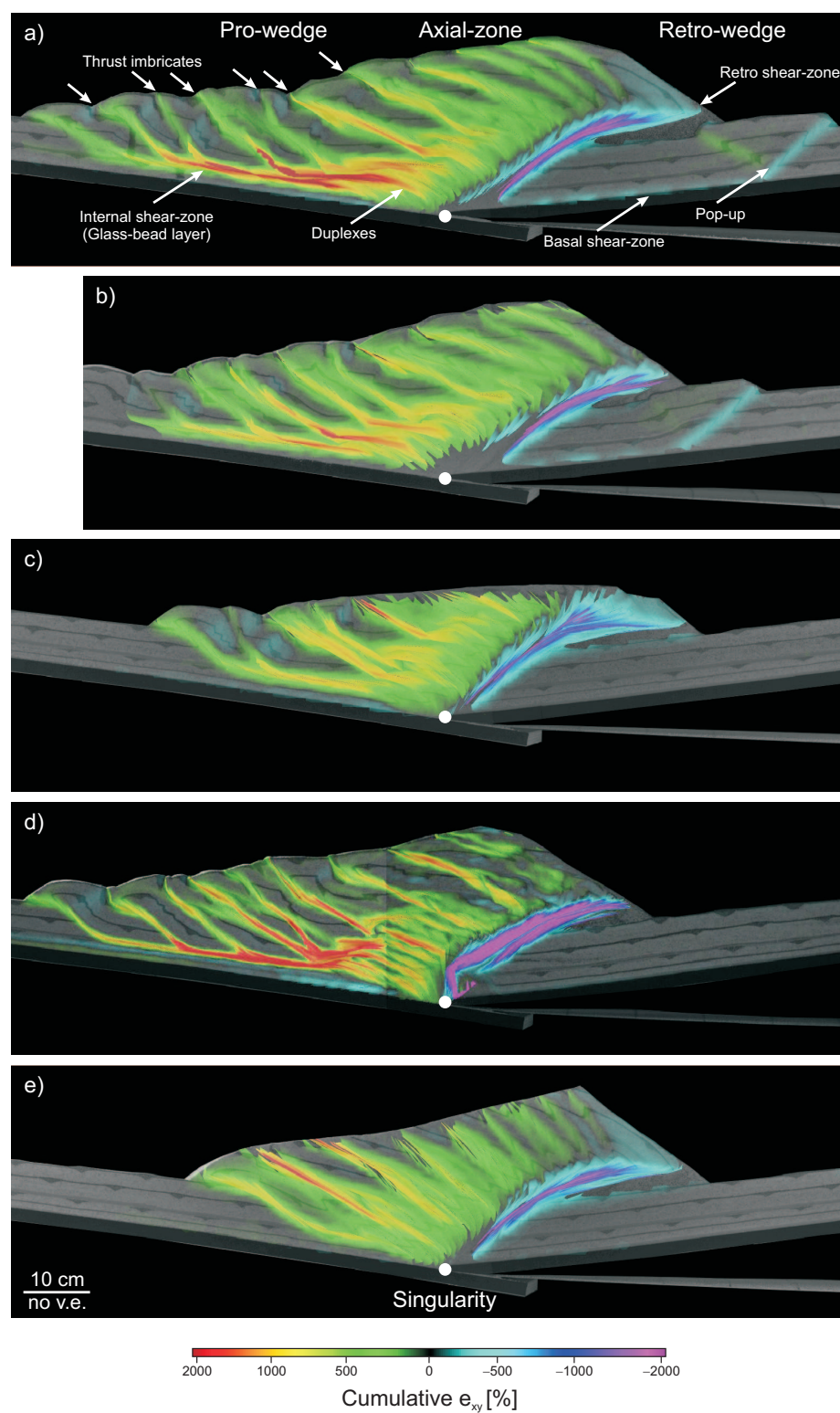


Figure 6.10: Finite  $e_{xy}$  after 140 cm of convergence. (a) Reference experiment; Distributed erosion of: (b) Retro-wedge, (c) Pro-wedge; Focused erosion of: (d) Retro-wedge, (e) Pro-wedge. Note the differing magnitudes of finite strain along the retro shear-zone and the glass bead-layer between experiments.

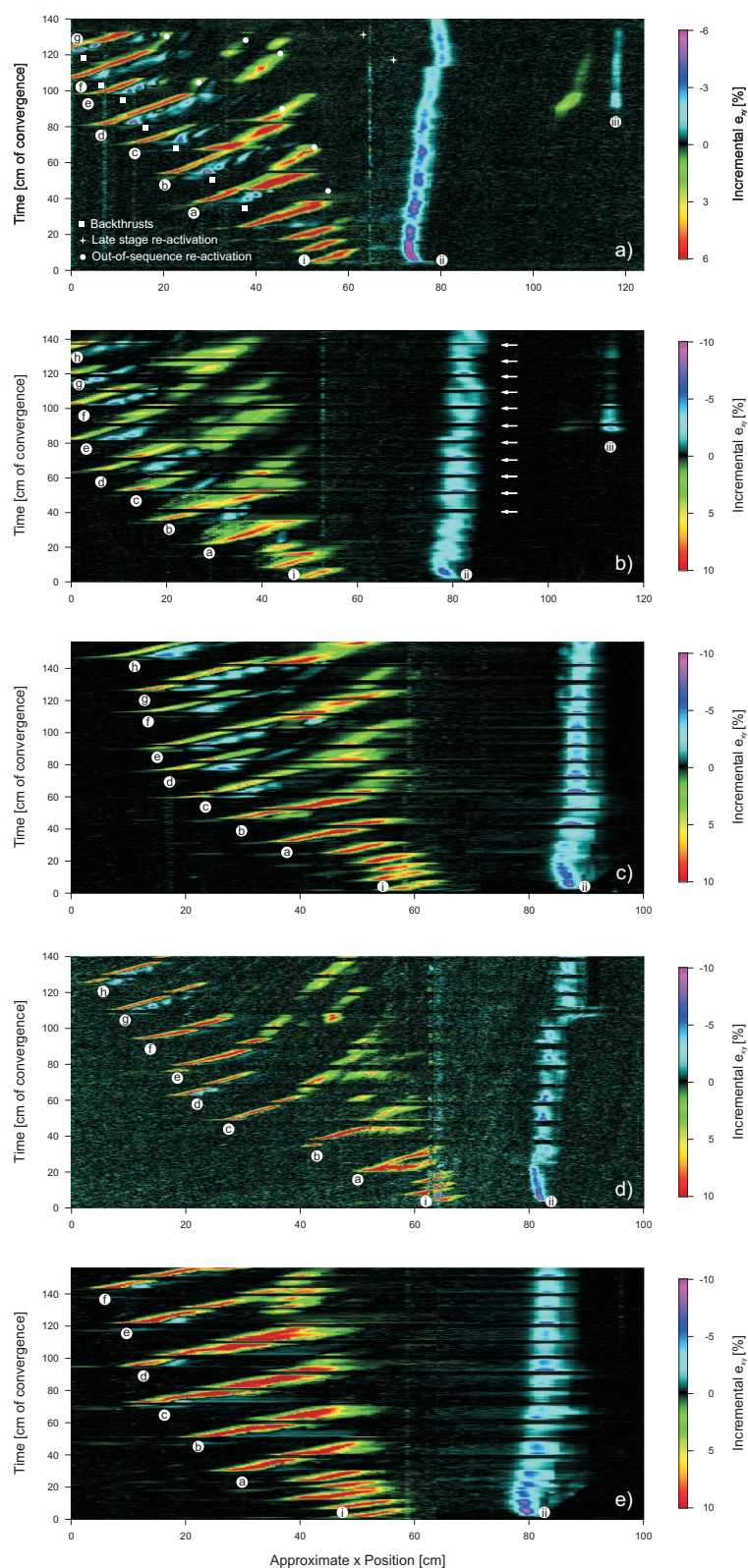


Figure 6.11: Evolution of deformation maps for all experiments of the 2<sup>nd</sup> experimental series. (a) Reference experiment; Distributed erosion of: (b) Retro-wedge, (c) Pro-wedge; Focused erosion of: (d) Retro-wedge, (e) Pro-wedge. Labels (a) to (g) refer to forethrusts within the pro-wedge. (i) denotes the pro-shear of the initial pop-up, (ii) the retro-shear and (iii) denotes the frontal accretion within the retro-wedge. The accretion cycle with its three phases can be recognised in all experiments. Black horizontal lines, pointed to by white arrows in (b) represent times of erosion. For erosion to be simulated, convergence was stopped. Note that no change of incremental  $e_{xy}$  accumulation occurs across erosion intervals.

tervals which might be considered artificial with respect to a continuously growing bivergent sand-wedge. If the applied erosion interval controls the evolution of the bivergent sand-wedge, one should expect an immediate response of the wedge with a frequency of the erosion interval. This however, was not recognised in the time series data, excluding the lowering of the height above the singularity. In addition, experiments from Konstantinovskaia and Malavieille (2005), which involve a 1 cm of convergence interval of erosion revealed similar results with respect to the final structural geometries, as presented in this study. We therefore assume that the interval with which the sand-wedge is denuded is of less importance than the mode and location of erosion as shown below.

Furthermore, there is growing evidence that erosion is far more episodic than often implicitly assumed. Storms, floods and landslides show a power-law distribution, which means that the bulk of erosional work is done by high-magnitude, low-frequency events (Fujii, 1969; Noever, 1993; Sugai et al., 1994; Hovius et al., 1997; Stark and Hovius, 2001; Guzzetti et al., 2002). The control of periodic (deglaciation, intense monsoon years, severe El Niños) and episodic (high-intensity rainstorms, earthquakes) processes on erosion has been observed in the Himalayas, in Taiwan, in New Zealand and in Papua New Guinea (Harbor and Warburton, 1993; Densmore and Hovius, 2000; Guzzetti et al., 2002; Dadson et al., 2003; Keefer et al., 2003; Korup et al., 2004; Barnard et al., 2004; Thiede et al., 2004; Ji et al., 2005). Finally, thermochronometric methods can only bracket the time span of an erosion episode. Following this view, Burbank and Beck (1991) speculated that 90% of erosion may have been accomplished in 10% of the time. Taken all together we suggest that the erosion approach followed here is justified by the above observations.

### 6.3.3 Influence of erosion on bivergent wedge kinematics

Crustal-scaled processes of mountain building have been successfully described numerically by minimum work theory (Hardy et al., 1998; Masek and Duncan, 1998; Gutscher et al., 1998; Gerbault and Garcia-Castellanos, 2005) and we therefore propose that the results shown in this study might be explained again in the light of this concept. Following this view, a bivergent sand-wedge subject to erosion has several possibilities to respond to continued convergence by: (i) the initiation of a new thrust either within the upper or the lower plate; (ii) continued slip along the deformation front; (iii) reactivation of one or more internal thrusts; (iv) slip along the retro-shear zone; (v) footwall or hangingwall shortcuts and (vi) internal deformation. Which of these possibilities is “chosen” by the sand-wedge depends on the respective gravitational and frictional work. Whereas the former is controlled by the lateral distribution of erosion, the latter is determined by the strength of the undeformed material, which in turn depends on its thickness, as well as the degree of both strain softening and strain hardening.

This interpretation is exemplified with the propagation of frontal accretion within the pro-wedge. It is evident from figure (6.6) that the spacing of thrusts is fairly constant throughout all experiments, which agrees well with theoretical considerations and results from sandbox simulations (e. g., Bombolakis (1986); Boyer (1995) and section (5.2)). In contrast, the wavelength of frontal accretion, which is defined as the time expressed in convergence between two consecutive thrust initiation events, depends on the mode and location of erosion (Fig. 6.6, Table 6.1). A permanent unloading of the deformation front, as observed in the focused pro-wedge erosion experiment, leads to an increase of slip along successive thrust imbricates, which in turn retards the propagation of deformation into the foreland (Fig. 6.6, Fig. 6.7). Evidence for increased slip during the

focused pro-wedge erosion experiment is derived from the cumulative thrust lengths (Fig. 6.9) and the resulting out-of sequence displacement index, which is the lowest among all experiments. This observation does not contradict predictions either derived from the CCW concept (e. g., Davis et al., 1983) or from sandbox simulations (e. g., Storti et al., 2000), which state that erosion promotes internal deformation. Instead, focused erosion of the very frontal part of the pro-wedge is considered to represent a special case, which has been previously overlooked or not explicitly dealt with. Also, only the experiment with focused pro-wedge erosion exposes the glass-bead layer at the toe of the pro-wedge (Fig. 6.4). Further support for increased slip is derived from the fact that only six imbricate thrusts are needed to accommodate 140 cm of convergence, whereas all other experiments show eight imbricates. This agrees well with observations from other sandbox simulations (Persson et al., 2004), who showed that erosion tends to lengthen the lifetime of individual thrusts.

Focused erosion of the deformation front leads also to a lack of sufficient overthrust length needed to activate the internal glass-bead layer (Kukowski et al., 2002). Thus, frontal accretion by thrust imbrication and basal accretion by duplex formation are in phase throughout the experiment and form one dynamical system. This might explain the observed lowest variability with respect to the wavelength of both accretion modes.

On the contrary, the wavelength of frontal accretion during distributed pro-wedge erosion shows the highest variability (Table 6.1). During this experiment, the highest erosion rates occur at the central and at the rearward part of the pro-wedge. Also, erosion rates at the respective toward part show a higher degree of variability through time as the corresponding part in the focused pro-wedge erosion experiment (Fig. 6.8). It follows that unloading of the deformation front is more variable through time as well, which in turn influences the wavelength of frontal accre-

tion. Furthermore, in order to restore its critical taper, the pro-wedge deforms internally, i. e., through re-activation of older thrusts. It follows that the propagation of deformation into the foreland is retarded, which agrees with the results from Schlunegger (1999) and Hovius (2000). The preference of internal deformation is mirrored in the diffuse pattern of finite strain and the highest out-of-sequence displacement index among all experiments (Fig. 6.10, Table 6.1) and is thus in accordance with Willett et al. (1993). Depending on the magnitude of internal deformation, propagation of deformation into the foreland is retarded and thus adds to its variability.

Retro-wedge erosion unloads the axial-zone and especially the retro-shear zone, which eases translation of pro-wedge derived material towards the upper plate. It follows that in favour of internal deformation, the propagation of frontal accretion can be retarded. The resultant variability of the respective wavelength is similar for both retro-wedge erosion experiments but higher than the one from the reference experiment (Table 6.1). This highlights the a significant spatial offset between cause (retro-wedge erosion) and response (propagation of deformation within the pro-wedge).

Basal accretion is more sensitive to changes of the load gradient determined by erosion, since the respective thrust spacing and the corresponding wavelengths differ significantly within and between experiments (Fig. 6.6, Table 6.1). The formation of duplexes depends on the load imposed by the frontally accreted material, the rotation of the glass-bead layer resulting from the stacking and backward translation of the duplexes and the load upon the retro-shear zone. As noted above, retro-wedge erosion unloads the axial-zone and especially the retro-shear zone. It follows that duplexes can be more easily stacked and transferred towards the upper plate. Two consequences emerge. At the expense of lateral growth of the pro-wedge, vertical growth of the axial-zone and the retro-wedge is promoted. Despite the fact that



material is removed, both experiments with retro-wedge erosion have a higher elevation above the singularity than the reference or the pro-wedge erosion experiments. This is consistent with the observed acceleration of basally accreted particles (Fig. 6.4) and the prominent maximum in ISU within the retro-wedge (Fig. 6.8). We therefore suggest that retro-wedge erosion enhances particle flow of basal accretion. Note that during pro-wedge erosion frontal accretion is accelerated (Fig. 6.4). A further consequence of the unloading of the axial-zone and the retro-wedge is that longer undeformed sand-sheets can be drawn beneath the internal glass-bead layer towards the singularity until failure occurs and thus reduces shorter wavelength activity. This is consistent with the predictions from minimum work calculations by Gutscher et al. (1998).

Taken all together, our results suggest that the location of erosion with respect to the convergence geometry as well as the erosion mode have a profound effect on the ratio between piggy-back thrusting versus internal deformation. This is supported by a recent study in the Himalayas. Based on  $^{40}\text{Ar}/^{39}\text{Ar}$  and AFT dating, Thiede et al. (2005) showed that pronounced erosion during the last 10 Ma lead to increased rock uplift and exhumation within the central part of the Himalayan pro-wedge in favour of the propagation of deformation towards the southern foreland. Although, the rate of Eurasia-India convergence is thought to have remained constant since that time, the Himalayan deformation front has only migrated 20 to 50 km southward (Thiede et al., 2005).

#### 6.4 Implications and predictions for natural orogens

In this study we have investigated the influence of the location of erosion with respect to the convergence geometry and the mode of erosion, i. e., distributed or focused, which are thought to represent end-members, on the kinematics of biver-

gent sand-wedges (Fig. 6.12). We re-emphasise the scale-invariance of brittle behaviour and point out that the implications and predictions derived from the second experimental series are not limited to bivergent orogens and may have some bearing for fold and thrust belts as well. Note however, that this study is focused on lower temperature orogens where brittle behaviour prevails. Therefore, some caution must be taken while transferring and applying our results to natural examples. High exhumation rates may finally lead to the removal of the highest strength part of the continental crust, which significantly reduces its integrated strength. At this stage ductile processes might start to dominate (Beaumont et al., 2001; Zeitler et al., 2001; Koons et al., 2002).

Similar to Willett (1999) we predict that the location of erosion with respect to the convergence geometry determines the outcrop pattern of metamorphic facies. We further propose that deformation responds immediately to erosion. Retro-wedge erosion amplifies the displacement of the basally accreted material, whereas pro-wedge erosion accelerates and additionally redirects the particle flow of the frontally accreted material. Pro- and retro-wedge erosion retard the propagation of deformation within the pro-wedge. This effect is stronger for pro-wedge erosion.

The evolution of Borneo is consistent with the last prediction. Strong synkinematic erosion under tropical conditions prohibited the growth of a wide thin-skinned fold-and-thrust belt. The resulting crustal load was not sufficient to generate a foreland basin (Hall and Nichols, 2002). Similarly, Schlunegger and Simpson (2002) demonstrated for the European Alps that a significant decrease in the erosional efficiency during the Early Miocene led to a change from vertical extrusion associated with rapid exhumation during the Late Oligocene to a mainly horizontally directed extrusion, i. e., the formation of the Jura fold and thrust belt and the southern Alps during Middle to Late Miocene times.

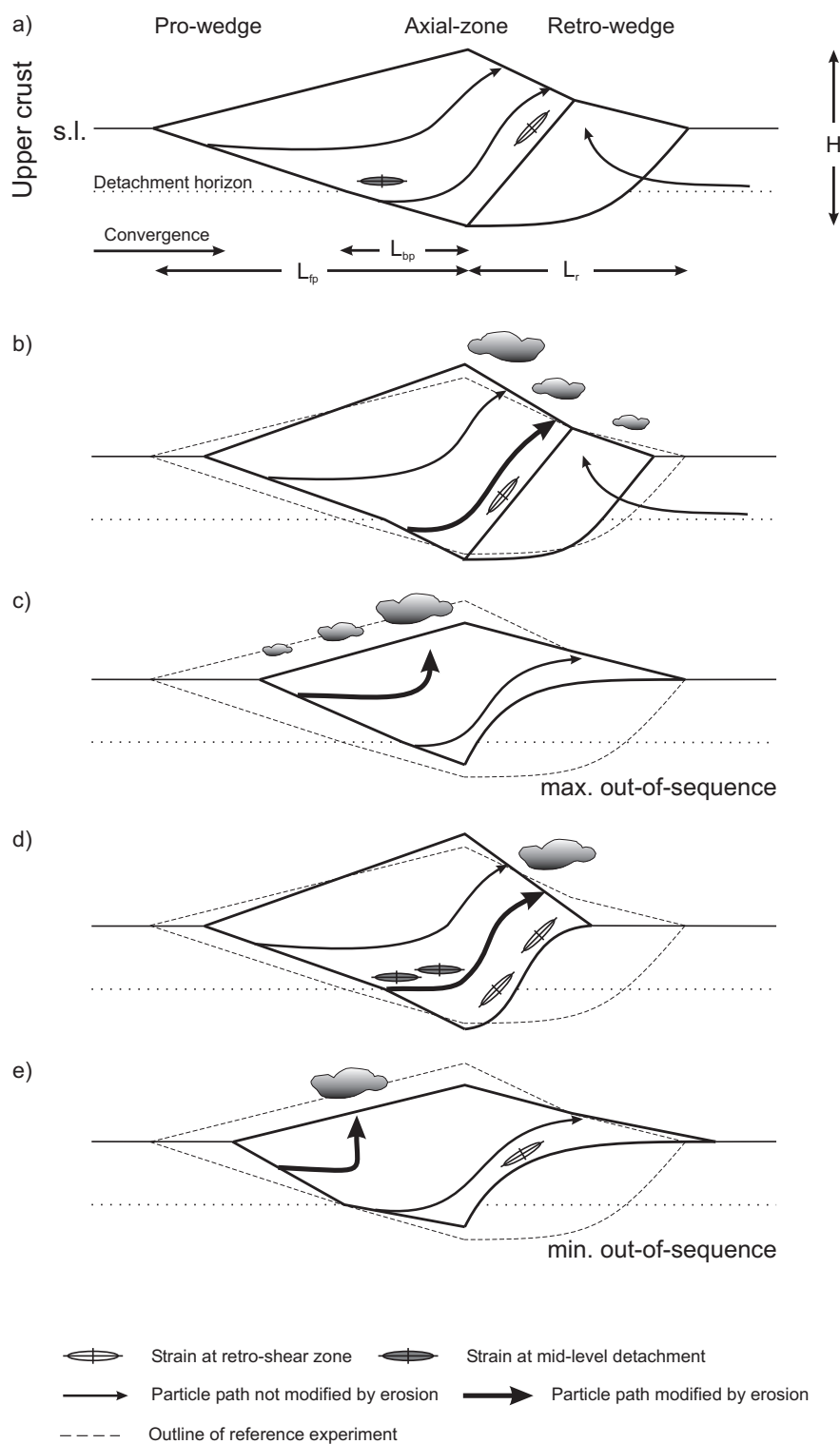


Figure 6.12: Synopsis of results. Outlines indicate trends of bivergent wedge growth in dependence of the location and the mode of erosion. Magnitude and direction of schematic particle paths, as well as locations of high finite strain are given. Schematic particle are derived from  $\sim 120$  calculated particle paths as given in Fig. 6.5d. (a) Reference experiment; Distributed erosion of: (b) Retro-wedge, (c) Pro-wedge; Focused erosion of: (d) Retro-wedge, (e) Pro-wedge.

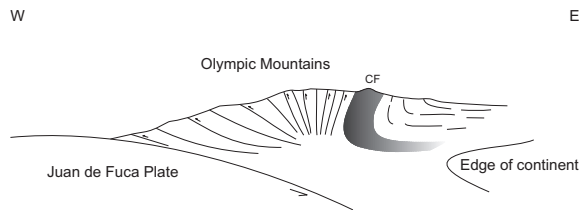


Figure 6.13: Generalised section through the Olympic Mountains as postulated from field work. Subduction of the Juan de Fuca plate beneath North America results in the formation of an accretionary complex - Olympic Mountains. Note rotation of forethrusts and the absence of a prominent backthrust, which has also not been imaged on seismic profiles (Brandon and Calderwood, 1990). CF, Crescent Formation, which may have acted as a backstop. The Olympic Mountains are assumed to be in a mass steady-state since  $\sim 14 Ma$  (Pazzaglia and Brandon, 2001). Modified after Tabor and Cady (1978).

Also, we suggest that retro-wedge erosion amplifies vertical growth and leads to strain accumulation along the retro shear-zone and the mid-level-detachment. This indicates that for retro-wedge erosion cause (erosion) and response (deformation) are significantly offset in space. Thus, the cause for a certain seismicity pattern observed in the pro-wedge might be the eroding retro-wedge, hundreds of kilometers away. In contrast, pro-wedge erosion evokes a complete decoupling of the retro-wedge from the pro-wedge. Here cause and response are spatially more closely related. Both results highlight the need for orogen-wide climate-tectonics studies.

Intense erosion of the rearward part of the pro-wedge and the adjacent axial-zone may result in a fanning of the retro-shear zone, i. e., slip is taken up by an array of retro-shear zones rather than one single, long-lived structure. This might explain why no prominent backthrust has been documented from the Olympic Mountains, which are assumed to be in a mass steady-state for the last  $\sim 14 Ma$  (Brandon and Calderwood, 1990; Pazzaglia and Brandon, 2001). Instead, Tabor and Cady (1978) point out that several vertical thrusts take up slip (Fig. 6.13). We found that more focused erosion is associated with a more focused

tectonic response. This interpretation is supported by observations from the Chugach/St. Elias Range in Southern Alaska. There, the windward position of the ELA coincides with a narrow zone of active upper plate deformation associated with high rates of rock uplift (Meigs and Sauber, 2000; Sheaf et al., 2003). Also, strong fluvial erosion in both Himalayan syntaxes has led to high exhumation and deformation rates (Zeitler et al., 2001).

A change from distributed to focused erosion may lead to a continued activation of a certain structure, e. g., deformation front and may thus retard the propagation of deformation into the foreland and may also determine which detachment layer is favoured.

Although all of our sandbox simulations exhibit a clear forward breaking or piggy-back sequence of thrusting, considerable displacement is accumulated out-of-sequence by re-activation of older thrusts. The magnitude of the latter is strongly controlled by the location and mode of erosion. Within this respect it is interesting to note, that Mouthereau et al. (2001) showed that the increase of erosion rates was associated with an increase of the number of re-activated or out-of-sequence thrusts in the Taiwan fold and thrust belt. Similarly, Hodges et al. (2004) demonstrated that strong orographic forcing of precipitation lead to concentrated erosion and out-of-sequence thrusting in the Higher Himalayan Ranges.

Finally, we speculate that a bivergent wedge is very robust with respect to its boundary conditions, e. g., mechanic stratigraphy and erosion. Erosion modifies but does not inhibit the segmentation of a bivergent wedge or the simultaneous propagation of frontal and basal accretion. This gains support from a recent study in the Himalayas where the tectonic displacement field is focused by erosion but does not mimic its asymmetric distribution (Burbank et al., 2003). If however, a certain threshold is either exceeded or reached, the kinematics might change their mode.

## 7 Deformation versus erosion

A recent debate has centred on the chicken or egg question (England and Molnar, 1990), i. e., whether erosion controls deformation or vice versa. Based on the insight gained during the course of this study, we follow Hodges et al. (2004) and consider both processes not as antagonists, but as part of one dynamic system - the orogenic wedge. Additionally, field and experimental data indicate that the degree of sensitivity of a bivergent wedge with respect to kinematic boundary conditions and to surface processes may depend on the scale and on the object of observation.

As outlined in chapter (3), bivergent orogens show several common features, which have been used to constrain the CCW concept (Davis et al., 1983). Given the wealth and variability of tectonic and climatic pre-conditions of orogenic evolution, it follows that specific kinematic boundary conditions or surface processes are not needed for these phenomena to emerge. This is consistent with an observation of Montgomery and Brandon (2002), who pointed out that all mountain belts, despite their specific tectonic context or climate zone have a similar local relief, ranging between 1 and 2 km.

The scale invariance of these phenomena additionally underlines their independence on specific boundary conditions and allowed the use of sandbox experiments to simulate bivergent wedge-evolution. We showed that neither the implementation of different kinematic boundary conditions nor the simulation of erosion has hindered the bivergent sand-wedges to follow a four staged evolutionary pathway. In addition, deformation in all experiments was controlled by the accretion cycle with its three phases. These observations highlight once again the robustness of bivergent wedges to kinematic boundary conditions or

to surface processes. Further support for this prediction is derived from the good agreement between results of this study and previously published work, which involves other methodological approaches (e. g., Willett, 1999; McClay and Whitehouse, 2004).

There are however, some trends within the experimentally derived data, which deserve discussion. As demonstrated in section (5.3.7), the evolution of the height and the width of the pro-wedge can be well described with a power law, which is consistent with theoretical predictions (Dahlen, 1990). We further found that the scatter of the power-law coefficients, related to the height of the pro-wedge, is higher for the first experimental series than for the second one (Table 7.1). Thus, power law coefficients of the erosion experiments are very similar to the one observed in experiment 9.05, which has the same kinematic boundary conditions but lacks erosion. This would indicate that changes of the kinematic boundary conditions would have a more profound effect on how the wedge grows vertically than erosion (Table 7.1). A likewise observation can be made for the out-of-sequence indexes calculated for each experiment. The respective scatter is again higher for the first experimental series (Table 7.1) and the OOSD indexes of the erosion experiments are again very similar to the one of the reference experiment. There is, however, a prominent exception. Focused pro-wedge erosion has resulted in a continuous unloading of the deformation front, which inhibited the activation of the internal glass-bead layer to serve as a detachment. This observation suggests that a certain erosion mode can determine the active detachment level.

In more general terms, we postulate that kinematic boundary conditions such as flexure, mechanic stratigraphy, basal and internal properties of the incoming layer and the orogenic wedge, as well as fluid pressures determine the active detachment level, the spatio-temporal propagation of deformation and thus the ratio between piggy-

Experimental series	Experiment	oOSD	Lateral growth of pro-wedge	Height above singularity
1 <sup>st</sup>	9.15	0.62	$y = 0.79t^{0.48}$	$y = 0.85t^{0.29}$
	9.05	3.73	$y = 1.06t^{0.44}$	$y = 1.03t^{0.26}$
	9.20	8.1	$y = 0.80t^{0.50}$	$y = 0.76t^{0.33}$
	9.35	3.95	$y = 1.80t^{0.32}$	$y = 0.48t^{0.42}$
	9.25	0.46	$y = 0.97t^{0.43}$	$y = 1.00t^{0.23}$
2 <sup>nd</sup>	9.05	3.73	$y = 1.06t^{0.44}$	$y = 1.03t^{0.26}$
	9.06*	3.42	$y = 1.17t^{0.40}$	$y = 1.12t^{0.24}$
	9.09†	4.16	$y = 1.08t^{0.37}$	$y = 1.10t^{0.19}$
	9.10§	0.97	$y = 1.34t^{0.30}$	$y = 1.00t^{0.24}$
	9.11‡	3.16	$y = 0.90t^{0.47}$	$y = 0.92t^{0.27}$

\* Distributed retro-wedge erosion.  
† Distributed pro-wedge erosion.  
§ Focused pro-wedge erosion.  
‡ Focused retro-wedge erosion.

Table 7.1: Selected indexes

back thrusting and internal deformation. With respect to the influence of erosion, two scenarios can be envisaged. If erosion changes only the ratio between piggy-back thrusting and internal deformation, the orogenic wedge is thought to be still driven by “kinematics”. If however, erosion changes the detachment level and thus modifies the volume of material accreted to the orogen, we argue that erosion has taken the lead. Following this view, an erosion-induced slowdown or halt of the propagation of deformation towards the foreland, as observed for the Himalayan orogen during the last 10 *Ma* (Thiede et al., 2005), does not necessarily mark the transition from a tectonically to an erosionally controlled orogen. Further evidence with respect to changes of the detachment level would be required to address this question.

The above considerations indicate that surface processes and kinematic boundary conditions can evoke similar phenomena. Thus, the ascription of certain observations to changes of the local to regional climate or to changes of thrust-kinematics, hundreds of kilometers away – or even on the other side of a bivergent orogen, remains difficult, but should be taken into account. Within this respect, we note that these far-field interactions bear some importance for either landslide or seismic hazard assessment studies.

Feedback processes provide an additional challenge, since an originally tectonic signal might be converted into a climatic one (e. g., rain shadow), which finally may convert to a tectonic signal again (e. g., propagation of deformation). Such a scenario might explain the observed oscillatory filling and excavation of the Quebrada del Toro basin in NW Argentina (Hilley and Strecker, 2005). Time series analysis, in conjunction with detailed regional to orogen-wide studies, may provide insight, but are still left with the challenge, to decide, whether two observations occur coincidentally or causally linked. In order to address these issues, we propose that a stronger integration of field and simulation studies is required, and that time series from the former should be used to constrain the latter. This raises the need to provide more testable predictions from simulation studies and we hope that we have made a step toward this direction.

# 8 Foreland basin evolution and the growth of an orogenic wedge

## 8.1 Introduction

Peripheral foreland basin systems (DeCelles and Giles, 1996) result from the flexural downbending of continental lithosphere in response to tectonic and topographic loading during continent-continent collision (Price, 1973). The spatial evolution of the associated depozones, i. e., wedge-top, foredeep, forebulge and backbulge (Fig. 8.1) and their respective sedimentary infill, is strongly dependent on (i) the effective elastic thickness ( $T_e$ ) of the involved lithospheres; (ii) the level of horizontal stresses; (iii) the magnitude of the loads imposed on the foreland by the orogenic wedge and the subducted lithospheric slab; (iv) the dip-angle of the latter; (v) the rate and direction of convergence; (vi) the amount of erosion of the orogenic wedge and the dispersal system within the foreland and (vii) eustasy (Beaumont, 1981; Turcotte and Schubert, 2002; Allen et al., 1991; Sinclair, 1997b; Ziegler et al., 2002). Numerous field studies have demonstrated that almost all foredeeps evolve from an underfilled to a filled or overfilled depositional state (Covey, 1986; Sinclair, 1997a). The underfilled state is characterised by deep-marine (Flysch type) sediments, high thrust advance rates, and low exhumation rates. In contrast, the overfilled state shows shallow marine to continental (Molasse type) deposits and a dominance of exhumation versus frontal advance of the orogen (Sinclair and Allen, 1992). Classically, the Flysch to Molasse transition is interpreted as recording the migration of the thrust wedge and the associated foredeep over the hinge-

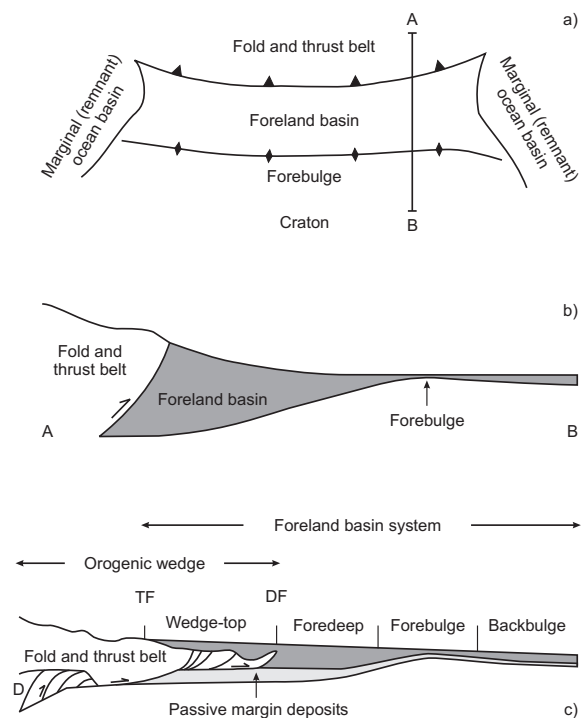


Figure 8.1: (a) Schematic map view of a foreland basin, bounded longitudinally by a pair of marginal ocean basins. The scale is not specified, but would be of the order of  $10^2$  to  $10^3$  km. Vertical line at right indicates the orientation of a cross-section that would resemble what is shown in (b). (b) The generally accepted notion of foreland-basin geometry in transverse cross-section. Note the unrealistic geometry of the boundary between the basin and the thrust belt. Vertical exaggeration is of the order of 10 times. (c) Schematic cross-section depicting a revised concept of a foreland basin system, with the wedge-top, foredeep, forebulge and backbulge depozones shown at approximately true scale. Topographic front of the thrust belt is labeled TF. The foreland basin system is shown in dark grey; area in light grey indicates passive margin deposits, which are incorporated into (but not shown within) the fold-thrust belt toward the left of diagram. A schematic duplex (D) is depicted in the hinterland part of the orogenic wedge. Note the substantial overlap between the front of the orogenic wedge and the foreland basin system. Modified after DeCelles and Giles (1996).

line of the inherited passive margin of the underthrust plate (Dewey, 1982). Numerical simulations in conjunction with field studies in the Swiss Alps however, suggest that the rate of frontal advance of the orogenic wedge and the sediment transport coefficient ( $K$ ) are the main control on

the state of the foredeep infill, whereas an increase of the flexural rigidity or the surface slope of the orogenic wedge is only of minor importance (Sinclair et al., 1991; Sinclair, 1997b).

Additionally, most forward modelling studies, which are aimed at unravelling the influence of the above parameters on the stratigraphic architecture of foreland basins (Flemings and Jordan, 1990; Jordan and Flemings, 1991; Sinclair et al., 1991; Crampton and Allen, 1995; Galewsky, 1998; Allen et al., 2001; Clevis et al., 2004), assume that the respective orogenic load results from either a lithospheric scaled fault-bend fold (Flemings and Jordan, 1990) or from a pro-wedge sensu Willett et al. (1993). However, sandbox simulations of bivergent orogens (like this study) have demonstrated that strain is partitioned between the pro- and the retro-wedge. It follows that processes acting either upon or within the retro-wedge control the load distribution within the pro-wedge as well, which in turn influences the geometry of the pro-foredeep. Consequently, cause and effect would be considerably offset in space.

Thus, the purpose of this study, which is based on scaled-sandbox simulations as well as analytical considerations, is twofold. First, we explore how the lateral growth of an orogenic wedge controls the spatio-temporal evolution of the pro-foredeep and thus the Flysch to Molasse transition. Second, we focus on the influence of the coupling between the pro- and the retro-wedge on the evolution of the pro-foredeep. In order to address both issues we consider a reference experiment (9.05) and one experiment with pro- and another with retro-wedge erosion (9.09, 9.06). Finally, sedimentary basins and thus foreland basins provide the most significant sources of energy-related commodities, such as hydrocarbons, coal, uranium and many metals (Kyser and Hiatt, 2003). Consequently, the formulation of conceptual models and the detection of far-field relations may help to constrain future exploration strategies.

## 8.2 Method

Time series of the horizontal distance between the deformation front of the pro-wedge and the singularity [ $L_{fp}/H_0$ ] as well as the height of the axial-zone above the singularity [ $H/H_0$ ] provide an approximation of the triangular shape of the pro-wedge throughout its evolution. Although these data represent dimensionless lengths, they are scaled by  $10^5$ , a factor commonly used in sandbox experiments (e. g., Malavieille, 1984; Storti et al., 2000). Both converted time series ( $L$  and  $H$ ) are used to calculate the flexure of a hypothetical foreland lithosphere in response to orogenic loading for each time (convergence) step according to Turcotte and Schubert (2002):

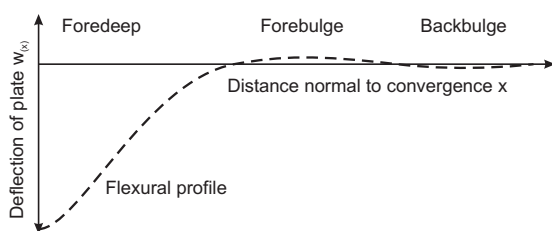
$$V_0 = W \rho_{orogen} g L H \quad (8.1)$$

$$\alpha = \left( \frac{4D}{(\rho_m - \rho_s)g} \right)^{1/4} \quad (8.2)$$

$$w_0 = \frac{\left( \frac{4D}{(\rho_m - \rho_s)g} \right)^{3/4} V_0}{4D} \quad (8.3)$$

$$w_x = w_0 e^{-x/\alpha} \cos x / \alpha \quad (8.4)$$

whereby  $V_0$  is the vertical load in  $N$ ,  $W$  is the width of the hypothetical orogen =  $1m$ ,  $L$  is the converted length of the pro-wedge in  $m$ ,  $H$  is the converted height of the axial-zone above the singularity in  $m$ ,  $\alpha$  is the flexural parameter,  $D$  is the flexural rigidity of the plate, chosen to be  $10^{22} Nm$ ,  $g$  is the acceleration due to gravity ( $9.81 m/s^2$ ),  $\rho_{orogen}$  is the density of a hypothetical orogen ( $2600 kg/m^3$ ),  $\rho_m$  is the density of the mantle ( $3300 kg/m^3$ ),  $\rho_s$  is the density of sediments, filling the foredeep ( $2300 kg/m^3$ ),  $w_0$  is the deflection of the plate at  $x = 0$  and  $w(x)$  is the deflection of the plate at point  $x$ . Density values are



at  $x = 0; V_0, w_0$

Figure 8.2: Theoretical deflection of an elastic broken plate under a line load applied at its end. Modified from Allen and Allen (2005).

mean values and have been taken from Turcotte and Schubert (2002). A schematic flexural profile is shown in figure (8.2). As in previous modelling studies (Karner and Watts, 1983; Sinclair et al., 1991; Crampton and Allen, 1995; Roddaz et al., 2005) orogenic overthrusting of the foreland plate is simulated by two-dimensional a priori loading of a broken elastic plate. Flexural response to loading is treated as instantaneous, since the response time for isostatic adjustment is on the order of  $10^3$  to  $10^5$  years (Crampton and Allen, 1995).

Lateral migration of the pro-wedge gravity-center was not taken into account. This would have resulted in slight changes of the foredeep geometry only. Effects of horizontal stresses on the foreland basin system are neglected, since they would only slightly magnify the effects of flexure and would not change the overall geometries. Sea level variations would have a similar negligible effect on plate flexure (Crampton and Allen, 1995). The influence of different flexural rigidities on the foreland basin system is well known (e. g., Flemings and Jordan, 1989; Sinclair et al., 1991). High flexural rigidities lead to the formation of a broad, shallow depression with a low, wide forebulge, whereas low flexural rigidities give rise to a deep, narrow peripheral trough and a relatively high forebulge. This means that, as the load advances across the plate, the onset of subsidence at a given point on the profile will be later, and the rate of subsidence higher for a low compared to a high flexural rigidity (Sinclair et al., 1991; Cramp-

ton and Allen, 1995). In a sediment-filled basin the forebulge will be less high, because the flexural response to the sediment load interferes with the one from the orogenic load, resulting in a less well developed forebulge. Since we are interested in the Flysch to Molasse transition, we assume that the foredeep is completely filled with sediments.

### 8.3 Results and discussion

Flexural profiles derived from the above calculations image three out of the four depozones associated with foreland basin systems, i. e., the foredeep, the forebulge and the backbulge. Although, the shape of the flexural profile depends on a multitude of factors as outlined above, the corresponding magnitudes of either downbending or uplift agree with field observations. According to DeCelles and Giles (1996) foredeep depozones are commonly 2 to 8 km thick, forebulges are  $\sim 10m$  to several 100m high and backbulges are generally not deeper than 200m. Maximum calculated values are 2km, 150m and 20m, respectively (Fig. 8.3). The temporal evolution of the flexural profiles further indicates that:

- i. During early stages of orogenic evolution, incremental deepening of the foredeep as well as incremental uplift of the forebulge is high, but decreases with further convergence. This is to be expected, since both the width and the height of the pro-wedge, are best described by a power law (section 5.3.7).
- ii. Each thrust initiation phase is followed by a deepening of the foredeep and uplift of the forebulge, an observation, which has been documented by Jordan and Flemings (1991) as well. Thrust episodes lead to depth changes of  $\sim 1m$  of the backbulge region.
- iii. For a given lateral position, thrust induced change of the depth of the foredeep decreases with increasing proximity to the orogen. In



contrast, each thrust event has a profound effect on the height of the forebulge, which is consistent with previous analytical studies (e. g., Jordan and Flemings (1991)).

Although associated with lower magnitudes, these three phenomena can be as well observed in both the pro- and the retro-wedge erosion case (Fig. 8.3b, c). Furthermore, we found that also retro-wedge erosion has a significant influence on the spatio-temporal evolution of the pro-foredeep. The above results confirm thus, the expected and well established link between the evolution of orogenic belts and their foreland basin system (DeCelles and Giles, 1996). There are however, some implications, which deserve further discussion.

The CCW concept predicts and sandbox simulations confirmed that the lateral and vertical growth of an orogenic wedge follows a power law (Dahlen, 1990; Mulugeta and Koyi, 1992; Hoth et al., 2006). The disagreement between theoretically predicted and experimentally derived power law coefficients is not considered here, but was discussed in section (5.3.7). If the width and the height of an orogenic belt grow proportional to the convergence ( $t$ ) by  $t^{0.5}$ , then the respective incremental change, which is described by the first derivation ( $-0.5t^{-0.5}$ ), decreases with time. It follows that the associated increase of the load of the orogenic wedge onto its foreland and thus the resulting increase of the deflection decreases through time as well. At the same time however, the surface of the wedge, prone to be eroded, grows proportional to the convergence ( $t$ ) by  $2t^{0.5}$  and is thus twice as fast as the lateral and vertical growth. If one further assumes a constant erosion rate of the wedge and a constant sedimentation rate within the foredeep, a change from underfilled (fast addition of new accommodation), to overfilled (slow addition of new accommodation) would result. This transition would be thus an emergent consequence of the imposed kinematic boundary conditions. We therefore propose a two-staged evolutionary model. During early stages of

convergence the rate of orogenic growth/advance is high and so is the rate of flexure induced subsidence within the foredeep. Debris derived from the orogen is deposited in a deep and probably underfilled foredeep (Flysch-type). At a later stage of convergence the rate of flexure induced subsidence within the foredeep decreases. The latter is successively filled and may reach a point in its evolution where all sediments are bypassed (overfilled or Molasse-type). There is thus no need to invoke a halt of convergence or a slab breakoff to explain the Flysch to Molasse transition. A slow-down of thrust front advance associated with the Flysch to Molasse transition has been documented for the Swiss Alps and the Longmen Shan Thrust Belt (Sinclair, 1997b; Yong et al., 2003; Kempf and Pfiffner, 2004) and has been postulated for the Pyrenees as well (Labaume et al., 1985).

The influence of erosion on the orogen-foredeep system would be twofold. First, erosion controls the geometry and the propagation of an orogenic wedge and thus determines the incremental addition of load responsible for the flexure. Second, erosion provides the debris with which the foredeep is filled. Consequently, intense erosion of the pro-wedge promotes the Flysch to Molasse transition within the pro-foredeep and would thus lead to a short-lived underfilled foreland basin system. This might explain the scarcity of early Flysch deposits in the foredeep of the Himalayas, Taiwan and the Pyrenees, which were subject to intense erosion on their respective pro-wedges (Covey, 1986; Fitzgerald et al., 1999; Najman et al., 2004).

We further highlight the far-field connection between retro-wedge erosion and the spatio-temporal evolution of the pro-foredeep. In a previous section (6.2) we demonstrated that retro-wedge erosion influences thrust activity within the pro-wedge and thus seismicity. Consequently, retro-wedge erosion does also change the load distribution of the pro-wedge and thus the flexure of the pro-lithosphere. Given that the magnitude of strain transfer between the pro- and the retro-

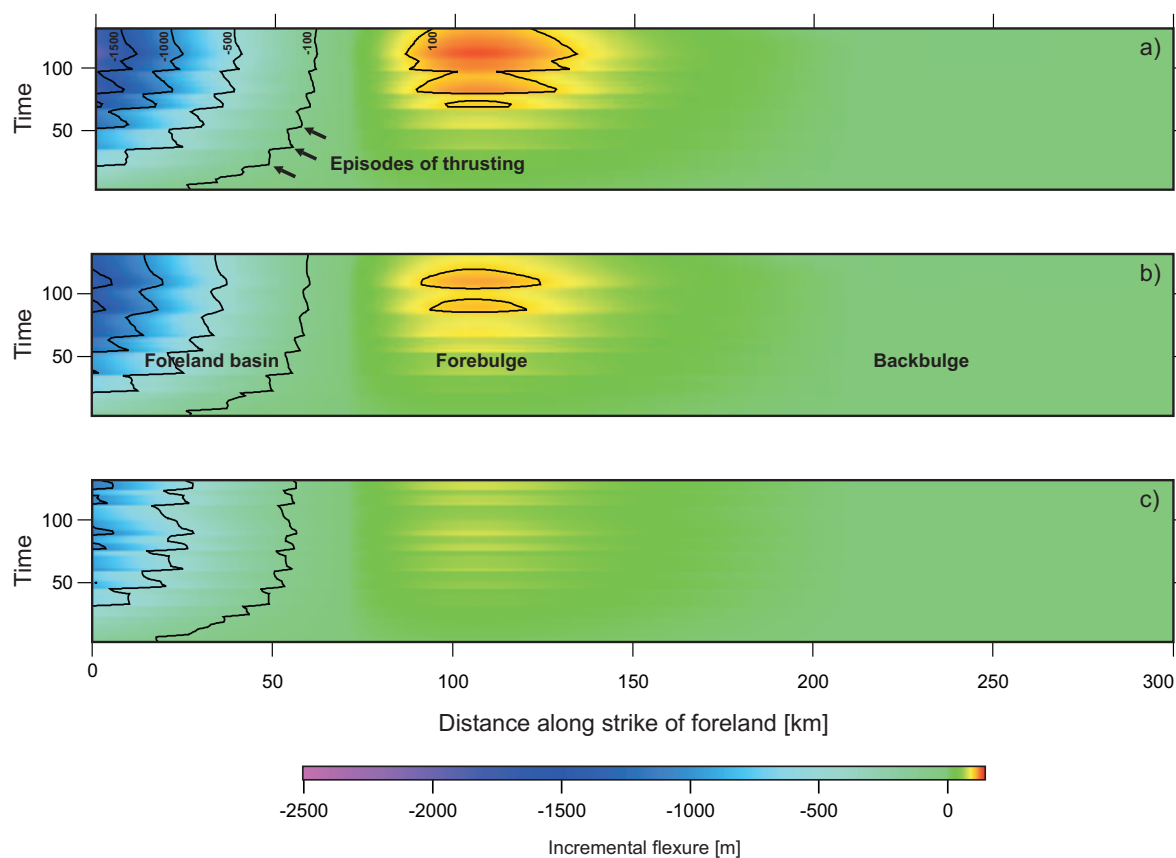


Figure 8.3: Spatio-temporal evolution of hypothetical foreland basins. See text for derivation. (a) Reference experiment; Distributed erosion of: (b) Retro-wedge, (c) Pro-wedge.

wedge decreases while the former grows laterally, the above far-field influence might be only detectable during early stages of convergence.

Episodes of thrust activity result in transgression-regression cycles, where transgressions on the distal side correlate with regressions on the proximal or forebulge side (Fig. 8.3, Flemings and Jordan (1990)). Such a scenario is supported by observations from the Karoo Basin, which formed in response to the advance of the Cape Fold Belt (Catuneanu and Elango, 2001). The Late Permian to Early Triassic Balfour Formation, which was deposited during the overfilled phase of the Karoo Basin, consists of six third-order depositional sequences separated by prominent subaerial unconformities.

In the absence of any evidence for a climatic or eustatic forcing, these six sequences are thought to result from thrust episodes within the Cape Fold Belt (Catuneanu and Elango, 2001). The average duration of each cycle was calculated to be  $0.66Ma$ .

Similarly, thrusting within the Swiss Alps might explain the stepwise nature of transgressions within the North Alpine Foreland basin between  $50Ma$  and  $37Ma$  (Kempf and Pfiffner, 2004). This observation has been previously attributed to crustal-scaled inhomogeneities, which tend to focus plate bending (Waschbusch and Royden, 1992). Thus, further analysis of the kinematic evolution of the advancing Alpine orogen is required to address this issue.

Migration of an orogen towards its foreland is associated with a coevally migrating flexural wave. In submarine foreland basins forebulges are preferred sites for carbonate platforms to develop (Crampton and Allen, 1995; DeCelles and Giles, 1996). Consequently, sites of active carbonate deposition may first experience uplift and erosion, associated with karstification and are finally drowned due to the submergence beneath the photic zone (Galewsky, 1998). Carbonate platform drowning is controlled by the maximum upward growth potential of the platform-building organisms and the rate of sea level rise relative to the platform. The latter depends on the tectonically induced subsidence and on eustatic sea-level variations. It follows that the interplay between deformation and surface processes within the advancing orogen controls the duration of forebulge uplift and thus the degree of karstification (Crampton and Allen, 1995) and finally the rate of drowning. In the North Alpine Foreland basin, karstification below the drowning unconformity surface reaches up to 100m down into the limestones, resulting in an extensive interconnected system of macropores, which may finally form hydrocarbon reservoirs (Crampton and Allen, 1995). Thus, the understanding of the eroding orogen may finally help to predict forebulge plays. Furthermore, forebulge unconformities are preferred sites of Mississippi Valley Type deposits (Leach et al., 2001; Bradley and Leach, 2003). Their formation might be induced by an eroding orogen, hundreds of kilometers away.

## 9 Perspectives

Scaled 2D sandbox simulations were used to investigate the influence of kinematic boundary conditions as well as erosion on bivergent wedge-evolution. Analysis of experimentally derived data focused on: (i) the spatio-temporal distribution of deformation, (ii) the associated surface uplift and (iii) particle paths. These results were compared with observations from other simulation as well as field studies and were found to be in general agreement. A variety of predictions has been derived, among them: (i) the four-staged evolutionary model, (ii) the accretion cycle, which imposes an internal clock to wedge-scaled deformation, (iii) strain partitioning in time and space, (iv) the system-immanent variability in strain accumulation, (v) the derivation of an end-member model, i. e., time-predictable versus spacing-predictable, which bears some implications for hazard assessment studies, (vi) far-field effects, i. e., retro-wedge erosion influences the deformation within the pro-wedge and thus the evolution of the proforedeep, (vii) the Flysch to Molasse transition and finally, (viii) implications for fluid flow and associated ore/hydrocarbon deposits in continental collision zones. Nevertheless this study could be faced with the question that no individual natural laboratory has been used to tie and to compare with. However, two arguments are raised in favour of the strategy, which investigates parameters first and looks at specific mountain belts second. First, not all data needed to compare experimental results with nature are available for one orogen or for a specific time interval. Second, and probably most importantly, boundary conditions do matter. The perception of how nature works commonly guides the setup of physical and numerical simulations. The respective results and interpretations do however only mirror the interplay of the kinematic and dynamic boundary conditions and thus reflect finally the initial perception. In addition,

subtle parameter variations, whose natural variations are poorly known, may not be appropriate for a first order study, unless testable predictions are derived. We finally conclude that changing the boundary conditions during simulations, identifying their equivalents in nature while transferring experimentally derived time-series to nature, is and remains a very crucial issue to unravel such beautiful processes as mountain building. Future work shall be aimed at testing the above predictions and hypotheses.



# Acknowledgements

This work would not have been possible without the encouraging words, the stimulating discussions as well as the patience assistance during experimental runs of those, with whom I had the pleasure to share ideas and enthusiasm with.

I am indebted to Prof. Onno Oncken for fruitful discussions and for providing the freedom to explore ideas. Prof. Manfred Strecker is kindly thanked for introducing me to the world of surface processes and for the push from the rear. Prof. Onno Oncken and Prof. Manfred Strecker are thanked as well for writing the expertise. I am grateful to Dr. Nina Kukowski for encouraging and very stimulating discussions during long nights of science and non-science. Prof. Anke Friedrich is kindly thanked for providing insight to palaeoseismology and for encouraging me to use time series.

I am very much indebted to Arne Hoffmann-Rothe for his enthusiasm and his dedication to address challenges. I did very much appreciate our discussions on strain partitioning, the grand unifying theory and the meaning of life.

Many thanks go to Tim Vietor for sharing his knowledge and for his commitment while exploring experimental data.

Jürgen Adam and Jo Lohrmann are thanked for introducing me to analogue simulations.

I also would like to thank all those, with whom I had the pleasure to share discussion with, namely: Sean Willett, George Hilley, Adrian Pfiffner, Dimitrios Sokoutis, Hugh Sinclair, Guy Simpson, Niels Hovius, Jan Pfeifer, Rasmus Thiede and Dirk Scherler. Stimulating reviews by Fabrizio Storti and Peter O. Koons are greatly appreciated. Ulrich Riller is thanked for suggestions on an earlier version of the GSA paper.

Stefan Heinz helped with great enthusiasm to endeavor the maths behind the critical wedge theory. An introduction to  $\LaTeX$  was kindly and sometimes patiently provided by Arne Hoffmann-Rothe and Stefan Heinz. Karsten Pfeiffer from LaVision is thanked for addressing all the challenges imposed by DaVis, often in the latest minute - just before an experiment was due to start.

Charlotte Krawczyk is thanked for guiding me through group-dynamic processes. Helmut Echter is thanked for his fatherly attitude. Maike Buddensiek is kindly thanked for her assistance while calculating an  $\alpha - \beta$  stability field and for proofreading. Remaining errors are, of course, my responsibility. Raik Bachmann and Tina Lohr are thanked for a pleasant atmosphere, while sharing the office and for being patient with me during the last weeks of writing up.

I also would like to thank Manuela Dziggel and Andreas Hendrich for their help concerning graphics and layout. Brigitte Stöcker helped to improve the appearance of the experiment photos. Petra Paschke and Gisela Wolff provided administrative support.

All experiments were carried out in the Geodynamics Laboratory of the GeoForschungsZentrum Potsdam, Germany, with the patient assistance of the Analogue-Lab-Crew, Ulricke Schönrock and Aissa Rechlin. Günther Tauscher with his famous hands built the experimental setup. Funding was kindly provided by Deutsche Forschungsgemeinschaft (DFG Leibniz-Program), Sonderforschungsbereich 267 project F1 and CSAG.

Finally, I would like to thank Angela and Arthur for their encouragement, their understanding, and loving support.



# References

- Adam, J., Urai, J., Wieneke, B., Oncken, O., Pfeiffer, K., Kukowski, N., Lohrmann, J., Hoth, S., van der Zee, W. and Schmatz, J. (2005). Shear localisation and strain distribution during tectonic faulting—new insights from granular-flow experiments and high-resolution optical image correlation techniques. *Journal of Structural Geology*, 27(2), 283–301.
- Adams, J. (1980). Contemporary uplift and erosion of the Southern Alps, New Zealand. *Geological Society of America Bulletin*, 91(1), I 2–I 4, II 1–II 114.
- Ahnert, F. (1970). Functional relationships between denudation, relief, and uplift in large, mid-latitude drainage basins. *American Journal of Science*, 268(3), 243–263.
- Ahnert, F. (1999). *Einführung in die Geomorphologie*. Eugen Ulmer, Stuttgart, 2 edition.
- Allaby, A. and Allaby, M. (1999). *The concise Oxford dictionary of Earth sciences*. Oxford University Press, Oxford, 2 edition.
- Allen, P. and Allen, J. (2005). *Basin analysis, Principles and applications*. Blackwell Publishing, Oxford, 2 edition.
- Allen, P. A., Burgess, P. M., Galewsky, J. and Sinclair, H. D. (2001). Flexural-eustatic numerical model for drowning of the Eocene perialpine carbonate ramp and implications for Alpine geodynamics. *Geological Society of America Bulletin*, 113(8), 1052–1066.
- Allen, P. A., Crampton, S. L. and Sinclair, H. D. (1991). The inception and early evolution of the North Alpine foreland basin, Switzerland. *Basin Research*, 3(3), 143–163.
- Avouac, J. P. and Burov, E. B. (1996). Erosion as a driving mechanism of intracontinental mountain growth. *Journal of Geophysical Research*, B, 101(8), 17,747–17,769.
- Badertscher, N. P., Beaudoin, G., Therrien, R. and Burkhard, M. (2002). Glarus overthrust: A major pathway for the escape of fluids out of the Alpine orogen. *Geology*, 30(10), 875–878.
- Bangs, N. L. B., Shipley, T. H., Moore, J. C. and Moore, G. F. (1999). Fluid accumulation and channeling along the northern Barbados Ridge décollement thrust. *Journal of Geophysical Research*, B, 104(9), 20,399–20,414.
- Barnard, P. L., Owen, L. A., Sharma, M. C. and Finkel, R. C. (2004). Late Quaternary (Holocene) landscape evolution of a monsoon-influenced high Himalayan valley, Gori Ganga, Nanda Devi, NE Garhwal. *Geomorphology*, 61(1-2), 91–110.
- Barr, T. D. and Dahlen, F. A. (1989). Brittle frictional mountain building; 2, Thermal structure and heat budget. *Journal of Geophysical Research*, B, 94(4), 3923–3947.
- Barr, T. D., Dahlen, F. A. and McPhail, D. C. (1991). Brittle frictional mountain building; 3, Low-grade metamorphism. *Journal of Geophysical Research*, B, 96(6), 10,319–10,338.
- Barrier, L., Nalpas, T., Gapais, D., Proust, J. N., Casas, A. and Bourquin, S. (2002). Influence of syntectonic sedimentation on thrust geometry; field examples from the Iberian Chain (Spain) and analogue modelling. *Sedimentary Geology*, 146(1-2), 91–104.
- Batt, G. E. and Braun, J. (1999). The tectonic evolution of the Southern Alps, New Zealand: Insights from fully thermally coupled dynamical modelling. *Geophysical Journal International*, 136(2), 403–420.
- Beaumont, C. (1981). Foreland basins. *Geophysical Journal, Royal Astronomical Society*, 65(2), 291–329.
- Beaumont, C., Ellis, S., Hamilton, J. and Fullsack, P. (1996). Mechanical model for subduction-collision tectonics of alpine-type compressional orogens. *Geology*, 24(8), 675–678.
- Beaumont, C., Fullsack, P. and Hamilton, J. (1992). Erosional control of active compressional orogens. In McClay, K. R., editor, *Thrust tectonics*, pages 1–18. Chapman and Hall, London, United Kingdom.
- Beaumont, C., Jamieson, R. A., Nguyen, M. H. and Lee, B. (2001). Himalayan tectonics explained by extrusion of a low-viscosity crustal channel coupled to focused surface denudation. *Nature (London)*, 414(6865), 738–742.



- Beaumont, C., Munoz, J. A., Hamilton, J. and Fullsack, P. (2000). Factors controlling the Alpine evolution of the central Pyrenees inferred from a comparison of observations and geodynamical models. *Journal of Geophysical Research, B*, 105(4), 8121–8145.
- Bernal, A., Hardy, S., Gawthorpe, R. and Finch, E. (2004). Stratigraphic expression of the lateral propagation and growth of isolated fault-related uplifts. *Basin Research*, 16(2), 219–233.
- Bilham, R., Larson, K. M., Freymueller, J. T., Jouanne, F., Le, F. P., Leturmy, P., Mugnier, J. L., Gamond, J. F., Glot, J. P., Martinod, J., Chaudury, N. L., Chitrakar, G. R., Gautam, U. P., Koirala, B. P., Pandey, M. R., Ranabhat, R., Sapkota, S. N., Shrestha, P. L., Thakuri, M. C., Timilsina, U. R., Tiwari, D. R., Vidal, G., Vigny, C., Galy, A. and de, V. B. (1997). GPS measurements of present-day convergence across the Nepal Himalaya. *Nature (London)*, 386(6620), 61–64.
- Bombolakis, E. G. (1986). Thrust-fault mechanics and origin of a frontal ramp. In *Thrusting and deformation*, volume 8; 3-4, pages 281–290. Pergamon, Oxford-New York, International.
- Bonini, M., Sokoutis, D., Talbot, C. J., Boccaletti, M. and Milnes, A. G. (1999). Indenter growth in analogue models of Alpine-type deformation. *Tectonics*, 18(1), 119–128.
- Bookhagen, B., Thiede, R. C. and Strecker, M. R. (2005). Late Quaternary intensified monsoon phases control landscape evolution in the northwest Himalaya. *Geology*, 33(2), 149–152.
- Boyer, S. E. (1992). Geometric evidence for synchronous thrusting in the southern Alberta and Northwest Montana thrust belts. In McClay, K. R., editor, *Thrust tectonics*, pages 377–390. Chapman and Hall, London, United Kingdom.
- Boyer, S. E. (1995). Sedimentary basin taper as a factor controlling the geometry and advance of thrust belts. *American Journal of Science*, 295(10), 1220–1254.
- Boyer, S. E. and Elliott, D. (1982). Thrust systems. *American Association of Petroleum Geologists Bulletin*, 66(9), 1196–1230.
- Brace, W. F. and Kohlstedt, D. L. (1980). Limits on lithospheric stress imposed by laboratory experiments. *Journal of Geophysical Research, B*, 85(11), 6248–6252.
- Bradley, D. C. and Leach, D. L. (2003). Tectonic controls of Mississippi Valley-type lead-zinc mineralization in orogenic forelands. *Mineralium Deposita*, 38(6), 652–667.
- Brandon, M. T. and Calderwood, A. R. (1990). High-pressure metamorphism and uplift of the Olympic subduction complex. *Geology*, 18(2), 1252–1255.
- Burbank, D. and Anderson, R. (2001). *Tectonic Geomorphology*. Blackwell Publishing, Oxford, 1 edition.
- Burbank, D. W. (2002). Rates of erosion and their implications for exhumation. *Mineralogical Magazine*, 66(1), 25–52.
- Burbank, D. W. and Beck, R. A. (1991). Rapid, long-term rates of denudation. *Geology*, 19(12), 1169–1172.
- Burbank, D. W., Blythe, A. E., Putkonen, J., Pratt, S. B., Gabet, E., Oskin, M., Barros, A. and Ojha, T. P. (2003). Decoupling of erosion and precipitation in the Himalayas. *Nature (London)*, 426(6967), 652–655.
- Burbidge, D. R. and Braun, J. (1998). Analogue models of obliquely convergent continental plate boundaries. *Journal of Geophysical Research, B*, 103(B7), 15221–15237.
- Butler, R. W. H. (1987). Thrust sequences. *Journal of the Geological Society of London*, 144(4), 619–634.
- Butler, R. W. H. (2004). The nature of "roof thrusts" in the Moine thrust belt, NW Scotland: implications for the structural evolution of thrust belts. *Journal of the Geological Society of London*, 161(5), 849–859.
- Butler, R. W. H. and Bowler, S. (1995). Local displacement rate cycles in the life of a fold-thrust belt. *Terra Nova*, 7(4), 408–416.
- Byerlee, J. (1978). Friction of rocks. *Pure Appl. geophys.*, 116(4-5), 615–626.

- Byrne, D. E., Davis, D. M. and Sykes, L. R. (1988). Loci and maximum size of thrust earthquakes and the mechanics of the shallow region of subduction zones. *Tectonics*, 7(4), 833–857.
- Byrne, D. E., Wang, W. h. and Davis, D. M. (1993). Mechanical role of backstops in the growth of forearcs. *Tectonics*, 12(1), 123–144.
- Cadell, H. M. (1888). Experimental researches in mountain building. *Transactions of the Royal Society of Edinburgh*, 35.
- Calassou, S., Larroque, C. and Malavieille, J. (1993). Transfer zones of deformation in thrust wedges; an experimental study. *Tectonophysics*, 221(3-4), 325–344.
- Catuneanu, O. and Elango, H. N. (2001). Tectonic control on fluvial styles: The Balfour formation of the Karoo Basin, South Africa. *Sedimentary Geology*, 140(3-4), 291–313.
- Chapple, W. (1978). Mechanics of thin-skinned fold-and-thrust belts. *Bulletin of the Geological Society of America*, 89, 1189–1198.
- Clevis, Q., De Boer, P. L. and Nijman, W. (2004). Differentiating the effect of episodic tectonism and eustatic sea-level fluctuations in foreland basins filled by alluvial fans and axial deltaic systems: insights from a three-dimensional stratigraphic forward model. *Sedimentology*, 51(4), 809–835.
- Cobbold, P. R., Durand, S. and Mourgues, R. (2001). Sandbox modelling of thrust wedges with fluid-assisted detachments. *Tectonophysics*, 334(3-4), 245–258.
- Conrad, C. P. and Lithgow Bertelloni, C. (2004). The temporal evolution of plate driving forces: Importance of "slab suction" versus "slab pull" during the Cenozoic. *Journal of Geophysical Research*, B, 109(10), B10407 1–14.
- Corrado, S., Di Bucci, D., Naso, G. and Faccenna, C. (1998). Influence of palaeogeography on thrust system geometries: An analogue modelling approach for the Abruzzi-Molise (Italy) case history. *Tectonophysics*, 296(3-4), 437–453.
- Corti, G., Bonini, M., Conticelli, S., Innocenti, F., Manetti, P. and Sokoutis, D. (2003). Analogue modelling of continental extension: A review focused on the relations between the patterns of deformation and the presence of magma. *Earth Science Reviews*, 63(3-4), 169–247.
- Coutand, I., Strecker, M. R., Arrowsmith, J. R., Hilley, G., Thiede, R. C., Korjenkov, A. and Omuraliev, M. (2002). Late Cenozoic tectonic development of the intramontane Alai Valley, (Pamir-Tien Shan region, central Asia): An example of intracontinental deformation due to the Indo-Eurasia collision. *Tectonics*, 21(6), 3–1 – 3–19.
- Couzens-Schultz, B. A., Vendeville, B. C. and Wiltshko, D. V. (2003). Duplex style and triangle zone formation: Insights from physical modeling. *Journal of Structural Geology*, 25(10), 1623–1644.
- Covey, M. (1986). The evolution of foreland basins to steady state: evidence from the western Taiwan foreland basin. In Allen, P. A. and Homewood, P., editors, *Foreland basins*, pages 77–90. Blackwell Scientific; Special Publication International Association of Sedimentologists 8.
- Crampton, S. L. and Allen, P. A. (1995). Recognition of forebulge unconformities associated with early stage foreland basin development: example from the north Alpine foreland basin. *American Association of Petroleum Geologists Bulletin*, 79(10), 1495–1514.
- Craw, D. and Campbell, J. R. (2004). Tectonic and structural setting for active mesothermal gold vein systems, Southern Alps, New Zealand. *Journal of Structural Geology*, 26(6-7), 995–1005.
- Craw, D., Koons, P. O., Horton, T. and Chamberlain, C. P. (2002). Tectonically driven fluid flow and gold mineralisation in active collisional orogenic belts: Comparison between New Zealand and western Himalaya. *Tectonophysics*, 348(1-3), 135–153.
- Crider, J. G. and Peacock, D. C. P. (2004). Initiation of brittle faults in the upper crust: A review of field observations. *Journal of Structural Geology*, 26(4), 691–707.
- Dadson, S. J., Hovius, N., Chen, H., Dade, W. B., Hsieh, M. L., Willett, S. D., Hu, J. C., Horng, M. J.,

- Chen, M. C., Stark, C. P., Lague, D. and Lin, J. C. (2003). Links between erosion, runoff variability and seismicity in the Taiwan Orogen. *Nature (London)*, 426(6967), 648–651.
- Dahlen, F. A. (1984). Noncohesive critical Coulomb wedges; an exact solution. *Journal of Geophysical Research, B*, 89, 10,125–10,133.
- Dahlen, F. A. (1990). Critical taper model of fold-and-thrust belts and accretionary wedges. *Annual Review of Earth and Planetary Sciences*, 88, 55–99.
- Dahlen, F. A. and Barr, T. D. (1989). Brittle frictional mountain building; 1, Deformation and mechanical energy budget. *Journal of Geophysical Research, B*, 94(4), 3906–3922.
- Dahlen, F. A. and Suppe, J. (1988). Mechanics, growth, and erosion of mountain belts. In Clark, S., Burchfield, B. c. and Suppe, J., editors, *Processes in Continental Lithospheric Deformation*, volume 218, pages 161–178.
- Dahlen, F. A., Suppe, J. and Davis, D. (1984). Mechanics of fold-and-thrust belts and accretionary wedges; cohesive Coulomb theory. *Journal of Geophysical Research, B*, 89, 10,087–10,101.
- Davis, D., Suppe, J. and Dahlen, F. A. (1983). Mechanics of fold-and-thrust belts and accretionary wedges. *Journal of Geophysical Research, B*, 88(2), 1153–1172.
- DeCelles, P. G. and Giles, K. A. (1996). Foreland basin systems. *Basin Research*, 8(2), 105–123.
- Del Castello, M., Pini, G. A. and McClay, K. R. (2004). Effect of unbalanced topography and overloading on Coulomb wedge kinematics: Insights from sandbox modeling. *Journal of Geophysical Research, B*, 109(5), 1–17.
- Densmore, A. L., Ellis, M. A. and Anderson, R. S. (1998). Landsliding and the evolution of normal-fault-bounded mountains. *Journal of Geophysical Research, B*, 103(7), 15,203–15,219.
- Densmore, A. L. and Hovius, N. (2000). Topographic fingerprints of bedrock landslides. *Geology*, 28(4), 371–374.
- Dewey, J. F. (1982). Plate tectonics and the evolution of the British Isles. *Journal of the Geological Society of London*, 139(4), 371–412.
- DiLeonardo, C. G., Moore, J. C., Nissen, S. and Bangs, N. (2002). Control of internal structure and fluid-migration pathways within the Barbados Ridge décollement zone by strike-slip faulting: Evidence from coherence and three-dimensional seismic amplitude imaging. *Bulletin of the Geological Society of America*, 114(1), 51–63.
- Dixon, J. S. (1982). Regional structural synthesis, Wyoming salient of Western Overthrust belt. *American Association of Petroleum Geologists Bulletin*, 66(10), 1560–1580.
- Dominguez, S., Lallemand, S. E., Malavieille, J. and von Huene, R. (1998). Upper plate deformation associated with seamount subduction. *Tectonophysics*, 293(3-4), 207–224.
- Elger, K., Oncken, O. and Glodny, J. (2005). Plateau-style accumulation of deformation - the Southern Altiplano. *Tectonics*, 24, TC4020 1–22.
- Ellis, S. (1996). Forces driving continental collision: reconciling indentation and mantle subduction tectonics. *Geology*, 24(8), 699–702.
- Ellis, S., Fullsack, P. and Beaumont, C. (1995). Oblique convergence of the crust driven by basal forcing: implications for length-scales of deformation and strain partitioning in orogens. *Geophysical Journal International*, 120(1), 24–44.
- England, P. C. and Molnar, P. (1990). Surface uplift, uplift of rocks, and exhumation of rocks. *Geology*, 18(12), 1173–1177.
- Filizola, N., Fraizy, P., Guyot, J. L. and Seyler, F. (2002). Actual erosion by rivers in the Bolivian Andes. In *Andean Geodynamics (ISAG)*, pages 211–214, Toulouse. Institut recherche pour le développement (IRD).
- Fitzgerald, P. G., Munoz, J. A., Coney, P. J. and Baldwin, S. L. (1999). Asymmetric exhumation across the Pyrenean Orogen; implications for the tectonic evolution of a collisional orogen. *Earth and Planetary Science Letters*, 173(3), 157–170.

- Flemings, P. B. and Jordan, T. E. (1989). A synthetic stratigraphic model of foreland basin development. *Journal of Geophysical Research*, B, 94(4), 3851–3866.
- Flemings, P. B. and Jordan, T. E. (1990). Stratigraphic modeling of foreland basins; interpreting thrust deformation and lithosphere rheology. *Geology*, 18(5), 430–434.
- Fujii, Y. (1969). Frequency distribution of the magnitude of the landslides caused by heavy rain-fall. *Zisin = Jishin*, 22(2), 244–247.
- Galewsky, J. (1998). The dynamics of foreland basin carbonate platforms: tectonic and eustatic controls. *Basin Research*, 10(4), 409–416.
- Gerbault, M. and Garcia-Castellanos, D. (2005). Fluvial transport and tectonics: cyclic growth of relief in orogenic high plateau setting. In *EGU*, volume 7, page 2, Vienna. European Geosciences Union.
- Goff, D. and Wiltschko, D. V. (1992). Stresses beneath a ramping thrust sheet. *Journal of Structural Geology*, 14(4), 437–449.
- Gutscher, M. A., Kukowski, N., Malavieille, J. and Lallemand, S. (1996). Cyclical behavior of thrust wedges; insights from high basal friction sandbox experiments. *Geology*, 24(2), 135–138.
- Gutscher, M. A., Kukowski, N., Malavieille, J. and Lallemand, S. E. (1998). Episodic imbricate thrusting and underthrusting; analog experiments and mechanical analysis applied to the Alaskan accretionary wedge. *Journal of Geophysical Research*, B, 103(5), 10,161–10,176.
- Guzzetti, F., Malamud, B. D., Turcotte, D. L. and Reichenbach, P. (2002). Power-law correlations of landslide areas in central Italy. *Earth and Planetary Science Letters*, 195(3-4), 169–183.
- Hall, R. and Nichols, G. (2002). Cenozoic sedimentation and tectonics in Borneo; climatic influences on orogenesis. In *Sediment flux to basins; causes, controls and consequences*, pages 5–22. Geological Society London; Special Publication 191, London.
- Hallet, B., Hunter, L. and Bogen, J. (1996). Rates of erosion and sediment evacuation by glaciers; a review of field data and their implications. *Global and Planetary Change*, 12(1-4), 213–235.
- Harbor, J. and Warburton, J. (1993). Relative rates of glacial and nonglacial erosion in alpine environments. *Arctic and Alpine Research*, 25(1), 1–7.
- Hardy, S., Duncan, C., Masek, J. and Brown, D. (1998). Minimum work, fault activity and the growth of critical wedges in fold and thrust belts. *Basin Research*, 10, 365–373.
- Hay, W. W. (1996). Tectonics and climate. *International Journal of Earth Sciences*, 85(3), 409–437.
- Hilley, G. and Strecker, M. (2005). Processes of oscillatory basin filling and excavation in a tectonically active orogen: Quebrada del Toro Basin, NW Argentina. *Bulletin of the Geological Society of America*, 117(7-8), 887–901.
- Hilley, G. E. and Strecker, M. (2004). Steady state erosion of critical Coulomb wedges with applications to Taiwan and the Himalaya. *Journal of Geophysical Research*, B, 109(01411 1-17).
- Hilley, G. E., Strecker, M. R. and Ramos, V. A. (2004). Growth and erosion of fold-and-thrust belts with an application to the Aconcagua fold-and-thrust belt, Argentina. *Journal of Geophysical Research*, B, 109(1), 01410 1–19.
- Hodges, K. V., Wobus, C., Ruhl, K., Schildgen, T. and Whipple, K. (2004). Quaternary deformation, river steepening, and heavy precipitation at the front of the Higher Himalayan ranges. *Earth and Planetary Science Letters*, 220(3-4), 379–389.
- Hoffmann-Rothe, A., Kukowski, N. and Oncken, O. (2004). Phase dependent strain partitioning in obliquely convergent settings. In *Bollettino di Geofisica*, volume 45 (1 suppl), pages 93–97. GeoMod2004.
- Horton, B. K. (1999). Erosional control on the geometry and kinematics of thrust belt development in the Central Andes. *Tectonics*, 18(6), 1292–1304.
- Hoth, S., Adam, J., Kukowski, N. and Oncken, O. (2006). Influence of erosion on the kinematics of

- bivergent orogens. Results from scaled sandbox simulations. In Willett, S., Hovius, N., Brandon, M. and Fisher, D., editors, *Tectonics, Climate and Landscape Evolution, GSA Special Paper 398, Penrose Conference Series*, pages 201–225.
- Hovius, N. (1996). Regular spacing of drainage outlets from linear mountain belts. *Basin Research*, 8(1), 29–44.
- Hovius, N. (1998). Controls on sediment supply by large rivers. In *Relative role of eustasy, climate, and tectonism in continental rocks*, volume 59, pages 3–16. Society for Sedimentary Geology (SEPM), Tulsa, OK, United States.
- Hovius, N. (2000). Macroscale process systems of mountain belt erosion. In Summerfield M., A., editor, *Geomorphology and global tectonics*, pages 77–205. John Wiley, Chichester, United Kingdom.
- Hovius, N., Stark, C. P. and Allen, P. A. (1997). Sediment flux from a mountain belt derived by landslide mapping. *Geology*, 25(3), 231–234.
- Howard, A. D., Dietrich, W. E. and Seidl, M. A. (1994). Modeling fluvial erosion on regional to continental scales. *Journal of Geophysical Research*, B, 99(7), 13,971–13,986.
- Hubbert, M. (1937). Theory of scale models as applied to the study of geological structures. *Bulletin of the Geological Society of America*, 48, 1459–1520.
- Hubbert, M. K. and Rubey, W. W. (1959). Mechanics of fluid-filled porous solids and its application to overthrust faulting, [Part] 1 of Role of fluid pressure in mechanics of overthrust faulting. *Geological Society of America Bulletin*, 70(2), 115–166.
- Hubert-Ferrari, A., Suppe, J., Van Der Woerd, J., Xin, W. and Lu, H. (2005). Irregular earthquake cycle along the southern Tianshan front, Aksu area, China. *Journal of Geophysical Research*, B, 110, 06402 1–18.
- Jackson, J., Ritz, J.-F., Siame, L., Raisbeck, G., Yiou, F., Norris, R., Youngson, J. and Bennett, E. (2002). Fault growth and landscape development rates in Otago, New Zealand, using in situ cosmogenic <sup>10</sup>Be. *Earth and Planetary Science Letters*, 195(3-4), 185–193.
- Jamison, W. R. (1993). Mechanical stability of the triangle zone: the backthrust wedge. *Journal of Geophysical Research*, B, 98(11), 20,015–20,030.
- Ji, J., Shen, J., Balsam, W., Chen, J., Liu, L. and Liu, X. (2005). Asian monsoon oscillations in the north-eastern Qinghai-Tibet Plateau since the late glacial as interpreted from visible reflectance of Qinghai Lake sediments. *Earth and Planetary Science Letters*, 233(1-2), 61–70.
- Jones, M. A., Heller, P. L., Roca, E., Garces, M. and Cabrera, L. (2004). Time lag of syntectonic sedimentation across an alluvial basin: Theory and example from the Ebro Basin, Spain. *Basin Research*, 16(4), 467–488.
- Jordan, T. E. and Flemings, P. B. (1991). Large-scale stratigraphic architecture, eustatic variation, and unsteady tectonism: a theoretical evaluation. *Journal of Geophysical Research*, B, 96(4), 6681–6699.
- Jordan, T. E., Schlunegger, F. and Cardozo, N. (2001). Unsteady and spatially variable evolution of the Neogene Andean Bermejo foreland basin, Argentina. *Journal of South American Earth Sciences*, 14(7), 775–798.
- Karner, G. D. and Watts, A. B. (1983). Gravity anomalies and flexure of the lithosphere at mountain ranges. *Journal of Geophysical Research*, B, 88(12), 10449–10477.
- Keefer, D. K., Moseley, M. E. and deFrance, S. D. (2003). A 38 000-year record of floods and debris flows in the Ilo region of southern Peru and its relation to El Niño events and great earthquakes. *Palaeogeography, Palaeoclimatology, Palaeoecology*, 194(1-3), 41–77.
- Kempf, O. and Pfiffner, O. A. (2004). Early Tertiary evolution of the North Alpine Foreland Basin of the Swiss Alps and adjoining areas. *Basin Research*, 16(4), 549–567.
- Konstantinovskaia, E. and Malavieille, J. (2005). Erosion and exhumation in accretionary orogens: Experimental and geological approaches. *Geochemistry Geophysics Geosystems*, 6(2), 1–25.
- Koons, P. O. (1990). Two-sided orogen; collision and erosion from the sandbox to the Southern Alps, New Zealand. *Geology*, 18(8), 679–682.

- Koons, P. O. (1995). Modeling the topographic evolution of collisional belts. *Annual Review of Earth and Planetary Sciences*, 23, 375–408.
- Koons, P. O., Norris, R. J., Craw, D. and Cooper, A. F. (2003). Influence of exhumation on the structural evolution of transpressional plate boundaries; an example from the Southern Alps, New Zealand. *Geology*, 31(1), 3–6.
- Koons, P. O., Zeitler, P. K., Chamberlain, C. P., Craw, D. and Meltzer, A. S. (2002). Mechanical links between erosion and metamorphism in Nanga Parbat, Pakistan Himalaya. *American Journal of Science*, 302(9), 749–773.
- Kopp, H. and Kukowski, N. (2003). Backstop geometry and accretionary mechanics of the Sunda margin. *Tectonics*, 22(6), 11–1 – 11–16.
- Korup, O., McSaveney, M. J. and Davies, T. R. H. (2004). Sediment generation and delivery from large historic landslides in the Southern Alps, New Zealand. *Geomorphology*, 61(1-2), 189–207.
- Koyi, H. (1995). Mode of internal deformation in sand wedges. *Journal of Structural Geology*, 17(2), 293–300.
- Kuhlemann, J. (2000). Post-collisional sediment budget of circum-Alpine basins (Central Europe). *Memorie di Scienze Geologiche*, 52(1), 1–91.
- Kukowski, N., Lallemand, S. E., Malavieille, J., Gutscher, M.-A. and Reston, T. J. (2002). Mechanical decoupling and basal duplex formation observed in sandbox experiments with application to the Western Mediterranean Ridge accretionary complex. *Marine Geology*, 186(1-2), 29–42.
- Kukowski, N., von, H. R., Malavieille, J. and Lallemand, S. E. (1994). Sediment accretion against a buttress beneath the Peruvian continental margin at 12 degrees S as simulated with sandbox modeling. *Geologische Rundschau*, 83(4), 822–831.
- Kummerow, J., Kind, R., Oncken, O., Giese, P., Ryberg, T., Wylegalla, K. and Scherbaum, F. (2004). A natural and controlled source seismic profile through the Eastern Alps: TRANSALP. *Earth and Planetary Science Letters*, 225(1-2), 115–129.
- Kutzbach, J. E., Prell, W. L. and Ruddiman, W. F. (1993). Sensitivity of Eurasian climate to surface uplift of the Tibetan Plateau. *The Journal of Geology*, 101(2), 177–190.
- Kyser, K. and Hiatt, E. E. (2003). Fluids in sedimentary basins: An introduction. *Journal of Geochemical Exploration*, 80(2-3), 139–149.
- Labaume, P., Seguret, M. and Seyve, C. (1985). Evolution of a turbiditic foreland basin and analogy with an accretionary prism; example of the Eocene South-Pyrenean Basin. *Tectonics*, 4(7), 661–685.
- Lacombe, O. and Mouthereau, F. (2002). Basement-involved shortening and deep detachment tectonics in forelands of orogens; insights from recent collisions belts; Taiwan, Western Alps, Pyrenees. *Tectonics*, 21, 12–1 – 12–22.
- Lallemand, S. E., Schnuerle, P. and Malavieille, J. (1994). Coulomb theory applied to accretionary and nonaccretionary wedges; possible causes for tectonic erosion and/ or frontal accretion. *Journal of Geophysical Research*, B, 99(6), 12,033–12,055.
- Lavé, J. and Avouac, J. (2001). Fluvial incision and tectonic uplift across the Himalayas of central Nepal. *Journal of Geophysical Research*, B, 106(11), 26,561–26,591.
- Le Pichon, X., Lallemand, S. J., Chamot Rooke, N., Lemeur, D. and Pascal, G. (2002). The Mediterranean Ridge backstop and the Hellenic nappes. *Marine Geology*, 186(1-2), 111–125.
- Leach, D. L., Bradley, D., Lewchuk, M. T., Symons, D. T. A., de Marsily, G. and Brannon, J. (2001). Mississippi Valley-type lead-zinc deposits through geological time: Implications from recent age-dating research. *Mineralium Deposita*, 36(8), 711–740.
- Leeder, M. R. (1991). Denudation, vertical crustal movements and sedimentary basin fill. *Geologische Rundschau*, 80(2), 441–458.
- Leturmy, P., Mugnier, J. L., Vinour, P., Baby, P., Colletta, B. and Chabron, E. (2000). Piggyback basin development above a thin-skinned thrust belt with two detachment levels as a function of interactions between tectonic and superficial mass transfer; the case of the Subandean Zone (Bolivia). *Tectonophysics*, 320(1), 45–67.

- Lin, J. C. (2000). Morphotectonic evolution of Taiwan. In Summerfield M., A., editor, *Geomorphology and global tectonics*, pages 135–146. John Wiley, Chichester, United Kingdom.
- Liu, H., McClay, K. R. and Powell, D. (1992). Physical models of thrust wedges. In *Thrust tectonics*, pages 71–81. Chapman and Hall, London, United Kingdom.
- Lohrmann, J., Kukowski, N., Adam, J. and Oncken, O. (2003). The impact of analogue material properties on the geometry, kinematics, and dynamics of convergent sand wedges. *Journal of Structural Geology*, 25(10), 1691–1711.
- Luján, M., Storti, F., Balanya, J. C., Crespo Blanc, A. and Rossetti, F. (2003). Role of décollement material with different rheological properties in the structure of the Aljibe thrust imbricate (Flysch Trough, Gibraltar Arc): An analogue modelling approach. *Journal of Structural Geology*, 25(6), 867–881.
- Macedo, J. and Marshak, S. (1999). Controls on the geometry of fold-thrust belt salients. *Geological Society of America Bulletin*, 111(12), 1808–1822.
- Malavieille, J. (1984). Modélisation expérimentale des chevauchements imbriqués: application aux chaînes de montagnes. *Société Géologique de France, Bulletin*, 7, 129–138.
- Malavieille, J., Lallemand, S., Dominguez, S., Deschamps, A., Lu, C. Y., Liu, C. S. and Schnuerle, P., Angelier, J., Collot, J. Y., Deffontaines, B., Fournier, M., Hsu, S. K., Le, F., Liu, S. Y., Sibuet, J. C., Thureau, N. and Wang, F. (2002). Arc-continent collision in Taiwan; new marine observations and tectonic evolution. In Byrne, T. and Liu, C., editors, *Geology and geophysics of an arc-continent collision, Taiwan*, volume 358, pages 187–211. GSA.
- Mandl, G., de, J. L. N. J. and Maltha, A. (1977). Shear zones in granular material; an experimental study of their structure and mechanical genesis. *Rock Mechanics*, Supplementum 9(2-3), 95–144.
- Marques, F. O. and Cobbold, P. R. (2002). Topography as a major factor in the development of arcuate thrust belts; insights from sandbox experiments. *Tectonophysics*, 348(4), 247–268.
- Marshak, S. (2004). Salients, recesses, arcs, oroclines, and syntaxes; a review of ideas concerning the formation of map-view curves in fold-thrust belts. In *Thrust tectonics and hydrocarbon systems*, volume 82, pages 131–156. American Association of Petroleum Geologists, Memoir, Tulsa, OK, United States.
- Marshak, S. and Wilkerson, M. S. (1992). Effect of overburden thickness on thrust belt geometry and development. *Tectonics*, 11(3), 560–566.
- Martinez, A., Malavieille, J., Lallemand, S. and Collot, J. Y. (2002). Strain partitioning in an accretionary wedge, in oblique convergence: Analogue modelling. *Bulletin de la Société Géologique de France*, 173(1), 17–24.
- Masferro, J. L., Bulnes, M., Poblet, J. and Eberli, G. P. (2002). Episodic folding inferred from syntectonic carbonate sedimentation: The Santaren anticline, Bahamas foreland. *Sedimentary Geology*, 146(1-2), 11–24.
- Masek, J. G. and Duncan, C. C. (1998). Minimum-work mountain building. *Journal of Geophysical Research*, B, 103(1), 907–917.
- McClay, K. R. (1992). Glossary of thrust tectonics terms. In McClay, K. R., editor, *Thrust tectonics*, pages 419–433. Chapman and Hall, London, United Kingdom.
- McClay, K. R. (1996). Recent advances in analogue modelling; uses in section interpretation and validation. In Buchanan, P. G. and Nieuwland, D., editors, *Modern developments in structural interpretation, validation and modelling*, pages 201–225. Geological Society London; Special Publication 99.
- McClay, K. R. and Whitehouse, P. S. (2004). Analog modeling of doubly vergent thrust wedges. In *Thrust tectonics and hydrocarbon systems*, volume 82, pages 184–206. American Association of Petroleum Geologists, Memoir, Tulsa, OK, United States.
- McClay, K. R., Whitehouse, P. S., Dooley, T. and Richards, M. (2004). 3-D evolution of fold and thrust belts formed by oblique convergence. *Marine and Petroleum Geology*, 21(7), 857–877.

- Meigs, A. and Sauber, J. (2000). Southern Alaska as an example of the long-term consequences of mountain building under the influence of glaciers. *Quaternary Science Reviews*, 19(14-15), 1543–1562.
- Meigs, A. J. (1997). Sequential development of selected Pyrenean thrust faults. *Journal of Structural Geology*, 19(3-4), 481–502.
- Meigs, A. J. and Burbank, D. W. (1997). Growth of the south Pyrenean orogenic wedge. *Tectonics*, 16(2), 239–258.
- Meigs, A. J., Verges, J. and Burbank, D. W. (1996). Ten-million-year history of a thrust sheet. *Geological Society of America Bulletin*, 108(12), 1608–1625.
- Merle, O. and Abidi, N. (1995). Approche expérimentale du fonctionnement des ramps émergentes. *Société Géologique de France, Bulletin*, 166(5), 439–450.
- Milliman, J. D. and Syvitski, J. P. M. (1992). Geomorphic/ tectonic control of sediment discharge to the ocean; the importance of small mountainous rivers. *Journal of Geology*, 100(5), 525–544.
- Mitra, G. and Boyer, S. E. (1986). Energy balance and deformation mechanisms of duplexes. *Journal of Structural Geology*, 8(3-4), 291–304.
- Molnar, P. and Lyon, C. H. (1988). Some simple physical aspects of the support, structure, and evolution of mountain belts. In *Processes in continental lithospheric deformation*, volume 218; pages 179–207. Geological Society of America, Boulder, CO, United States.
- Montgomery, D. R., Balco, G. and Willett, S. D. (2001). Climate, tectonics, and the morphology of the Andes. *Geology*, 29(7), 579–582.
- Montgomery, D. R. and Brandon, M. T. (2002). Topographic controls on erosion rates in tectonically active mountain ranges. *Earth and Planetary Science Letters*, 201(3-4), 481–489.
- Moore, V. M. and Wiltschko, D. V. (2004). Syn-collisional delamination and tectonic wedge development in convergent orogens. *Tectonics*, 23(2), TC2005 1–27.
- Morellato, C., Redini, F. and Doglioni, C. (2003). On the number and spacing of faults. *Terra Nova*, 15(5), 315–321.
- Moretti, I., Labaume, P., Sheppard, S. and Boulegue, J. (2000). Compartmentalisation of fluid flow by thrust faults, Sub-Andean Zone, Bolivia. *Journal of Geochemical Exploration*, 69-70, 493–497.
- Morley, C. K. (1988). Out-of-sequence thrusts. *Tectonics*, 7(3), 539–561.
- Morris, R. G., Sinclair, H. D. and Yelland, A. J. (1998). Exhumation of the Pyrenean orogen; implications for sediment discharge. In *Basin research; thematic set on sediment supply to basins*, volume 10; 1, pages 69–85. Blackwell, Oxford, United Kingdom.
- Mouthereau, F., Lacombe, O., Deffontaines, B., Angelier, J. and Brusset, S. (2001). Deformation history of the southwestern Taiwan foreland thrust belt; insights from tectono-sedimentary analyses and balanced cross-sections. *Earth and Planetary Science Letters*, 333(1-2), 293–322.
- Mugnier, J. L., Baby, P., Colletta, B., Vinour, P., Bale, P. and Leturmy, P. (1997). Thrust geometry controlled by erosion and sedimentation; a view from analogue models. *Geology*, 25(5), 427–430.
- Muir-Wood, R. (1994). Earthquakes, strain-cycling and the mobilization of fluids. In Parnell, J., editor, *Geofluids: origin, migration and evolution of fluids in sedimentary basins*, pages 85–98. Geological Society London; Special Publication 78.
- Mulugeta, G. (1988). Modelling the geometry of Coulomb thrust wedges. *Journal of Structural Geology*, 10(8), 847–859.
- Mulugeta, G. and Koyi, H. (1992). Episodic accretion and strain partitioning in a model sand wedge. *Tectonophysics*, 202(2-4), 319–333.
- Najman, Y., Johnson, K., White, N. and Oliver, G. (2004). Evolution of the Himalayan foreland basin, NW India. *Basin Research*, 16(1), 1–24.
- Naylor, M., Sinclair, H., Willett, S. and Cowie, P. A. (2005). A Discrete Element Model for Orogenesis and Accretionary Wedge Growth. *Journal of Geophysical Research*, B, 110, 12403 1–16.



- Nicol, A., Gillespie, P. A., Childs, C. and Walsh, J. J. (2002). Relay zones between mesoscopic thrust faults in layered sedimentary sequences. *Journal of Structural Geology*, 24(4), 709–727.
- Nieuwland, D. A., Leutscher, J. H. and Gast, J. (2000). Wedge equilibrium in fold-and-thrust belts; prediction of out-of-sequence thrusting based on sandbox experiments and natural examples. *Geologie en Mijnbouw*, 79(1), 81–91.
- Nieuwland, D. A. and Walters, J. V. (1993). Geomechanics of the South Furious Field; an integrated approach towards solving complex structural geological problems, including analogue and finite-element modelling. *Tectonophysics*, 226(1-4), 143–166.
- Noever, D. A. (1993). Himalayan sandpiles. *Physical review*, 47(1), 724–725.
- Panian, J. and Wiltschko, D. (2004). Ramp initiation in a thrust wedge. *Nature (London)*, 427(6975), 624–627.
- Pavlis, T. L., Hamburger, M. W. and Pavlis, G. L. (1997). Erosional processes as a control on the structural evolution of an actively deforming fold and thrust belt; an example from the Pamir-Tien Shan region, Central Asia. *Tectonics*, 16(5), 810–822.
- Pazzaglia, F. J. and Brandon, M. T. (2001). A fluvial record of long-term steady-state uplift and erosion across the Cascadia forearc high, Western Washington State. *American Journal of Science*, 301(4), 385–431.
- Persson, K. S., Garcia-Castellanos, D. and Sokoutis, D. (2004). River transport effects on compressional belts: First results from an integrated analogue-numerical model. *Journal of Geophysical Research*, B, 109, 01409 1–11.
- Persson, K. S. and Sokoutis, D. (2002). Analogue models of orogenic wedges controlled by erosion. *Tectonophysics*, 356(4), 323–336.
- Pfiffner, O. A., Ellis, S. and Beaumont, C. (2000). Collision tectonics in the Swiss Alps; insight from geodynamic modeling. *Tectonics*, 19(6), 1065–1094.
- Platt, J. P. (1986). Dynamics of orogenic wedges and the uplift of high-pressure metamorphic rocks. *Geological Society of America Bulletin*, 97(9), 1037–1053.
- Platt, J. P. (1993). Exhumation of high-pressure rocks; a review of concepts and processes. *Terra Nova*, 5(2), 119–133.
- Price, R. A. (1973). Large-Scale Gravitational Flow of Supracrustal Rocks, Southern Canadian Rockies. In *Gravity and tectonics*. Pages 491-502.
- Ramberg, H. (1981). *Gravity, deformation and the earth's crust*. Academic Press, New York.
- Ranalli, G. (1995). *Rheology of the Earth*. Chapman and Hall, London, 2 edition.
- Rider, M. (2000). *The geological interpretation of well logs*. Whittles Publishing, Caithness, 2 edition.
- Ring, U., Brandon, M. T., Willett, S. D. and Lister, G. S. (1999). Exhumation processes. In *Exhumation processes; normal faulting, ductile flow and erosion*, pages 1–27. Geological Society London; Special Publication 154, London.
- Roddaz, M., Baby, P., Brusset, S., Hermoza, W. and Maria Darrozes, J. (2005). Forebulge dynamics and environmental control in Western Amazonia: The case study of the Arch of Iquitos (Peru). *Tectonophysics*, 399(1-4), 87–108.
- Rouré, F., Nazaji, S., Mushka, K., Fili, I., Cadet, J. P. and Bonneau, M. (2004). Kinematic evolution and petroleum systems; an appraisal of the outer Albanides. In *Thrust tectonics and hydrocarbon systems*, volume 82, pages 474–493. American Association of Petroleum Geologists, Memoir, Tulsa, OK, United States.
- Schäfer, F., Oncken, O., Kemnitz, H. and Romer, R. L. (2000). Upper-plate deformation during collisional orogeny; a case study from the German Variscides (Saxo-Thuringian Zone). In Franke, W., Haak, V., Oncken, O. and Tanner, D., editors, *Orogenic processes; quantification and modelling in the Variscan Belt*, pages 281–302. Geological Society London; Special Publication 179, London.

- Schellart, W. P. (2000). Shear test results for cohesion and friction coefficients for different granular materials; scaling implications for their usage in analogue modelling. *Tectonophysics*, 324(1-2), 1–16.
- Schlunegger, F. (1999). Controls of surface erosion on the evolution of the Alps; constraints from the stratigraphies of the adjacent foreland basins. *International Journal of Earth Sciences*, 88(2), 285–304.
- Schlunegger, F., Melzer, J. and Tucker, G. (2001). Climate, exposed source-rock lithologies, crustal uplift and surface erosion: a theoretical analysis calibrated with data from the Alps/North Alpine Foreland Basin system. *International Journal of Earth Sciences*, 90, 484–499.
- Schlunegger, F. and Simpson, G. (2002). Possible erosional control on lateral growth of the European Central Alps. *Geology*, 30(10), 907–910.
- Schlunegger, F. and Willett, S. D. (1999). Spatial and temporal variations in exhumation of the central Swiss Alps and implications for exhumation mechanisms. In Ring, U., Brandon, M. T., Lister, G. and Willett, S. D., editors, *Exhumation processes; normal faulting, ductile flow and erosion*, pages 157–179. Geological Society London; Special Publication 154, London.
- Schmidt, K. M. and Montgomery, D. R. (1995). Limits to relief. *Science*, 270(5236), 617–620.
- Schulze, D. (1994). Entwicklung und Anwendung eines neuartigen Ringschergerätes. *Aufbereitungstechnik*, 35(10), 524–535.
- Seidl, M. A. and Dietrich, W. E. (1992). The problem of channel erosion into bedrock. In *Functional geomorphology; landform analysis and models*, volume 23, pages 101–124. Catena-Verlag Rohdenburg.
- Selby, M. J. (1982). Controls on the stability and inclinations of hillslopes formed on hard rock. *Earth Surface Processes and Landforms*, 7(5), 449–467.
- Sheaf, M. A., Serpa, L. and Pavlis, T. L. (2003). Exhumation rates in the St. Elias Mountains, Alaska. *Tectonophysics*, 367(1-2), 1–11.
- Sibson, R. H. (1994). Crustal stress, faulting and fluid flow. In Parnell, J., editor, *Geofluids: origin, migration and evolution of fluids in sedimentary basins*, pages 69–84. Geological Society London; Special Publication 78.
- Silver, E. A. and Reed, D. L. (1988). Backthrusting in accretionary wedges. *Journal of Geophysical Research*, B, 93(4), 3116–3126.
- Simpson, G. (2004). Role of river incision in enhancing deformation. *Geology*, 32(4), 341–344.
- Simpson, G. and Schlunegger, F. (2003). Topographic evolution and morphology of surfaces evolving in response to coupled fluvial and hillslope sediment transport. *Journal of Geophysical Research*, B, 108(6), ETG 7–1 – 7–16.
- Sinclair, H. D. (1997a). Flysch to molasse transition in peripheral foreland basins; the role of the passive margin versus slab breakoff. *Geology*, 25(12), 1123–1126.
- Sinclair, H. D. (1997b). Tectonostratigraphic model for underfilled peripheral foreland basins; an Alpine perspective. *Geological Society of America Bulletin*, 109(3), 324–346.
- Sinclair, H. D. and Allen, P. A. (1992). Vertical versus horizontal motions in the Alpine orogenic wedge: stratigraphic response in the foreland basin. *Basin Research*, 4, 215–232.
- Sinclair, H. D., Coakley, B. J., Allen, P. A. and Watts, A. B. (1991). Simulation of foreland basin stratigraphy using a diffusion model of mountain belt uplift and erosion; an example from the Central Alps, Switzerland. *Tectonics*, 10(3), 599–620.
- Soto, R., Casas, A. M., Storti, F. and Faccenna, C. (2002). Role of lateral thickness variations on the development of oblique structures at the Western end of the South Pyrenean Central Unit. *Tectonophysics*, 350(3), 215–235.
- Spotila, J. A., Buscher, J. T., Meigs, A. J. and Reiners, P. W. (2004). Long-term glacial erosion of active mountain belts; example of the Chugach-St. Elias Range, Alaska. *Geology*, 32(6), 501–504.

- Stark, C. P. and Hovius, N. (2001). The characterization of landslide size distributions. *Geophysical Research Letters*, 28(6), 1091–1094.
- Storti, F., Marin, R. S., Faccenna, C. and Sainz, A. C. (2001). Role of the backstop-to-cover thickness ratio on vergence partitioning in experimental thrust wedges. *Terra Nova*, 13(6), 413–417.
- Storti, F. and McClay, K. R. (1995). Influence of syn-tectonic sedimentation on thrust wedges in analogue models. *Geology*, 23(11), 999–1002.
- Storti, F., Salvini, F. and McClay, K. R. (2000). Synchronous and velocity-partitioned thrusting and thrust polarity reversal in experimentally produced, doubly-vergent thrust wedges; implications for natural orogens. *Tectonics*, 19(2), 378–396.
- Strecker, M. R., Hilley, G. E., Arrowsmith, J. R. and Coutand, I. (2003). Differential structural and geomorphic mountain-front evolution in an active continental collision zone; the Northwest Pamir, southern Kyrgyzstan. *Geological Society of America Bulletin*, 115(2), 166–181.
- Stüwe, K. (2000). *Geodynamics of the Lithosphere An introduction*. Springer Verlag, Berlin.
- Sugai, T., Ohmori, H. and Hirano, M. (1994). Rock control on magnitude-frequency distribution of landslide. *Transactions of the Japanese Geomorphological Union*, 15(3), 233–251.
- Summerfield, M. A. and Brown, R. W. (1998). Geomorphic factors in the interpretation of fission-track data. In Van den Haute, P. and De Corte, F., editors, *Advances in fission-track geochronology*, pages 19–32. Kluwer, Dordrecht.
- Summerfield, M. A. and Hulton, N. J. (1994). Natural controls of fluvial denudation rates in major world drainage basins. *Journal of Geophysical Research*, B, 99(7), 13,871–13,883.
- Tabor, R. and Cady, W. (1978). The structure of the Olympic Mountains, Washington - Analysis of a subduction zone. Technical Report 1033, USGS Professional Paper 1033.
- Thiede, R. C., Arrowsmith, J. R., Bookhagen, B., McWilliams, M. O., Sobel, E. R. and Strecker, M. R. (2005). From tectonically to erosionally controlled development of the Himalayan Orogen. *Geology*, 33(8), 689–692.
- Thiede, R. C., Bookhagen, B., Arrowsmith, J. R., Sobel, E. R. and Strecker, M. R. (2004). Climatic control on rapid exhumation along the Southern Himalayan Front. *Earth and Planetary Science Letters*, 222(3-4), 791–806.
- Tippett, J. M. and Hovius, N. (2000). Geodynamic processes in the Southern Alps, New Zealand. In Summerfield M., A., editor, *Geomorphology and global tectonics*, pages 109–134. John Wiley, Chichester, United Kingdom.
- Travé, A., Calvet, F., Sans, M., Verges, J. and Thirlwall, M. (2000). Fluid history related to the Alpine compression at the margin of the south-Pyrenean Foreland basin: The El Guix anticline. *Tectonophysics*, 321(1), 73–102.
- Tucker, G. E. and Slingerland, R. (1996). Predicting sediment flux from fold and thrust belts. *Basin Research*, 8(3), 329–349.
- Turcotte, D. and Schubert, G. (2002). *Geodynamics*. Cambridge University Press, Cambridge, 2 edition.
- Turcotte, D. L. and Malamud, B. D. (2004). Landslides, forest fires, and earthquakes: examples of self-organized critical behavior. *Physica A: Statistical Mechanics and its Applications*, 340(4), 580–589.
- Upton, P., Craw, D., Caldwell, T. G., Koons, P. O., James, Z., Wannamaker, P. E., Jiracek, G. J. and Chamberlain, C. P. (2003). Upper crustal fluid flow in the outboard region of the Southern Alps, New Zealand. *Geofluids*, 3(1), 1–12.
- Vergés, J., Millan, H., Roca, E., Munoz, J. A., Marzo, M., Cires, J., Den, B. T., Zoetemeijer, R. and Cloetingh, S. (1995). Eastern Pyrenees and related foreland basins; pre-, syn- and post-collisional crustal-scale cross-sections. In *Special issue on Integrated basin studies*, volume 12; 8, pages 903–915. Butterworth [in conjunction with the] Geological Society, Surrey, United Kingdom.
- Vietor, T. and Oncken, O. (2005). Controls on the shape and kinematics of the Central Andean plateau

- flanks: Insights from numerical modeling. *Earth and Planetary Science Letters*, 236(3-4), 814–827.
- Wang, W. H. and Davis, D. M. (1996). Sandbox model simulation of forearc evolution and noncritical wedges. *Journal of Geophysical Research*, B, 101(5), 11,329–11,339.
- Waschbusch, P. J. and Royden, L. H. (1992). Episodicity in foredeep basins. *Geology*, 20(10), 915–918.
- Whipple, K. X. and Meade, B. J. (2004). Controls on the strength of coupling among climate, erosion, and deformation in two-sided, frictional orogenic wedges at steady state. *Journal of Geophysical Research*, F, 109, F01011 1–24.
- White, N., Pringle, M., Garzanti, E., Bickle, M., Najman, Y., Chapman, H. and Friend, P. (2002). Constraints on the exhumation and erosion of the High Himalayan Slab, NW India, from foreland basin deposits. *Earth and Planetary Science Letters*, 195(1-2), 29–44.
- Willett, S., Beaumont, C. and Fullsack, P. (1993). Mechanical model for the tectonics of doubly vergent compressional orogens. *Geology*, 21(4), 371–374.
- Willett, S. D. (1999). Orogeny and orography; the effects of erosion on the structure of mountain belts. *Journal of Geophysical Research*, B, 104(12), 28,957–28,982.
- Willett, S. D., Fisher, D., Fuller, C., Yeh, E. C. and Lu, C. Y. (2003). Erosion rates and orogenic-wedge kinematics in Taiwan inferred from fission-track thermochronometry. *Geology*, 31(11), 945–948.
- Willett, S. D. and Pope, D. C. (2004). Thermo-mechanical models of convergent orogenesis; thermal and rheologic dependence of crustal deformation. In *Rheology and deformation of the lithosphere at continental margins*, pages 179–222. Columbia University Press, New York, NY, United States.
- Willett, S. D., Slingerland, R. and Hovius, N. (2001). Uplift, shortening, and steady state topography in active mountain belts. *American Journal of Science*, 301(4-5), 455–485.
- Wiltschko, D. and Eastman, D. (1983). Role of basement warps and faults in localizing thrust fault ramps. In *Contributions to the tectonics and geophysics of mountain chains*, volume 158; pages 177–190. Geological Society of America, Boulder, CO, United States.
- Wobus, C. W., Hodges, K. V. and Whipple, K. X. (2003). Has focused denudation sustained active thrusting at the Himalayan topographic front? *Geology*, 31(10), 861–864.
- Wojtal, S. and Mitra, G. (1986). Strain hardening and strain softening in fault zone from foreland thrusts. *Geological Society of America Bulletin*, 97(6), 674–687.
- Yong, L., Allen, P. A., Densmore, A. L. and Qiang, X. (2003). Evolution of the Longmen Shan Foreland Basin (Western Sichuan, China) during the Late Triassic Indosinian Orogeny. *Basin Research*, 15(1), 117–138.
- Zeitler, P. K. (1985). Cooling history of the NW Himalaya, Pakistan. *Tectonics*, 4(1), 127–151.
- Zeitler, P. K., Koons, P. O., Bishop, M. P., Chamberlain, C. P., Craw, D., Edwards, M. A., Hamidullah, S., Jan, M. Q., Khan, M. A., Khattak, M. U. K., Kidd, W. S. F., Mackie, R. L., Meltzer, A. S., Park, S. K., Pecher, A., Poage, M. A., Sarker, G., Schneider, D. A., Seeber, L. and Shroder, J. F. (2001). Crustal reworking at Nanga Parbat, Pakistan; metamorphic consequences of thermal-mechanical coupling facilitated by erosion. *Tectonics*, 20(5), 712–728.
- Ziegler, P., Bertotti, G. and Cloetingh, S. A. P. L. (2002). Dynamic processes controlling foreland development. The role of mechanical (de)coupling of orogenic wedges and forelands. In *EGU Stephan Müller Special Publication Series*, volume 1, pages 17–56. EGU.



# Appendices



# A Abbreviations and symbols

## Abbreviations

CCW	Critical Coulomb Wedge theory
EDM	Evolution of Deformation Map
ELA	Equilibrium Line Altitude
ISU	Incremental Surface Uplift
OOSD	Out-Of-Sequence Displacement index
PIV	Particle Image Velocimetry

## Symbols related to CCW

$x, y, z$	Cartesian coordinates [ $m$ ]
$\tau$	Shear stress [ $Pa$ ]
$\tau_b$	Basal shear stress [ $Pa$ ]
$\mu_0$	Coefficient of internal friction
$\mu_b$	Coefficient of basal friction
$\phi_0$	Angle of internal friction [ $^\circ$ ]
$\phi_b$	Angle of basal friction [ $^\circ$ ]
$C$	Cohesion [ $Pa$ ]
$\sigma_N$	Normal stress [ $Pa$ ]
$p_f$	Fluid pressure [ $Pa$ ]
$\rho$	Density of wedge [ $kg/m^3$ ]
$g$	Acceleration due to gravity = 9.81 [ $m/s^2$ ]
$H_w$	height of wedge [ $m$ ]
$\rho_w$	Density of water [ $kg/m^3$ ]
$D$	Height of the water column [ $m$ ]
$\lambda_0$	Internal Hubbert and Rubey pore fluid ratio
$\lambda_b$	Basal Hubbert and Rubey pore fluid ratio
$K$	Push from the rear
$\alpha$	Surface slope [ $^\circ$ ]
$\beta$	Dip of the detachment [ $^\circ$ ]
$\Psi_0$	Angle between $\sigma_1$ and the surface slope [ $^\circ$ ]
$\Psi_b$	Angle between $\sigma_1$ and the detachment [ $^\circ$ ]

## Symbols related to the scaling of analogue experiments

$S$	Scaling factor
$C$	Cohesion of natural rocks [ $Pa$ ]
$\rho$	Density of natural rocks [ $kg/m^3$ ]
$g$	Acceleration due to gravity = 9.81 [ $m/s^2$ ]
$C_M$	Cohesion of analogue materials [ $Pa$ ]
$\rho_M$	Density of analogue materials [ $kg/m^3$ ]
$a$	Acceleration during analogue experiments = 9.81 [ $m/s^2$ ]



**Symbols related to experiment analysis**

$H_0$	Height of the undeformed multilayer [ $m$ ]
$H$	Height above the singularity [ $m$ ]
$L_{fp}$	Horizontal distance between the deformation front of frontal accretion and the singularity [ $m$ ]
$L_{bp}$	Horizontal distance between the deformation front of basal accretion and the singularity [ $m$ ]
$L_r$	Horizontal distance between the deformation front of the retro-wedge and the singularity [ $m$ ]
$U$	Uplift [ $m$ ]
$E$	Erosion [ $m$ ]
$D$	Length of a thrust [ $m$ ]
$e_{xy}$	Horizontal shear strain [%]
$s_{fw}$	Sample standard deviation of wavelength of frontal accretion
$s_{fs}$	Sample standard deviation of spacing of frontal accretion
$s_{bw}$	Sample standard deviation of wavelength of basal accretion

**Symbols related to the calculation of flexure**

$V_0$	Vertical load of orogen [ $N$ ]
$W$	Width of the hypothetical orogen = 1 [ $m$ ]
$L$	Converted length of the pro-wedge [ $m$ ]
$H_c$	Converted height of the axial-zone above the singularity [ $m$ ]
$\alpha$	Flexural parameter [ $m$ ]
$D$	Flexural rigidity of the plate [ $Nm$ ]
$g$	Acceleration due to gravity = 9.81 [ $m/s^2$ ]
$\rho_{orogen}$	Density of a hypothetical orogen [ $kg/m^3$ ]
$\rho_{sed}$	Density of sediments with which the foredeep is filled with [ $kg/m^3$ ]
$w_0$	Deflection of plate at $x = 0$ [ $m$ ]

## B Supplementary data on DVD

Experiment 9.05:	9.05 basis.avi 9.05 $v_x$ .avi 9.05 $v_y$ .avi 9.05 $e_{xy}$ .avi	Experiment 9.35:	9.35 basis.avi 9.35 $v_x$ .avi 9.35 $v_y$ .avi 9.35 $e_{xy}$ .avi
Experiment 9.06:	9.06 basis.avi 9.06 $v_x$ .avi 9.06 $v_y$ .avi 9.06 $e_{xy}$ .avi		
Experiment 9.09:	9.09 basis.avi 9.09 $v_x$ .avi 9.09 $v_y$ .avi 9.09 $e_{xy}$ .avi		
Experiment 9.10:	9.10 basis.avi 9.10 $v_x$ .avi 9.10 $v_y$ .avi 9.10 $e_{xy}$ .avi		
Experiment 9.11:	9.11 basis.avi 9.11 $v_x$ .avi 9.11 $v_y$ .avi 9.11 $e_{xy}$ .avi		
Experiment 9.15:	9.15 basis.avi 9.15 $v_x$ .avi 9.15 $v_y$ .avi 9.15 $e_{xy}$ .avi		
Experiment 9.20:	9.20 basis.avi 9.20 $v_x$ .avi 9.20 $v_y$ .avi 9.20 $e_{xy}$ .avi		
Experiment 9.25:	9.25 basis.avi 9.25 $v_x$ .avi 9.25 $v_y$ .avi 9.25 $e_{xy}$ .avi		



## C Technical specifications of tested springs

Number of spring	Diameter of wire [mm]	Mean diameter of spring [mm]	External diameter of spring [mm]	$F_{Nmax}$ [N]
KM 3315	1.6	20.0	21.6	57.25
KM 3349	1.8	18.2	20.0	101.60
KM 3375	2	19.0	21.0	84.16
KM 3415	2.5	20.0	22.5	200.70
KM 3447	3.0	19.8	22.8	407.60
KM 3465	3.2	20.0	23.2	442.20

Table C.1: Technical specifications of tested springs.



## D List of experiments

### Test-experiments Group A

Material	Sand: S30T 1 <sup>st</sup> charge, 20 – 630 $\mu m$ Glass beads: 300 – 400 $\mu m$ Sandpaper: < 400 $\mu m$
Setup	No flexure, thickness of lower (upper) plate 5 (10) <i>cm</i> , position of glass-bead layer in lower (upper) plate at 2.5 (5) <i>cm</i>
Documentation	Photos at every 10 <i>cm</i> of convergence, video

Experiment	Location of erosion	Mode of erosion*
4.06	∅	∅
4.07	pro-wedge	distributed
4.08	retro-wedge	distributed

\* Erosion was simulated after 40 *cm* of convergence, at every 10 *cm* of convergence (see section 4.2).

Table D.1: Test-experiments Group A

### Test-experiments Group B

Material	Sand: S30T 2 <sup>nd</sup> charge, 20 – 630 $\mu m$ Glass beads: 300 – 400 $\mu m$ Sandpaper: < 400 $\mu m$
Setup	Flexure (spring KM3415 [4 in text])
Documentation	Photos at every 10 <i>cm</i> of convergence, video

Experiment	Distance spring - free end [ <i>cm</i> ]	Thickness of lower/upper plate [ <i>cm</i> ]	Thicknessratio lower : upper sand unit*
9.01	44	3/10	1 : 1
9.02	44	6/6	1 : 1
9.03	44	6/6	1 : 2
9.04 <sup>†</sup>	30	6/6	1 : 2

\* Lower sand unit is located beneath, upper sand unit is located above the glass-bead layer.

<sup>†</sup> No photographic documentation.

Table D.2: Test-experiments Group B

## 1<sup>st</sup> experimental series

Material	Sand: S30T 2 <sup>nd</sup> charge, 20 – 630 $\mu m$ Glass beads: 300 – 400 $\mu m$ Sandpaper: < 400 $\mu m$
Setup	Flexure (spring KM3415 [4 in text] 30 <i>cm</i> from free end) No change of the mechanic stratigraphy across the singularity. An additional glass-bead layer is located between upper plate base and sand. Thickness of the sand layer 6 <i>cm</i> .
Documentation	Photos at every 10 <i>cm</i> of convergence, video, PIV

Experiment	Flexure	Number of detachments	Height of detachment layer(s) above conveyor belt [ <i>cm</i> ]
9.05	✓	1	2
9.15	✓	0	∅
9.20	✓	2	2 and 4
9.25	∅	1	2
9.35*	✓	0	∅

\* Upper plate consists of mortar.

Table D.3: Kinematic boundary conditions of 1<sup>st</sup> experimental series.

## 2<sup>nd</sup> experimental series

Material	Sand: S30T 2 <sup>nd</sup> charge, 20 – 630 $\mu m$ Glass beads: 300 – 400 $\mu m$ Sandpaper: < 400 $\mu m$
Setup	Flexure (spring KM3415 [4 in text] 30 <i>cm</i> from free end) Mechanic stratigraphy is the same as in experiment 9.05, which is used as reference. An additional glass-bead layer is located between upper plate base and sand.
Documentation	Photos at every 10 <i>cm</i> of convergence, video, PIV

Experiment	Location of erosion	Mode of erosion*
9.05 <sup>†</sup>	∅	∅
9.06	retro-wedge	distributed
9.07	pro-wedge	§
9.08	retro-wedge	distributed <sup>‡</sup>
9.09	pro-wedge	distributed
9.10	pro-wedge	focused
9.11	retro-wedge	focused

\* See section 4.2 for further description. Erosion was simulated after 40 *cm* of convergence, at every 10 *cm* of convergence.  
<sup>†</sup> Reference experiment.  
<sup>§</sup> Maximum erosion (distributed) of 1 *cm* per 10 *cm* of convergence at the toe of the pro-wedge.  
<sup>‡</sup> Maximum erosion 2 *cm* was simulated at every 20 *cm* convergence.

Table D.4: Kinematic boundary conditions of 2<sup>nd</sup> experimental series.

### 3<sup>rd</sup> experimental series

Material	Sand: S30T 2 <sup>nd</sup> charge, 20 – 630 $\mu\text{m}$ Glass beads: 300 – 400 $\mu\text{m}$ Sandpaper: < 400 $\mu\text{m}$
Setup	Flexure (spring KM3415 [4 in text] 30 <i>cm</i> from free end) Mechanic stratigraphy is the same as in experiment 9.05, which is used as reference. An additional glass-bead layer is located between upper plate base and sand.
Documentation	Photos at every 10 <i>cm</i> of convergence, video, PIV

Experiment	Mode of erosion*	Maximum erosion of pro-/retro-wedge [ <i>cm</i> ] <sup>†</sup>
9.12	distributed	0.5/1
9.16	focused	0.5/1
9.17	distributed	1/0.5
9.18	focused	1/0.5

\* See section 4.2 for further description. Erosion was simulated after 40 *cm* of convergence.  
<sup>†</sup> Per 10 *cm* convergence.

Table D.5: Kinematic boundary conditions of 3<sup>rd</sup> experimental series.



### 4<sup>th</sup> experimental series

Material	Sand: S30T 2 <sup>nd</sup> charge, 20 – 630 $\mu m$ Glass beads: 300 – 400 $\mu m$ Sandpaper: < 400 $\mu m$
Setup	Flexure (spring KM3415 [4 in text] 30 <i>cm</i> from free end) Mechanic stratigraphy is the same as in experiment 9.05, which is used as reference. An additional glass-bead layer is located between upper plate base and sand.
Documentation	Photos at every 10 <i>cm</i> of convergence, video, PIV

Experiment	Mode of erosion*	Location of erosion	Maximum erosion [ <i>cm</i> ] <sup>†</sup>
9.21	distributed	retro-wedge	0.5
9.22	distributed	retro-wedge	2

\* See section 4.2 for further description. Erosion was simulated after 40 *cm* of convergence.  
<sup>†</sup> Per 10 *cm* convergence.

Table D.6: Kinematic boundary conditions of 4<sup>th</sup> experimental series.

### 5<sup>th</sup> experimental series - Cascadia (Conducted by Dirk Scherler and Silvan Hoth)

Material	Sand: S30T 2 <sup>nd</sup> charge, 20 – 630 $\mu m$ Glass beads: 300 – 400 $\mu m$ Sandpaper: < 400 $\mu m$
Setup	Flexure (spring KM3415 [4 in text] 30 <i>cm</i> from free end) No change of the mechanic stratigraphy across the singularity, except a glass-bead layer between upper plate base and sand. Exp. 9.23. Mechanic stratigraphy is the same as in experiment 9.15. Exp. 9.24. Incoming layer consists of 3 <i>cm</i> sand, upper plate is made up of mortar, which also covers the first 70 <i>cm</i> of the lower plate.
Erosion	Exp. 9.23. Erosion pattern resembles the one observed in Cascadia. Erosion was simulated at every 10 <i>cm</i> of convergence, after 100 <i>cm</i> of initial convergence. Exp. 9.24. Erosion pattern resembles the one observed in Cascadia. Erosion was simulated at every 20 <i>cm</i> of convergence, after 290 <i>cm</i> of initial convergence.
Documentation	Photos at every 10 <i>cm</i> of convergence, video, PIV

# Curriculum vitae

Name: Silvan Hoth  
Born: 3. September 1974, Schwedt an der Oder  
Citizenship: German

## School

1981 – 1989 Polytechnische Oberschule Neubrandenburg, Germany  
1989 – 1990 Erweiterte Oberschule Neubrandenburg, Germany  
1990 – 1994 Gymnasium Großburgwedel, Germany  
Degree: Abitur

## University

1995 – 1999 Freiberg University of Mining and Technology, Germany  
1999 – 2000 Royal Holloway and Bedford New College, University of London, UK  
Degree: Master of Science in Basin evolution and Dynamics  
Master Thesis (Royal Holloway, Freiberg):  
*Structural and sedimentological evolution of Block 53/10 South Hewett Basin during the Upper Rotliegend II. A seismic attribute approach.*  
1998 – 2000 Scholarship of Studienstiftung des deutschen Volkes

## Research

2001 – 2005 Research Assistant at GFZ Potsdam, Germany; Section 3.1  
»Lithosphere Dynamics« (Prof. Onno Oncken)